# WIDE ANGLE X-RAY SCATTERING PROBES CHAIN ORDER AND IDENTIFIES LIQUID-LIQUID PHASE COEXISTENCE IN ORIENTED LIPID MEMBRANES

A Dissertation

Presented to the Faculty of the Graduate School

of Cornell University

In Partial Fulfillment of the Requirements for the Degree of

Doctor of Philosophy

by

Thalia Tilden Mills

August 2007

# WIDE ANGLE X-RAY SCATTERING PROBES CHAIN ORDER AND IDENTIFIES LIQUID-LIQUID PHASE COEXISTENCE IN ORIENTED LIPID MEMBRANES

Thalia Tilden Mills, Ph.D.

Cornell University 2007

We have used grazing incidence wide-angle x-ray scattering (GIWAXS) on oriented lipid multilayers to measure chain order and to examine liquid-liquid coexistence in the system DOPC/DPPC/cholesterol, a model for the outer leaflet of the cell plasma membrane. Coexistence of liquid-disordered (Ld) and liquid-ordered (Lo) domains is thought to be related to "rafts" in the cell membrane, cholesterol-rich lipid heterogeneities which provide platforms for protein sorting. Many of the methods used for measuring liquid-liquid coexistence in model membranes require a potentially perturbing probe, while x-ray scattering is probe-free. In unoriented (powder) x-ray data, scattering from the Ld and Lo phases looks very similar, whereas in GIWAXS patterns from oriented samples, these phases are easily distinguishable because of the differences in their chain orientational order. By using a simple analytical model to relate the GIWAXS data to the chain orientational distribution, we fit our data to obtain the average chain orientational order parameter, $S_{mol}$. While this type of analysis has been well-used for liquid crystals, it is not commonly applied to model membrane systems. For DOPC/cholesterol and DPPC/cholesterol mixtures, composition and temperature dependent trends in $S_{mol}$ determined by GIWAXS are consistent with earlier NMR data. Addition of 40% cholesterol to liquid-phase DPPC or DOPC more than doubles $S_{mol}$. In addition to measuring chain orientational order parameters for binary mixtures of DOPC/cholesterol and DPPC/cholesterol, we have measured GIWAXS for ternary mixtures where fluorescence microscopy and NMR

indicate the coexistence of Ld and Lo phases below the miscibility transition temperature, $T_{mix}$. In order to fit to the GIWAXS data for these mixtures at low temperature, we required two values of $S_{mol}$, which we interpret as evidence of coexisting Ld and Lo phases. Our $T_{mix}$ values based on x-ray work agree reasonably (to within the 5-10˚C temperature steps used) with the $T_{mix}$ values based on the NMR and microscopy work of Veatch et al. (Veatch and Keller, 2003b; Veatch et al., 2004; Veatch et al., 2007b). This approach provides a new method for examining phase coexistence in model membranes without the need to add a potentially perturbing probe.

# BIOGRAPHICAL SKETCH

Thalia Tilden Mills attended Swarthmore College, where she received a B.A. in 2000 with majors in physics and chemistry. She started Cornell University in the physics Ph.D. program in the Fall of 2000. Her most significant accomplishment during seven years of graduate school was making (and eating) many, many pans of brownies from Rosie's cookbooks (introduced to her by her friend Otavia). Thalia highly recommends purchasing both cookbooks by Judy Rosenberg: *Rosie's Bakery All-Butter, Fresh Cream, Sugar-Packed, No-Holds-Barred Baking Book* and *Rosie's Bakery Chocolate-Packed Jam-Filled Butter-Rich No-Holds-Barred Cookie Book*. Her favorite recipe is probably the peanut butter brownies, but the most popular seem to be the cream cheese brownies ("boom booms").

*To Mom ("D." or "S.") and Dad*

# ACKNOWLEDGMENTS

Many thanks to my thesis advisor, Dr. Gerald Feigenson, and Drs. Stephanie Tristram-Nagle and John Nagle, my current employers and collaborators on the thesis project who were very helpful with both experiments and supervision of the thesis writing process. I learned much from the collaboration between the Feigenson and Nagle labs. This work greatly benefited by being able to combine expertise in lipid phase diagrams (Feigenson lab) with expertise in lipid x-ray scattering (Nagle lab).

I owe a great debt to Gil Toombes. I am very happy that Gil shared his idea for the GIWAXS project with me. In addition to giving me the idea for the project, Gil also helped with the analysis. Without Gil's help, I may have ended up with a very big pile of pretty x-ray data and no way to analyze it.

This work would not have been possible without the support of my labmates in the Feigenson lab: Nelson Morales, Fred Heberle, Jiang Zhao, and Jing Wu. They spent many hours at CHESS helping to collect data and preventing me from melting down. Dr. Norbert Kučerka (formerly Nagle lab) also helped collect data.

I thank Drs. Detlef Smilgies and Arthur Woll for their help with the CHESS experiments. I appreciate that the CHESS staff are so willing to take risks on people and projects. Two years ago Detlef got the ball rolling on this project by offering me a week of beamtime after a brief meeting.

I thank Drs. Mark Tate and Gil Toombes for their help with the rotating anode work. I particularly appreciated their patience.

I thank Dr. Sarah Veatch, Dr. Adam Hammond, Dr. Jonathan Sachs, and Elaine Farkas for their encouragement and interest in this project. Sarah was kind enough to supply me with her NMR data before publication.

Jianjun Pan, my office-mate for the bulk of the thesis writing process, has definitely lived up to the gold standard set by my former labmates.

I thank my committee members, Drs. Sol Gruner, Carl Franck, and Jim Sethna for critical reading of the thesis.

I thank the following sources of support for this thesis work: NIH Molecular Biophysics Training Grant, NSF MCB-0315330 to G. W. Feigenson, NIH Grant GM 44976 to the Nagle group, NSF DMR-0225180 to CHESS, and DOE DE-FG02-97ER62443 for support of the Gruner anode.

In addition to the work presented in this thesis, I was fortunate to work with a number of people on a variety of projects at Cornell. While in the Feigenson lab, I learned about neutron scattering from lipids from Drs. Jeremy Pencer, David Worcester, Susan Krueger, and John Katsaras. While in the Pollack group, I learned about nanofabrication and x-ray scattering from nucleic acids from my advisor, Dr. Lois Pollack, from my labmates Lisa Kwok (Dr. Lisa now) and Greg Maskel, and from CHESS scientists Drs. Ken Finkelstein and Ernie Fontes. I thank Lisa and Greg for putting up with me and for providing me with some of my best memories from graduate school. Drs. Sol Gruner, Don Bilderback, and David Barbano mentored me during a summer of x-ray scattering from cheese, which makes a great conversation starter.

Thanks to my undergraduate thesis advisors: Profs. Robert Pasternack and Peter Collings. They and my other Swarthmore professors were always encouraging.

My family has been supportive throughout this process. Mom, Dad, Debby, Stephanie, Nate, Alicia, and Tilden: I thank you for continuing to send me postcards and phone me despite serious neglect on my part.

Thanks to Elizabeth and Dana for being great housemates for 6.5 years; because of you, Ithaca became home. And thanks to Gil for looking after me, for writing my family postcards and for sending them cookies.

And thanks to everyone who helped make great memories for me during graduate school including: "The Roadtrip" to start out graduate school, Swarthmore reunions in Ithaca, the Fit Bird Society, hiking and camping adventures, Cortland trips, IM basketball, berry picking, Spike's, Mrs. Hysters, the Mermaid Inn, the Gilmore Girls, and trips to the Dairy Bar. Special thanks to Henri, Anthony Trollope, Rosie's cookbooks, and Lisa's Rum Cookery for providing me with endless sources of entertainment.

# TABLE OF CONTENTS

# LIST OF FIGURES

# LIST OF TABLES

# LIST OF ABBREVIATIONS

| | |
|---|---|
| BP | beam picture |
| BSM | brain sphingomyelin |
| CARS | coherent anti-Stokes Raman spectroscopy |
| CCD | charge-coupled device |
| CHESS | Cornell High Energy Synchrotron Source |
| Chol | cholesterol |
| DLPC | 1,2-dilauroyl-*sn*-glycero-3-phosphocholine |
| DLPE | 1,2-dilauroyl-*sn*-glycero-3-phosphoethanolamine |
| DMPC | 1,2-dimyristoyl-*sn*-Glycero-3-Phosphocholine |
| DOPC | 1,2-dioleoyl-*sn*-glycero-3-phosphocholine |
| DPPC | 1-2-dipalmitoyl-*sn*-glycero-3-phosphocholine |
| DPPC-d62 | 1-2-dipalmitoyl-D62-*sn*-glycero-3-phosphocholine |
| DSC | differential scanning calorimetry |
| DSPC | 1-2-distearoyl-*sn*-glycero-3-phosphocholine |
| EPR | electron paramagnetic resonance |
| ESM | egg sphingomyelin |
| ESR | electron spin resonance |
| FRET | fluorescence resonance energy transfer |
| FWHM | full-width at half-maximum |
| GIWAXS | grazing incidence wide-angle x-ray scattering |
| GUV | giant unilamellar vesicle |
| HPLC | high performance liquid chromatography |
| HWHM | half-width at half-maximum |
| IR | infrared |
| LAXS | low-angle x-ray scattering |
| LB | light background |
| LUV | large unilamellar vesicle |
| MD | molecular dynamics |
| MLV | multilamellar vesicle |
| NMR | nuclear magnetic resonance |
| OPPC | 1-oleoyl-2-palmitoyl-*sn*-glycero-3-phosphocholine |
| PC | phosphatidylcholine |
| PE | phosphatidylethanolamine |
| POPC | 1-palmitoyl-2-oleoyl-*sn*-glycero-3-phosphocholine |
| POPE | 1-palmitoyl-2-oleoyl-*sn*-glycero-3-phosphoethanolamine |
| PS | phosphatidylserine |
| RH | relative humidity |
| RMSE | root mean square error |
| RSE | rapid solvent exchange |
| RTD | resistance temperature detector |
| SANS | small-angle neutron scattering |
| SAXS | small-angle x-ray scattering |
| SM | sphingomyelin |
| SOPC | 1-stearoyl-2-oleoyl-*sn*-glycero-3-phosphocholine |

| | |
|---|---|
| *SSE* | summed square of the residuals |
| *SST* | sum of squares about the mean |
| TFE | trifluoroethanol |
| TLC | thin layer chromatography |
| WAXS | wide-angle x-ray scattering |

# LIST OF SYMBOLS

**LATIN ALPHABET**

| | |
|---|---|
| $a$ | interchain spacing proposed by Spaar and Salditt and Sega et al. |
| $A$ | $I(\phi)$ fitting parameter: proportionality constant (has subscript "1" or "2" in the double order parameter fit); $A_{tot}$ refers to $A$ (single order parameter fit or $A_1 + A_2$ (double order parameter fit) |
| $A_c$ | area/chain in the direction perpendicular to the chain |
| $A_L$ | area/lipid (or headgroup) |
| $A(\mathbf{q})$ | Fourier transform of electron density |
| $b$ | beam size |
| $d$ | general Bragg spacing ($=2\pi/q$) |
| $d_{cc}$ | chain-chain correlation distance ($=2\pi/q_{cc}$) |
| $d_L$ | lamellar repeat distance |
| $d_{rod}$ | rod spacing in Leadbetter model ($=d_{cc}$ for lipid membranes) |
| $D$ | Dawson's integral |
| $D_W$ | water thickness |
| $E$ | x-ray energy |
| $f$ | sample footprint |
| $f(\beta)$ | orientational distribution function |
| $I$ | scattering intensity |
| $I_0$ | modified Bessel function of the first kind |
| $I_{back}$ | $I(\phi)$ fitting parameter: constant background |
| $I_T$ | total scattering intensity |
| $\mathbf{k}_i$ | incident x-ray wavevector (with magnitude $k$) |
| $\mathbf{k}_f$ | final x-ray wavevector (with magnitude $k$) |
| $K_A$ | area compressibility modulus |
| $l$ | distance traveled by x-rays through sample in absorption calculation |
| $L$ | length of rod (or chain) |
| Lβ | gel phase (untilted chains) |
| Lβ' | gel phase (tilted chains) |
| Ld | liquid disordered phase |
| Lo | liquid ordered phase |
| $M_1$ | $^2$H NMR first moment |
| $m$ | $I(\phi)$ fitting parameter: describes the width of the Maier-Saupe distribution (has subscript "1" or "2" in the double order parameter fit) |
| $\mathbf{n}$ | membrane normal |
| $\mathbf{n}_L$ | local director for group of rods ("grain") in Leadbetter model |
| $p$ | pixel position on the detector |
| $P$ | pressure |
| $P_1$ and $P_2$ | phase fractions: fraction of sample composed of each orientational distribution (1 or 2) as determined by the double order parameter fits |
| Pβ | ripple phase |
| $\mathbf{q}$ | scattering wavevector (with magnitude $q$ and components $q_x$, $q_y$, and $q_z$) |
| $q_{cc}$ | maximum of lipid WAXS (chain-chain correlation peak) |

| | |
|---|---|
| $q_r$ | $\sqrt{q_x^2 + q_y^2}$ (horizontal component of scattering wavevector) |
| $\mathbf{r}_{CD}$ | vector in plane of methylene group (perpendicular to $\mathbf{r}_{mol}$) |
| $\mathbf{r}_{mol}$ | vector along the carbon-carbon axis |
| $R^2$ | coefficient of determination |
| $S$ | sample-to-detector distance |
| $S_{CD}$ | NMR segmental order parameter |
| $S_{mol}$ | average molecular order parameter |
| $S_{mol}^n$ | molecular order parameter (per methylene) |
| $t$ | 5 μm, or one half the thickness of a lipid oriented sample |
| $T$ | temperature |
| $T_m$ | main gel-fluid transition (melting) temperature |
| $T_{mix}$ | miscibility transition temperature |
| $V$ | volume |
| $V_W$ | water volume |
| $Z$ | Maier-Saupe normalization constant |

**GREEK ALPHABET**

| | |
|---|---|
| $\alpha$ | angle of incidence of x-rays on the sample |
| $\beta$ | angle between chain (rod) axis and membrane normal |
| $\delta\nu_{max}$ | maximum value of the quadrupolar coupling constant for a deuteron on a CH bond |
| $\theta$ | scattering angle |
| $\lambda$ | x-ray wavelength |
| $\mu$ | absorption length |
| $\nu$ | degrees of freedom |
| $\xi$ | correlation length |
| $\phi$ | angle measured from the horizontal ($q_r$ or $x$-axis) on the detector |
| $\phi_L$ | angle between **q** and the sample plane |
| $\rho(r)$ | electron density |
| $\sigma_i$ | error for data point $i$ |
| $\chi$ | azimuthal angle in the sample coordinate system |
| $\chi^2$ | Chisquare |

# Chapter 1 - Introduction

## 1.1 Overview

The study of liquid-liquid phase coexistence in model membranes has received much attention in the last decade because of possible connections to cell membrane lipid heterogeneities rich in cholesterol ("rafts"). Rafts, which provide platforms for sorting of certain proteins, have been implicated in numerous cellular processes such as signaling and transport. The focus of this thesis is on the use of wide-angle x-ray scattering from oriented lipid multilayers as a tool for characterizing chain order in liquid phases (liquid-ordered and liquid-disordered) and for identifying liquid-liquid phase coexistence in the ternary mixture DOPC/DPPC/cholesterol, a model for the outer leaflet of the cell plasma membrane. The first part of this chapter presents an overview of the raft hypothesis, the structure of different lamellar phases, characterization of chain order, and methods for identifying phase coexistence in model membranes. The last part of the chapter is an introduction to x-ray scattering from model membranes, with an emphasis on the potential of wide-angle scattering from oriented multilayers for characterizing liquid phases.

## 1.2 Cell membranes and the raft hypothesis

Lipids, surfactant molecules with a hydrophilic headgroup and hydrophobic chains, self-assemble into bilayer structures in the presence of water. Cell membranes are complex structures, consisting of a lipid bilayer composed of a large number of different lipids with embedded proteins (Fig. 1.1). In 1972 Singer and Nicholson proposed the "fluid mosaic model" for the membrane. In this model, the cell membrane consists of a fluid matrix composed of an asymmetric lipid bilayer in the liquid-phase, which provides a semi-impermeable barrier between the interior and exterior of the cell. The membrane proteins are either partially embedded in one of

the membrane leaflets or span the entire thickness of the membrane (trans-membrane proteins). Within the lipid matrix, the proteins are free to diffuse laterally and rotate along axes normal to the plane of the membrane, but the proteins do not tumble at significant rates due to their hydrophilic anchors in the aqueous phase. According to the fluid mosaic model, the lipids play the passive role of providing the structural glue holding the membrane together.

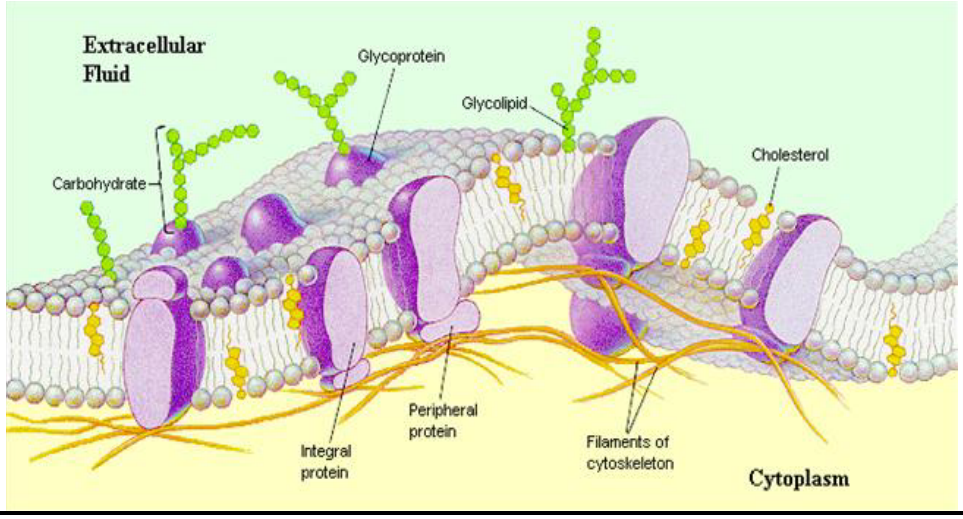


Figure 1.1. Cartoon of the cell plasma membrane (from Chiras, 1999).

In 1988 Simons and van Meer proposed a physiologically important role for lipid heterogeneities in cell membranes. They postulated that lipid domains rich in sphingolipids and glycerolipids interact preferentially with certain proteins, helping with the process of protein sorting into epithelial cell precursors in the Golgi apparatus. In 1997 Simons and Ikonen coined the term "rafts," small domains rich in sphingolipids and cholesterol into which certain proteins preferentially partition. These rafts form a platform for cellular processes which require close proximity of proteins, such as signaling and trafficking.

The evidence for these cellular lipid domains, which are too small to be observed with optical microscopy, relies on indirect methods such as detergent

extraction and cholesterol depletion (Munro, 2003). In detergent resistance experiments, membrane fractions which are insoluble in non-ionic detergents have been found to be enriched in sphingolipids, cholesterol, and "raft-associated" proteins (Brown and London, 1997). The affinity of certain proteins for the detergent-insoluble fraction can be increased by clustering and crosslinking events (Holowka et al., 2005). Cholesterol depletion is another commonly used method for studying rafts (Munro, 2003; London, 2005). In cholesterol depletion experiments, methyl-beta-cyclodextrin removes cholesterol from the cell. If a cellular process slows or stops after cholesterol depletion, it is assumed that the process was raft-mediated. Cholesterol depletion and detergent resistance experiments are very complex and yet often interpreted simplistically. For example, detergent fractionating is usually conducted at 4˚C, significantly below the typical mammalian body temperature of 37˚C. These low temperatures and the detergent itself may promote the formation of cholesterol-rich domains which would not exist under normal conditions (Heerklotz, 2002). Cholesterol depletion may disrupt the cytoskeleton network and may cause the formation of domains of solid-phase lipid in the membrane (London, 2005; Nishimura et al., 2006).

While lipid heterogeneities in the cell membrane are too small to be observed by optical microscopy, macroscopic liquid-liquid phase separation has been observed in models of the outer leaflet of the cell membrane, consisting of ternary mixtures of cholesterol, sphingomyelin or a saturated phospholipid, and an unsaturated phospholipid (see Veatch and Keller, 2005b for a review). In these model membranes, liquid-ordered (Lo) domains, rich in saturated lipid and cholesterol, separate from liquid-disordered (Ld) domains, rich in the unsaturated lipid (phases discussed further in Section 1.3). The Lo domains in model membranes have been linked to the detergent-resistant fractions in cell membranes, although the exact relationship

between liquid-liquid phase coexistence in model membranes and rafts in cell membranes is unclear. Various proposals have been made to connect the macroscopic phase coexistence in model membranes and submicroscopic rafts in cells, including critical fluctuations and regions of limited diffusion, perhaps caused by corrals in the cytoskeleton network (Feigenson, 2006; Hancock, 2006; Kusumi and Suzuki, 2005; London, 2005; Silvius, 2003; Simons and Vaz, 2004; Veatch, 2007). For models of the plasma membrane inner leaflet, which has a much higher percentage of unsaturated lipid, macroscopic phase coexistence has not been observed (Wang and Silvius, 2001); however, raft-mediated protein sorting on the inner leaflet has been implicated in cell signaling (Holowka et al., 2005). Coupling mechanisms between the outer leaflet and inner leaflet have been suggested, but the connection between outer leaflet and inner leaflet heterogeneities in unclear (Edidin, 2003). When interpreting experiments on model membranes, it is important to remember that model membranes are in equilibrium and are symmetric bilayers, while cell membranes are asymmetrical and nonequilibrium structures.

The word "raft" has no universal meaning. Definitions of "raft" include the following: a detergent resistant complex of lipids and proteins; any lipid-based lateral heterogeneity in a plasma membrane; the stable thermodynamic Lo phase in model membranes; or a two-dimensional platform in a plasma membrane involved in immune signal transduction, synapse function, viral entry and exit, protein targeting, or membrane transport (Simons and Vaz, 2004). In this thesis, we will limit the use of the word "raft" to lateral heterogeneities in the cell membrane, while we will use liquid-liquid (or Ld/Lo) phase coexistence to refer to macroscopic domains in model membranes.

Understanding the physical origin and behavior of membrane rafts in vivo will be aided by a better understanding of inhomogeneities in model lipid mixtures that

contain cholesterol. In addition to observation of phase coexistence and phase boundaries, thorough structural characterization of different lamellar lipid phases will help in understanding the structure-function relationships in processes which occur in the cell membrane. For example, matching of the hydrophobic length of proteins with the hydrophobic thickness of the bilayer is one of the mechanisms thought to play a role in protein sorting in cell membranes (see Dumas et al., 1999 and the references therein). Membranes rich in cholesterol are known to have increased hydrophobic thickness (Yeagle, 1985). X-ray scattering provides a tool for structural characterization of the phases.

## 1.3 Lamellar lipid phases

Lipids can form many different structures (hexagonal, lamellar, and others) depending on their headgroup structure, chain length, degree of unsaturation, level of hydration, and temperature. One of the most important principles in determining the lipid phase is the relative size of the hydrophilic headgroups and hydrophobic tails (Israelachvili, 1985). Lipids with hydrophilic and hydrophobic regions roughly equal in size will tend to form bilayers. This thesis focuses on bilayer lamellar lipid phases. Although the cell membrane is thought to be composed of fully-hydrated lamellar-phase lipids, other lipid structures may play a role in certain cellular events such as membrane fusion (Yang and Huang, 2002). Figure 1.2 shows cartoons of the four lamellar phases which we will focus on in this thesis: two gel phases (Lβ and Lβ') and two liquid phases (Ld and Lo).

Both Lβ and Lβ' are characterized by slow lateral diffusion ($\sim 10^{-11}$-$10^{-10}$ $cm^2/s$; Almeida et al., 1993; Rubenstein et al., 1979). In the Lβ phase the highly ordered chains are all parallel to the membrane normal, while in the Lβ' phase, the chains are all tilted at an angle relative to the bilayer normal. The Ld and Lo phases are both

characterized by fast lateral diffusion (~$10^{-8}$-$10^{-7}$ $cm^2/s$; Almeida et al., 1992; Lindblom et al., 1981; Rubenstein et al., 1979). In the Ld phase, the chains are orientationally disordered compared to the gel phases, while the Lo phase is characterized by a higher degree of orientational order than the Ld phase. The Ld, Lβ, and Lβ' phases can all occur for pure lipids; the Lo phase, on the other hand, only forms in mixtures of lipid and cholesterol (or other sterols).

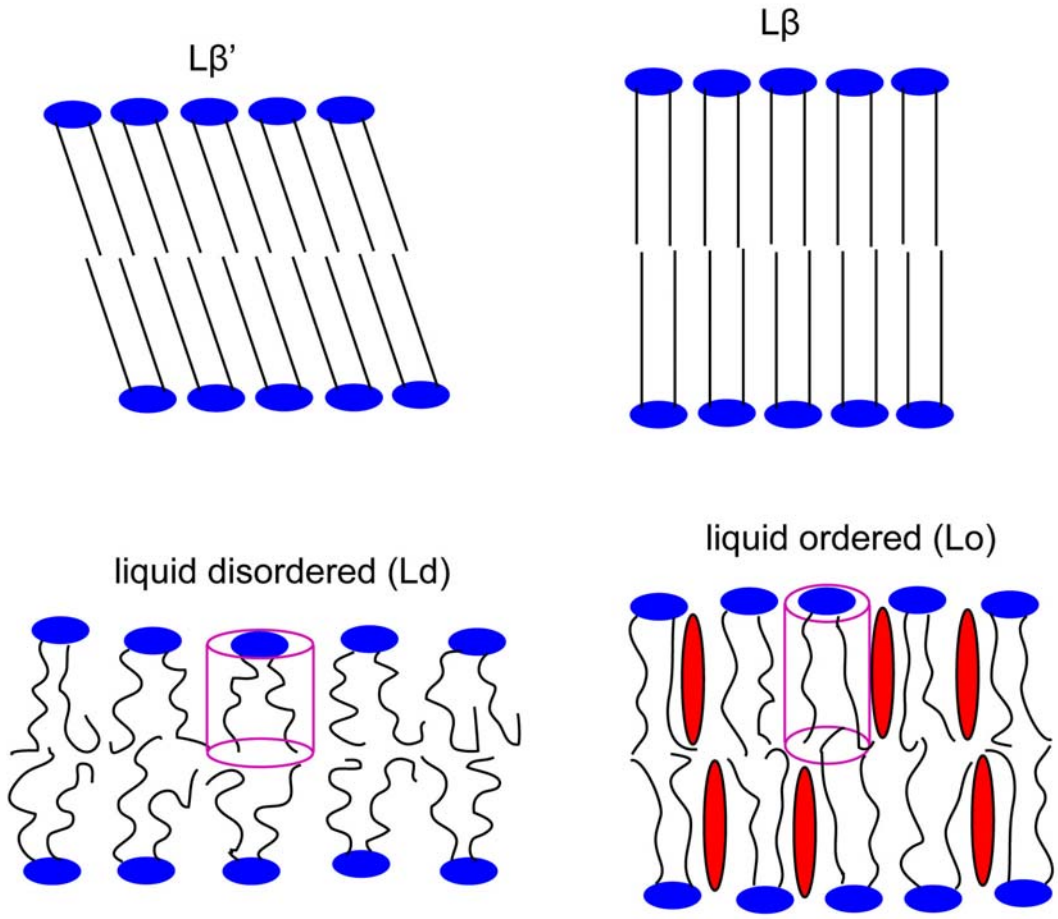


Figure 1.2. Structure of lamellar phases: Lβ', Lβ, Ld, and Lo. Phospholipids are represented with a blue headgroup and two chains. Cholesterol molecules are in red. The cylinders show the volume occupied by a single lipid. In the Lo phase, the chains extend and the lipid area decreases in comparison with the Ld phase.

The temperature at which a lipid transitions from a gel phase to a liquid phase is known as the main transition (or melting) temperature ($T_m$) and is commonly measured by differential scanning calorimetry (DSC) [see Finegold and Singer, 1993]. The melting temperature is dependent on the length of the acyl chains and on the degree of unsaturation (see Gennis, 1989, p. 65-70). Longer chains result in more van der Waals interactions and a higher melting temperature (Nagle and Wilkinson, 1978). Unsaturation causes kinks in the chain which disrupt packing and lower the melting temperature. In discussing lipid phase behavior, it is convenient to divide lipids into three classes (see Fig. 1.3 for examples): (1) high-melting lipids (long-chain saturated phospholipids or sphingomyelins); (2) low melting lipids (unsaturated phospholipids, lipids with highly branched chains, and short chain lipids); (3) cholesterol and other sterols. The low-$T_m$ DOPC and the high-$T_m$ DPPC are examples of phosphatidylcholines (PCs; refererred to as "lecithin" in the older literature). Although DOPC is often used in models for the outer leaflet of the cell membrane, this doubly unsaturated lipid is not naturally occurring in the cell membrane. Mono-unsaturated lipids, with one saturated chain and one unsaturated chain, such as POPC and SOPC, are common components in the cell membrane. While the outer leaflet of the cell membrane is rich in saturated lipid (mostly sphingomyelins), the inner leaflet is thought to be composed mostly of lipid with one unsaturated and one saturated chain: PCs, phosphatidylethanolamines (PEs), and anionic lipid such as phosphatidylserines (PSs) [see Wang and Silvius, 2001]. The partitioning of cholesterol between the two leaflets is unknown, but there may be significantly more cholesterol on the inner leaflet (Edidin, 2003).

Because of its very small hydrophilic headgroup (a single hydroxyl), pure cholesterol crystallizes in water. When cholesterol is adjacent to a lipid chain in the liquid phase, the rigid ring structure of cholesterol restricts the flexibility of the chain

and thus orders the chain (Stockton and Smith, 1976). Increased chain order leads to increased hydrophobic thickness and a decrease in the area per lipid, the well-known cholesterol condensing effect (Yeagle, 1985). In the gel phase, cholesterol can act as an impurity which inhibits highly ordered chain packing (Estep et al., 1978). The role of cholesterol in phospholipid phase behavior is discussed further in Section 1.5.

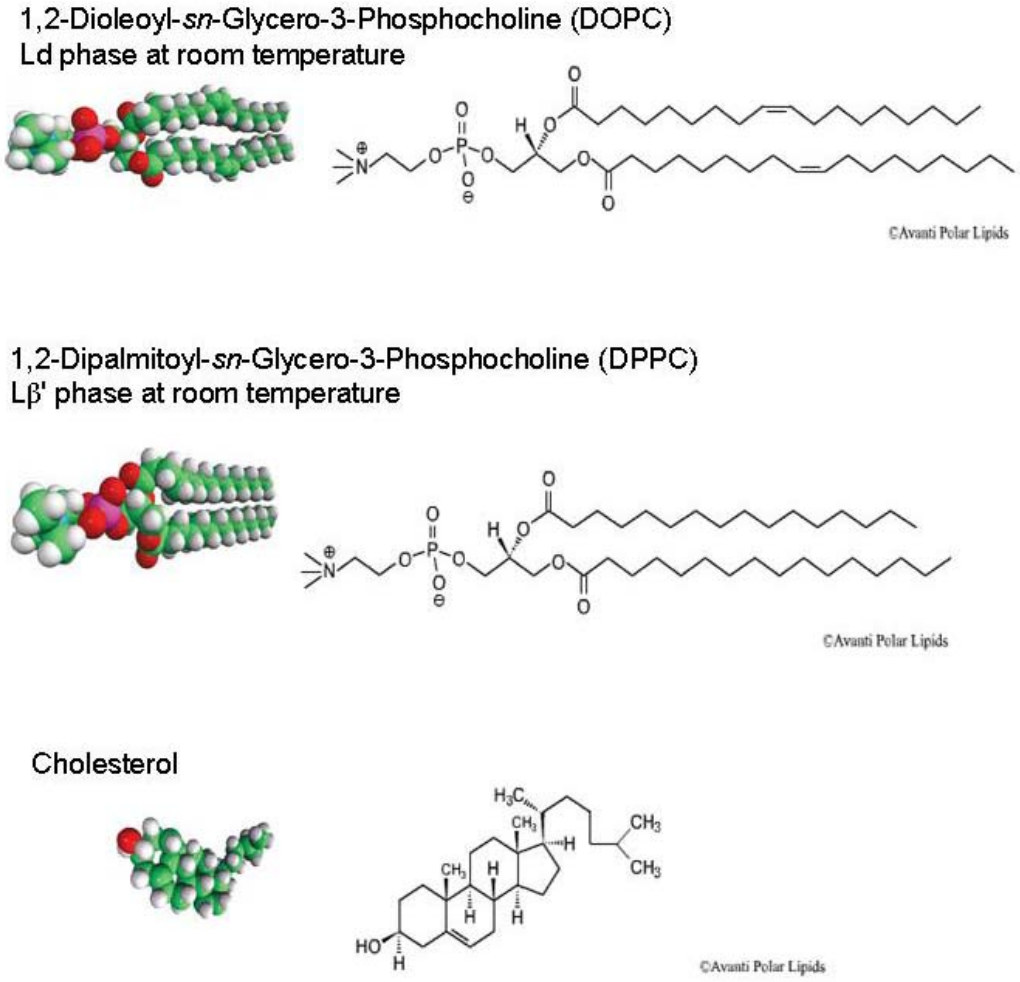


Figure 1.3. Structure of lipids studied in this thesis: DOPC, a low $T_m$ (-17˚C) lipid; DPPC, a high $T_m$ (41.4˚C) lipid; and cholesterol. At 25˚C, DOPC is in the Ld phase, while DPPC is in the Lβ' phase. Compared with PCs, cholesterol has a very small hydrophilic headgroup (hydroxyl) and does not form bilayers by itself. Structures are from the Avanti Polar Lipids website.

## 1.4 Chain order

### 1.4.1 Definitions of orientational order, conformational order, and lateral positional order

Chain order is one of the main properties which distinguishes the different lipid phases. The liquid-ordered phase is interesting because in some properties it is gel-like (chain orientational order) while in other properties it is fluid-like (lateral diffusion, lateral positional ordering). One of the main goals of this thesis is to characterize the effect of temperature and sample composition, particularly the amount of cholesterol, on lipid chain ordering using wide-angle x-ray scattering. Before describing in more detail what is known about the effect of cholesterol on lipid phase behavior, it is useful to define the different types of chain ordering and the relationship between order and the dynamical property of diffusion.

There are three types of chain order which will be referred to in this thesis:

1. The chain conformational order refers to the ratio of *trans*/*gauche* isomers along the chain. In a completely extended chain, all of the segments are in the *trans* conformation, and the chain conformational order is high.
2. The chain orientational order refers to the orientation of the chain (or chain segment), usually taken with respect to the membrane normal. This orientation is described by the angle between the direction of the chain (or chain segment) and the preferred director, the membrane normal (see Section 1.4.2).
3. Lateral positional order refers to the arrangement of a chain with respect to its neighbors. In the case of gel phases, the lateral positional order is high because the chains form a two-dimensional lattice with a well-defined distance between nearest neighbors, clear from the sharp x-ray chain-chain correlation band (see Section 1.7.4). In the liquid phases (Ld or Lo), lateral positional

order is low: the chains form a fluid-like in-plane structure with a wide distribution of nearest-neighbor distances, as shown by the wide x-ray chain-chain correlation band (see Section 1.7.4).

These three types of chain order are not unrelated but also not synonymous or simply correlated. Kodati and Lafleur (1993) have compared infrared (IR) methylene stretching frequencies, sensitive to chain conformational order, with $^2$H NMR quadrupolar splittings, sensitive to chain orientational order. NMR orientational order parameters depend on the *trans*/*gauche* isomer ratio as well as changes in the orientation of the director caused by tilting of the chains (as in the Lβ' phase) and membrane surface undulations. Because of the strong correlation observed between NMR order parameters and IR stretching frequencies as a function of temperature and membrane composition, Kodati and Lafleur (1993) concluded that both techniques were mostly sensitive to the ratio of *trans*/*gauche* isomers, in agreement with previous reports (Seelig and Seelig, 1974; Schindler and Seelig, 1975). In the case of the gel-Ld transition, the orientational order, which is more long range than the lateral positional order, changes spontaneously and the lateral positional order changes as a consequence (Jähnig, 1981). However, orientational order and lateral positional order are not always coupled, as in the case of the Lo phase.

Chain order is a time-averaged structural property. An orientational order parameter gives no information about the rate of angular motion of the chains. Although systems with high lateral positional order often have slow lateral diffusion (and systems with low positional order have fast diffusion), two counterexamples are glass and beta brass. Glasses are disordered structures with slow diffusion, while beta brass has crystalline packing but fast diffusion of atoms.

### 1.4.2 Chain order parameters

Different methods for measuring chain orientational order parameters, including NMR, ESR, and fluorescence polarization, are reviewed in Gennis, 1989. Fluorescence polarization and ESR require potentially perturbing probe molecules, while in $^2$H NMR, the deuterium is thought to have a minimal effect on bilayer phase behavior. Therefore, we focused on comparing our x-ray results for chain orientational order to NMR data (Ch. 4-6). This section focuses on defining NMR order parameters and their relationship to x-ray order parameters.

For chain perdeuterated molecules, each methylene segment gives rise to a different quadrupolar splitting. These quadrupolar splittings are proportional to the segmental order parameter $S_{CD}$, defined as (Seelig and Niederberger, 1974):

$$S_{CD} = \frac{1}{2}\left(3\left\langle \cos^2 \theta_{CD} \right\rangle - 1\right). \tag{1.1}$$

where $\theta_{CD}$ is the angle between the vector $\mathbf{r}_{C\text{-}D}$ and the bilayer normal (see Fig. 1.4A). The brackets imply a time and ensemble average. We are most interested in the molecular order parameter $S_{mol}^{n}$, which describes the orientation of each chain segment with respect to the bilayer normal (Seelig and Neiderberger, 1974):

$$S_{mol}^{n} = \frac{1}{2}\left(3\left\langle \cos^2 \theta_{mol} \right\rangle - 1\right) = -2S_{CD}\,. \tag{1.2}$$

where $\theta_{mol}$ is the angle between $\mathbf{r}_{mol}$ and the bilayer normal (see Fig. 1.4A). Note that the relationship between $S_{mol}^{n}$ and $S_{CD}$ in Eq. 1.2 requires assumptions and simplifications; for instance, this relationship is not valid in the case of a double bond (see Douliez et al., 1995 and Oldfield et al., 1978 for a more detailed discussion of NMR order parameters).

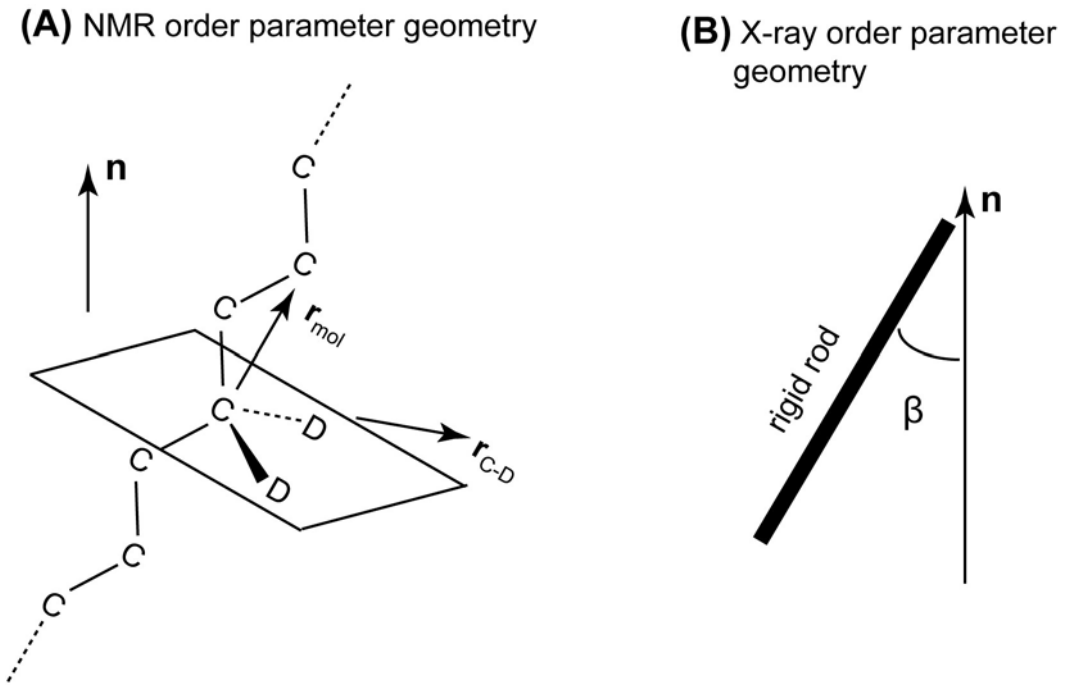


Figure 1.4. (A) Illustration of the geometry for NMR order parameters, which are calculated for each chain segment. $S_{CD}$ is defined in reference to the angle between **n** (the membrane normal) and $\mathbf{r}_{C\text{-}D}$. $S_{mol}$ is defined in reference to the angle between **n** and $\mathbf{r}_{mol}$ (modeled after a figure in Gennis, 1989). (B) The x-ray method assumes the chains are rigid rods. The single x-ray order parameter is defined in reference to the angle $\beta$ between **n** and the rod axis.

The chains in the Ld phase are often modeled with two divisions, one closer to the headgroup region and one closer to the middle of the bilayer. Orientational order of the chain segments closest to the headgroup region (from C-2 to C-8 or C-10) is relatively constant, while the methylene segments toward the middle of the bilayer have significantly more disorder than the segments closer to the surface (see Gennis, 1989, p. 52-55 and the references therein). This behavior is not sensitive to lipid structure as long as the lipid is in the Ld phase (Seelig and Browning, 1978). In an order parameter profile (see Fig. 1.5), the relatively constant order parameter region for segments closer to the headgroups is often referred to as the "plateau region." With the addition of cholesterol to fluid-phase lipid to form the Lo phase, the

orientational order in the plateau region increases, while the segments closer to the middle of the bilayer remain disordered (Nezil and Bloom, 1992; Smondyrev and Berkowitz, 1999).

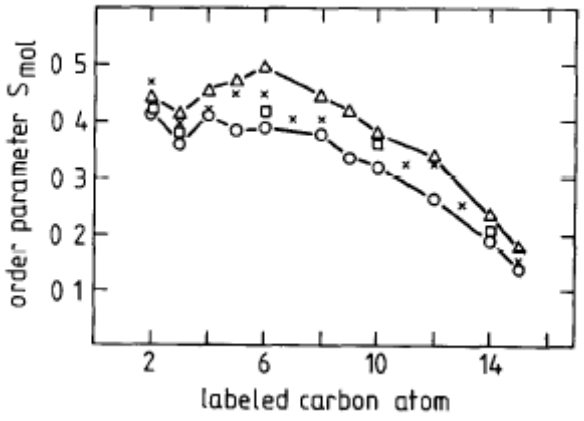


Figure 1.5. Normalized order parameter profile of different lipids, with the molecular order parameter ($S^{n}_{mol}$) as a function of the methylene segment position, with lower numbers closer to the headgroup. Circles, DPPC; triangles, POPC; squares, DPPS; crosses, *Acholeplasma laidlawii* membranes. Taken from Seelig and Browning, 1978.

Often, the NMR first moment, $M_1$, is reported, which is proportional to the average of the quadrupolar splittings over all chain segments (Davis, 1979). In Ch. 5-6, we use an equation that relates $M_1$ to the average molecular order parameter $S_{mol}$, defined as:

$$S_{mol} = \left\langle S^{n}_{mol} \right\rangle = 2\left\langle \left| S_{CD} \right| \right\rangle . \tag{1.3}$$

We have been careful to distinguish between the order parameter for each segment, $S^{n}_{mol}$, and the average molecular order parameter, $S_{mol}$. In the literature, $S_{mol}$ is used for both quantities. Assuming that the average orientation of the chains is directed along the membrane normal, $S_{mol}$ can take on values between 0 and 1, with 0 corresponding to complete orientational disorder and 1 corresponding to perfect orientational order.

The x-ray method (described in Ch. 3) assumes that the acyl chains are rigid rods. In this case, the molecular order parameter is defined as:

$$S_{\mathrm{mol}} = \frac{1}{2}\left(3\left\langle \cos^2 \beta \right\rangle - 1\right). \tag{1.4}$$

where $\beta$ is the angle between the rod axis and the membrane normal (see Fig. 1.4B) and the brackets denote a spatial average. In the liquid crystal literature $S$ is often used in place of $S_{\mathrm{mol}}$. Note that although we use the same name for the NMR $S_{\mathrm{mol}}$ (Eq. 1.3) and the x-ray $S_{\mathrm{mol}}$ (Eq. 1.4), these quantities are not the same. The major difference is that the NMR determination of $S_{\mathrm{mol}}$ does not assume that the chains are rigid rods. In comparing NMR and x-ray order parameters, we focus on trends instead of absolute values.

## 1.5 Role of cholesterol in phospholipid phase behavior

Binary mixtures of phospholipids and cholesterol have been studied with a variety of techniques. Cholesterol has interesting effects on phospholipid phase behavior. Above and below the phospholipid's $T_{\mathrm{m}}$, addition of cholesterol (~40%) leads to the formation of the Lo phase. (Percentages refer to mole percent of a component.) Although there is controversy about the phase diagrams of binary phospholipid/cholesterol mixtures (see Ch. 5), there is general agreement about the following experimental observations and interpretations, which provide a framework for the ternary phase diagrams discussed in Section 1.6.1 ($T_{\mathrm{m}}$ refers to the melting temperature of the lipid, e.g. DPPC):

1. With cholesterol addition, the temperature range for the gel to fluid transition is broadened, as observed by differential scanning calorimetry (DSC). The main gel to fluid transition disappears at high cholesterol concentrations (Ladbrooke et al., 1968; Mabrey et al., 1978; Yeagle, 1985).

2. Below $T_m$, the lateral diffusion coefficient increases with increasing cholesterol concentration, from gel-like (~$10^{-11}$-$10^{-10}$ $cm^2/s$) to fluid-like (~$10^{-8}$-$10^{-7}$ $cm^2/s$). Above $T_m$, the diffusion coefficient decreases as a function of cholesterol concentration, but not drastically as the system remains fluid-like (Almeida et al., 1992, 1993; Filippov et al., 2003; Lindblom et al., 1981; Rubenstein et al., 1979).
3. The effect of cholesterol on lateral diffusion, a dynamic property, is mirrored by its effect on lateral chain organization, a static structural property. Below $T_m$, the lateral chain packing changes from well-ordered (gel-like) to more disordered (fluid-like): cholesterol causes an increase in the distribution of nearest-neighbor distances shown by an increase in the width of the x-ray wide angle scattering. Above $T_m$ the chain packing remains disordered: wide-angle scattering remains broad (see Finean, 1990 and the references therein).
4. In contrast to cholesterol's effect on diffusion (2) and lateral positional order (3), below $T_m$, the addition of cholesterol has only a small effect on chain orientational order: the chains remain highly ordered (Huang et al., 1993). Above $T_m$, cholesterol causes a large increase in chain orientational order, as has been observed with a variety of techniques, including NMR (Haberkorn et al., 1977) and x-ray scattering (Levine and Wilkins, 1971).
5. DPPC (and other saturated PCs) are in the Lβ' phase below $T_m$ for a wide temperature range. With the addition of ~7.5% cholesterol, chain tilt is gone and the system is in the Lβ phase (Ladbrooke et al., 1968).

Both below and above $T_m$, the addition of cholesterol (~40%) results in the formation of the Lo phase. Ipsen et al. (1987) note that cholesterol effectively acts as to "decouple" chain orientational (or conformational) order and lateral positional order. Lindblom et al. (1981) note that there appears to be no connection between the chain

order parameter, a static quantity, and diffusion, a dynamic quantity. The Lo phase is characterized by orientationally ordered chains (gel-like) but low lateral positional order and rapid diffusion (liquid-like). We have spoken in very general terms about orientational order, lateral chain packing, and lateral diffusion. For example, above $T_m$ cholesterol increases the chain orientational order, but the increase in segmental NMR order parameters is much greater for the methylene groups closer to the headgroup region (Nezil and Bloom, 1992; Smondyrev and Berkowitz, 1999). The methyl ends of the chains remain disordered in the Lo phase. While gel phases are well-defined, liquid phases can have a broad range of properties. Often, the liquid-ordered phase is mistakenly referred to as if it had a single set of values for the various properties. Reinl et al. (1992) and Clarke et al. (2006) have used a variety of techniques to examine how the Lo phase changes as a function of temperature and composition in DPPC/cholesterol mixtures.

The umbrella model provides a useful way of understanding the interaction of cholesterol and phospholipids (Huang and Feigenson, 1999). By itself, cholesterol forms crystals and not bilayers because its very small hydrophilic hydroxyl group is not sufficiently large to shield its nonpolar region from water in a bilayer structure. When cholesterol is added to a pure phospholipid, the phospholipid headgroups (umbrellas) are large enough to cover the hydrophobic lipid chains as well as the cholesterol. To accommodate even more cholesterol, the chains straighten (if $T>T_m$) or lose their chain tilt (if $T<T_m$) to allow more space under the phospholipid headgroup. Eventually, the bilayer cannot accommodate more cholesterol, and cholesterol precipitates out in crystals. Note that there are many more models describing cholesterol-lipid interactions (see McConnell and Vrljic, 2003; Zuckermann et al., 1993).

## 1.6 Phase coexistence in model membrane systems

### 1.6.1 The DOPC/DPPC/cholesterol phase diagram

Over the last ten years, there has been a great deal of interest in ternary phase diagrams consisting of a low-$T_m$ lipid, a high-$T_m$ lipid, and cholesterol. Such phase diagrams are often referred to as "pseudo-ternary" with water, the fourth component, in excess. Ternary model membrane phase diagrams are reviewed in Veatch and Keller, 2005b. Figure 1.6 shows a schematic for DOPC/DPPC/cholesterol phase behavior, a model for the outer leaflet of the cell plasma membrane. Figure 1.6 is based on fluorescence microscopy of giant unilamellar vesicles (GUVs) by Veatch and Keller (2003b). Liquid-liquid coexistence in ternary mixtures was first reported using this technique in 2001 (Dietrich et al., 2001; Samsonov et al., 2001), while gel-fluid coexistence in phospholipid mixtures had been observed earlier (see Korlach et al., 1999 and the references therein). In the fluorescence microscopy technique, GUVs, typically 10-50 microns in diameter, are labeled with a fluorescent dye which partitions preferentially into a certain phase. The type of phase coexistence (gel/liquid vs. liquid/liquid) can be determined by the shape of the domains: liquid/liquid coexistence is characterized by circular domains with smooth boundaries, while gel/liquid coexistence is characterized by angular domains with rough boundaries (see offset GUV images in Fig. 1.6). Figure 1.6 summarizes the microscopy results for a single temperature, but the phase behavior has been studied over a range of temperatures. The temperature above which phase coexistence disappears for a given composition is termed the miscibility transition temperature ($T_{mix}$). Values for $T_{mix}$ have been measured for many compositions (Veatch and Keller, 2003b).

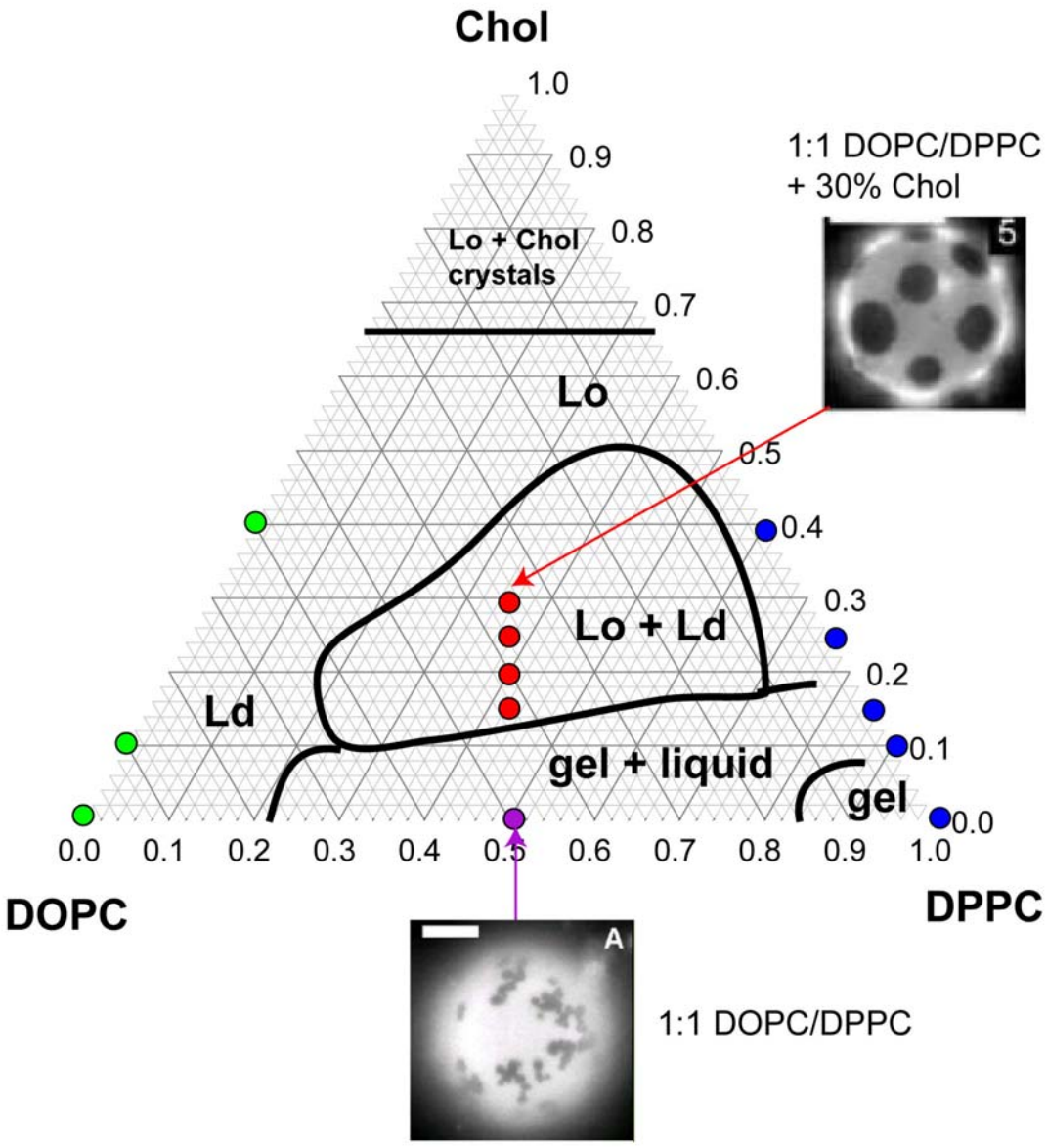


Figure 1.6. Schematic showing regions of liquid-liquid (Lo/Ld) and gel/liquid phase coexistence for DOPC/DPPC/cholesterol at 25˚C based on the fluorescence microscopy work of Veatch et al. (Veatch and Keller, 2003b; Veatch et al., 2004). The GUV images were reproduced from Veatch, 2004. Numbers on the bottom refer to mole fraction of DPPC. Numbers on the right side refer to the mole fraction of cholesterol. The colored dots are samples studied in this thesis using x-ray scattering.

We refer to Fig. 1.6 as a schematic and not a phase diagram because it simply summarizes the GUV results; the existence and type (gel/liquid vs. liquid/liquid) of phase coexistence. In the phase diagram, the gel/Ld region is separated from the Ld/Lo region by a three-phase gel/Ld/Lo region (see Fig. 1.7).

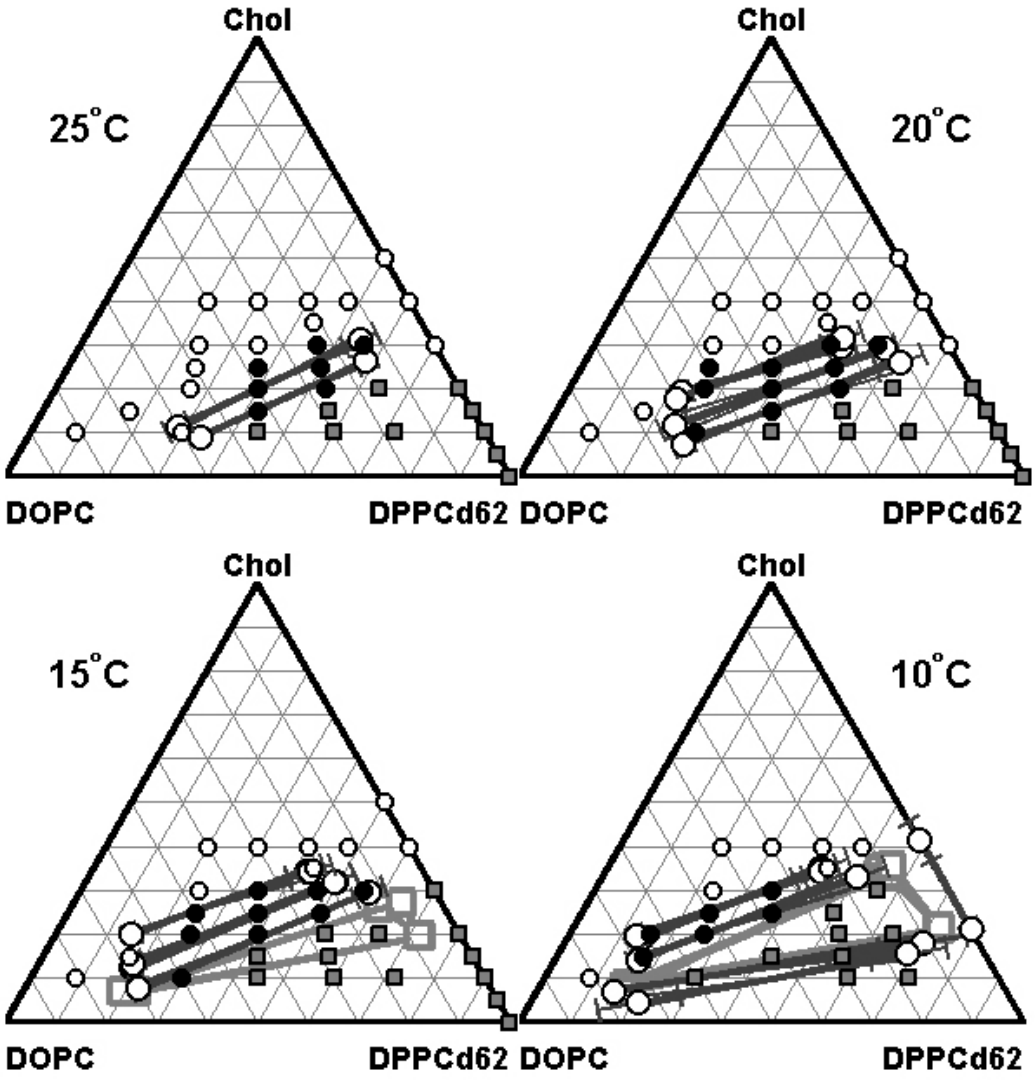


Figure 1.7. Phase diagram of DOPC/DPPC-d62/cholesterol at various temperatures determined by $^{2}$H NMR (Veatch et al., 2007b). Each symbol corresponds to a certain type of phase behavior: one liquid (small open circles); two liquids (small black circles); contains some gel (small gray squares). The large open circles correspond to Ld/Lo tie-line endpoints. The large open squares represent endpoints of the three phase region (the gray triangle).

The phase boundaries for the three-phase region and compositions of the coexisting phases (the directions of the tie lines) in the two-phase Ld/Lo region and the three-phase Ld/Lo/Lβ region were determined by $^2$H NMR (Veatch et al., 2007b; see Veatch et al., 2004 and Veatch et al., 2006 for description of the method). In the $^2$H NMR experiments, chain-perdeuterated DPPC (DPPC-d62) was used in place of DPPC. DPPC-d62 has a slightly lower melting temperature than DPPC ($\Delta T_m$=-2.5˚C), but is otherwise expected to exhibit very similar phase behavior to DPPC (Veatch et al., 2004). The two-phase Ld/Lo region according to NMR (Fig. 1.7) is smaller when compared with the microscopy results (Fig. 1.6). Also, the $T_{mix}$ temperatures are lower according to $^2$H NMR, which cannot be explained by a 2.5˚C shift due to the lower $T_m$ of DPPC-d62. A possible explanation for these different results is the influence of perturbing probe on the microscopy data (Veatch et al., 2007a), discussed further in Section 1.6.2.

The DOPC/DPPC/cholesterol phase diagram forms the starting point for our x-ray work. The samples we studied are shown by colored dots in Fig. 1.6. Because the method of analysis we apply to the wide-angle scattering data is not well-used for studying chain order in model membranes, we wanted to choose a well-characterized system. The effect of cholesterol on chain orientational order has been investigated with NMR and other techniques for the binary mixtures DOPC/cholesterol and DPPC/cholesterol, allowing us to calibrate our x-ray measurements of chain orientational order. We can also compare our x-ray results for $T_{mix}$ temperatures in the Ld/Lo coexistence region with the NMR and microscopy data.

Although the DOPC/DPPC/cholesterol phase diagram is well-studied, some of the regions of the diagram are still controversial, particularly binary mixtures of DPPC/cholesterol. Fluorescence images of GUVs are uniform for DPPC/cholesterol at all temperatures and compositions (Feigenson and Buboltz, 2001; Veatch, 2004;

Veatch and Keller, 2005b), but other evidence suggests that there is gel/Lo coexistence at low temperature and Ld/Lo phase coexistence at high temperature in this system (discussed in detail in Ch. 5).

In contrast to the DPPC/cholesterol system, there is general agreement that phase coexistence does not occur in binary mixtures of DOPC and cholesterol; however, as cholesterol is added the properties of the liquid phase change from Ld to more Lo-like (see Ch. 4 and the references therein). Since liquid phases can have a large range of properties, the Ld and Lo phases are only clearly differentiated in the case of Ld/Lo phase coexistence.

### 1.6.2 Comparison of methods for detecting phase coexistence

Commonly-used methods for detecting phase coexistence in model membranes include fluorescence microscopy, spectroscopic methods (NMR and ESR), non-optical fluorescence methods such as FRET and fluorescence polarization, and DSC. Table 1.1 summarizes important features of the various techniques, such as the time and distance scales associated with each technique. The distance scale determines the lower limit of domain size which can be observed with a technique. For a domain to be detectable in fluorescence microscopy, it must be at least a micron in size, explaining why other shorter distance scale methods may suggest phase coexistence in regions where GUVs are uniform (see Feigenson and Buboltz, 2001 for an example).

Fluorescence microscopy has a major advantage over other techniques for detecting phase coexistence: domains are directly visualized. Other methods are more indirect, often involving comparison to other data and models. In addition to detecting phase coexistence and giving a rough measure of the fraction of each phase,

fluorescence microscopy of GUVs can be used to measure physical properties in the coexisting phases (see for example Baumgart et al., 2003).

Table 1.1. Comparison of common methods used for detecting phase coexistence in model membranes.

| Method | Time/ Distance scale* | Probe required? | Comments/References |
|---|---|---|---|
| Fluorescence microscopy | >1 micron | Yes-fluorescent dye | method reviewed in Veatch and Keller, 2005b |
| FRET | <5 nm (~Förster radius of dye)<br>Can detect small domains (10's of nm) | Yes-fluorescent dye (smaller quantities than microscopy) | method reviewed in Heberle et al., 2005 |
| ESR | $<10^{-8}$ sec<br>>1 nm | Yes-spin probe | Recktenwald and McConnell, 1981<br>Chiang et al., 2005 |
| $^{2}$H NMR | $<10^{-5}$ sec<br>>20 nm | No-Deuterated lipid is a mixture component | Vist and Davis, 1990<br>Veatch et al., 2006 |
| DSC | non-equilibrium measurement | No | Mabrey et al., 1978 |

*Time and distance scale information come from Bloom and Thewalt, 1995 and Fung and Stryer, 1978.

Despite the advantages of microscopy, it requires using fluorescent probe, possibly perturbing the system. Ayuyan and Cohen (2006) have shown that illumination of fluorescent dye can cause photooxidation of the unsaturated chains of DOPC, leading to photoinduced phase separation in mixtures of DOPC, egg sphingomyelin (ESM), and cholesterol. Note that compositions just outside a phase boundary (with high cholesterol content) are particularly prone to photo-induced phase separation. Using fluorescence microscopy Ayuyan and Cohen did observe large domains in the absence of photooxidation for some DOPC/ESM/cholesterol compositions, confirming that this system does indeed separate into coexisting fluid phases without the presence of contaminant. Zhao et al. (2007b) have shown that photooxidation is particularly problematic for mixtures of POPC, cholesterol, and various sphingomyelins. Their work suggests that in the absence of probe,

POPC/SM/cholesterol systems do not phase separate, in conflict with previous phase diagrams published for these mixtures using fluorescent probes (Veatch and Keller, 2005a). Veatch et al. (2007a) have used NMR to investigate the effect of fluorescent probe on lipid phase behavior; they showed that probe concentrations as low as 0.05 mol%, well below the 0.5 mol% dye used in many GUV preparations, can strongly affect phase behavior. Such reports may cause general skepticism about evidence of Ld/Lo phase coexistence that rely upon potentially perturbing fluorescent probes.

There are relatively few widely used probe-free methods for detecting phase coexistence in model membranes, particularly biologically relevant liquid-liquid coexistence in ternary mixtures. Veatch et al. (2004, 2006, 2007b) extended the NMR method used by Vist and Davis (1990) to examine liquid-liquid coexistence in ternary mixtures of DOPC (or diphytanoyl PC), DPPC-d62, and cholesterol. Pencer et al. (2005) have used small-angle neutron scattering (SANS) to observe phase coexistence in mixtures of DOPC, DPPC-d62, and cholesterol. Potma and Xie (2005) have used coherent anti-stokes Raman spectroscopy (CARS) to visualize liquid-liquid domains in giant unilamellar vesicles composed of DOPC, deuterated DSPC, and cholesterol. Note that we consider $^{2}$H NMR, SANS, and CARS experiments to be probe-free because the deuterated lipid is one of the three components. NMR and SANS provide indirect evidence of phase coexistence; domains are not directly visualized for these techniques. Although CARS provides pictures of domains, at present this technique is highly specialized and not widespread. Similarly, the availability of neutron scattering facilities is limited.

Another probe-independent method for detecting Ld/Lo phase coexistence would be of value considering the possible perturbative effects of probes. In the next section, we discuss how x-ray scattering, a noninvasive, probe-free method, can be used to distinguish between the different lamellar lipid phases.

## 1.7 X-ray scattering from model membranes

### 1.7.1 X-ray scattering basics

Figure 1.8 shows a general x-ray scattering geometry. The following equations relate the incident wavevector ($\mathbf{k}_i$), outgoing wavevector ($\mathbf{k}_f$), and the scattering wavevector ($\mathbf{q}$) to the x-ray wavelength ($\lambda$) and the scattering angle ($2\theta$):

$$\begin{aligned} \mathbf{q} &= \mathbf{k}_f - \mathbf{k}_i \\ k_i &= k_f = k = 2\pi/\lambda \\ q &= 2k\sin\theta = \left(\frac{4\pi}{\lambda}\right)\sin\theta \end{aligned} \tag{1.5}$$

where we have assumed elastic scattering.

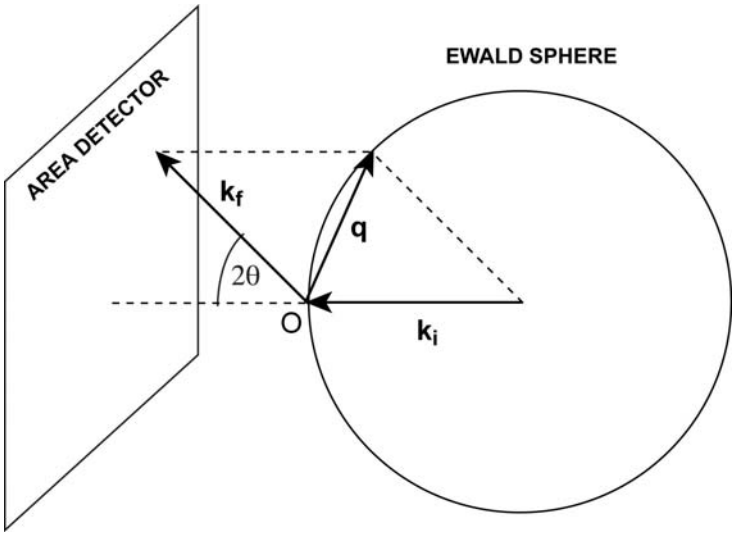


Figure 1.8. Ewald sphere construction, showing the allowed **q** values for a given sample (at point O) orientation in respect to the direction of incoming x-rays, $\mathbf{k}_i$. The area detector image is a flat projection of a slice through reciprocal space on the surface of the Ewald sphere. For further discussion, see Guinier, 1963.

An image observed on a detector is often referred to as a "reciprocal space mapping", while coordinates for the sample are referred to as "real space". Reciprocal

space mappings are useful for structure determination because the x-ray scattering intensity is related to the Fourier transform of the electron density distribution, according to the following basic equation (Guinier, 1963) :

$$I(\mathbf{q}) = |A(\mathbf{q})|^2 = \int\int \rho(\mathbf{r}_1)\rho(\mathbf{r}_2)\exp[-i\mathbf{q}\bullet(\mathbf{r}_2 - \mathbf{r}_1)]d^3\mathbf{r}_1 d^3\mathbf{r}_2 . \quad (1.6)$$

where $I(\mathbf{q})$ is the intensity for a given wavevector $\mathbf{q}$, $\rho(r)$ is the electron density at point $r$ in real-space, and $A(\mathbf{q})$ is the Fourier transform of the electron density. Eq. 1.6 represents the scattering over all atoms in the system, which is important to keep in mind as we try to separate out the various scattering components (such as phospholipid chain-chain scattering from cholesterol-chain scattering and headgroup-headgroup scattering).

When there is a repeating structural unit in the sample (e.g. lipid chains organized on a hexagonal lattice or stacks of bilayers), we can apply Bragg's law (see Kittel, 1957 for a derivation):

$$n\lambda = 2d\sin\theta \quad (1.7)$$

where $d$ is the distance between atomic planes in the real-space crystalline lattice and $n$ is an integer and is referred to as the diffraction "order". Bragg's law can also be written as:

$$d = n \times \frac{2\pi}{q_n} \quad (1.8)$$

where $q_n$ is the scattering wavevector magnitude for order $n$. For three-dimensional crystals, Bragg's law limits scattering to particular values of $q_x$, $q_y$, and $q_z$. That is, scattering is only observed at points in reciprocal space. In a two-dimensional lattice, the restriction is only on two reciprocal space directions. In the following section, we will use Bragg's law in relation to two types of structure in model membranes: the lamellar structure and the chain-chain ordering.

### 1.7.2 Structure in model membranes: lamellar and chain-chain ordering

In order for sharp peaks to occur, the sample must have a repeating structural unit. Lipid multilayers have two such units: (1) the lamellar stacks normal to the bilayer and (2) the hexagonal ordering of chains in the plane of the bilayer (see Fig. 1.9). The lamellae result in scattering at $q=2\pi/d_L$. We refer to lamellar scattering as low-angle x-ray scattering (LAXS). Note that much of the lipid literature refers to the lamellar scattering as small-angle x-ray scattering (SAXS). The hexagonal packing (which can be distorted or disordered) of the chains results in scattering at $q_{cc}\sim 2\pi/d_{cc}$, which is referred to as wide-angle x-ray scattering (WAXS) and has been compared to scattering from paraffin chains (see Levine and Wilkins, 1971; Luzzati, 1968; Warren, 1933). Note that $d_{cc}$ refers to the distance between rows in a perfect hexagonal lattice, while the distance to nearest neighbors is $2\, d_{cc}/\sqrt{3}$.

### 1.7.3 Types of samples: oriented vs. powder

Figure 1.10 compares x-ray scattering geometries for oriented lipid multilayers and for multilamellar lipid vesicles (unoriented or powder samples). This thesis presents data from both of these types of samples. Although preparation and hydration of oriented samples is more challenging, oriented lipid multilayers are advantageous because lateral structure in the plane of the membrane (e.g. lipid chain packing) can be easily distinguished from structure perpendicular to the plane of the membrane (e.g. the lamellae). In the grazing incidence geometry (Fig. 1.10A) scattering in the $q_r$ direction ($\phi\sim 0^\circ$) results from lateral structure while scattering in the $q_z$ direction ($\phi\sim 90^\circ$) results from structure perpendicular to the bilayer. In a grazing incidence wide angle x-ray scattering (GIWAXS) image, scattering from untilted chains in a perfect hexagonal lattice will be centered on the $q_r$ axis ($\phi=0^\circ$). If the

chains are tilted, the center of the wide angle scattering spot will have a $q_z$ and $q_r$ component (nonzero $\phi$) [discussed in the next section].

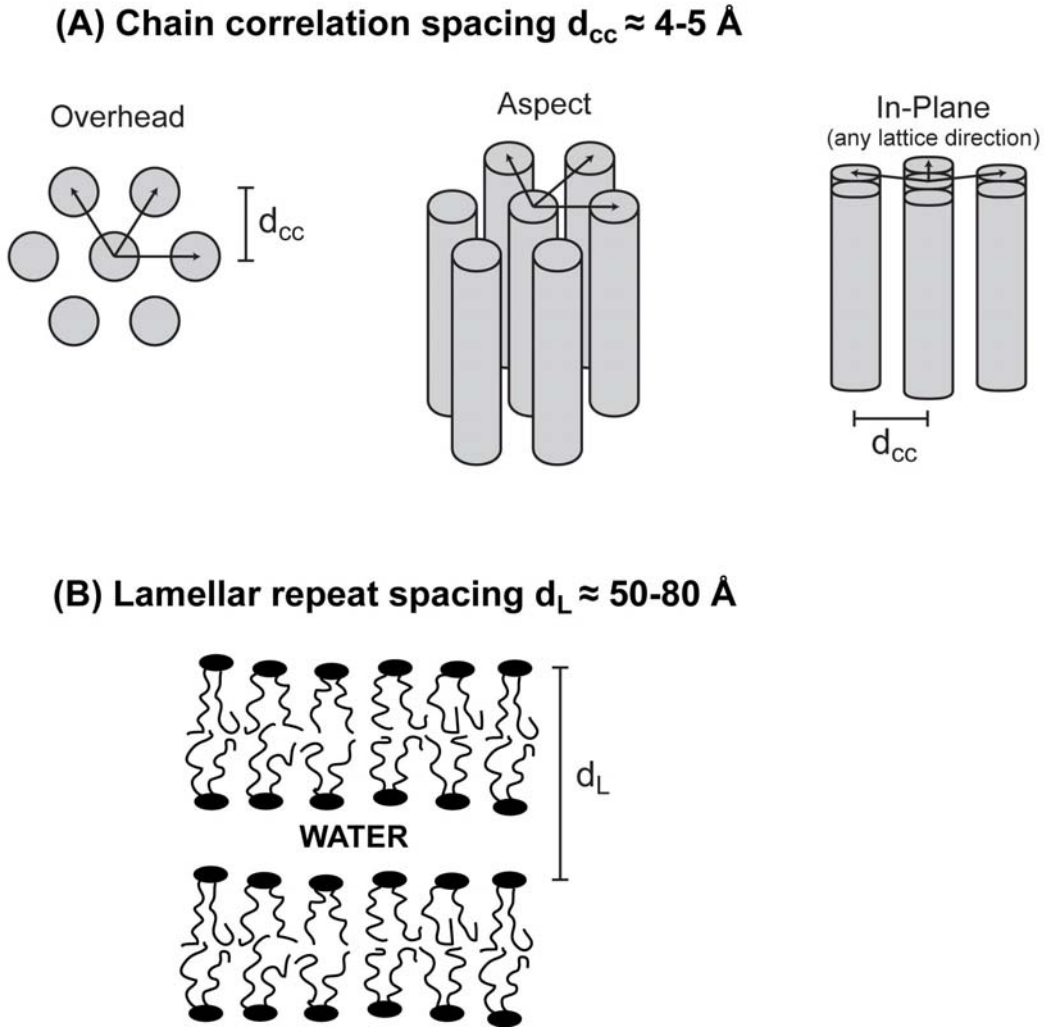


Figure 1.9. (A) Hexagonal lattice of lipid chains. The rows of chains are spaced a distance $d_{cc}$ apart. Original drawing by G. E. S. Toombes. (B) The lamellar repeat spacing ($d_L$) consists of a single bilayer + water layer.

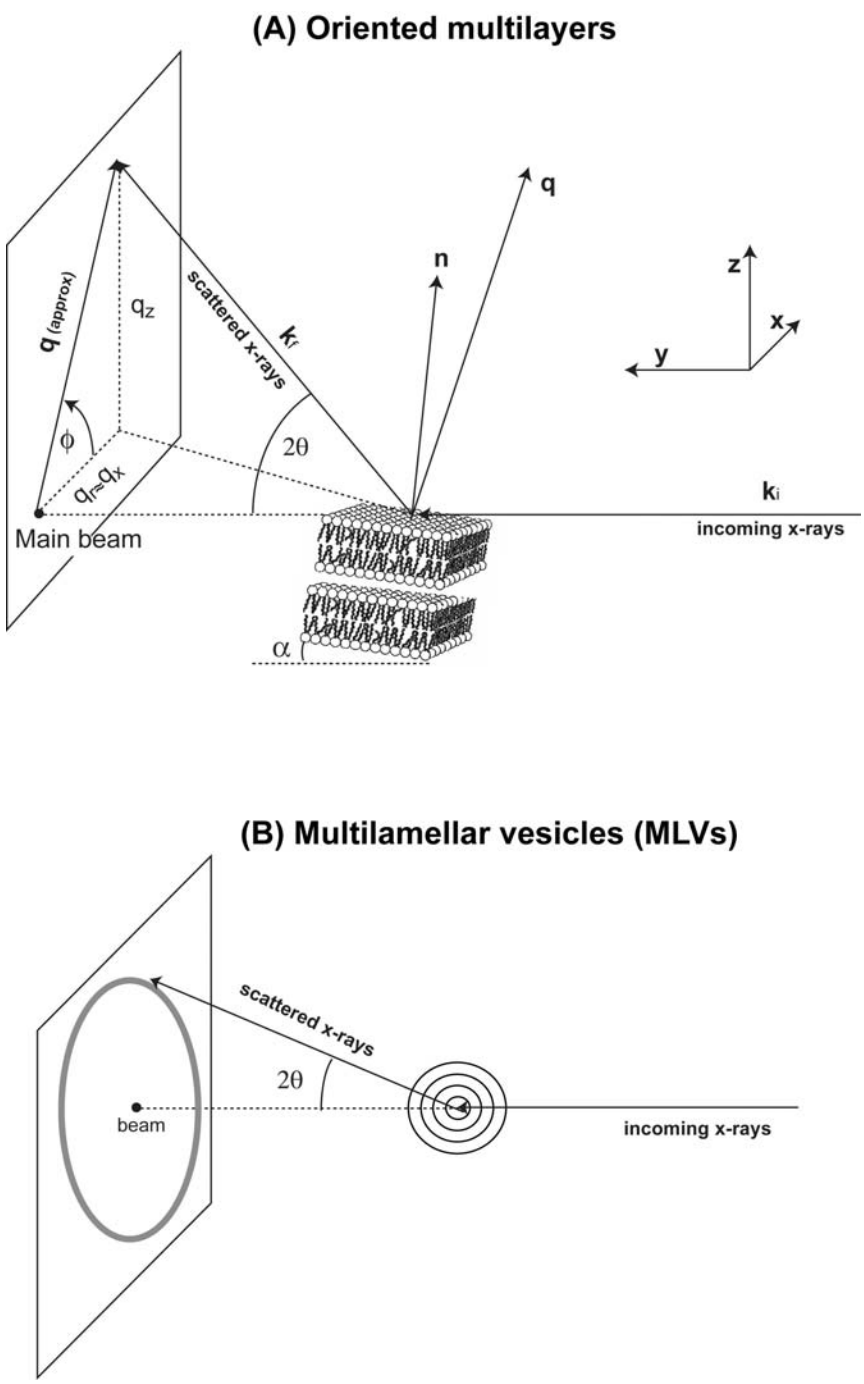


Figure 1.10. Scattering geometry for oriented multilayers in the grazing incidence geometry (A) and multilamellar vesicles (B). For the oriented multilayers in the grazing incidence geometry, scattering in the $q_z$ direction is from structure perpendicular to the plane of the membrane (e.g. lamellae), while scattering in the $q_r$ direction is from lateral structure in the plane of the membrane (e.g. chain lattice). For multilamellar vesicles, the scattering is isotropic. (A) is revised from the original figure, which appears in Busch et al., 2007.

### 1.7.4 The different lipid lamellar phases: what do x-rays see?

One goal of this thesis is to be able to use x-ray scattering to identify regions of phase coexistence, in particular liquid-liquid coexistence. This relies on using LAXS (lamellar scattering) and WAXS (chain scattering) data to distinguish between the different lamellar phases (Ld, Lo, Lβ, and Lβ') discussed in Section 1.3. The observation of two lamellar repeat ($d_L$) spacings or two chain correlation ($d_{cc}$) spacings can give direct evidence of phase coexistence; however, the absence of two $d_L$ or $d_{cc}$ spacings does not imply the absence of phase coexistence (See Section 3.4 for a detailed discussion). This section discusses how the angular distribution (along $\phi$ in Fig. 1.10A) of wide-angle scattering from oriented multilayer samples may be useful for identifying liquid-liquid phase coexistence.

One of the motivations for this work was the observation of only a single lamellar repeat spacing in 1:1:1 DOPC/brain sphingomyelin (BSM)/cholesterol by Gandhavadi et al. (2002); in this same system, Dietrich et al. (2001) had observed Ld/Lo phase coexistence using fluorescence microscopy. In order to observe two lamellar repeat spacings in a phase-separated mixture, the two spacings must be different enough to be resolvable and the different phases must align on top of each other across different bilayers (see Section 3.4 for further discussion). Looking for two lamellar repeat spacings can be an unreliable method for detecting the presence or absence of phase coexistence because a null result does not imply the absence of phase coexistence.

In order to observe two $d_{cc}$ spacings, there is no requirement of alignment of the phases between different bilayers; however, the two $d_{cc}$ spacings must be resolvable. For MLV (powder) samples, the wide-angle x-ray scattering pattern from the gel phase is easily distinguished from the fluid phase. Gel-phase WAXS consists of a narrow band near $d_{cc}$~4.2 Å (two bands for a distorted hexagonal lattice), while

liquid-phase WAXS consists of a broad band near $d_{cc}$~4.5 Å. Although the position of the liquid-phase band changes as a function of temperature and cholesterol content (Clarke et al., 2006; Maulik and Shipley, 1996a, 1996b), the width is very similar in the Ld and Lo phases. Given a powder sample with coexisting Ld and Lo phases, we expect the wide bands to overlap. On the other hand, we would expect to be able to identify gel/fluid coexistence in powder WAXS data.

GIWAXS from oriented lipid multilayers can give additional information about chain ordering not available from powder samples. Figure 1.11 compares GIWAXS data from examples of the four different phases discussed in Section 1.3. The figure shows the large changes in chain order resulting from temperature changes or compositional changes (e.g. the addition of cholesterol). The simplest scattering comes from the Lβ phase (untilted chains in a hexagonal lattice): the Lβ phase is characterized by a single Bragg rod centered along the $q_r$ axis and with $q_z$ intensity dependence described by a sinc function (see Section 3.2.5 for further discussion). Pure DPPC forms the Lβ' phase, not the Lβ phase. The example shown in Fig. 1.11B (DPPC + 10% cholesterol at 25˚C) is sometimes referred to as a disordered gel phase. Pure PEs, which have a smaller headgroup than PCs, do form the Lβ phase. For the DPPC Lβ' phase (a distorted hexagonal lattice with tilting towards nearest neighbors), scattering consists of two Bragg rods: one at the equator and the other off the equator; such scattering is characteristic of tilted chains in a distorted hexagonal lattice (for more about GIWAXS from gel-phase oriented multilayers, see Smith et al., 1988; Tristram-Nagle et al., 1993).

Lateral positional disorder in fluid phases results in broadening of the peaks in the $q_r$ direction: the chains have a large distribution of nearest neighbor distances. While scattering from the Ld and Lo phases is similarly broad in the $q_r$ direction, the angular ($\phi$) distribution of scattering is larger in the Ld phase than in the Lo phase.

The angular distribution of scattering is sensitive to chain orientational order: more orientationally ordered samples will have a narrower distribution of scattering. Levine and Wilkins (1971) reported this effect for oriented multilayers of egg lecithin/cholesterol. In this thesis we will refer to the lateral width of the GIWAXS peak as the *q*-width and the angular width as the $\phi$-width.

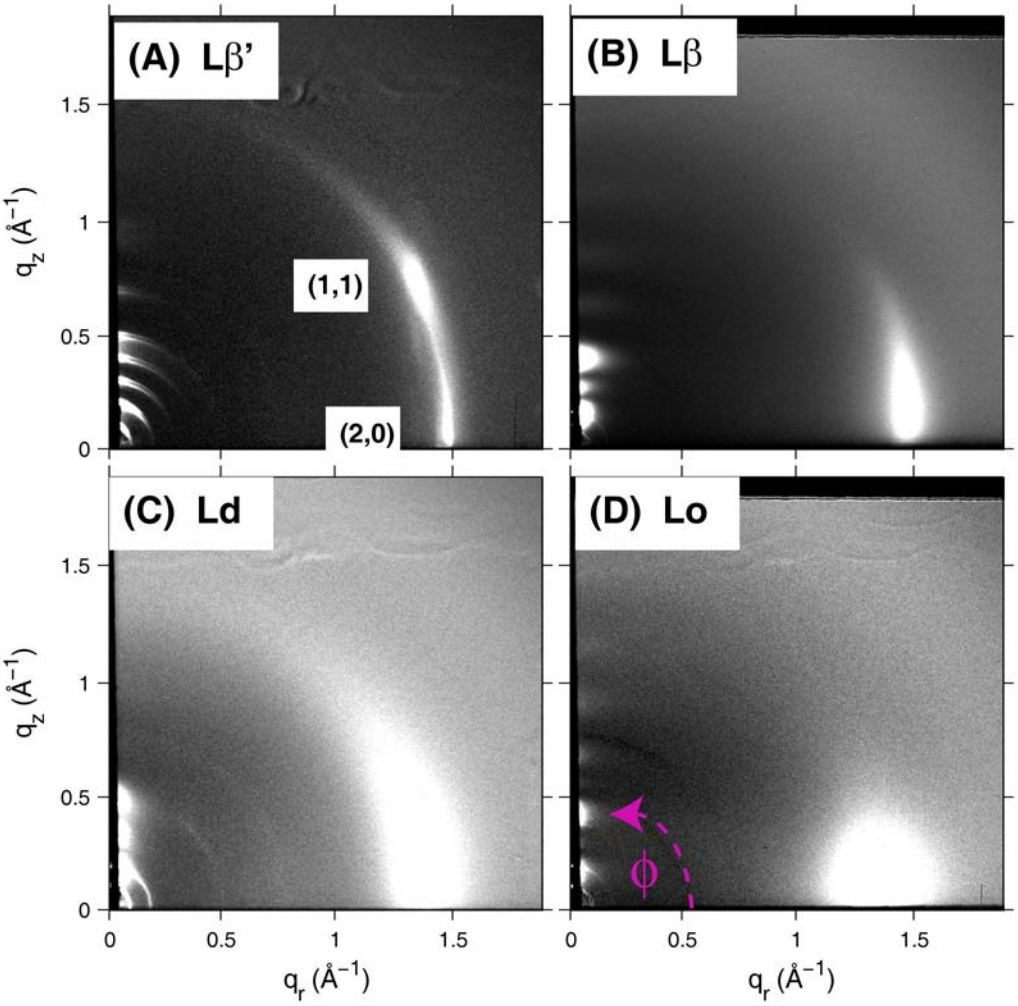


Figure 1.11. GIWAXS images for: (A) DPPC (*T*=25˚C) in the Lβ' phase; (B) DPPC + 10% cholesterol (*T*=25˚C) in the Lβ phase; (C) DPPC (*T*=45˚C) in the Ld phase; (D) DPPC + 40% cholesterol (*T*=45˚C) in the Lo phase. (Data taken at CHESS D-1 station, February 2006)

Figure 1.12 compares wide-angle scattering data from an oriented liquid-phase DOPC sample with wide angle scattering data from a powder DOPC sample. The scattering from the powder sample is characteristic of liquid-phase samples (Ld or Lo), while the oriented sample data are characteristic of the Ld phase. In powder samples, we lose the information about the angular distribution of scattering.

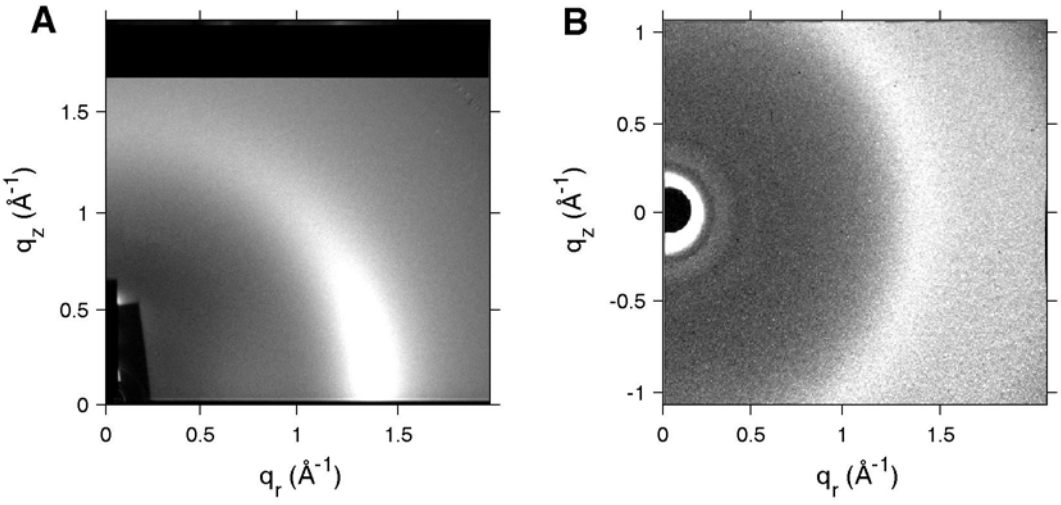


Figure 1.12. (A) GIWAXS image for DOPC ($T$=25˚C), taken at CHESS G-1 station in October 2006. (B) Powder WAXS image for MLVs of DOPC ($T$=25˚C), taken on the Gruner rotating anode. The powder data was included in a radially integrated form in Zhao et al., 2007a; this paper also discusses sample preparation. Unlike the rest of the powder MLV data presented in this thesis (see Ch. 2), the data presented in (B) was hydrated at a 1:1 (v/v) water: lipid ratio.

### 1.7.5 Potential of GIWAXS on oriented lipid multilayers in the context of previous x-ray work on model membranes

Levine and Wilkins performed a seminal study of egg lecithin/cholesterol mixtures using lamellar and wide-angle x-ray scattering of oriented lipid multilayers (Levine, 1970; Levine and Wilkins, 1971). The ordering of the egg lecithin chains by cholesterol was apparent in their wide-angle x-ray data: the angular distribution of

scattering was narrower for egg lecithin/cholesterol than for egg lecithin alone. Their electron density profiles constructed from the lamellar repeat data showed that the bilayer thickness increased with cholesterol addition, consistent with an increase in chain order; more ordered chains have a longer effective chain length.

More recently, Spaar and Salditt (2003) have shown the value of comparing experimental GIWAXS data from Ld-phase oriented multilayers with molecular dynamics (MD) simulations. In addition to single component Ld-phase membranes, the Salditt group has also studied phospholipid/peptide mixtures with a combination of GIWAXS and molecular dynamics simulations (Spaar et al., 2004).

For gel phases, WAXS from powder samples (Janiak et al., 1976; Tardieu et al., 1973; Sun et al., 1994) and oriented samples (Smith et al., 1988; Tristram-Nagle et al., 1993) give detailed structural information including chain tilt and lipid area. Reports of wide-angle x-ray scattering from liquid phases usually focus on changes in the position of the wide-angle band (for examples see Clarke et al., 2006; Finean, 1990; Maulik and Shipley, 1996a, 1996b). More in-depth analysis of liquid-phase WAXS data is less common. Levine and Wilkins (1971) used a simple analytical model, commonly used in liquid crystal research, to analyze their GIWAXS data (see Ch. 3). In addition to Spaar and Salditt's work comparing MD simulations with GIWAXS data, Sega et al. (2007) have compared Ld-phase powder WAXS data to MD simulations. Note that we are focusing on work on bilayers, while much lipid x-ray scattering work has also been done on monolayers (See Ege et al., 2006 for a recent example which uses grazing incidence wide angle scattering to examine the effect of cholesterol on the structure of fluid-phase monolayers). The connection between monolayer and bilayer phase behavior is unclear (Stottrup et al., 2005).

In the context of recent literature on liquid-liquid coexistence in ternary mixtures, we felt it promising to more fully explore the GIWAXS technique as applied

to mixtures of phospholipid and cholesterol. This thesis focuses on applying an analytical method, often used in liquid crystal research, for quantitatively analyzing the angular distribution of GIWAXS data to obtain the chain orientational order parameters for liquid-phase samples. In order to develop a tool for identifying Ld/Lo phase coexistence, we extend this method to analyze cases where the angular distribution of scattering is a convolution of two distributions (i.e. from the Ld and Lo phases).

## 1.8 Thesis Summary

GIWAXS from oriented multilayers can give information about lateral positional ordering and chain orientational ordering without the use of a perturbing probe. The goal of this thesis is to answer the following questions by using the GIWAXS method:

1. Can we quantitatively analyze the angular distribution of scattering to obtain chain orientational order parameters for liquid-phase lipid samples? What are the effects of cholesterol on lipid chain order (both orientational and lateral positional order)? How do the trends we observe in orientational order as a function of sample composition compare with NMR order parameter data?
2. For samples known to have liquid-liquid phase coexistence, can we deconvolve the angular distribution of scattering to identify phase coexistence and determine miscibility transition temperatures ($T_{mix}$)? If so, how do the $T_{mix}$ values compare with those from the NMR and fluorescence microscopy work of Veatch et al.?

We will answer the above questions for DOPC/DPPC/cholesterol mixtures. This system is a good test system for calibrating the GIWAXS method because chain orientational order has been well studied in the binary mixture DPPC/cholesterol using

a variety of techniques (and to a lesser extent DOPC/cholesterol). Also, liquid-liquid coexistence in this ternary mixture has been studied with both NMR and fluorescence microscopy.

In the following two chapters, we present the experimental techniques and theory. Chapter 2 discusses the experimental procedure and challenges associated with obtaining high-quality GIWAXS data. Chapter 3 presents the theory used to analyze the angular distribution of the GIWAXS data in order to calculate chain order parameters and identify phase coexistence. The end of Ch. 3 discusses criteria for phase coexistence based on chain-correlation scattering (WAXS) and scattering from the lamellae (LAXS) data.

Chapters 4-6 present our GIWAXS data from oriented samples and LAXS data from powder samples. Chapter 4 focuses on chain order in DOPC/cholesterol mixtures (green circles in Fig. 1.6) and discusses how lipid areas can be calculated for fluid phases from the GIWAXS data. Chapter 5 evaluates our x-ray scattering data from both oriented and powder samples for DPPC/cholesterol mixtures (blue circles in Fig. 1.6) in the context of controversial and inconsistent reports of phase coexistence (gel/liquid at low temperature and liquid/liquid at high temperature) in this system. Chapter 6 presents evidence of phase coexistence in ternary DOPC/DPPC/cholesterol mixtures (red circles in Fig. 1.6) from both GIWAXS data and lamellar scattering from MLV samples. These data are compared to NMR and microscopy results (Veatch et al.) for order parameters (found separately in each coexisting phase) and $T_{mix}$ values.

# Chapter 2 - Experimental

## 2.1 Introduction

The quality of the GIWAXS data we obtained is shown in Fig. 2.1. The width of the sharp features for gel-phase DPPC (Fig. 2.1A) is limited by instrumental resolution in our setup. The focus of this thesis is analyzing the broader GIWAXS patterns of fluid phases (Fig. 2.1B and 2.1C). The resolution for the gel phase data shows that the much broader features we observe in the fluid phase data are not affected by instrumental resolution.

Figure 2.1 is a good example of the drastic effects of changes in temperature and composition on the GIWAXS images. At 25˚C, DPPC is in the Lβ' phase, with tilted chains packed regularly in a distorted hexagonal lattice (Fig. 2.1A). At 45˚C, DPPC is in the Ld phase: the chains do not form a regular lattice with a well-defined spacing, as can be seen by the large width of the peak in the $q_r$ direction, characteristic of fluid-like lateral positional ordering (Fig. 2.1B). Also, the chains are orientationally disordered, as can be seen by the wide angular distribution of scattering; this information about chain orientational order cannot be obtained from a powder WAXS pattern. Adding 40 % cholesterol to DPPC at 45˚C orientationally orders the chains, as can be seen by the narrower angular distribution of scattering; however the disordered fluid-like positional ordering of the DPPC chains is maintained, characteristic of the Lo phase (Fig. 2.1C). All of this information is contained in the GIWAXS data, but we must ensure that our data are free from artifacts in order to be confident in our interpretations.

This chapter describes our method for collecting high-quality GIWAXS data. The features labeled in Fig. 2.1C will be described in more detail in the sections which follow.

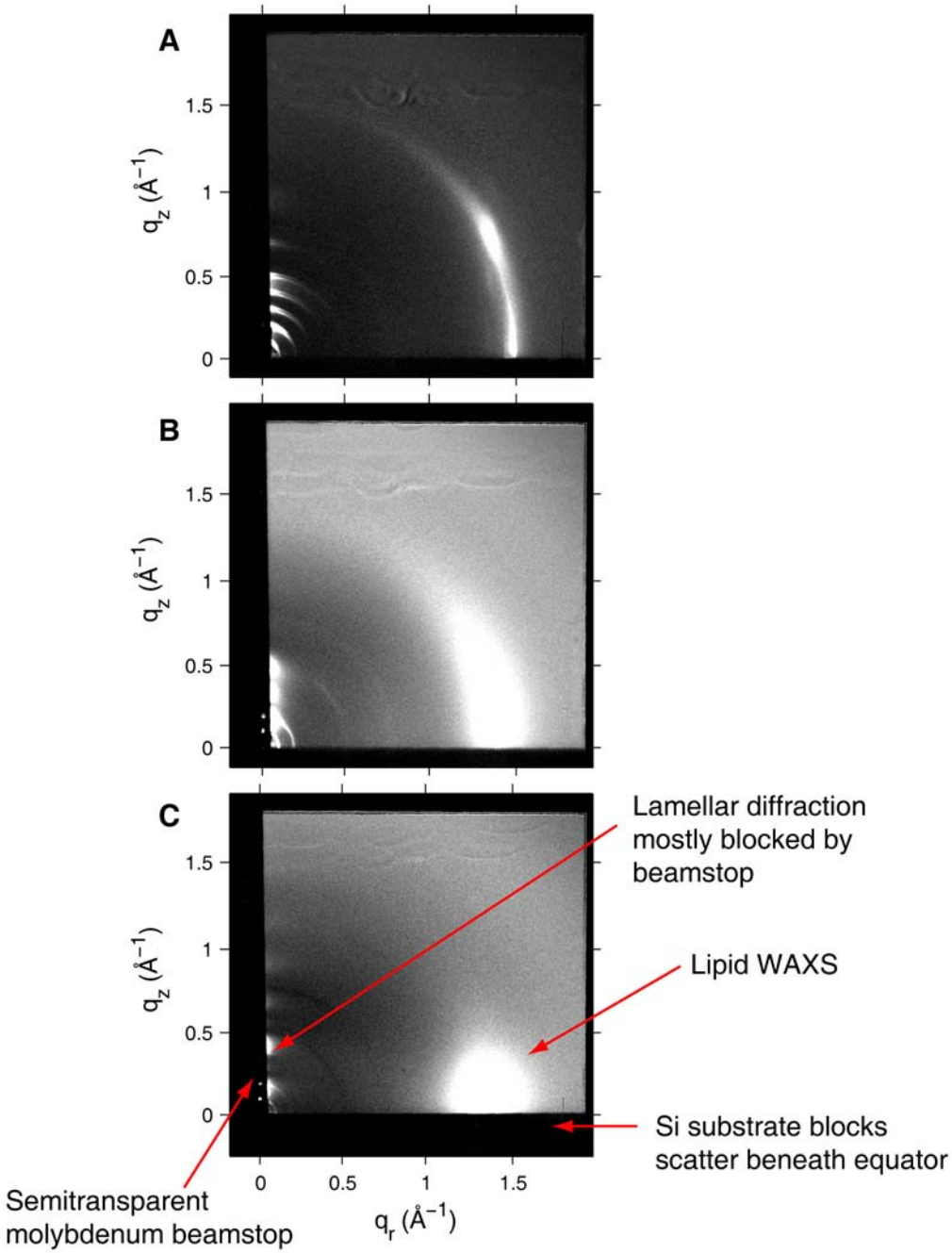


Figure 2.1. 2D GIWAXS images for: (A) gel phase DPPC at 25˚C; (B) fluid phase DPPC at 45˚C; (C) DPPC + 40% cholesterol at 45˚C. (D-1, February 2006)

## 2.2 X-ray sources

The x-ray scattering data presented in this thesis were obtained using two types of sources: a rotating anode and a synchrotron. The grazing incidence diffraction experiments were performed at the Cornell High Energy Synchrotron Source (CHESS). A rotating anode (maintained by Sol Gruner's group) was also used to help characterize samples. Als-Nielsen and McMorrow (2001) provide a good introduction to x-ray sources and x-ray optics.

Some of the GIWAXS experiments used the D-1 station, a bending magnet beamline, and some used the G-1 station, a wiggler beamline. Wigglers and bending magnets both produce a wide beam with a broad range of energies, a so-called "white beam." Monochromators, based on reflection of x-rays from multilayered materials with a definite periodic spacing, are used to select a particular wavelength from the "white beam." Slits, usually metal blades, define the beam size.

In principle, the GIWAXS experiments on model membranes could be performed on a rotating anode: preliminary experiments show that reasonable signal can be collected under an hour using a rotating anode, with typical intensities on the order of $10^7$ photons/mm$^2$/sec, compared with intensities of $10^{11}$-$10^{13}$ photons/mm$^2$/sec at CHESS. Our exposures at CHESS were two minutes or less, but sample equilibration can take over an hour. Thus, exposure time is not the time-limiting factor in our experiments. The short exposure times at CHESS may be beneficial in limiting radiation damage, which involves destruction of the lipid by free radicals produced by interaction of the x-rays with the water in the sample. Since the free radicals take time to act, radiation damage is a function of the exposure time as well as the total exposure.

The higher x-ray energies available at CHESS provide two advantages:

(1) With the current sample chamber (the Nagle group's NIH chamber), described later, a higher x-ray energy than the Cu Kα line is advantageous in order to collect larger $q$ values.

(2) Radiation damage is less problematic at higher energies because absorption of radiation by the sample is minimized at higher x-ray energies (Arndt, 1984).

Availability of a sample chamber was a major factor in choosing to do experiments at CHESS. The Nagle group's NIH sample chamber, capable of full hydration, was expensive and time-consuming to build. In addition to their sample chamber, the Nagle lab's expertise in scattering from oriented lipid samples greatly benefited this work. At CHESS, we were able to divide beamtime, and sometimes share samples, between the GIWAXS work and the Nagle group's low angle diffuse scattering work that focused on the scattering that is indicated in Fig. 2.1C as lamellar diffraction mostly blocked by the beamstop in our GIWAXS studies.

## 2.3 GIWAXS on oriented lipid multilayers

### 2.3.1 Preparation of oriented lipid multilayers

For the GIWAXS experiments, oriented samples with low mosaic spread are crucial. Oriented samples were prepared using the rock-and-roll method (Tristram-Nagle et al., 1993; Tristram-Nagle, 2007). A total lipid amount of 4 mg dissolved in 150-200 μL of organic solvent was deposited onto a 15 x 30 x 1 mm Si wafer, cleaned in methanol and chloroform. By gently rocking the wafer by hand, shearing action helps to align the lipid multilayers during solvent evaporation. To retard solvent evaporation and to allow for more even spreading, the procedure was performed in a glove box saturated with chloroform vapor. The samples were left in the saturated atmosphere glove box overnight; then the samples were allowed to dry on the lab bench for one day. The samples were trimmed to a 5 mm strip occupying only the

center of the 15 mm wide silicon wafer. The final sample thickness is ~10 μm, or about 2000 bilayers. The samples were stored for weeks in a glass dessicator with Drierite (W. A. Hammond DRIERITE Co., Xenia, OH) in a refrigerator with no degradation as judged by thin layer chromatography (TLC).

Chloroform mixtures of DOPC, DPPC, and cholesterol were prepared from stock mixtures in small (10 x 75 mm) borosilicate glass test tubes. (See the first paragraph of Section 2.4.1 for details on lipid mixture preparation, including the chemical companies and lot numbers and phosphate assay of stocks). After evaporation of the chloroform, the lipid was redissolved in a solvent mixture appropriate for the rock-and-roll procedure. The choice of solvent for the rock-and-roll method depends on the sample composition. Slowly evaporating solvents, such as methanol and trifluoroethanol (TFE), help to lower the contact angle of lipid with the hydrophilic silicon surface. However, pure methanol or pure TFE is not a good choice for mixtures of phospholipids and cholesterol because cholesterol and/or phospholipid may precipitate out of these solvents. Usually, a mixture of chloroform and another solvent, determined by trial and error, gives even spreading without precipitation. Table 2.1 shows the solvent mixture used for each lipid composition.

All of the oriented samples were annealed at 50˚C in a water-saturated atmosphere for 4-8 hours before being x-rayed. The annealing chamber was a plastic Nalgene container filled with sponges and water with a water-soaked sponge on the inside of the top cover. The samples sat in 50 mL cut, glass beaker halves below the top sponge. The annealing chamber was then placed in a small oven at 50˚C. The samples were observed periodically during the annealing process to assure proper hydration levels (the lipid should appear slick but not flooded with water droplets). Annealing serves two purposes: (1) Annealing can improve sample orientation; (2) When dealing with mixtures of lipids which can phase-separate, annealing at a

temperature well above the miscibility transition temperature ensures proper mixing of the components due to lateral diffusion. After at least 4 hours in the oven, the annealing chamber with the samples inside was placed in a styrofoam box to allow the samples to cool slowly. In the case of lipid mixtures which phase-separate, slow cooling instead of quenching helps prevent kinetically-trapped states, particularly problematic for the gel phase. When ready for data collection, the samples were transferred directly from the annealing chamber to the x-ray sample chamber.

Table 2.1. Solvent mixtures used for the rock-and-roll procedure.

| **Sample** | **Mole Percents** | | | **Solvent mixture** |
|---|---|---|---|---|
| | **% DOPC** | **% DPPC** | **% Chol** | |
| DOPC | 100 | 0 | 0 | 1:1 $CHCl_3$/TFE |
| DOPC + 10% Chol | 90 | 0 | 10 | 1:1 $CHCl_3$/TFE |
| DOPC + 40% Chol | 60 | 0 | 40 | 1:1 $CHCl_3$/TFE |
| | | | | |
| DPPC | 0 | 100 | 0 | 3:1 $CHCl_3$/MeOH |
| DPPC + 10% Chol | 0 | 90 | 10 | 5:1 $CHCl_3$/MeOH |
| DPPC + 15% Chol | 0 | 85 | 15 | 10:1 $CHCl_3$/MeOH |
| DPPC + 25% Chol | 0 | 75 | 25 | 20:1 $CHCl_3$/MeOH |
| DPPC + 40% Chol | 0 | 60 | 40 | 20:1 $CHCl_3$/MeOH |
| | | | | |
| 1:1 DOPC/DPPC | 50 | 50 | 0 | 2:1 $CHCl_3$/TFE |
| 1:1 DOPC/DPPC + 15% Chol | 42.5 | 42.5 | 15 | 2:1 $CHCl_3$/TFE |
| 1:1 DOPC/DPPC + 20% Chol | 40 | 40 | 20 | 2:1 $CHCl_3$/TFE |
| 1:1 DOPC/DPPC + 25% Chol | 37.5 | 37.5 | 25 | 2:1 $CHCl_3$/TFE |
| 1:1 DOPC/DPPC + 30% Chol | 35 | 35 | 30 | 2:1 $CHCl_3$/TFE |

An important question is whether annealing and exposure to x-rays causes breakdown of the sample (see Caffrey, 1984 for a study of x-ray radiation damage of lipid samples). Figure 2.2 shows a TLC comparing fresh DOPC to two DOPC samples which were annealed and then x-rayed in the October 2006 CHESS run at the G-1 station, which had a flux of $10^{12}$-$10^{13}$ photons/$mm^2$/sec. The TLC shows no

evidence of radiation damage for the bulk sample. To assess radiation damage, Caffrey (1984) did a more careful experiment in which only the part of the lipid capillary sample exposed to the x-ray beam was analyzed. If damage is limited to only a small amount of the sample, it may not be visible on our TLC plate. To limit radiation damage during the course of an experiment, the sample was moved periodically during the experiment to expose a fresh part of the sample to the beam (we limited exposure time to under 5-10 minutes).

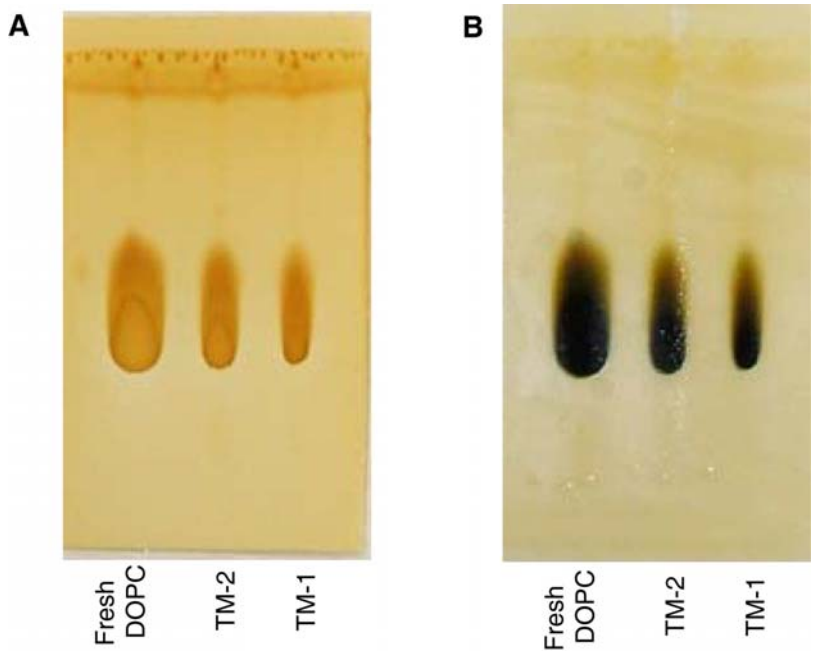


Figure 2.2. A TLC plate stained with (A) iodine vapor and (B) molybdic oxide/sulfuric acid. The TLC was run with the solvent mixture: 46:18:3 (v/v/v) chlorofrom/methanol/$NH_4OH$(7N). The lanes marked TM-1 and TM-2 were oriented DOPC samples that were annealed and x-rayed during the October 2006 G-1 run and stored refrigerated in a dessicator with Drierite until April 24, 2007 (date of TLC). The lipid was scraped off the silicon substrate with a razor blade and dissolved in chloroform and then was spotted on the TLC plate.

### 2.3.2 Sample chamber

We want to compare our x-ray scattering results with other experiments such as fluorescence microscopy of GUVs and NMR, where the lipid samples are immersed in water, so it is important that our oriented samples are also well hydrated, which is the most biologically relevant condition. For x-ray studies, oriented samples must be hydrated from water vapor because immersion in water disorients the sample unless a second substrate is used, and that attenuates the beam. For many years, experimenters observed that oriented lipid samples hydrated with water vapor under conditions of 100% relative humidity had a reduced level of hydration in comparison to vesicles in contact with bulk water; this phenomenon was called "the vapor pressure paradox." Katsaras (1997) showed that there was no vapor pressure paradox by achieving full hydration of oriented lipid samples in a neutron diffraction experiment; environmental chambers for neutrons can use thick aluminum and do not require windows, so humidity and temperature control is much easier. With consultation with J. Nagle, an x-ray chamber was subsequently constructed that also achieved full hydration (Katsaras and Watson, 2000). A Peltier element to cool the sample relative to the water vapor and a wet sponge near the sample to enhance evaporation were the design features that allowed for full hydration of oriented lipid samples.

The NIH sample chamber improved upon this original design (see Fig. 2.3 for a picture of the chamber). This chamber was designed by Drs. Stephanie Tristram-Nagle and John Nagle and built by Dr. Horia Petrache under the auspices of Dr. Adrian Parsegian at the NIH in Bethesda. The design and operation of the chamber have been described in detail elsewhere (Liu, 2003; Kučerka et al., 2005a). Essential design features of the chamber include:

1. A temperature-controlled water bath (at CHESS a Neslab was supplied).

2. A Peltier stage which cools or heats the sample relative to the rest of the chamber in order to vary the rate of sample hydration and achieve different hydration levels.
3. Wet filter paper above and close to the sample with one end in bulk water to wick water into the filter paper which has a large area for evaporation.
4. Double mylar windows which can be heated to prevent water drop condensation.
5. Helium ports which allow for the replacement of air by helium to reduce background scattering.
6. A rotation motor which rotates the sample holder independently from the rest of the chamber.

The size of the exit window determines the maximum scattering angle which can be obtained from the chamber, with a smaller angle allowed in the vertical direction than the horizontal direction (see Fig. 2.5A).

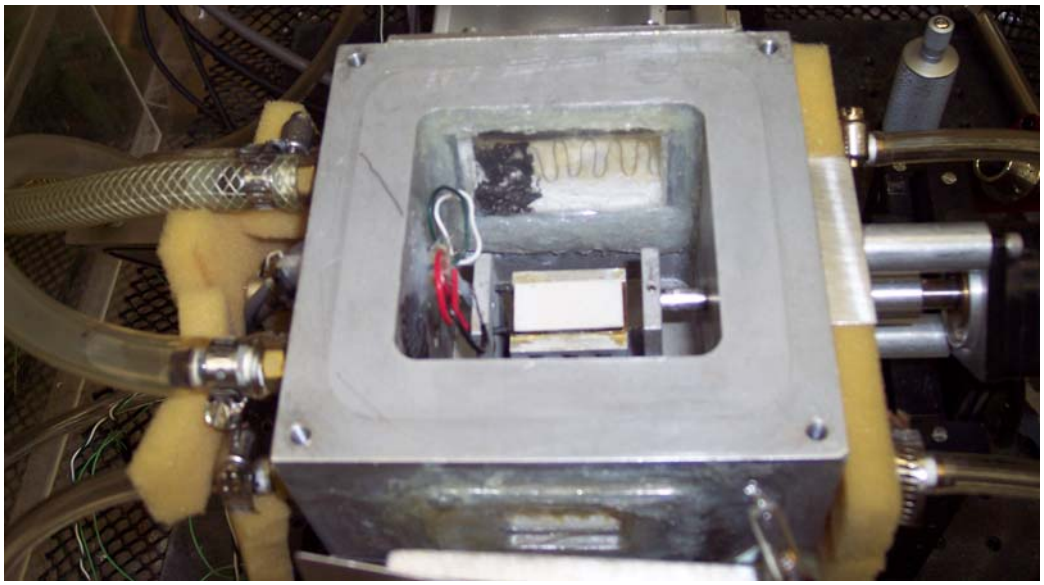

Figure 2.3. Top view of NIH sample chamber. The sample sits on the sample holder (white rectangle in the center of the picture).

We have found that our GIWAXS experiments are limited by the maximum scattering angle allowed by the NIH chamber. To collect GIWAXS data with larger scattering angles, Dr. Stephanie Tristram-Nagle directed Antony Vydrin in the design and construction of a new sample chamber with larger windows (referred to as the AV chamber). This cylindrical chamber also has double-walled construction with an inner chamber made from a stainless steel coffee thermos surrounded by PVC pipe. The chamber is still in the prototype stage, as control of hydration was difficult. This chamber was used to help diagnose the problem of water scattering which extends to higher angles (see Section 2.3.8.1). All of the data shown in the results chapters (Ch. 4-6) were taken with the NIH chamber.

### 2.3.3 Beamline description

#### 2.3.3.1 Overall schematic

Figure 2.4 shows the grazing angle of incidence experimental geometry (also shown in Ch. 1). The x-rays come in with an angle of incidence $\alpha$ and scatter through the scattering angle, $2\theta$. The angle $\phi$ is the angle measured from the *x*-axis on the detector. The angle $\phi_{\mathrm{L}}$ is the angle between the scattering wavevector **q** and the sample plane, or more precisely the angle complementary to the angle between **q** and the membrane normal **n**. Throughout this thesis, we make the following approximations: $\phi \approx \phi_{\mathrm{L}}$ (see Ch. 3 for discussion) and $q_r = \sqrt{q_x^2 + q_y^2} \approx q_x$. The exact relations between the different angles and vectors shown in Fig. 2.4 are:

$$\begin{aligned}
\mathbf{k}_{\mathrm{i}} &= k\hat{\mathbf{y}} \\
\mathbf{k}_{\mathrm{f}} &= k\left(\sin 2\theta \cos\phi\hat{\mathbf{x}} + \cos 2\theta\hat{\mathbf{y}} + \sin 2\theta \sin\phi\hat{\mathbf{z}}\right) \\
\mathbf{q} &= q\left(\cos\theta \cos\phi\hat{\mathbf{x}} - \sin\theta\hat{\mathbf{y}} + \cos\theta \sin\phi\hat{\mathbf{z}}\right) \\
\hat{\mathbf{n}} &= -\sin\alpha\hat{\mathbf{y}} + \cos\alpha\hat{\mathbf{z}} \\
\sin\phi_{\mathrm{L}} &= \hat{\mathbf{n}} \bullet \frac{\mathbf{q}}{q} = \sin\phi\cos\alpha\cos\theta + \sin\alpha\sin\theta
\end{aligned} \tag{2.1}$$

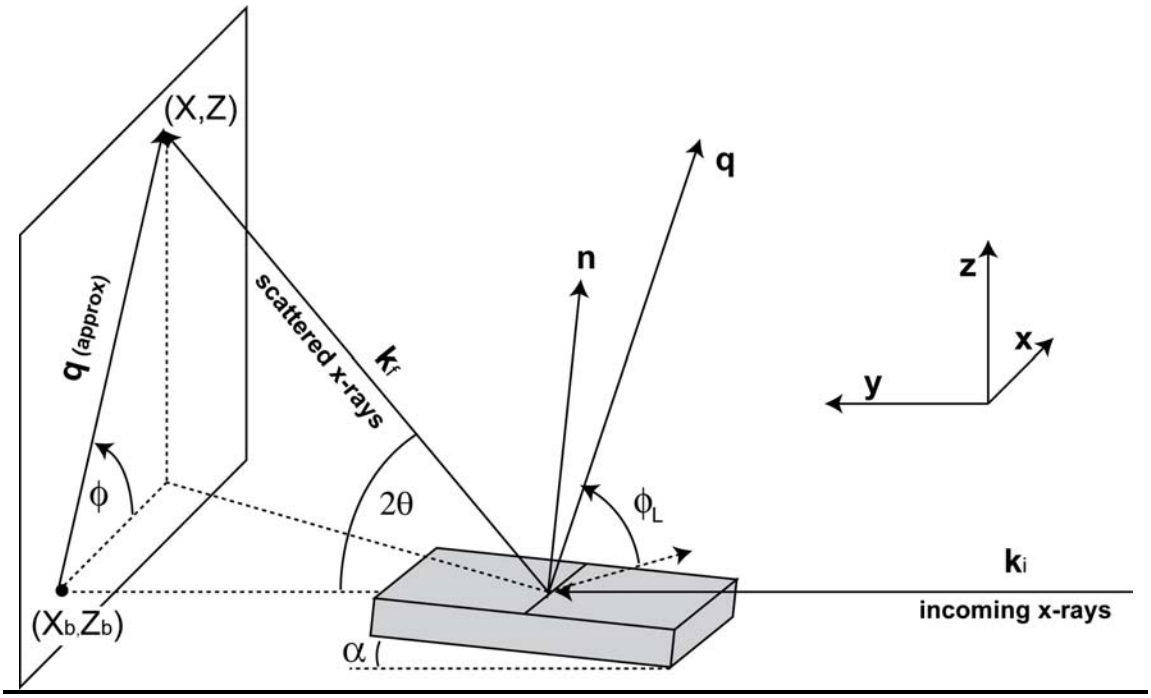


Figure 2.4. Experimental geometry for the grazing incidence setup (Drawing modified from a sketch by G. E. S. Toombes which appears in Busch et al., 2007).

Figure 2.5A shows a sketch of the experimental setup which applies to both beamlines. The sample chamber, detector, and beamstop were each mounted on separate motorized *x*-*z* translation stages (see also Fig. 2.6). In order to collect a full quadrant of the scattering pattern, the detector was positioned so that the beam hit the bottom corner of the detector as indicated in Fig. 2.4. The NIH chamber exit windows are wider than they are tall, and so the maximum scattering angle is most limited in the *z* direction ($2\theta_{zmax} \approx 27^{\circ}$). Also, styrofoam used to insulate the resistive wire used to heat the windows partially blocks the exit windows, further decreasing $2\theta_{zmax}$. However, it was also important to position the chamber horizontally (*x* direction) so that the scattered x-rays were not blocked in this direction; this meant that only about 2/3 of the 30mm sample could be used, but this was more than enough for all samples.

Shadows or complete cutoff of the WAXS pattern were obvious by simply collecting an image.

Figure 2.5B shows the beam in relation to the silicon substrate and lipid sample. As described in Section 2.3.2, the sample may be rotated independently within the stationary NIH chamber to control the incident angle, $\alpha$. For the AV chamber, the CHESS supplied G-1 rotation stage was used to rotate the entire chamber. As described in Section 2.3.4.3, the negative incidence angles are used to collect a "light background" which is subtracted from the GIWAXS data to eliminate scattering from the mylar windows.

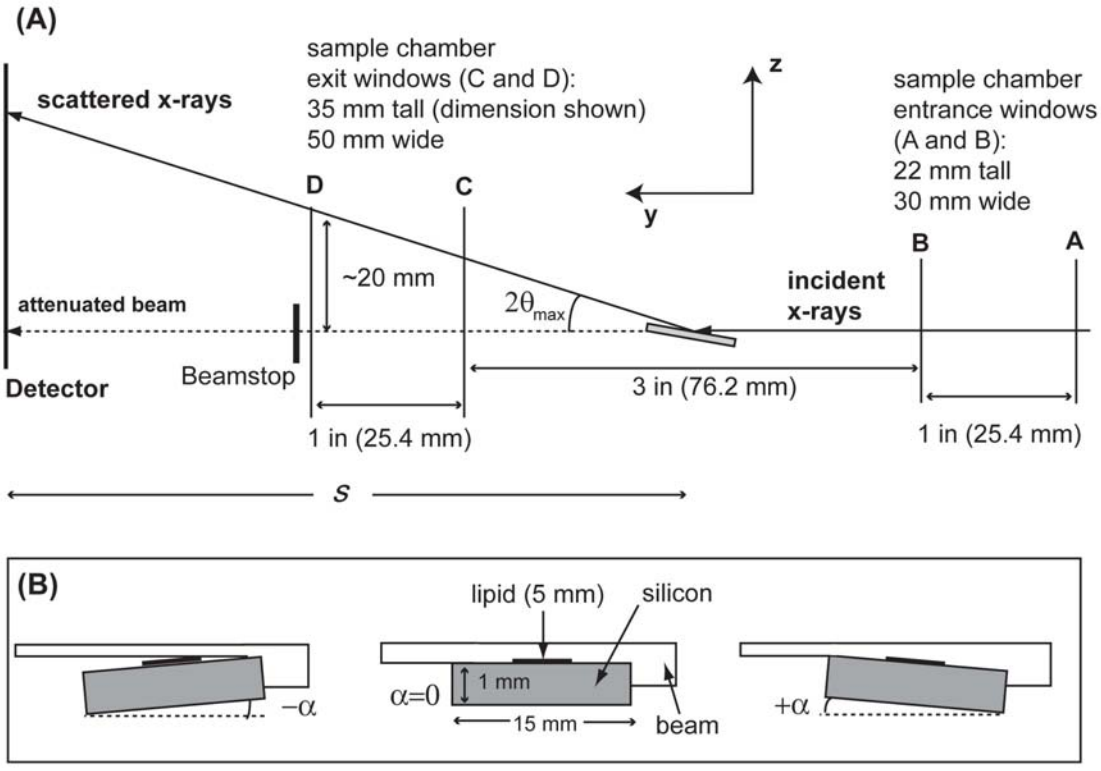


Figure 2.5. (A) Sketch of the experimental setup with a focus on dimensions of the sample chamber windows (A,B,C, and D), which limit $2\theta_{max}$ ($2\theta_{max} \approx 27^{\circ}$) and thus the maximum $q$ range allowed. (B) A closeup of the sample and beam geometry at different angles of incidence, $\alpha$.

#### 2.3.3.2 X-ray optical setup

The grazing incidence experiments were carried out at the D-1 station (May 2005 and February 2006) and the G-1 station (October 2006) at the Cornell High Energy Synchrotron Source (CHESS). D-1 is a bending magnet beamline, while G-1 is a wiggler beamline with 10-100 times or more intensity (depending on x-ray energy, optics such as the monochromator, etc.). Figure 2.6 shows the optical schematic for the G-1 beamline. The upstream slits S1 and S2 define the beam size, while the most downstream slits, SG, acts as guard slits to block parasitic scattering from slits, air, and other sources. During the October 2006 G-1 run, our slit configuration was as follows: S1 (0.55 mm vertical gap x 10.00 mm horizontal gap), S2 (0.55 mm vertical gap x 0.20 mm horizontal gap), SG (0.70 mm vertical gap x 0.25 mm horizontal gap). Upstream from the sample, the x-ray flightpath is filled with helium to reduce air scattering. The D-1 beamline has a similar 3-slit configuration with a helium-filled upstream flightpath.

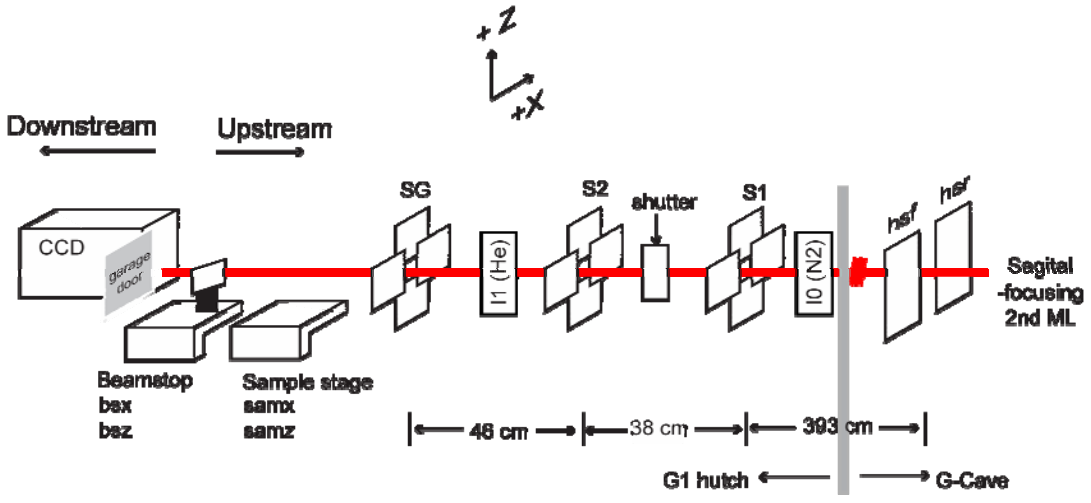


Figure 2.6. Optical schematic for G-1 beamline at CHESS (drawing from Arthur Woll).

At G-1, Mo:$B_4C$ multilayers (APS Optics Lab, Argonne, IL) ,with a 1.1 % full-width at half-maximum energy dispersion, were used to select x-rays with wavelength $\lambda$ = 1.274 Å ($E$=9.73 keV). The flux was 3 x $10^{11}$ photons/sec for the slit settings given above. At G-1, the beam was 0.25 mm x 0.6 mm. At D-1, a multilayer monochromator (Osmic, Detroit, MI) ,with a 0.66 % full-width at half-maximum energy dispersion, was used to select x-rays with wavelength $\lambda$ = 1.180 Å ($E$= 10.5 keV). At D-1, the beam was 0.3 x 0.3 mm square for most measurements presented (a 0.28 mm x 1.2 mm beam was used for the DPPC results). The beam heights and widths were selected to be compatible with the Nagle group's diffuse scattering LAXS measurements (tall beam required) and their LUV measurements (shorter, square beam required). Since the sample is only 10 microns high, only a small fraction of the beam height hits the sample for our wide-angle measurements. To reduce background scattering from sources such as mylar windows and air, a shorter beam would be advantageous for GIWAXS.

#### 2.3.3.3 Beamstop

A semitransparent molybdenum beamstop allowed for tracking of beam diagnostics (size, shape, intensity) throughout the experiment. The Mo beamstop works best when the x-ray energy is greater than 10 keV because the second harmonic is suppressed by the absorption edge near 20 keV. To minimize air scattering, the beamstop was placed as close as possible to the downstream end of the sample chamber. To minimize shadows caused by the beamstop cutting off background and the diffraction pattern, the beam should hit as close as possible to the edge of the rectangular beamstop.

Since each sample may have slightly different positions when mounted on the sample holder, the semitransparent beamstop is crucial for placing the sample in the

center of the beam and for finding the true $\alpha$=0. Figure 2.7 shows a typical image of the beam as seen through the semitransparent beamstop in which the sample is removed from the beam; this will be referred to as a beam picture (BP). The figure also shows slices through the image, which show how the plots in Fig. 2.8 and Fig. 2.9 were produced.

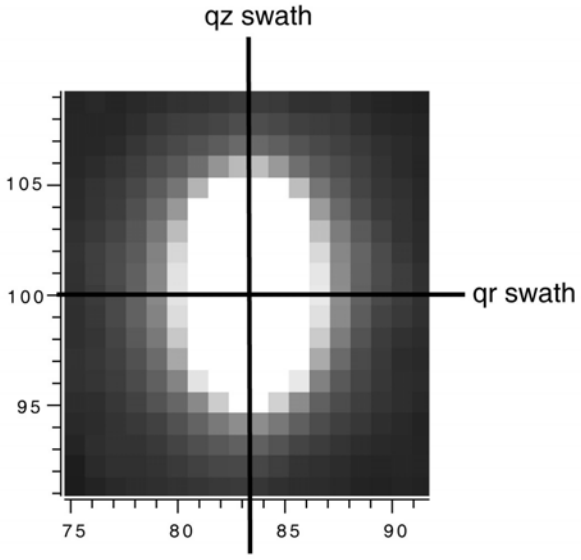


Figure 2.7. Beam picture (G-1, October 2006).

Figure 2.8 shows the beam profile in the horizontal ($p_r$ or $q_r$) direction. Figure 2.9 shows the beam profile in the vertical ($p_z$ or $q_z$) direction. Figure 2.9 also shows a vertical slice of the beam for an image in which the sample is cutting half of the beam ($\alpha$=0) and for an image for which the sample was continuously rotating through angles of -3˚ to 7˚ (used for lamellar repeat measurements, see Section 0). In TiffView, the program used for online analysis, these types of plots are termed qrplots and qzplots.

The qrplots and qzplots enable us to determine the beam center, which can change slightly from sample to sample. An arrow in Fig. 2.9 indicates the $p_z$=0 position. Note that the $p_z$=0 position is not in the middle of the peak in the qzplot but

is on the leading edge, corresponding to the top of the Si substrate. The $p_r$=0 position is in the middle of the peak in a qrplot.

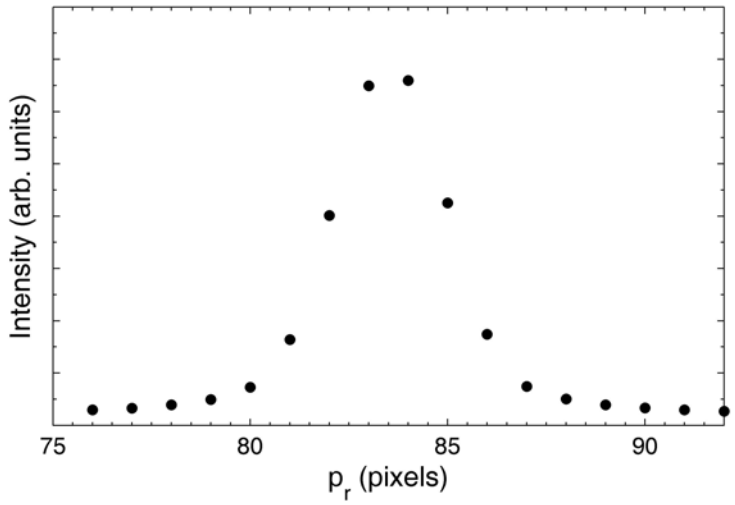


Figure 2.8. Beam profile in the $q_r$ direction (qrplot through BP shown in Fig. 2.7; G-1, October 2006).

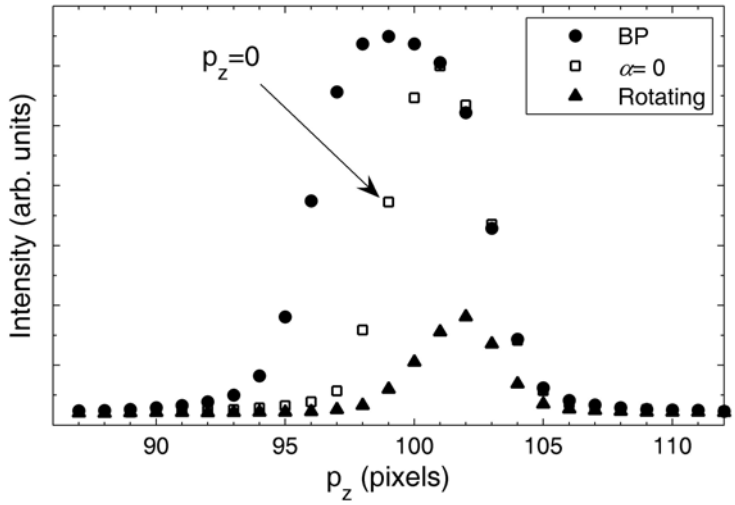


Figure 2.9. Intensity vs. $p_z$ (qzplots) for a beam picture (BP), image where $\alpha$=0, and image where the sample is continuously rotating through $\alpha$=-3 to 7˚. (G-1, October 2006).

#### 2.3.3.4 Detectors

For measurements at D-1, we used the "Medoptics" detector, a 1K (1024 X 1024 pixel) CCD detector, built at Cornell, with a pixel size of 0.04719 mm (total detector size ~48 mm x 48 mm). For measurements at the G-1 station, we used the "Flicam" detector, a 1K CCD detector, also built at Cornell, with a pixel size of 0.06978 mm (for a total size of ~71 mm x 71 mm). For most x-ray experiments, the following types of image corrections are standard and are provided by CHESS: dezingering, dark background subtraction, and distortion and intensity corrections (Barna et al., 1999).

**Zingers.** Zingers are very bright spots, only a few pixels in size, caused by cosmic rays or other sources of stray hard radiation (such as radioactive thorium in the fiberoptics taper). To remove zingers, two or more images taken back to back with the same exposure time are compared. It is unlikely that two short exposures taken in sequence with the same sample will have zingers in the same location. All bright spots in only one of the images are then removed. This process is called dezingering. Since the number of zingers scales with the length of the exposure, it is advantageous to add together many short (less than 5 minutes) exposures as opposed to taking one long exposure. Exposures were typically 120 seconds at D-1 (February 2006) and less than 20 sec at G-1 (October 2006).

**Dark background.** Even when not exposed to radiation, CCD detectors accumulate counts. In CCDs, there is thermally generated charge in the CCD chip, and so keeping the CCD chilled reduces this background intensity. A dark background is an exposure in which the incoming x-ray beam is completely blocked by the shutter. A dezingered dark background with the same exposure time as the image was subtracted from each image.

**Distortion and intensity corrections.** The CCD array is not a perfect grid, and so a geometrical distortion correction must be applied to produce the rectilinear diffraction image. The CCD pixels have different sensitivity to x-ray radiation, and so an intensity correction must also be applied. Saturating a CCD pixel (such as by exposing it to main beam) can change its sensitivity, and in some cases make it completely unresponsive. The CHESS staff periodically update the intensity correction files (see Barna et al., 1999).

#### 2.3.3.5 Calibration of sample-to-detector distance

The sample-to-detector distance (*S* in Fig. 2.5A) was chosen in order to obtain scattering at the widest angles possible compatible with the size of the chamber exit windows and their distance from the sample. The preferred *q* range would extend to at least $q$=2.5Å$^{-1}$ in order to observe the water scattering peak (see Section 2.3.8.1 for a detailed discussion). However, for the NIH chamber and for the x-ray energies used in the experiment (10.5 keV at D-1 and 9.7 keV at G-1), the upper part of the sample chamber exit window limits the *q* range to about 1.8 Å$^{-1}$ in the $q_z$ direction . Using higher x-ray energies to increase the *q* range is a possibility at the D-1 station but the preferred energy at the G-1 station is ~10 keV because the multilayer monochromator has tungsten which transmits less intensity above its absorption edge near 10.2 keV.

Given the window size and distance from the sample, a simple calculation gives the distance *S* of the CCD from the sample such that the CCD is just filled with the wide angle data permitted by the chamber exit window. After positioning the CCD, the accurate sample to detector distance, *S*, was found by calibration with silver behenate (spacing=58.367 Å). Like the lipid samples, the silver behenate is spread over a 5 mm strip in the middle of the 15 mm wide silicon piece. The silver behenate was rotated during data collection to sample all of the Bragg angles which results in

more accurate *d*-spacing measurements. For the AV chamber, fast rotations are not possible and so a fixed incident angle of 1.0˚ was used for calibration. From the known *d*-spacing, the sample to detector distance can be calculated based on the position of the silver behenate peaks (simply use Bragg's law). The TiffView program (written by Yufeng Liu; Liu, 2003) provides a useful interface for calculating sample-to-detector distances and *d*-spacings by minimizing errors in a linear, least-squares fit to the peak positions in pixels that are easily obtained in the TiffView quantitative plot window.

For the February 2006 D-1 experiment, the *S* distance was 115.7 mm. For the October 2006 G-1 experiment, the *S* distance was 151.7 mm for the NIH chamber and 121.2 mm for the AV chamber.

### 2.3.4 GIWAXS data collection protocol

When a new sample is placed in the chamber, the first step was to run helium through the chamber for at least 5 minutes to reduce background scattering by replacing air by helium. The sample was then aligned, hydrated and equilibrated at the desired temperature. The samples were aligned during hydration and temperature equilibration, which typically were allowed 30 minutes-1 hour. The following sections discuss the steps in the data collection process:

(1) Alignment

(2) Lamellar repeat ($d_L$-spacing) measurements during hydration

(3) GIWAXS data collection from lipid and "light background"

(4) Temperature changes and equilibration.

For analysis at the beamline, the program TiffView was used. This program has a GUI interface particularly convenient for online analysis during the alignment process and $d_L$-spacing measurements.

#### 2.3.4.1 Alignment

When a new sample was placed in the chamber, it was leveled (find $\alpha$=0) and properly aligned vertically (find samz=0). Usually, the zero positions from the last sample were roughly correct, but sometimes major re-alignment was necessary (for instance, when the sample holder was coated with a new layer of heatsink compound). Correct alignment is crucial for being able to subtract background scattering from the lipid GIWAXS pattern (see Section 2.3.4.3 ), so the alignment step should be done carefully.

Proper alignment was diagnosed by plotting I vs. $p_z$ for a vertical slice through the center of the beam. Refer to Fig. 2.10 for an example of qzplots for a properly aligned sample. The following are the steps in the alignment process:

1. A short exposure (typically 1 sec) was taken with the sample moved down fully out of the way of the beam (a "beam picture").
2. The sample was moved into the beam. (The zero positions for the last sample were good starting positions.) Then samz was adjusted until the beam was cut in half (refer to Fig. 2.5B). In the qzplot, the beam width at the zero position should be half as many pixels as in the beam picture. If not, samz was adjusted. We use "cutting of the beam" in reference to how much of the beam is blocked by the silicon substrate.
3. The $\alpha$=0 position was checked by taking exposures at positive and negative angles ($\pm 0.6^\circ$). The beam should be cut further relative to the nominal $\alpha$=0 cutting by the same number of pixels at the positive and negative angles. If not, the zero angle was adjusted according to the following geometric formula:

$$\alpha_0 = \frac{p(-\alpha) - p(+\alpha)}{2 \times \frac{7.5\,\text{mm}}{\text{pixel size}} \times \frac{2\pi}{360}}, \tag{2.2}$$

where the pixel size was 0.04719 mm for the Medoptics detector (D-1) and 0.06978 mm for the Flicam detector (G-1), and $p(-\alpha)$ and $p(+\alpha)$ are the pixel positions of the negative and positive angles.

4. If needed, the vertical position of the sample was adjusted again to ensure that the sample cut the beam in half and this position was reset to samz=0.

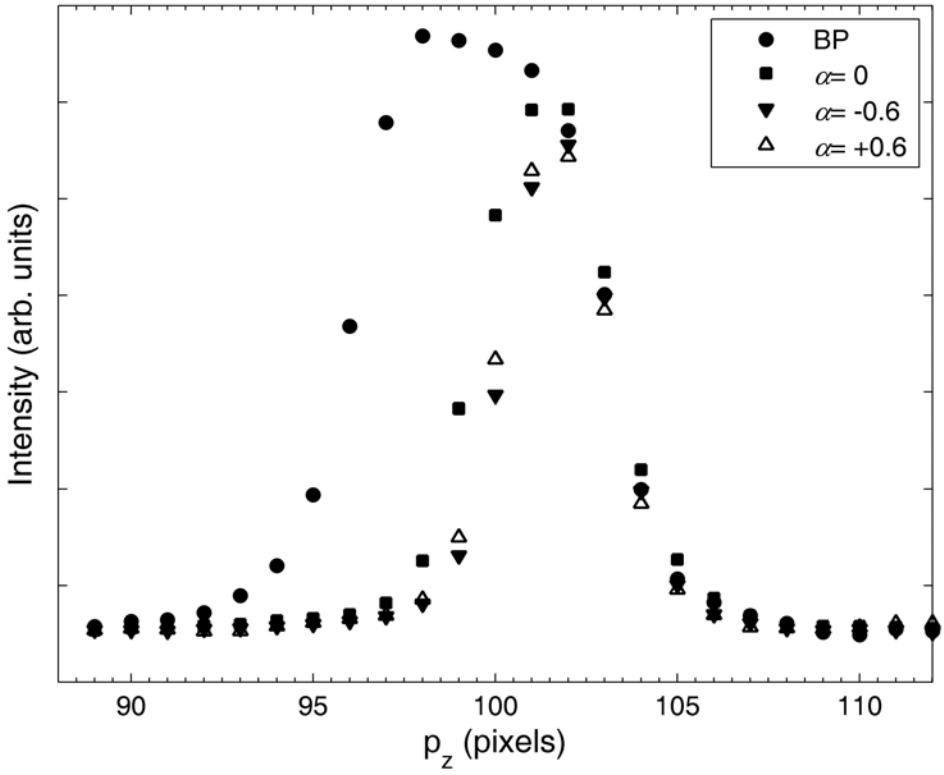


Figure 2.10. Example of qzplots ($I$ vs. $p_z$) for a well aligned sample. The height of the sample was adjusted so that the width of the $\alpha$=0˚ plot was half that of the beam picture (BP). The $\alpha$=-0.6˚ and $\alpha$=+0.6˚ plots should have exactly the same width if the nominal $\alpha$=0 were the true horizontal; the difference in widths in the figure corresponds to the $\alpha$=0˚ position being incorrect by less than 0.03˚. (G-1, October 2006, beam is 0.6 mm tall).

#### 2.3.4.2 Sample hydration and $d_L$-spacing measurements

For GIWAXS data collection, the aim is to take data within 1 to 5 Å of full hydration as measured by the lamellar repeat spacing ($d_L$-spacing) in comparison to fully hydrated powder MLV samples. As discussed in detail later in the chapter, water scattering is a problem near full hydration. Therefore, the $d_L$-spacing should be carefully monitored while the sample is hydrating to ensure that it is not "flooded" (water droplets begin to collect on the sample). Adjustment of the Peltier element in the sample chamber was used to speed up or slow down hydration. Typically, the target rate was full hydration 30 minutes-1 hour after the sample was loaded.

As with the silver behenate calibration, the $d_L$-spacing measurements were taken while cycling the sample angle $\alpha$ between -3˚ to 7˚ at 20˚/sec. At this rotation rate, the exposure time must be a minimum of 1 sec to ensure at least one complete rotation cycle. At the G-1 station, the lowest orders of lamellar repeat diffraction were so strong that two 25-micron molybdenum attenuators were placed before the sample in order to avoid detector saturation. Note that the $d_L$-spacing measurements were not taken from the same exposure as the WAXS collection for two reasons. Most important was that the WAXS data were taken at fixed incident angle while the sample was rotated during the collection of the lamellar repeat data. Also, the low order lamellar repeat scattering is much stronger and must be at least partially attenuated during WAXS collection. In practice, various attenuators were attached to the beamstop or different thicknesses of beamstop were employed and the beamstop assembly was moved in the $x$-direction to the appropriate position for the $d_L$-spacing measurements to uncover the lamellar repeat orders.

For the AV chamber, $d_L$-spacing measurements were taken at a fixed incident angle of 1.0˚. When taking lamellar repeat data at fixed angles, it is important to take data above the critical angle of silicon $\alpha_{Si} = 0.17$˚. At angles of incidence below $\alpha_{Si}$,

the incoming x-ray beam is completely reflected because in most material the refractive index of x-rays is less than 1 and closer to 1 in air. As shown in Fig. 2.11, the incoming and reflected beams have slightly different directions, $\mathbf{k}_{i1}$ and $\mathbf{k}_{i2}$. X-rays scattered by an angle of $2\theta$ from the incoming beam ($\mathbf{k}_{f1}$) travel at a slightly different angle to x-rays scattered by an angle of $2\theta$ from the reflected beam ($\mathbf{k}_{f2}$). Thus, for low incidence angles ($\alpha<\alpha_{Si}$) each lamellar "peak" splits into two spots corresponding to x-rays scattered from the incoming and reflected beams. This effect is important to keep in mind if future work is done in the AV chamber, for which $d_L$-spacing data must be taken at a fixed angle of incidence.

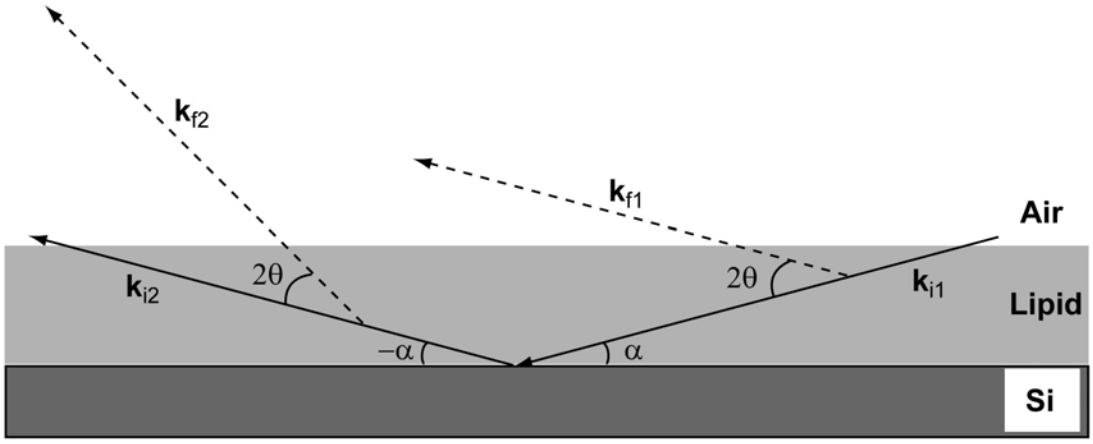


Figure 2.11. Illustration showing why the lamellar peaks are split when the incidence angle $\alpha$ is less than the critical angle of silicon, $\alpha_{Si}$=0.17˚. There are two main incident beam directions ($\mathbf{k}_{i1}$ and $\mathbf{k}_{i2}$) and therefore two scattered x-ray directions ($\mathbf{k}_{f1}$ and $\mathbf{k}_{f2}$), resulting in splitting of the peaks. For scattering at wide angles, the change in direction is very small in comparison with $2\theta$ and so no splitting is observable. In the picture, refraction of the beam at the air-lipid interface was ignored for simplicity.

Figure 2.12 shows examples of the scattering pattern from the lamellar repeat orders for a gel-phase lipid (DPPC at 25˚C), a fluid phase lipid (DOPC at 25˚C), and a ternary lipid mixture with two $d_L$-spacings, all taken at the D-1 station (no

attenuators). Note the spherical shape of the lamellar repeat lobes and the surrounding diffuse scatter for DOPC (Fig. 2.12B), in contrast to the sharp reflections for gel-phase DPPC (Fig. 2.12A).

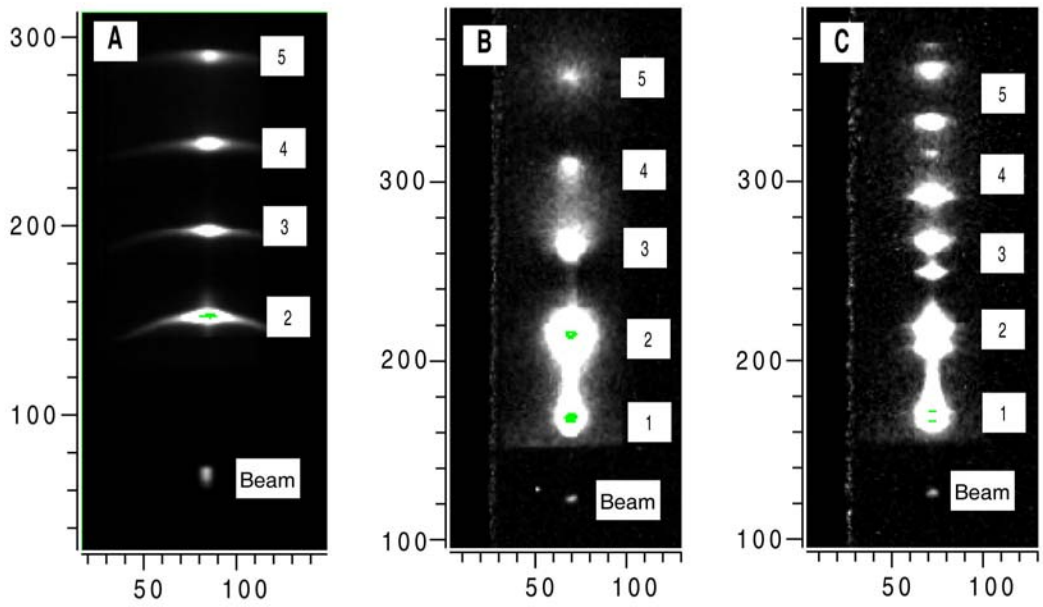


Figure 2.12. Diffraction images zoomed in on the lamellar repeat scattering for: (A) DPPC at 25˚C ($d_L$ =63.4 Å), (B) DOPC at 25˚C ($d_L$=60.9 Å), and (C) 1:1 DOPC:DPPC + 20% cholesterol at 15˚C ($d_L$=67.7 Å and 59.9 Å). All images were collected without attenuators during the February 2006 run and the intense first order peak in (A) was blocked by raising the beamstop. The numbers correspond to the lamellar repeat orders. On the left side, the images are cut off by a frame which was placed in front of the detector. The shadow at the bottom is from the beamstop.

Figure 2.13 shows the intensity vs. $p_z$ (qzplots) for DOPC and for a ternary mixture (see Fig. 2.13 caption). The first order peak is often saturated, and so the second and third orders were used to obtain the $d_L$-spacing with the utility "ds" subprogram in TiffView. Input to "ds" is the sample-to detector distance in

millimeters, the x-ray wavelength in angstroms, the detector pixel size in millimeters, and the position of the lamellar repeat orders in pixels. The program then uses Bragg's law to calculate an average $d_L$-spacing from the assigned Bragg orders. Correct assignment of the zeroth order (the beam position) is critical for obtaining an accurate $d_L$-spacing value for the fluid phases whose higher orders are corrupted by diffuse scattering. The inset in Fig. 2.13 shows an example of a correct $p_z$=0 assignment. Note that the $p_z$=0 position is the leading edge of the beam closest to the sample, not the middle of the peak in the qzplot (Fig. 2.9). TiffView plots the residuals (the difference between the average and the value for a particular order); minimizing the residuals is a good way to estimate the proper $p_z$=0 position. A difference in one pixel can change the $d_L$-spacing value by as much as 0.4 Å.

The example of two $d_L$-spacings shown in Fig. 2.13B is for a sample known to be in a two-phase Ld/Lo region. The $d_L$-spacing data for oriented samples must be interpreted cautiously because less than fully hydrated samples such as DOPC sometimes have two $d_L$-spacings at times during the approach to equilibrium. However, the behavior of the ternary mixtures in the Ld/Lo coexistence region was different. Typically for DOPC or another sample known to be in a single phase, the two $d_L$-spacings do not persist as full hydration conditions are approached. However, for the ternary mixtures the double $d_L$-spacings persisted at low temperatures even as the full hydration condition was approached but not at high temperatures, where these samples are known to be in a single Ld phase. This behavior is interesting, but again should be interpreted cautiously because we tried to avoid full hydration conditions because of problems with flooding and water scattering (see Section 2.3.8.1).

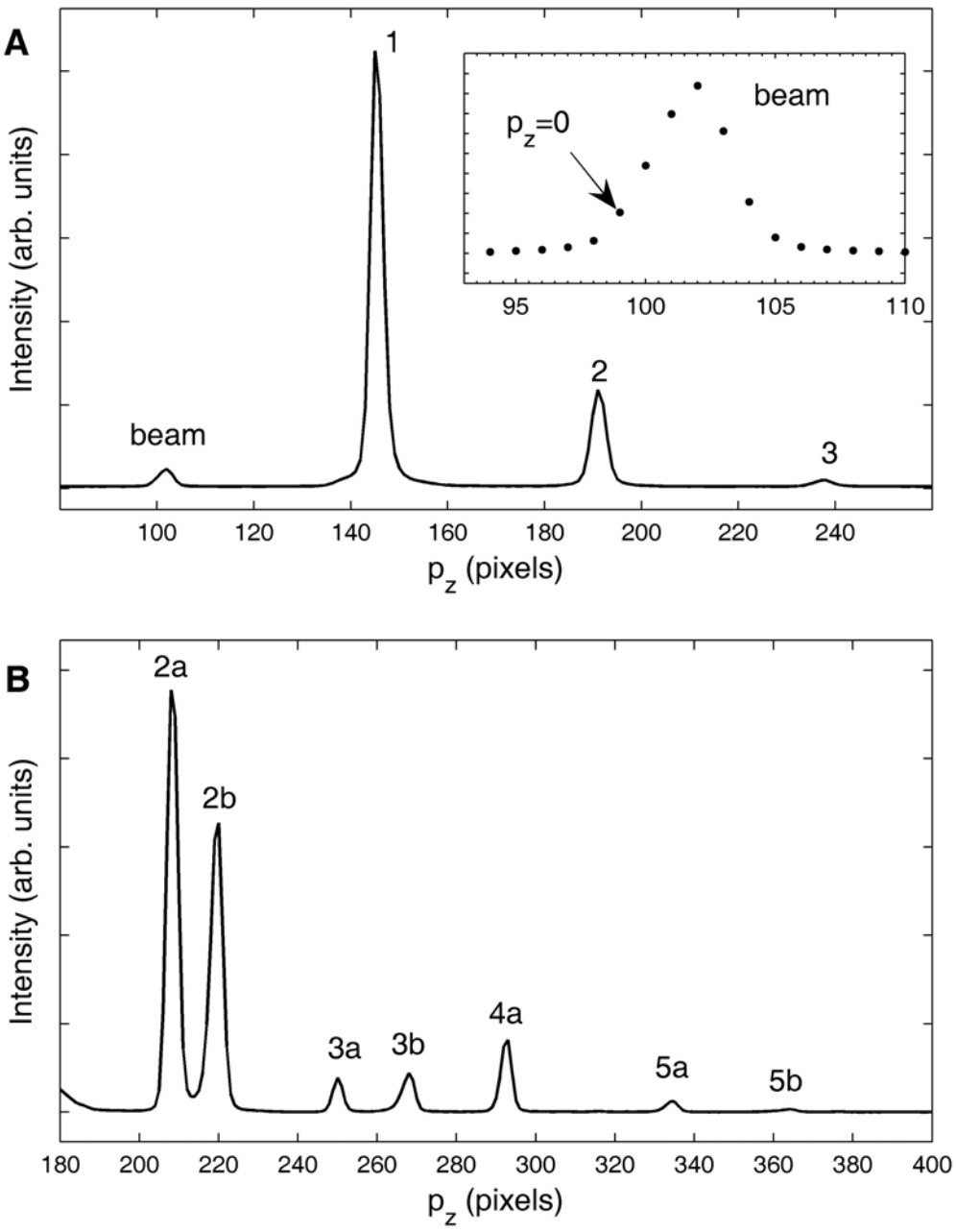


Figure 2.13. $I$ vs. $p_z$ (qzplots) showing the lamellar repeat peaks for: (A) DOPC ($d_L$=60.0 Å; G-1,October 2006) and (B) 1:1 DOPC:DPPC + 20% cholesterol at 15 ˚C ($d_L$=67.7 Å and 59.9 Å; D-1,February 2006; 2D diffraction image shown in Fig. 2.12C). The inset in (A) is the same as the "Rotating" qzplot shown in Fig. 2.9. The numbers on the peaks correspond to the lamellar repeat orders. In plot (B), "a" corresponds to the 67.7 Å lamellar repeat and "b" corresponds to the 59.9 Å lamellar repeat. Peak 4b is extinct.

#### 2.3.4.3 GIWAXS data collection: "light background" subtraction

A crucial part of the GIWAXS data collection was measurement of a "light background," an image in which the beam is partially blocked by silicon and does not hit the lipid sample. We use "cutting of the beam" in reference to how much of the beam is blocked by the silicon substrate. For the light background and sample data, cutting of the beam must be identical because upstream mylar (and air/He) scattering is different from the downstream mylar scattering.

Identical cutting of the beam was obtained in the following two ways (refer to Fig. 2.5B for picture of positive and negative angles of incidence):

1. The sample data were collected at $\alpha = +0.15^\circ$, and the light background was obtained at $\alpha = -0.15^\circ$.
2. The sample data were taken at $\alpha < \alpha_{critical}$ (the critical angle of lipid~$0.12^\circ$). The light background was taken at a negative angle with larger magnitude ($\alpha = -0.5^\circ$), and the sample chamber was lowered so that the beam cutting was still identical.

Method 1 will only work for $|\alpha| \geq 0.15^\circ$, as can be calculated from the dimensions of the lipid (5 mm wide and 10 μm high) on the substrate (1.5 mm wide). Method 2 allows smaller $\alpha$, but in practice obtaining the correct samz position for the light background was problematic. The samz position for the light background had to be adjusted by trial and error because the calculated position (based on the angle and dimensions of the substrate) often did not result in a good subtraction. As long as the sample is properly leveled, method 1 worked consistently. Method 2 (with $\alpha = 0.10^\circ$) was used during the February 2006 run at the D-1 station, while method 1 (with $\alpha = 0.15^\circ$) was used during the October 2006 run at G-1.

Figure 2.14 shows examples of GIWAXS images for the sample, light background, and subtracted image for data taken at the D-1 station in February 2006 and the G-1 station in October 2006. In Fig. 2.14B and 2.14E, the strongest mylar scattering ring is labeled according to the window causing the scattering (see Fig. 2.5A). There is more than one such mylar ring because each of the four mylar windows is a different distance from the detector. For the mylar windows upstream (A and B) from the sample, the sample cuts off the scattering below the equator, while the sample does not cut off the scattering for the downstream windows (C and D). Scattering from window D is not visible in Fig. 2.14E because the beamstop was moved closer to the sample chamber in the October 2006 G-1 experiment.

There are some obvious differences in the images from the two different runs. The WAXS beamstop in the February 2006 D-1 run was a tall vertical strip (see left side of Fig. 2.14A-C), whereas the top edge of the shorter beamstop for the October G-1 run is visible (see bottom left in Fig. 2.14D-F). The fuzzy shadows on the upper portions of the images are due to styrofoam and wires (used for heating the windows, see 2.3.4.4) around the sample chamber exit window. These shadows subtract out, as can be seen by comparing Fig. 2.14A with Fig. 2.14C and Fig. 2.14D with Fig. 2.14F. Because the x-ray wavelength was larger in the October 2006 G-1 setup than the February 2006 D-1 setup, the exit windows allowed for a slightly smaller $q_z$ range in the October 2006 run (compare Fig. 2.14F to Fig. 2.14C).

A $q$ range any smaller than that available in the October 2006 run would make data analysis challenging. This means we would not want to use x-rays with wavelengths larger than 1.27 Å with the NIH chamber. To use the rotating anode Cu Kα line ($\lambda$=1.54 Å), the experiment requires a chamber with bigger windows, such as the AV chamber.

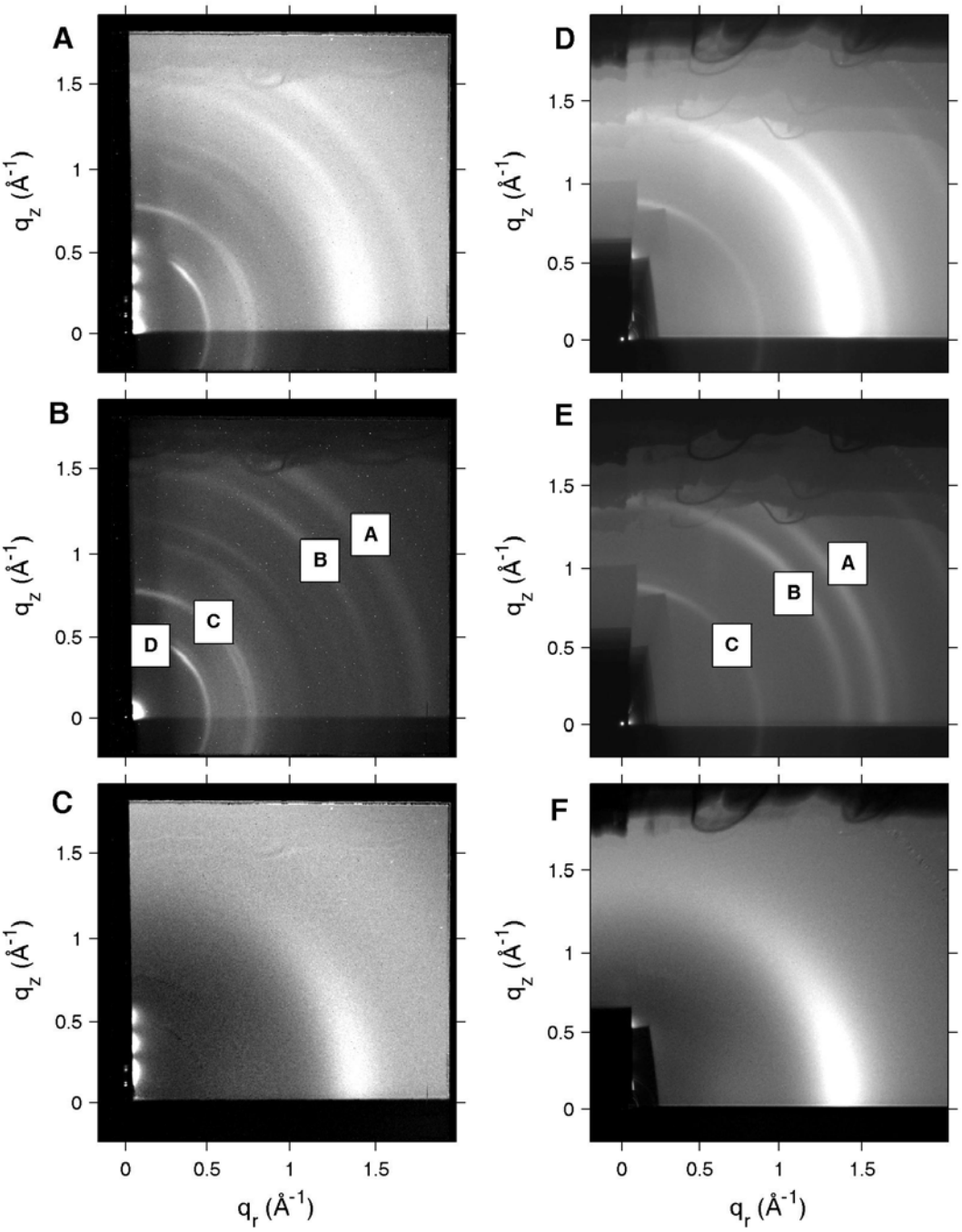


Figure 2.14. The left panel shows examples of 2D GIWAXS images for: (A) a DOPC sample before light background subtraction, (B) the light background, and (C) the sample after light background subtraction (NIH chamber, D-1 station, February 2006). The right panel (D-F) shows the corresponding images for a DOPC sample (NIH chamber, G-1 station, October 2006). Light background (B) was taken using method 2 (see text), while light background (E) was taken using method 1.

#### 2.3.4.4 Changing temperature

For samples in which data at many temperatures was desired, data were first collected at the lowest temperature and then the temperature was raised. This procedure was followed because for phase-separated mixtures, melting is easier than the phase separation process. Therefore, the miscibility transition for the heating cycle is more reproducible than for the cooling cycle. All of the samples underwent an annealing and slow cooling process before being loaded into the x-ray sample chamber (see Section 2.3.1).

Practically, heating tends to flood the sample, while cooling dehydrates the sample because the water vapor equilibrates to the new temperature faster than the sample. To avoid flooding, the Peltier was turned to +2M (dehydrating current direction) and helium was flowed through the sample chamber during the entire heating process. The temperature on the Neslab was increased in increments of no more than 3˚C; before increasing the temperature again, the sample chamber was allowed to reach the setpoint. At temperatures higher than room temperature, condensation drops on the inner sample chamber windows (B and C in Fig. 2.5A) can occur and distort the scattered intensity; for temperatures above 35˚C, the window current was set at 200 mA.

### 2.3.5 Instrumental resolution

The success of the experiment relies on being able to interpret the angular distribution and lateral width of the wide-angle scattering in terms of chain orientational order and lateral positional order. We want to make sure that the differences we see in our GIWAXS data are due to differences in the sample composition or temperature and are not affected by the experimental resolution. Fortunately, the gel phase of DPPC provides a direct measure of our instrumental

resolution with the (2,0) peak that occurs in Fig. 2.1A near $q_r$=1.49 Å$^{-1}$ and $q_z$=0. This peak is due to chain-chain scattering. It is elongated in the $q_z$ direction because the chains have finite length, but it is very narrow in the $q_r$ direction because of high lateral packing order. Because the chain packing is distorted from the hexagonal, it is standard to use a face-centered orthorhombic lattice, with two chains per unit cell, for peak indexing. (See Ashcroft and Mermin, 1976 for an explanation of Miller indices and Tristram-Nagle et al., 1993 for an example of the use of this indexing for lipids.) This peak has been resolved using an Si monochromator and analyzer crystal to have an intrinsic width only 0.004 Å$^{-1}$ (FWHM) (Sun et al., 1994). Therefore, our measured width 0.04 Å$^{-1}$ of this peak provides our $q_r$ instrumental resolution.

The theoretical analysis of instrumental resolution given in the remainder of this 2.3.5 subsection is consistent with the experiment and it provides insight into different experimental contributions.

#### 2.3.5.1 Sample mosaicity and rocking curves

Figure 2.15 shows three types of samples: (A) a well oriented sample with highly ordered chains, (B) a well oriented sample with disordered chains, and (C) a poorly oriented sample with highly ordered chains. In Fig. 2.15C, the angular distribution of bilayer normal vectors, termed mosaicity, is wide. In Fig. 2.15B, the distribution of chain tilt angles is wide. In both of these cases, the chain-chain correlation scattering will have a large angular spread in comparison with the case shown in Fig. 2.15A. Since we want the angular spread in the GIWAXS pattern to indicate the distribution of tilt angles (not the mosaicity), it is important to use well oriented samples for the GIWAXS experiment. In general, the sample orientation was monitored by observing the mosaic spread of the lamellar repeat peaks along the $q_z$ axis (see Fig. 2.12 for diffraction images of the lamellar peaks). In well-oriented

samples, the Bragg orders are short arcs while in a poorly oriented sample these arcs elongate. In the extreme example of a completely unoriented MLV powder sample, the Bragg peaks become isotropic rings.

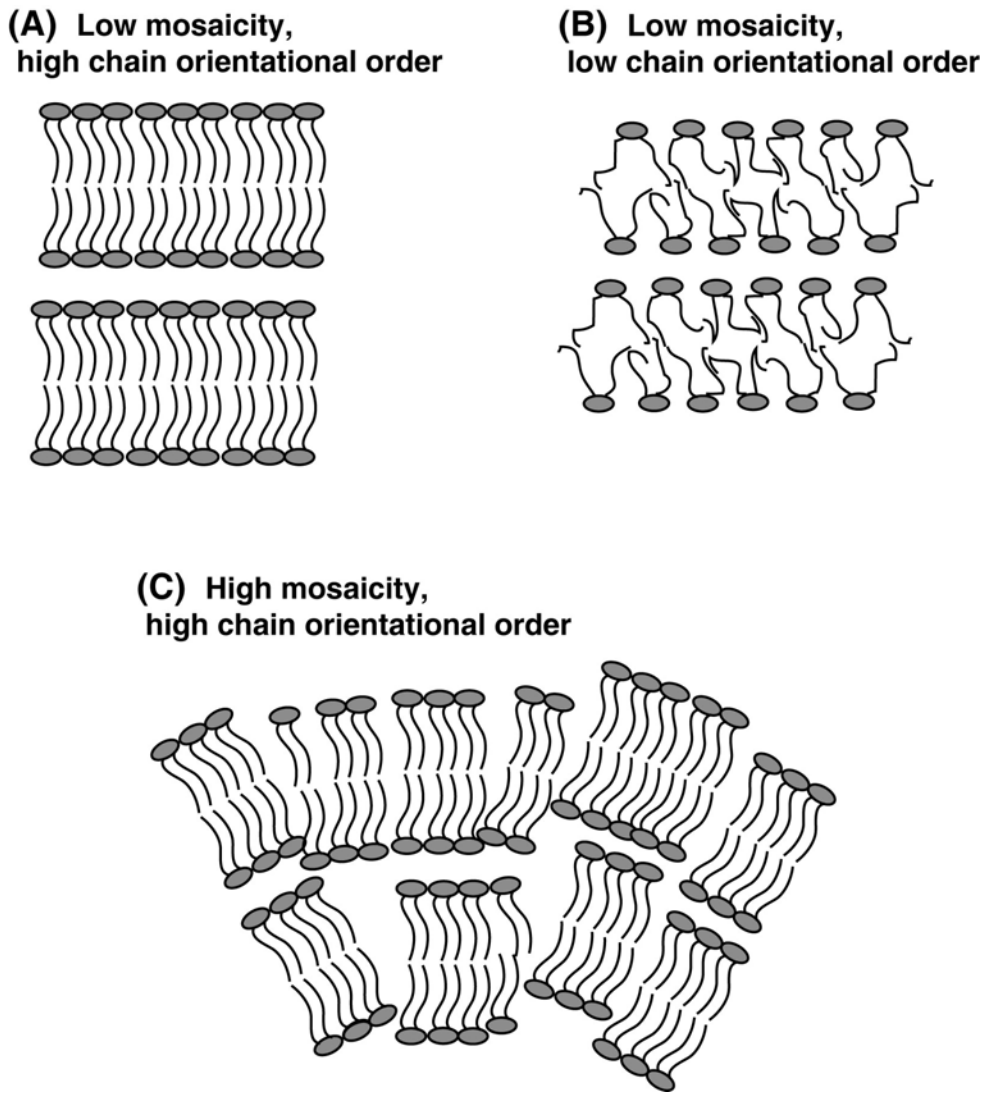


Figure 2.15. Cartoon showing: (A) a well oriented sample with highly ordered chains, (B) a well oriented sample with disordered chains, and (C) a poorly oriented sample with highly ordered chains. In (B) and (C), the chain-chain scattering will have a larger angular spread in comparison with (A).

The mosaic spread is a convenient measure of sample misorientation. Rocking curves provide a quantitative way to obtain mosaic spread. The intensity of a lamellar repeat order is measured as a function of the incident beam angle, $\alpha$, while holding the scattering angle $2\theta_n$, on the $n$th order peak, fixed. The rocking curve reports the distribution $g(\tau)$ of domains misoriented by the angle $\tau=\alpha-\theta_n$ from perfect orientation $\tau=0$. Assuming proper alignment of the sample (see Section 2.3.4.1), maximum scattering will occur when $\alpha=\theta_n$:

$$n\lambda = 2d_L \sin\theta_n . \tag{2.3}$$

For a rocking curve, the lamellar repeat spacing $d_L$ must be known and stable. Rocking curves should not be taken on hydrating samples or phase-separated samples. Figure 2.16 shows two examples of rocking curves for DOPC/DPPC/cholesterol mixtures taken at the D-1 station in February 2006 (plots B and C) compared with a rocking curve for DMPC from a previous Nagle lab experiment (plot A). For Fig. 2.16B and C, the second lamellar repeat order was used for the measurement. For example, in Fig. 2.16C the predicted angle for the maximum intensity was calculated from Eq. 2.3 with $n$=2, $\lambda$=1.180 Å$^{-1}$, and $d_L$=65.1 Å$^{-1}$, giving $\alpha_{max}$=1.04˚. Short exposures (less than 1 sec) were then taken for angles above and below $\alpha_{max}$. Because the minimum exposure length is 0.1 sec, a molybdenum attenuator was used to avoid detector saturation near $\alpha_{max}$. The intensity is integrated for a box surrounding the peak, with care to subtract the specular reflection from silicon, which moves through the peak as the incident angle is changed. The rocking curves indicate that the samples shown in Fig. 2.16B and C are well oriented, with sample mosaicities below 0.03˚ halfwidth at half maximum. The changes in angular spread of the GIWAXS peak observed as a function of temperature and sample composition are large in comparison to small differences in mosaicity from sample to sample.

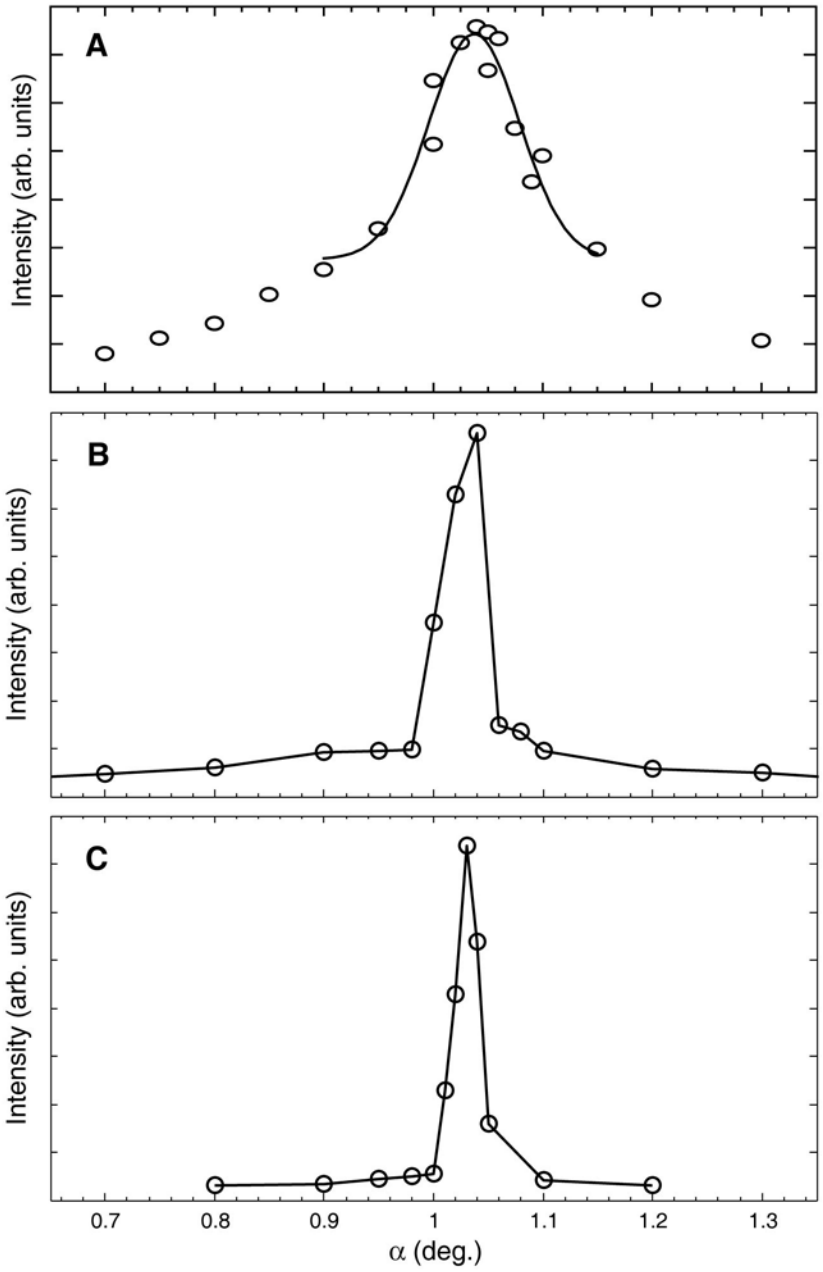


Figure 2.16. Rocking curves showing the intensity of the second lamellar repeat peak vs. $\alpha$ for (A) DMPC at 30˚C , (B) DPPC + 10% cholesterol at 45˚C, and (C) 1:1 DOPC:DPPC + 30% cholesterol at 45˚C. Plot (A) is from a previous Nagle lab experiment (Tristram-Nagle, 2007). In plot (A), the black line corresponds to a Gaussian fit, while in (B) and (C), the black lines connect the points as a guide to the eye. For (A), the HWHM from the Gaussian fit is 0.08˚. For (B), the intervals in the peaked region are 0.02˚ for $\alpha$=0.98-1.1˚. These intervals were too large for a good estimate of the HWHM, but we can say that the HWHM<0.03˚ for (B). For (C), the intervals in the peaked region are 0.01˚ for $\alpha$=1.0-1.05˚; the HWHM is ~0.01˚.

#### 2.3.5.2 Geometric broadening

Geometric broadening is spreading of the scattering intensity over a range of $q$ values due to the non-negligible size of the sample in comparison with the sample to detector distance. Figure 2.17 diagrams the lipid sample and considers the scattering which arrives at the detector a distance $S\tan\theta$ from the beam center. Scattering from the upstream part of the sample will arrive at a different point on the detector than scattering from the downstream end of the sample, causing scattering peaks to broaden. Figure 2.17 also takes into account the finite width of the x-ray beam, $b$.

On the detector, a peak that would be at $S\tan 2\theta$ neglecting geometric broadening will be spread over a distance $b + f\tan 2\theta$, where $b$ (~0.3 mm) is the size of the beam and $f$ is the sample footprint (always 5 mm in our experiments). The following equation gives the geometric broadening, $\Delta q$, in terms of the fraction of the scattering wavevector magnitude, $q$:

$$\frac{\Delta q_{\text{geom}}}{q} = \frac{b + f\tan 2\theta}{S\tan 2\theta} \tag{2.4}$$

Assuming $q$=1.4 Å$^{-1}$ (a common value for the lipid WAXS peak), we obtain $\Delta q_{\text{geom}}/q$=0.053 =5.3% for February 2006 D-1 setup and $\Delta q_{\text{geom}}/q$=0.040=4.0% for the October 2006 G-1 setup. Other experimental factors which can broaden the peak are the energy dispersion (~1.1% at G-1 in October 2006; 0.6% at D-1 in February 2006) and the beam divergence ($\Delta\theta_{\text{div}}^{\text{rad}}$ =10$^{-4}$ radians). The broadening due to the energy dispersion is:

$$\frac{\Delta q_{\text{energy}}}{q} = \frac{\Delta E}{E} = 0.01 = 1\% \tag{2.5}$$

The broadening due to the beam divergence is given by:

$$\frac{\Delta q_{\text{div}}}{q} \approx \frac{1}{q}\left(\frac{4\pi}{\lambda}\Delta\theta_{\text{div}}^{\text{rad}}\right) \tag{2.6}$$

With $q$=1.4 Å$^{-1}$, $\Delta q_{div}/q$<0.001 (or $\Delta q_{div}/q$<0.1%), which is negligible in comparison with the effects of geometric broadening and the energy dispersion. The total resolution is given by:

$$\frac{\Delta q_{tot}}{q} = \sqrt{\left(\frac{\Delta q_{geom}}{q}\right)^2 + \left(\frac{\Delta q_{energy}}{q}\right)^2} \tag{2.7}$$

For the G-1 setup, $\Delta q_{tot}/q$=0.041=4.1%. For the D-1 setup, $\Delta q_{tot}/q$=0.054=5.4%.

Assuming the samples are well aligned, geometric broadening is the main artifact causing smearing of the chain-chain correlation peak (the energy dispersion was much less in both setups). To reduce the effect of geometric broadening, the sample footprint could be shortened, although trimming the sample more would probably increase mosaic spread. Also, with a larger detector, the sample-to-detector distance can be increased, as it was for the experiment at G-1 in October 2006. Since the samples in this experiment for the most part have very wide chain-chain correlation peaks and we are most interested in trends in the data, the ~5% effect of geometric broadening does not pose a large problem in interpreting the GIWAXS data. We can compare our calculated value for the resolution to the full width at half maximum (FWHM) for the DPPC gel phase equatorial (2,0) peak, which should be a sharp peak (see Fig. 2.18B). For this sample: FWHM/$q$=0.04 Å$^{-1}$/1.48 Å$^{-1}$=3%. The 5% resolution calculated for the February 2006 D-1 experiment is actually somewhat larger than the broadening we observed in the DPPC gel-phase peak. This could be due to absorption of the x-rays by the sample that effectively reduces the sample footprint and the geometric broadening that is the major contributor to $q_r$ resolution.

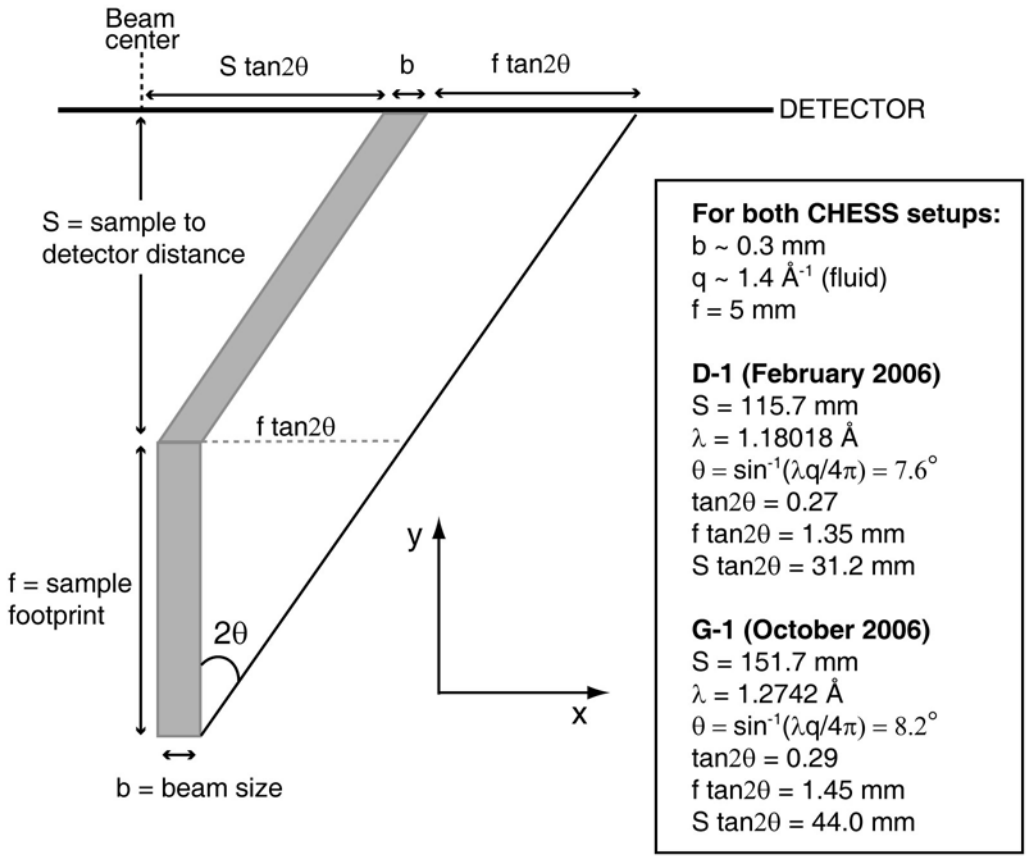


Figure 2.17. Schematic showing the effect of geometric broadening on the scattering which arrives at the detector.

### 2.3.6 Choice of incident angle

To determine an appropriate incident angle for the grazing incidence diffraction experiments, DPPC at 25˚C, in the Lβ' phase, was used as a control. Figure 2.18 shows GIWAXS data for DPPC at two angles below and two angles above the lipid critical angle of approximately 0.12˚. In the Lβ' phase, the tilted DPPC chains form a distorted hexagonal lattice, giving rise to two diffraction spots with intensity maxima at different values of $q$ and $\phi$. The equatorial (2,0) peak has $q$=1.48 Å$^{-1}$ and the (1,1) peak, which has an intensity maximum near $\phi$=32˚, has $q$=1.50 Å$^{-1}$ (Tristram-Nagle et al., 1993; Sun et al., 1994). For $\alpha$ = 0.2˚ and 0.5˚, splitting of the (2,0) peak can be observed (Fig. 2.18 C and D) . For $\alpha \leq 0.15$˚, no splitting is observed and the $q$ value for the (1,1) peak agrees with the literature (Fig. 2.18 A and B; data similar for $\alpha$=0.15˚). We cannot yet explain why the splitting occurs, but we attempted to avoid this artifact by collecting GIWAXS data at incident beam angles $\alpha \leq 0.15$˚. Collecting at smaller incident angles also minimizes the substrate's blockage of scattering at the smallest $\phi$ angles.

For fluid-phase lipids, the GIWAXS pattern appears to be independent of incident angle. Figure 2.19 shows GIWAXS images for fluid-phase DOPC at $\alpha$=0.1˚ and 0.5˚. Figure 2.19C compares the corresponding $I(q)$ plots (see Section 2.3.7.3) for radial slices ($\phi$=5-10˚) for these data. When normalized to have the same peak intensity, the data are nearly identical. The choice of incident angle is not crucial for fluid-phase lipids, but the data were taken at $\alpha \leq 0.15$˚ to avoid any possible splitting effects as observed in the gel phase.

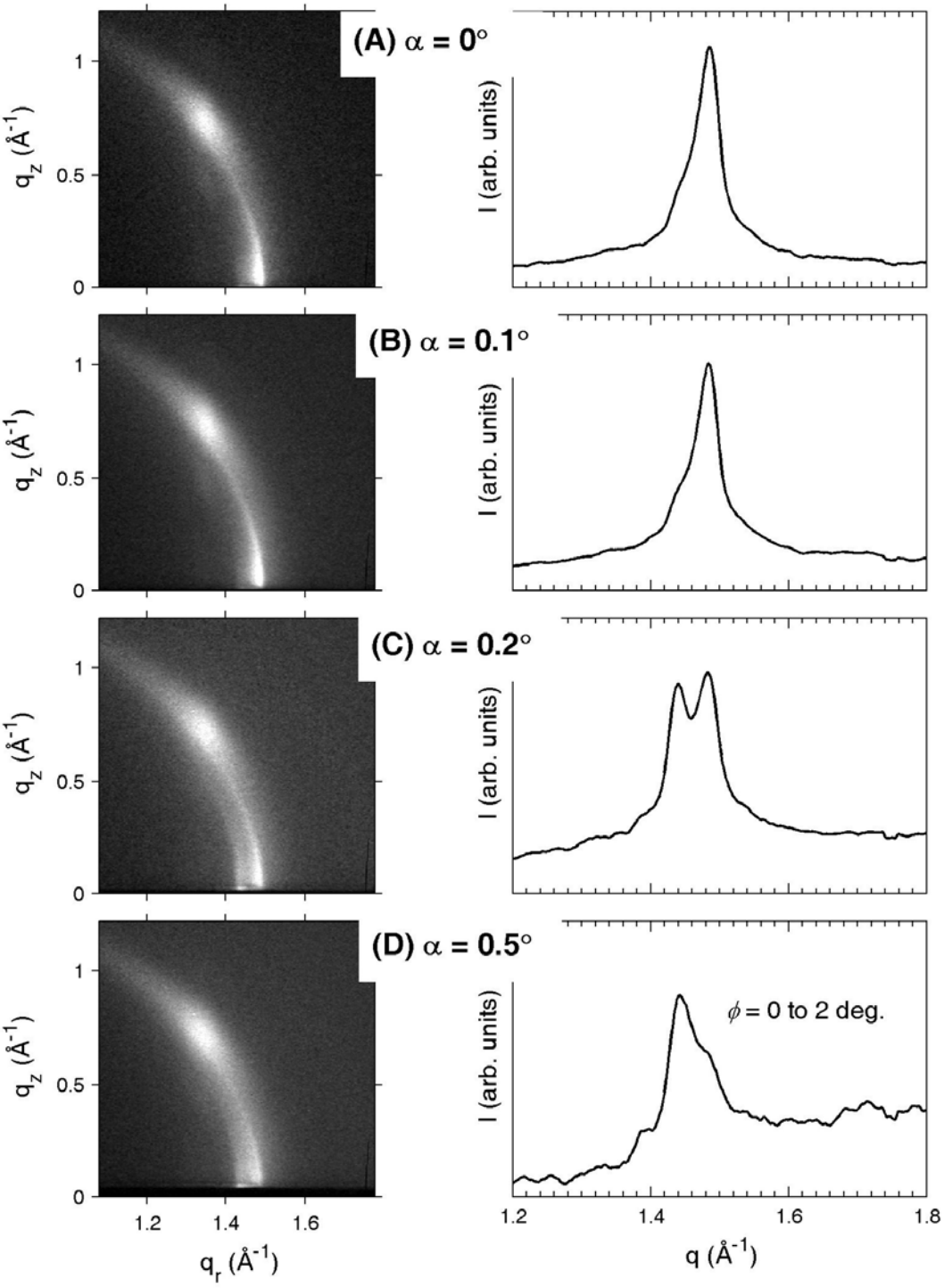


Figure 2.18. The left panel shows GIWAXS data for DPPC at incidence angles of (A) $\alpha = 0^{\circ}$; (B) $\alpha = 0.1^{\circ}$; (C) $\alpha = 0.2^{\circ}$; (D) $\alpha = 0.5^{\circ}$. The right panel shows the corresponding $I(q)$ plots (see Section 2.3.7.3) for an integrated radial slice ($\phi$=0-2˚) through the data. For $\alpha = 0.2^{\circ}$ and $0.5^{\circ}$, splitting of the (2,0) peak is visible.

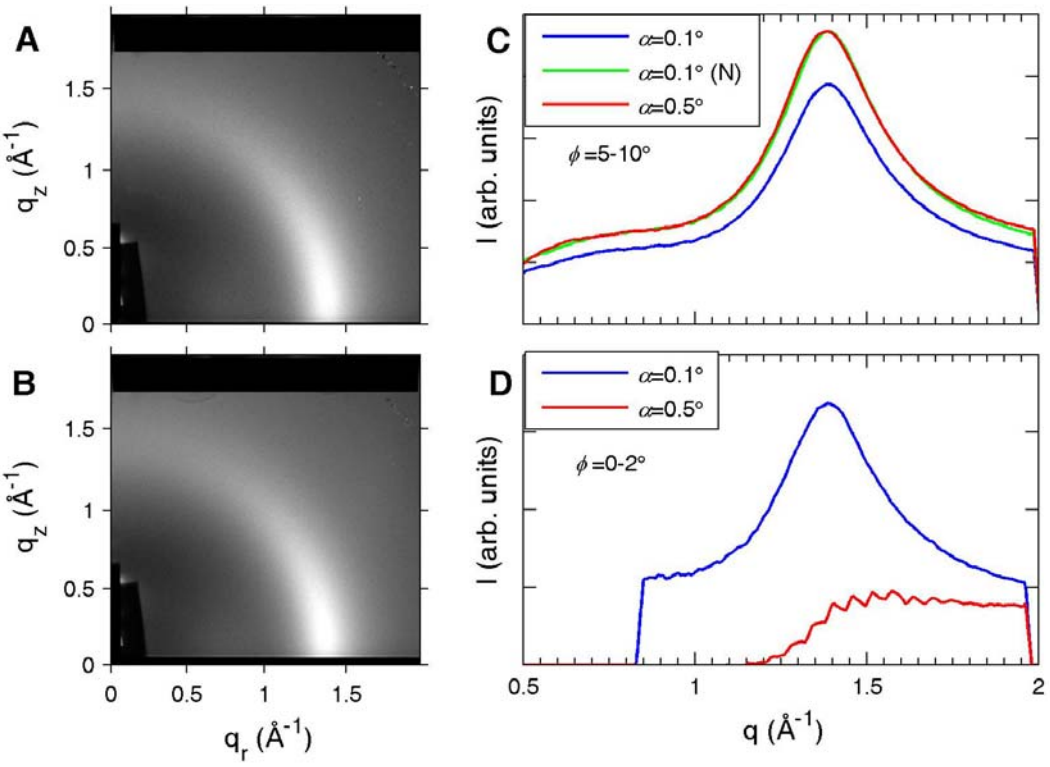


Figure 2.19. The left panel shows GIWAXS data for DOPC (T=25˚C) at incident angles of (A) $\alpha = 0.1^{\circ}$ and (B) $\alpha = 0.5^{\circ}$. The right panel shows the corresponding $I(q)$ plots (see Section 2.3.7.3) for integrated radial slices: (C) $\phi$=5-10˚ and (D) $\phi$=0-2˚ through the data. For plots (C) and (D), the blue ($\alpha = 0.1^{\circ}$ ) and red ($\alpha = 0.5^{\circ}$) traces are unnormalized. The green trace in (C) is for $\alpha = 0.1^{\circ}$, normalized to match the peak intensity in the red trace. Note that the equator is higher for $\alpha = 0.5^{\circ}$, causing cutoff of the data for small $\phi$, as readily seen in plot (D) and in image (B). (G-1, October 2006)

### 2.3.7 GIWAXS data analysis: from 2D diffraction images to one-dimensional plots

Although the 2D wide-angle diffraction images can provide qualitative information about chain ordering, our quantitative analysis requires the data to be in a different format. For powder samples, most of the quantitative information can be extracted from $I$ (scattering intensity) vs. $q$ plots, in which the scattering is radially integrated across the entire detector. For GIWAXS samples, such a plot hides the

information about intensity as a function of angle $\phi$; a plot of $I$ vs. $\phi$ is very useful for GIWAXS analysis. The width of the $I(\phi)$ plot gives information about chain orientational order (Levine and Wilkins, 1971; Spaar and Salditt, 2003). $I(q)$ plots are still valuable because they tell us about the lateral chain-chain packing correlations. The width and position of the lipid WAXS peak in an $I(q)$ plot gives information about the lateral positional ordering of the chains. (Interpretation of the width and scattering maximum of the WAXS data is complicated for the fluid phase, and will be discussed in more detail in Ch. 4). The GIWAXS data can tell us about chain orientational order (from $I(\phi)$ plots) as well as information about lateral positional order (from $I(q)$ plots). The following sections describe how the 2D diffraction images were processed to obtain the $I(\phi)$ and $I(q)$ plots.

The analysis package "MOA" (a set of MATLAB functions for x-ray data processing) by Gilman Toombes was used for data processing and analysis. MATLAB 7.1 (Mathworks, Natick, MA) was the program version used. Additional MATLAB functions, suited for analysis of the GIWAXS data, were written (with much help from Gilman Toombes) to supplement the MOA package. Both the MOA package and extra functions written specifically for the GIWAXS data have been archived on CD, with copies in the Feigenson lab (Cornell University, Dept. of Molecular Biology and Genetics) and the Nagle lab (Carnegie Mellon University, Dept. of Physics). Note that MATLAB and TiffView label the axes differently. For MATLAB, labeling the vertical axis in pixels starts from the top, as opposed to the bottom in TiffView. To avoid confusion, the pixels are converted to $q$ in $Å^{-1}$ or left unlabeled for the data shown in the thesis which was processed in MATLAB.

#### 2.3.7.1 Image processing

The GIWAXS data saved from the detector have been dark background subtracted, dezingered, and distortion and intensity corrected, as described in Section 2.3.3.4. Additional image processing which follows was done in MATLAB. Sometimes, the image was rotated because the substrate was slightly askew with respect to the horizontal. For the data presented in the thesis, the images were never rotated more than 1˚.

The next step was finding the beam center by making "qrplots" and "qzplots", as described in Section 2.3.3.3. With the beam center and sample-to-detector distance, $S$, known, distances from the beam center as measured on the detector in pixels, $\Delta p$, were converted to $q$ in $Å^{-1}$, using the following equation:

$$q = \frac{4\pi}{\lambda} \sin\left[\frac{1}{2}\tan^{-1}\left(\frac{\Delta p}{S}\right)\right]. \tag{2.8}$$

Once the beam center was found, the light background (see Section 2.3.4.3) was subtracted to remove the mylar scattering. Note that the beam center must be found before light background subtraction because the beam is also subtracted from the image.

#### 2.3.7.2 Masking

Parts of the image, such as the part covered by the beamstop, are not of use and should be masked out before any intensity integrations are carried out. The edges of the detector are often distorted and should also be masked. When $I(q)$ and $I(\phi)$ plots are produced as described in the following section, the masked out pixels are not counted in the integrated intensity. Figure 2.20 shows examples of masks used for the February 2006 experiment at D-1 and the October 2006 experiment at G-1. Note that for the October 2006 data, a larger section on the top of the detector was masked out.

We placed the CCD such that the October *S* distance was slightly smaller than the *S* distance calculated to match the February *q* range. Although the range in the $q_z$ direction was cut off by the sample chamber, the greater range in the $q_r$ and diagonal directions for the October setup enabled us to image part of the water peak (see Section 2.3.8.1).

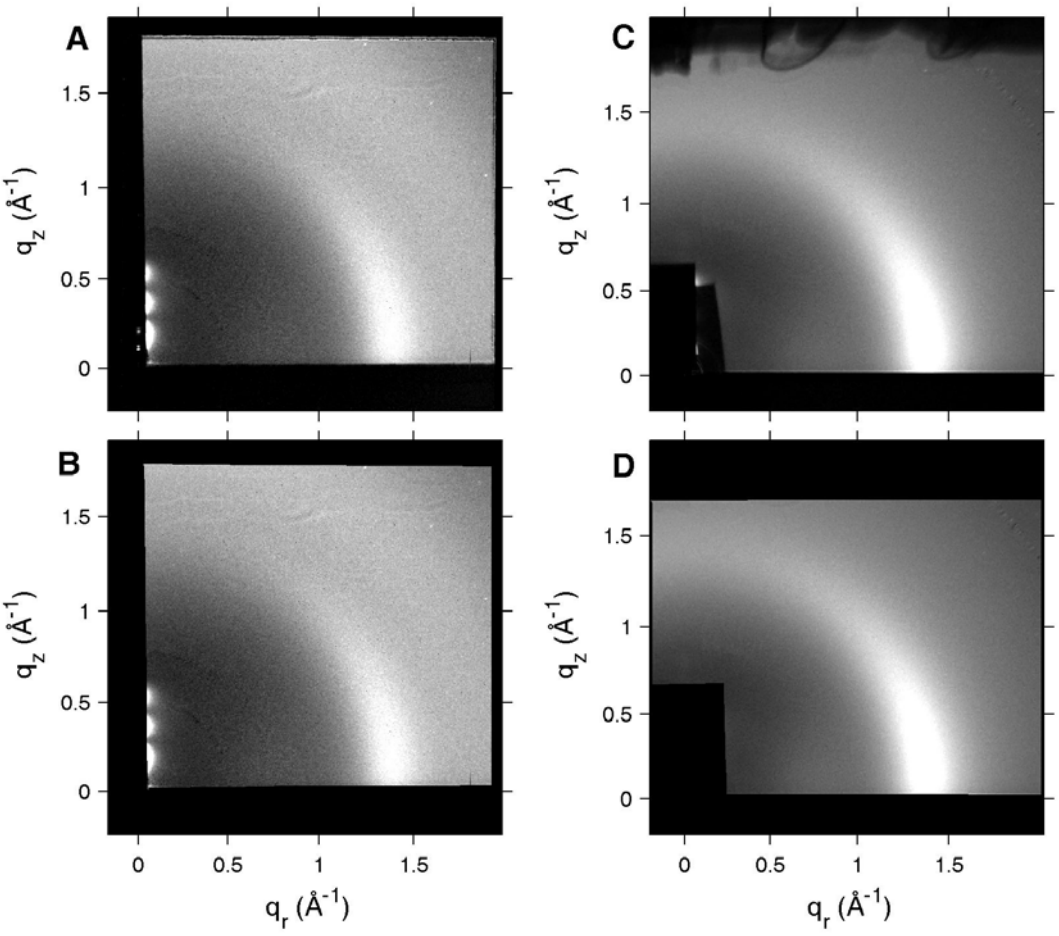


Figure 2.20. The left panel shows (A) an unmasked GIWAXS image and (B) a masked image for DOPC (T=25˚C, $d_L$=60.9 Å) taken at the CHESS D-1 station in February 2006. The right panel shows (C) an unmasked image and (D) a masked image for DOPC (T=25˚C, $d_L$=60.0 Å) taken at the G-1 station in October 2006. Similar masks were used for making integrated plots for all of the data collected during these CHESS runs. The rectangular shadows in the bottom lefthand corner in (C) are the molybdenum beamstop.

#### 2.3.7.3 Sector $I(q)$ plots and $I(\phi)$ plots

As discussed above, an $I(q)$ plot in which the entire image is radially integrated hides information contained in a GIWAXS image. However, plotting $I(q)$ for radially integrated slices for selected $\phi$ ranges preserves the angular information and still shows the position and width of the $I(q)$ peak, which informs us about the lateral positional correlation of the lipid chains. This type of plot is referred to throughout the thesis as a "sector plot." Figure 2.21A (right) shows an example of a sector plot, in which $I(q)$ is plotted for sectors with different $\phi$ ranges: 5-15˚, 15-25˚,..., 75-85˚. The data were smoothed using MATLAB's built-in "smooth" function with a smoothing span of 20 points. Note that the peak intensity decreases as $\phi$ increases. In the remainder of the thesis, sector plots are shown in black and white. Unless otherwise stated in the figure legends, the sectors in a "sector plot" are always $\phi$=5-15˚, 15-25˚,..., 75-85˚, as in Figure 2.21A. The lower traces always correspond to larger $\phi$ values. Each sector has a different range of $q$ values, with the largest $q$ range for $\phi$ values near 45˚; the cutoff in the $q$ range is seen by a sharp drop in intensity on the plot.

To produce $I(\phi)$ plots, a particular $q$ range is selected, and then the scattering intensity is integrated within that $q$ range for $\phi$ bins of 1˚. For all of the $I(\phi)$ plots shown in this thesis, 1˚ increments in $\phi$ were chosen, found to be a good compromise between resolution and smooth plots. Figure 2.21B shows an example of an $I(\phi)$ plot. Unless otherwise stated, the $I(\phi)$ plots shown in the remainder of the thesis are produced according to the above method and are not smoothed.

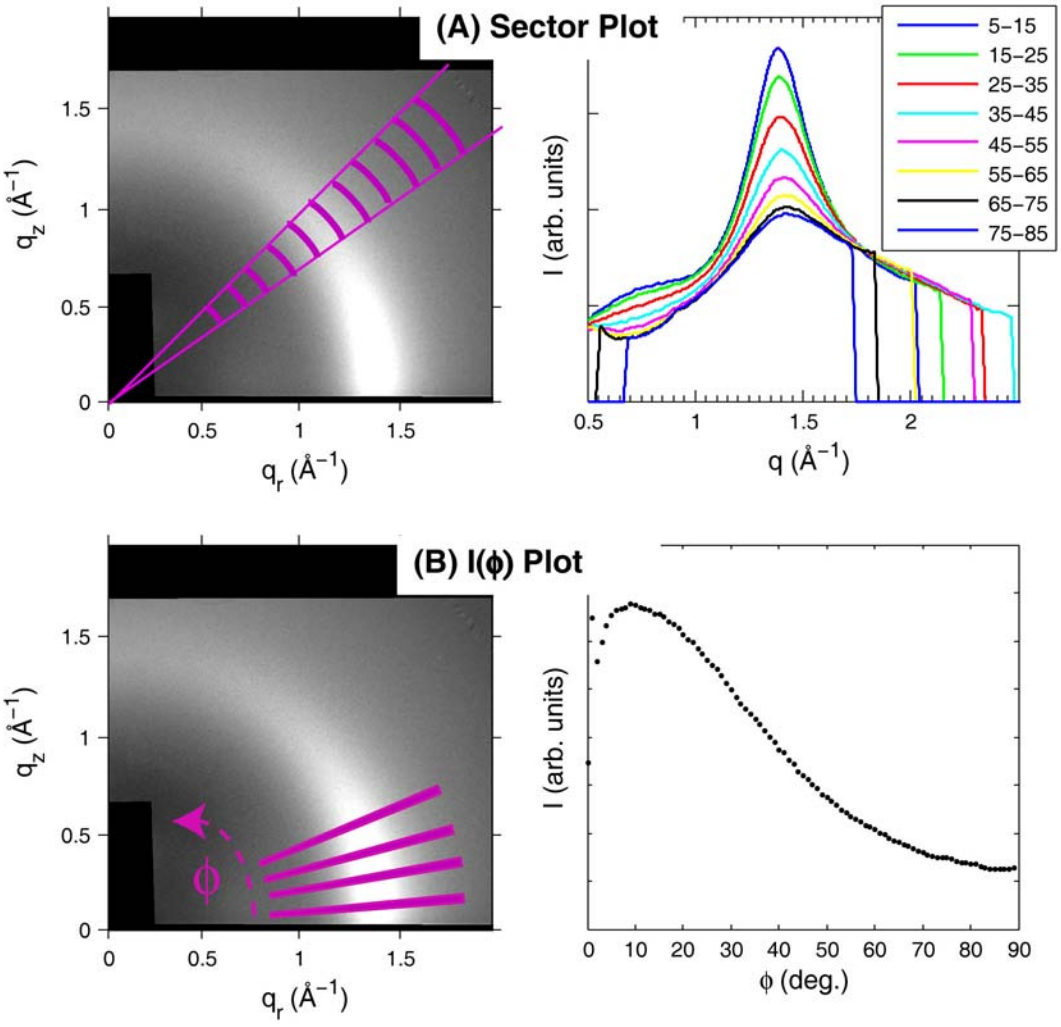


Figure 2.21. The left panel shows GIWAXS images for DOPC (T=25˚C, $d_L$=60.0 Å, G-1, October 2006, NIH chamber) with examples of: (A) radial slices for a fixed $\phi$ range and (B) slices with a fixed $q$ range of 0.8-1.8 Å$^{-1}$. The right panel shows the corresponding sector plot (A) and $I(\phi)$ plot (B). The legend in (A, right) gives the $\phi$ range for each sector. The abrupt dip in the $I(q)$ traces shows where the data for each $\phi$ range ends. The $q$ range is greatest for $\phi$~45˚. The $q$ range for the $I(\phi)$ plots was chosen to be within the maximum range for all sectors.

#### 2.3.7.4 $I(\phi)$ plots: Effect of absorption at low $\phi$

In the $I(\phi)$ plot in Fig. 2.21B, there is a peak in intensity near $\phi$=10˚. The decrease in intensity observed for $\phi$<10˚ is due to absorption of x-rays by the sample, which has a larger effect for smaller $\phi$. We can estimate the effect of absorption by assuming on average, the scattered x-rays must travel through half the thickness of the lipid sample ($t$=5 μm) in the direction of the membrane normal, **n**, before escaping the sample (see Fig. 2.22). The distance the scattered x-rays travel in the direction of the membrane normal is given by $l\hat{\mathbf{s}} \bullet \hat{\mathbf{n}}$, where $\hat{\mathbf{s}} = \sin 2\theta \cos\phi \hat{\mathbf{x}} + \cos 2\theta \hat{\mathbf{y}} + \sin 2\theta \sin\phi \hat{\mathbf{z}}$ is unit vector in the direction of the scattered x-rays, $\mathbf{k}_f$, and $\hat{\mathbf{n}} \approx \hat{\mathbf{z}}$ is a unit vector in the direction of the membrane normal. Setting $l\hat{\mathbf{s}} \bullet \hat{\mathbf{n}}$ equal to $t$ and solving for $l$ gives the distance the scattered x-rays must travel before escaping the sample:

$$l = \frac{t}{\hat{\mathbf{s}} \bullet \hat{\mathbf{n}}} = \frac{0.005\,\text{mm}}{\sin 2\theta \sin\phi}. \tag{2.9}$$

The x-ray intensity after traveling through the sample is given by:

$$I = I_T \exp\left(\frac{-l}{\mu}\right) = I_T \exp\left(\frac{-l}{2\,\text{mm}}\right), \tag{2.10}$$

where $I_T$ is the total scattering intensity and $\mu$=2 mm is the absorption length of the lipid for $\lambda = 1.27$ Å$^{-1}$. Table 2.2 lists $l$, the transmitted intensity ($I/I_T$), and the absorbed intensity (1- $I/I_T$) for some selected $\phi$ angles.

Table 2.2. Calculation of transmitted and absorbed intensities for various $\phi$ with $\theta$=8˚ (sin2$\theta$=0.28).

| $\phi$ (degrees) | $l$ (mm ) from Eq. 2.9 | Ratio transmitted $I/I_T$=exp(-$L$/2) | Ratio Absorbed 1- $I/I_T$ |
|---|---|---|---|
| 1 | 1.0232 | 0.600 | 0.400 |
| 5 | 0.2049 | 0.903 | 0.097 |
| 10 | 0.1028 | 0.950 | 0.050 |
| 20 | 0.0522 | 0.974 | 0.026 |
| 90 | 0.0179 | 0.991 | 0.009 |

For fitting purposes (see Ch. 3), the data were not used below the $\phi$ value where the maximum in intensity occurred (~5-10˚). This means that we only analyzed the data in a range where absorption was less than a 10% effect.

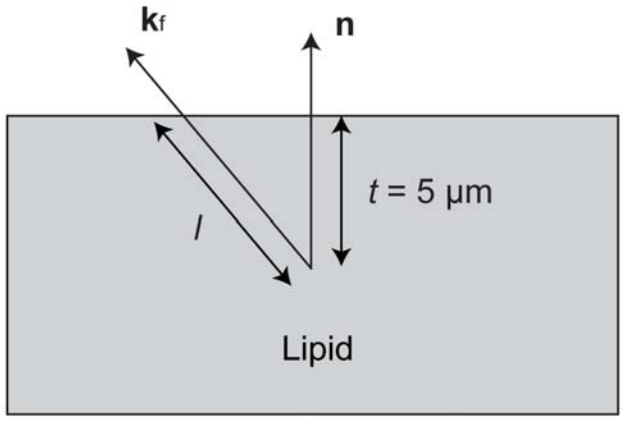


Figure 2.22. Schematic showing the distance *l* traveled by the scattered x-ray beam through the lipid assuming it scatters from a point midway through the total thickness (10 μm) of the sample.

#### 2.3.7.5 HWHM($\phi$) and $q_{cc}(\phi)$ plots

In order to quantify the positional correlation information contained in the sector plots, the peak position ($q_{cc}$) and $q$-width described by the half-width at half-maximum (HWHM) can be plotted as a function of the angle $\phi$. For well-behaved peaks with relatively flat baselines, a simple MATLAB function can determine the peak position, and pick out where the peak starts and ends; the half-width can then be calculated automatically. For our GIWAXS data, the baselines are not flat, and so it is difficult to determine where the peak starts and ends, particularly the high-$q$ end of the peak where water scattering (see Section 2.3.8.1) and cutoff of the scattering data

make it difficult to determine the baseline. Therefore, we determined the half-width from the low-$q$ half of the peak. The baseline intensity was always taken as $I(q=0.8\ \text{Å}^{-1})$. The computer program finds the $q$ values for the peak position and half-maximum positions automatically. Figure 2.23 points out the baseline, $q_{cc}$, and HWHM for an $I(q)$ plot integrated over a $\phi$=5-10˚ sector. Note that the baseline intensity position was somewhat arbitrary. Although this method for finding half-widths is not optimal, it is sufficient for comparing trends in peak intensity and HWHM as a function of $\phi$ for different sample compositions and temperatures.

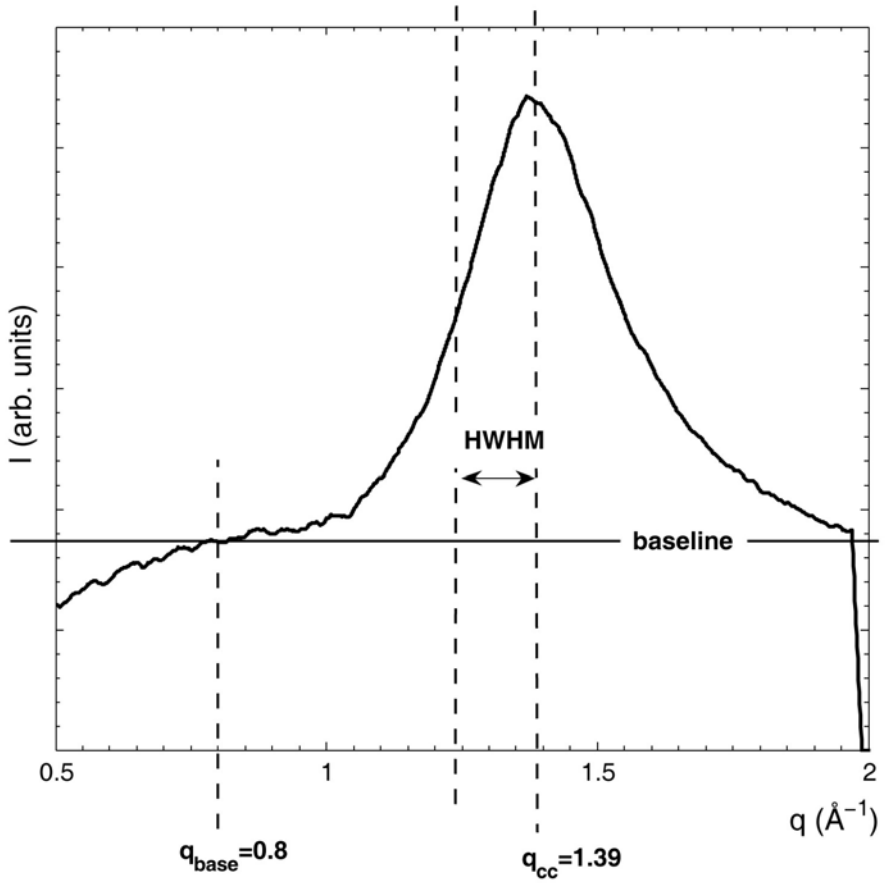


Figure 2.23. $I(q)$ for a $\phi$=5-10˚ sector for DOPC ($T$=25˚C, $d_L$=60.0 Å, October 2006 G-1, NIH chamber). The baseline, $q_{cc}$, and HWHM are pointed out on the plot.

Figure 2.24 shows examples of $q_{cc}(\phi)$ and HWHM($\phi$) plots for GIWAXS data from DOPC. The peak position and HWHM were plotted for sectors with $\phi$=5-10˚, 10-15˚,..., 75-80˚. The peak position and HWHM data are plotted as a function of the first $\phi$ value in the 5˚ range. Using a span smaller than 5˚ produces a very noisy plot.

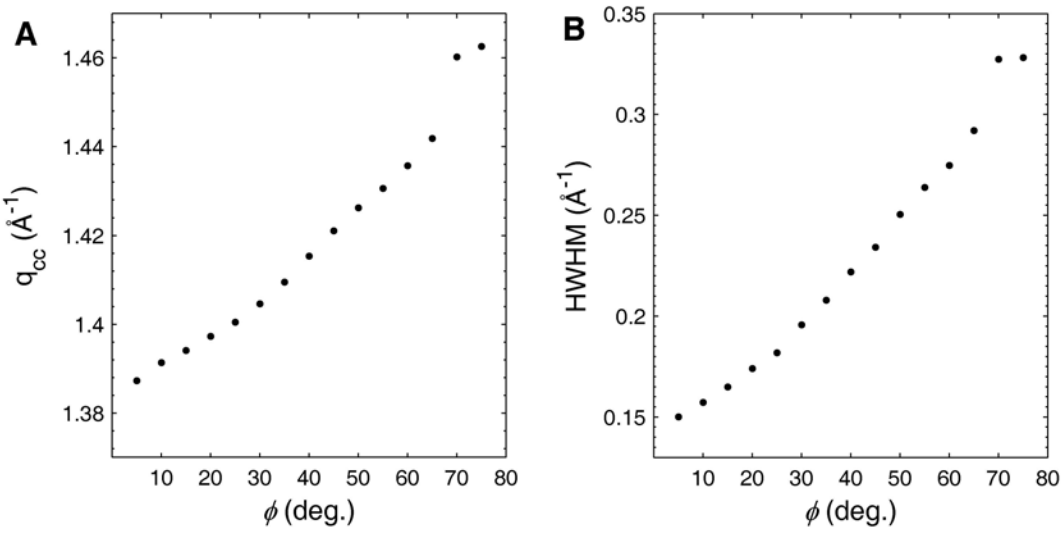


Figure 2.24. (A) Plot of $q_{cc}$ vs. $\phi$. (B) Plot of HWHM vs. $\phi$. The sample is the same as shown in Fig. 2.23 (DOPC, $T$=25˚C, $d_L$=60.0 Å, October 2006 G-1, NIH chamber).

### 2.3.8 Background subtraction challenges

Subtracting the light background from the GIWAXS image subtracts out the mylar scattering, but other sources of scattering in addition to the lipid chains remain in the image. We loosely refer to this non-chain scattering as "background." A major source of this background is water.

#### 2.3.8.1 Water: a big problem

The most obvious and problematic source of non-chain background scattering is water. The maximum scattering from water occurs for $q$ just over 2.0 $Å^{-1}$ (Hura et al., 2000; see also Fig. 2.26). The maximum lipid scattering (1.3-1.5 $Å^{-1}$) occurs on top of the steeply rising left hand side of the water scattering.

For the February 2006 experiment at D-1, our $q$ range did not allow for observation of the water scattering maximum, but an increase in the high-$q$ scattering was evident for samples near full hydration. The October 2006 setup allowed for observation of the water maximum in both sample chambers. Figure 2.25 shows 2D diffraction images and sector plots for DOPC at various levels of hydration (data taken in the NIH chamber). At conditions of full hydration (see Fig. 2.25D), part of the water maximum can be seen in the upper right hand corner of the image.

Figure 2.26 compares water scattering (Hura et al., 2000) with DOPC $I(q)$ plots integrated over a 35-45˚ sector for various levels of hydration (images shown in Fig. 2.25). At conditions of full hydration ($d_L$=63.3 Å), the water scattering begins to overwhelm the lipid chain scattering; we term this condition in which extra water is deposited on the lipid surface "flooding". In principle, full hydration can be reached in the NIH chamber without flooding, but hydration must be done very slowly. Typically, we took GIWAXS data 2-5 Å below full hydration to avoid flooding.

As seen in Fig. 2.27, the AV chamber allows for full observation of the water peak for the sample near full hydration. These data further confirm that the increase in high-$q$ scattering as full hydration is approached is indeed due to water. Note that in Fig. 2.27C ($d_L$=61.2 Å, AV chamber) the water scattering is larger but with a smaller $d_L$ spacing compared with Fig. 2.25C ($d_L$=62.1Å, NIH chamber). Flooding can happen before full hydration if the hydration process is done too quickly. In the NIH chamber, the Peltier current controls hydration. In the AV chamber, we did not have

as much control over the speed of hydration. To avoid flooding, it is important to carefully monitor the lamellar repeat spacing and to not hydrate too quickly: after sample loading hydration should take at least 30 minutes-hour (see Section 0). Also, if increasing the temperature, special steps must be undertaken to avoid flooding (see Section 2.3.4.4).

In order to quantify the amount of lipid scattering and how it changes as a function of $\phi$, clearly the water background must be subtracted. For MLV samples, the amount of water is known because the samples are prepared at a certain water:lipid ratio. Sources of background are scattering from water and scattering from the glass capillary. The water background image can be obtained easily from a capillary filled with water; scattering from an empty capillary gives the capillary background. The water background and capillary background are scaled according to the water:lipid ratio to produce a total background image. For instance, if the water:lipid ratio is 3:1, the total background is 1 part empty capillary scatter and 3 parts water plus capillary scatter. This total background can then be subtracted from the lipid + water + capillary scattering data to leave scattering from the lipid alone. This procedure was followed by Sun et al. (1994) in order to quantitatively analyze powder WAXS data from gel phase DPPC.

In the case of oriented samples, an unknown amount of water collects on the surface of the multilayer stack. Therefore, we cannot calculate the amount of water in the sample even though we can estimate the number of bilayers and the amount of water between them reasonably well. Since we cannot measure an appropriate water background, we chose to leave the background as a fitting parameter for the analysis described in Ch. 3.

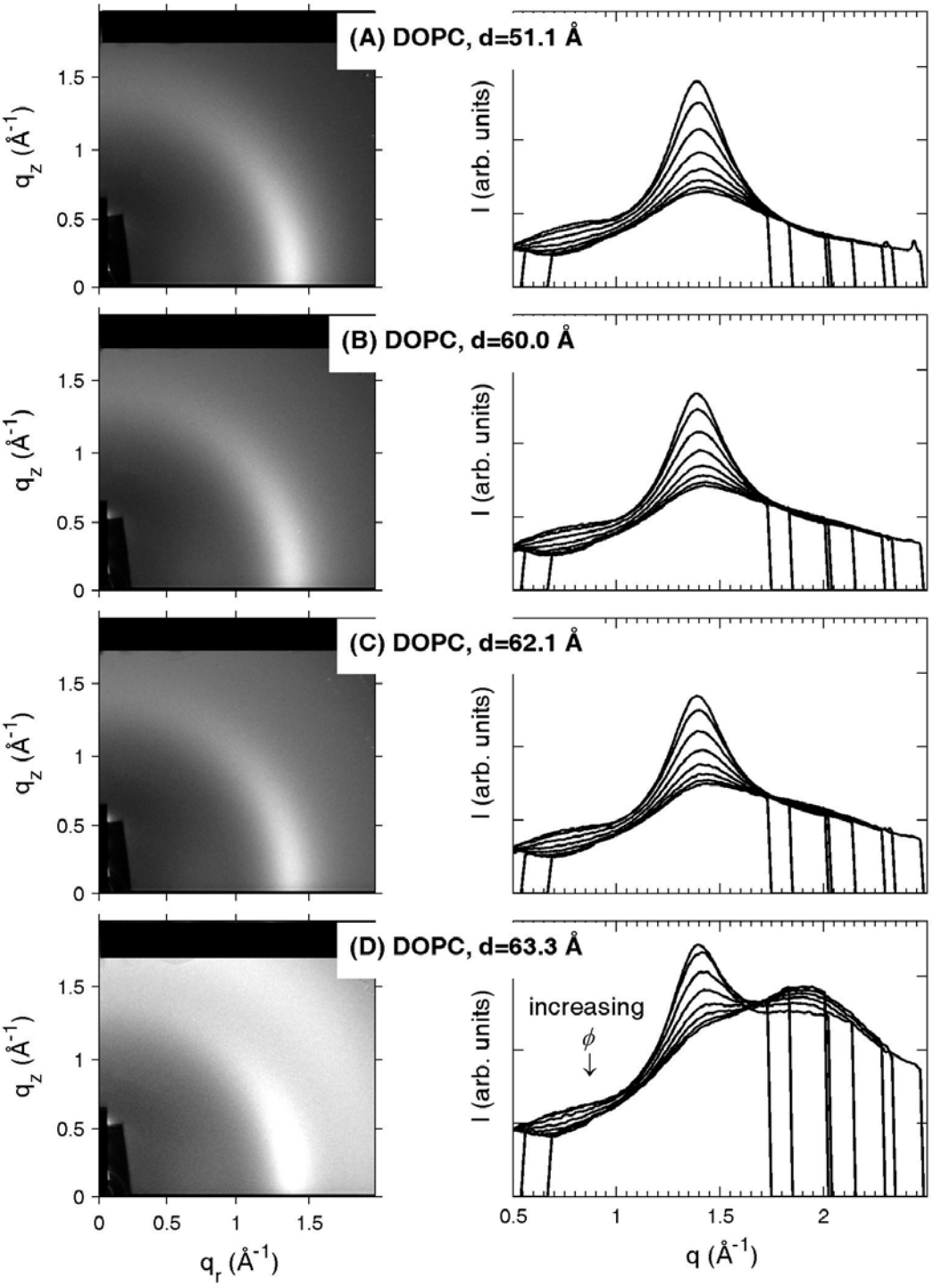


Figure 2.25. The left panel shows GIWAXS data for DOPC ($T$=25˚C) at different levels of hydration as measured by the lamellar repeat: (A) 51.1 Å, (B) 60.0 Å, (C) 62.1 Å, (D) 63.3 Å. The right panel shows the corresponding sector plots (see Section 2.3.7.3). (NIH chamber, G-1, October 2006).

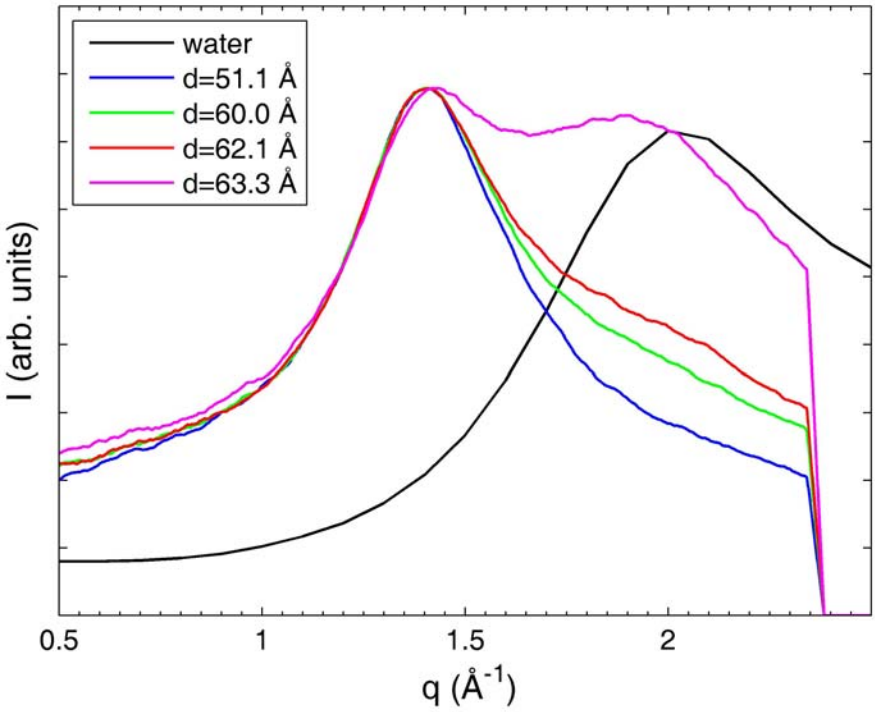


Figure 2.26. Scattering from water (Table 1 in Hura et al., 2000) is compared with $I(q)$ plots integrated over a $\phi$=35-45˚ range for DOPC at various levels of hydration (2D images shown in Fig. 2.25). All of the DOPC $I(q)$ curves were normalized so that their maximum scattering intensity at $q$=1.39 Å$^{-1}$ was the same. The water scattering was normalized to match the $d_L$=63.3 Å plot at $q$=2.0 Å$^{-1}$. The smoothing span for the DOPC $I(q)$ plots was 50 (normally 20 for sector plots).

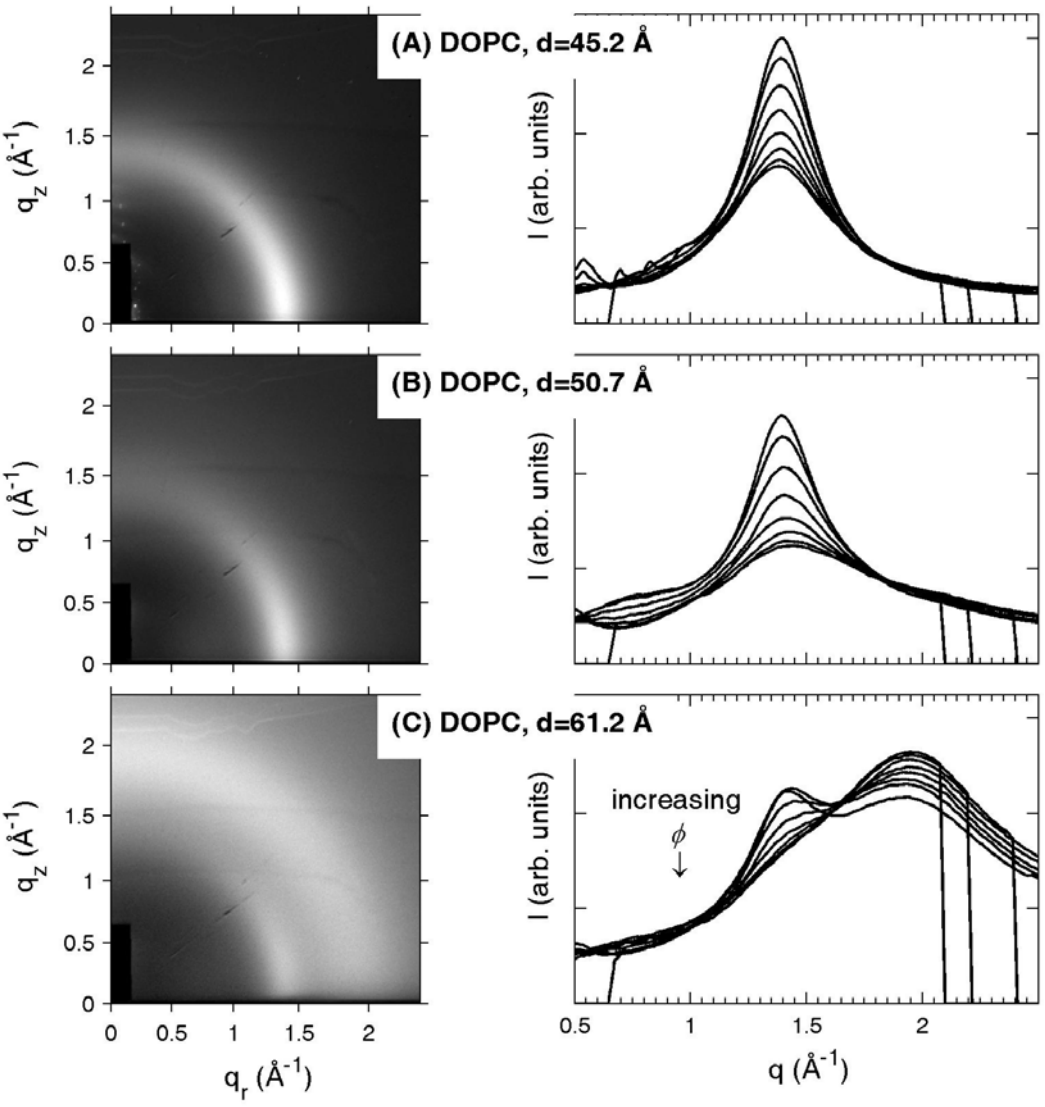


Figure 2.27. The left panel shows GIWAXS data for DOPC ($T$=25 ˚C) at different levels of hydration as measured by the lamellar repeat: (A) 45.2 Å, (B) 50.7 Å, (C) 61.2 Å. The right panel shows the corresponding sector plots (see Section 2.3.7.3). (AV chamber, G-1, October 2006).

Working at full hydration is problematic because of flooding, but we want to be able to compare our data to other experiments on fully-hydrated lipids. We can estimate a permissible range of $d_L$ spacings based on the structural effects of hydration such as change in the area per molecule and change in tilt angle in the gel phase as a function of the hydration level. Figure 2.28 shows a plot of the lamellar repeat spacing vs. relative humidity (RH) for DMPC at 30˚C, in the fluid phase (Chu et al., 2005). Note that the lamellar repeat changes steeply near 100% RH, helping to explain why the "vapor pressure paradox" was a problem for many years. At 98% RH, the $d_L$-spacing is approximately 10 Å below full hydration. The change in the area per molecule at a particular osmotic pressure $P$ compared with full hydration can be calculated using the following equation (Rand and Parsegian, 1989; see also Tristram-Nagle et al., 1998 and Nagle and Tristram-Nagle, 2000):

$$\frac{A_{L0} - A_L}{A_{L0}} = \frac{D_W P}{K_A}, \tag{2.11}$$

where $A_{L0}$ is the fully-hydrated area ($P$=0), $A_L$ is the area under osmotic pressure $P$, $D_W$ is the water thickness (~10 x $10^{-8}$ cm), and $K_A$ is the area compressibility modulus (~250 dyne/cm). The pressure can be calculated at a given relative humidity (RH):

$$P = \frac{-k_B T}{V_W} \ln \mathrm{RH}, \tag{2.12}$$

where $V_W$ is the volume of water (30 x $10^{-24}$ $cm^3$). At room temperature and 98% relative humidity, the pressure is given by:

$$P = \frac{-4 \times 10^{-14}\,\mathrm{erg}}{30 \times 10^{-24}\,\mathrm{cm}^3}(-0.02) \approx 2.5 \times 10^7\ \frac{\mathrm{dyne}}{\mathrm{cm}^2} \approx 25\,\mathrm{atm}, \tag{2.13}$$

Using the above result, we obtain for $(A_{L0}\text{-}A_L)/A_{L0} \approx 0.01$, or a 1% decrease in the area per molecule at room temperature and 98% RH compared with 100% RH.

The area per molecule is an indirect measure of chain orientational order: the more disordered the chains, the larger the area per molecule. A 1% change in the area

is acceptable, and so we would expect the wide-angle pattern to be very similar for samples 10 Å below full hydration in comparison with fully-hydrated samples (see Fig. 2.25 for examples of GIWAXS data for DOPC at various levels of hydration and see also Ch. 4 for a fuller discussion of the effect of hydration). In addition, the effect of hydration on tilt angle in gel-phase lipids can help us estimate an acceptable $d_L$-spacing range. The hydrocarbon chain tilt angle for gel-phase DMPC does not change if the lamellar repeat spacing is within 6 Å of full hydration (Tristram-Nagle et al., 2002). (Note that 6 Å below full hydration corresponds to an osmotic pressure of 45 atm and higher osmotic pressure required to compress a gel phase than a fluid phase).

We have only considered the effect of hydration on pure lipids, not mixtures which could phase-separate. In the case of phase-separated mixtures, working as close as possible to full hydration could be important to facilitate diffusion of molecules. Since we do not know the effect of hydration of phase-separated systems, we attempted to work as close as possible (within 5 Å) of full hydration while still avoiding flooding of the sample.

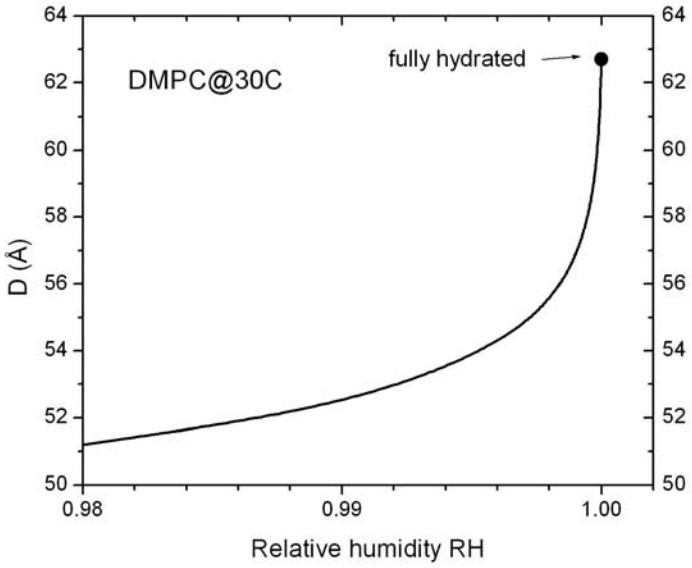


Figure 2.28. Lamellar repeat vs. RH for DMPC at 30˚C (Chu et al., 2005).

#### 2.3.8.2 Attempted fits to a Lorentzian plus linear background

Spaar and Salditt (2003) subtracted out non-chain scattering by fitting their $I(q)$ data for specified $\phi$ ranges (sector plots) to a Lorentzian plus linear background. To produce $I(\phi)$ plots, the scattering under the Lorentzians was then integrated and plotted as a function of $\phi$. This method of extracting the lipid scattering provides a simple way of obtaining the peak position and the HWHM as a function of $\phi$, since these values are simply fitting parameters for the Lorentzian.

Figure 2.29 shows a fit of our GIWAXS data for DOPC to a Lorentzian plus linear background, given by

$$I(q) = c_0 + c_1 q + \frac{I_{\max}}{1 + \left( \frac{q - q_{\max}}{q_w} \right)^2}, \tag{2.14}$$

where $c_0$ is the $y$-intercept and $c_1$ is the slope of the linear background, $I_{\max}$ is the peak height of the Lorentzian, $q_{\max}$ is the peak center, and $q_w$ is the peak half-width at half-maximum (see Busch et al., 2007 for an example of fitting polymer wide-angle data using this equation). This sample is a best case scenario, where the water background is very low. Although the fit looks reasonable, this method does not work for images with large water backgrounds. Samples with more highly ordered chains (samples in the Lo phase) have little scattering at the larger $\phi$ angles. In some cases, the peak in the $I(q)$ plot at large $\phi$ disappears, making a fit to a Lorentzian plus linear background unreasonable. Another problem with the fits is that the slope and $y$-intercept for the linear backgrounds change substantially for the different $\phi$ ranges. Spaar and Salditt (2003) only used their fitting procedure on samples in the Ld phase with $d_L$-spacings ~10 Å less than full hydration conditions. Because of these problems, we chose to produce $I(\phi)$ plots according to the method outlined in Section 2.3.7.3. Chapter 3 discusses our method for subtracting the background from non-chain sources.

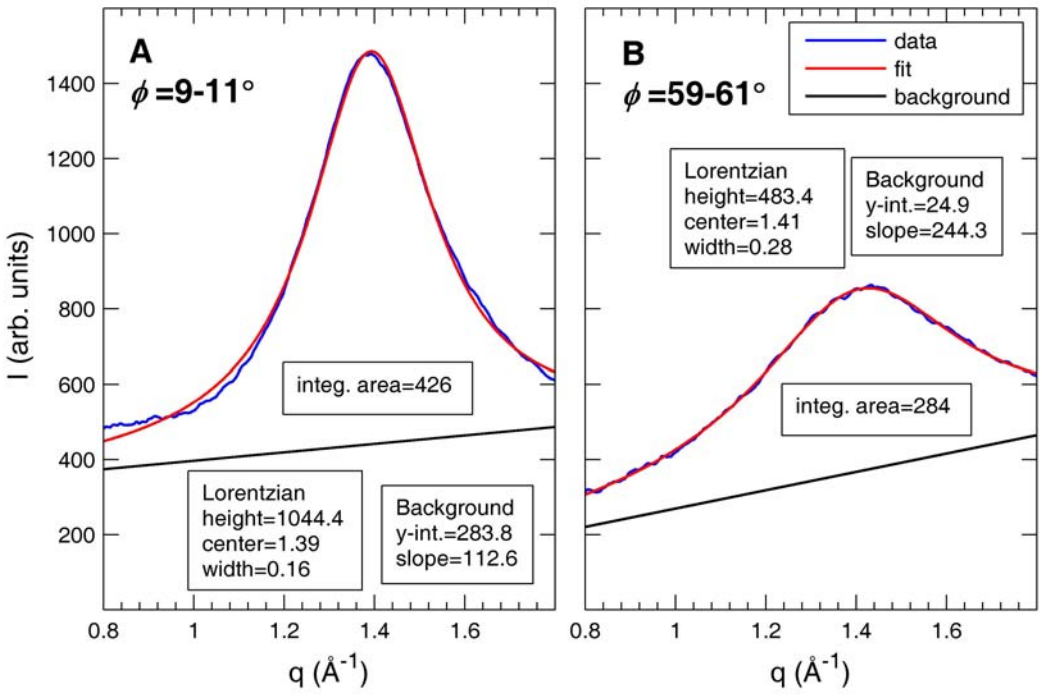


Figure 2.29. $I(q)$ for DOPC ($T$=25˚C, $d_L$=60.0 Å, G-1,Oct. 2006) for the following sectors: (A) $\phi$=9-11˚ and (B) $\phi$=59-61˚. Data are plotted in blue, and the results of a fit to Eq. 2.14 are plotted in red. The black line corresponds to the linear background. The fitting parameters and the integrated area under the Lorentzian (fit-background) are shown.

## 2.4 Powder diffraction

Rotating anode measurements on multilamellar vesicles in capillaries were done to measure the lamellar repeat ($d_L$-spacing) of the lipids in excess water. The lamellar repeat spacings of the oriented samples were compared to those of the MLVs to determine the level of hydration of the oriented samples.

### 2.4.1 Preparation of multilamellar vesicles (MLVs)

Mixtures of DOPC (Avanti Polar Lipids, Alabaster, AL; Lot # 181PC-211), DPPC (Avanti Polar Lipids; Lot # 160PC-270), and cholesterol (Nuchek Prep, Elysian, MN; Lot # CH-800-MA7-L and Lot # CH-800-AU25-Q) were prepared from HPLC-grade chloroform (Fisher Scientific, Pittsburgh, PA) stock solutions in disposable 6 x 50 mm borosilicate test tubes (Fisher Scientific). The appropriate volumes of each stock were delivered with a 100 μL Hamilton syringe (Reno, NV). The molar concentration of the phospholipid stock solutions was determined by a phosphate assay (Kingsley and Feigenson, 1979); a Hamilton PB600 repeating dispenser is used to measure precise quantities for the phosphate assay. As there is no accurate assay for cholesterol concentration, the cholesterol stock solution was prepared in a volumetric flask by carefully weighing the cholesterol powder on an analytical balance. The DOPC and DPPC were each found to migrate as a single spot as tested by thin-layer chromatography, using 65/25/4 chloroform/methanol/water (v/v/v) as a solvent system. The above procedure for preparing mixtures in chloroform was also used for the oriented samples (with the same lipid stocks).

After mixing of the lipids, the chloroform was evaporated using an Organomation (Berlin, MA) nitrogen evaporator. To assure complete solvent removal, the samples were placed in high vacuum overnight, until the vacuum gauge read less than 30 mtorr.

After solvent removal, MilliQ water was added to the lipid mixtures. The final ratio of water:lipid was 5:1 to 10:1 (v/v), with a total lipid mass of 5 mg. (To prepare a 10:1 water:lipid mixture, 50 μL of water was added to 5 mg of lipid.) The amount of water needed for full hydration varies with the lipid, but the weight concentration of the lipid at full hydration (lipid/lipid+water) is typically near 50% (see Lecuyer and Dervichian, 1969; Gruner et al., 1988). Since the densities of the phospholipids are close to 1 g/cm$^3$, this translates to a ~1:1 (v/v) water/lipid ratio required for full hydration. After adding water, the test tubes were covered with teflon tape and then with parafilm.

To speed hydration, the lipid/water mixtures in test tubes were then taken through three freeze-thaw cycles between -20˚C and 65˚C. For each freeze cycle, the samples remained in the freezer until partially frozen (~30 minutes). For each thaw cycle, the samples were placed on a 65˚C hotplate for 30 minutes. During each freeze (or thaw) cycle, the samples were vortexed vigorously for 3 minutes while still cold (or warm). The samples were then annealed from 65˚C to 25 ˚C at 2 ˚C/hour in a temperature-controlled Neslab water bath.

The samples were then loaded into the bell of 1mm glass capillaries (Charles Supper Company, Cambridge, MA) with a Drummond pipette (Broomall, PA). The samples were centrifuged on a table-top centrifuge for less than a minute. Denser lipids, such as DPPC, tend to pellet out at the bottom of the capillary, while DOPC remains fairly evenly dispersed in the water. The capillaries were sealed with vacuum grease and then 5-minute epoxy; the seal must be vacuum-tight for the rotating anode sample chamber, which is under vacuum.

### 2.4.2 Rotating anode setup

The rotating anode measurements presented in this thesis were carried out in the Gruner lab in January 2006 using the "Christine" beamline and September-October 2006 using the "El Producto" beamline. A more thorough description of these beamlines can be found in Hajduk, 1994. X-ray measurements were carried out using a Ni-filtered Cu Kα line (λ =1.5418 Å) from a Rigaku (The Woodlands, TX) RU300 rotating anode x-ray source operated at 38 kV and 50 mA. X-rays were focused using orthogonal Franks mirrors. Tantalum slits at the sample stage trimmed the beam to a ~1 mm square, with an intensity of ~ 3 x $10^7$ rays/s. Sample temperature was controlled with a water-cooled Peltier controller (Melcor Inc., Trenton, NJ) and monitored with a 100Ω platinum RTD sensor (Omega Inc., Stamford, CT). Images were collected on homebuilt CCD detectors (Tate et al., 1997). The El Producto beamline has a 1024 x 1024 pixel CCD with a pixel size of 50.1 μm (the CCD was operated in bin 2 mode, making the pixel size 100 μm). The Christine CCD is a 512 x 512 pixel CCD with a 95 μm pixel size. Both detectors have a 50 mm x 50 mm total area. The sample-detector distance was calibrated with silver behenate to convert detector pixels into $q=4\pi/\lambda\sin\theta$, where $\theta$ is the scattering angle. For the measurements on El Producto, the sample-to-detector distance was 38.58 cm, while the sample-to-detector distance for the Christine setup was 30.67 cm. Exposure times were 300 sec, with a total of 3-5 exposures collected per measurement.

### 2.4.3 Measurement difficulties

Even in excess water, full hydration of multilamellar vesicles can be challenging. Thermal history and small amounts of salt can affect hydration. An obvious sign of dehydrated lipid is the presence of two lamellar repeat spacings for a single-component lipid or for a mixture known to be in a single phase. Observation of

only a single $d_L$-spacing does not assure full hydration. Temperature hysteresis should be examined to assure full hydration was achieved. For these experiments, the samples were first measured near room temperature (25˚C or 30˚C) and then cycled to 45˚C (above the DPPC melting temperature) and back again to 25˚C and re-measured.

The $d_L$-spacing for DOPC as a function of temperature is known (Gruner et al., 1988). Therefore, DOPC was used as a standard to determine if the sample preparation conditions resulted in full hydration. Consistently, the sample preparation conditions reported above resulted in a $d_L$-spacing which was about 1 Å smaller than that reported in the literature: 63.1 Å at 30˚C (Tristram-Nagle et al., 1998) and 63-64 Å for temperatures of 0-40˚C (Gruner et al., 1988). Annealing the capillary at 45˚C and even at high temperatures (up to 90˚C) did not result in a significant change in $d_L$-spacing when the DOPC sample was cooled back down to 25˚C. However, when the DOPC capillaries were cooled to -20˚C and then re-measured at 25˚C, the $d_L$-spacing was 1 Å higher. This phenomenon was observed on several occasions with separate samples. For mixtures of 2 or more lipid components, freezing can result in demixing; therefore, we did not fully explore the effect of freezing the capillaries on hydration.

Lyophilization of lipid from a solvent such as cyclohexane to form a fine powder can speed subsequent hydration. Cyclohexane is convenient for lyophilization because it has a relatively high melting temperature (6.5˚C). However, phospholipids and cholesterol have different solubilities in most solvents, and so lyophilization from cyclohexane is not a viable option for mixtures containing a significant amount of cholesterol. Chloroform is a good solvent for both cholesterol and phospholipids. Juyang Huang developed a procedure termed "low-temperature trapping," which is basically lyophilization from chloroform at low temperature (Huang et al., 1999). However, this procedure is best-suited for small quantities of lipid (<1 mg) at higher water:lipid ratios. For previous x-ray work in the Feigenson lab, rapid solvent

exchange (Buboltz and Feigenson, 1999) followed by ultracentrifugation was used to prepare samples. For mixtures containing low-density lipids (e.g. DOPC), this method is not appropriate because the sample does not concentrate during centrifugation.

For some experiments, measuring $d_L$-spacings to within less than 1 Å of full hydration is important. An example is structural studies in which the number of waters per lipid is calculated (Nagle and Tristram-Nagle, 2000). For the work presented in this thesis, the purpose of measuring the lamellar repeat spacings for powder samples in excess water was to ensure that the oriented multilayers were within 5 Å of full hydration before collecting GIWAXS data because we want to be able to compare our data to experiments on fully-hydrated samples.

Table 2.3 shows the $d_L$-spacing values for the MLVs and the oriented samples (see Section 0 for protocol) for the DOPC/DPPC/cholesterol mixtures studied. Typically, we obtained GIWAXS data at more than one $d_L$-spacing. Table 2.3 lists the values which correspond to the GIWAXS data presented in this thesis (Ch. 4-6). The data were chosen that were closest to full hydration without being flooded (see Section 2.3.8.1). The other data were analyzed, and were in agreement with the data chosen for presentation. A discussion of the effects of hydration on the DOPC data and analysis is presented in Ch. 4. The DOPC $d_L$-spacing value presented in Table 2.3 was for a sample studied during the February 2006 D-1 experiment. This sample was used for comparison to the DOPC + cholesterol samples, which were measured during the same CHESS run. The DOPC hydration study was performed in October 2006.

In Table 2.3, if the oriented sample $d_L$ value was more than 5 Å from full hydration, this is because this was the best image avoiding flooding conditions. For example, for DOPC + 40% cholesterol, GIWAXS data were also taken closer to full hydration ($d_L$=65.1 Å) and were very similar to the data used in the thesis ($d_L$=59.7 Å). If two $d_L$ values are listed, two lamellar repeats were observed (see Ch. 6).

Table 2.3. Lamellar repeat spacings as a function of temperature for fully-hydrated MLVs and oriented samples.

| Sample | Temp. (˚C) | MLVs $d_L$ (Å) | Oriented $d_L$ (Å) |
|---|---|---|---|
| DOPC | 25 | 61.9 (should be ~63) | 60.9 |
| DOPC + 10% Chol | 25 | 63.0 ($T$=30˚C) | 60.0 |
| DOPC + 40% Chol | 25 | 66.6 | 59.7 (also took data with $d_L$=65.1-results in agreement) |
| DPPC | 25 | 63.4 | 63.4 |
| | 45 | 65.5 | 66.8 |
| DPPC + 10% Chol | 25 | 80.5 | 77.5 |
| | 45 | 67.4 | 64.5 |
| DPPC + 15% Chol | 25 | 78.4 | 75.9 |
| | 45 | 67.7 | 64.3 |
| DPPC + 25% Chol | 25 | 73.5 | 68.2 |
| | 45 | 68.4 | 64.4 |
| DPPC + 40% Chol | 25 | 67.3 | 66.7 |
| | 45 | 66.1 | 65.2 |
| 1:1 DOPC/DPPC | 25 | 63.2 | 62.8 |
| | 45 | 62.8 | 60.8 |
| 1:1 DOPC/DPPC + 15% Chol | 15 | 72.4, 63.7 | 71.2, 60.2 |
| | 20 | 71.6, 63.9 | 71.0, 60.8 |
| | 25 | 70.5, 64.3 | 69.2, 59.5 |
| | 30 | 68.8, 64.9 | 69.1, 61.4 |
| | 35 | 65.4 | 63.4 |
| | 40 | 65.0 | 62.0 |
| | 45 | 64.8 | 61.5 |
| 1:1 DOPC/DPPC + 20% Chol | 15 | 70.5, 63.9 | 67.7, 59.9 |
| | 20 | 69.7, 64.0 | ----- |
| | 25 | 68.9, 64.2 | 65.9, 59.3 |
| | 30 | 67.6, 64.7 | ----- |
| | 35 | 65.3 | 61.6 |
| | 40 | 64.9 | ----- |
| | 45 | 64.6 | 61.6 |
| 1:1 DOPC/DPPC + 25% Chol | 15 | 69.2, 64.8 | 68.1, 61.3 |
| | 20 | 68.6, 65.0 | 67.4, 60.5 |
| | 25 | 67.8, 65.5 | 66.7, 61.0 |
| | 30 | 66.2 | 67.0, 63.8 |
| | 35 | 66.0 | 63.2 |
| | 40 | 65.8 | 63.5 |
| | 45 | 65.6 | 62.7 |
| 1:1 DOPC/DPPC + 30% Chol | 15 | 68.5, 65.3 | 66.4, 60.8 |
| | 20 | 68.0, 65.4 | ----- |
| | 25 | 66.8 | 64.5, 60.5 |
| | 30 | 66.4 | ----- |
| | 35 | 66.2 | 64.3 |
| | 40 | 66.1 | ----- |
| | 45 | 66.0 | 63.2 |

# Chapter 3 - An analytical model for chain-chain scattering: theory and fitting

## 3.1 Introduction

Despite the biological relevance of fluid-phase lipids, much of the work involving wide-angle scattering from model membranes has been focused on gel-phase lipids. For crystalline packing in which the chains are essentially rigid rods, the most important features of the scattering pattern can be predicted by analytical models which consider the chain tilt angle and the dimensions of the crystalline lattice (Sun et al., 1994 and Tristram-Nagle et al., 1993 and the references therein). For disordered fluid phases, however, there is a distribution of tilt angles and a distribution of interchain packing distances.

An analytical model addressing all of the features of wide-angle scattering from fluid phase lipids would be very complex and require many parameters. Instead, we follow an approach commonly used in the liquid crystal literature for systems of rodlike molecules with fluid-like disorder which was popularized by Leadbetter et al. (Leadbetter, 1979; Leadbetter and Norris, 1979; Leadbetter and Wrighton, 1979). The model (referred to in this thesis as the "Leadbetter model") focuses on describing the angular distribution of scattering based on the distribution of rod orientations, described by a chain orientational distribution function. The major assumption of the model is that the scatterers are infinitely long rigid rods, and therefore the form factor of each molecule can be neglected. Leadbetter and others are careful to note that this simplistic model does not work equally well in all situations and must be applied and interpreted with caution (for a review see Davidson et al., 1995).

In Section 3.2, we focus on the theory and development of analytical equations for fitting the x-ray scattering data and discuss problems in the approach. Section 3.3

describes how we fit the data to obtain the chain orientational distribution function, from which we can calculate the order parameter $S_{mol}$. Section 3.3 also describes situations where the data fitting shows indirect evidence of phase coexistence. In Section 3.4, we describe the criteria for phase coexistence from our x-ray scattering data which we will use to evaluate our data in Ch. 4-6.

## 3.2 Analytical model for chain scattering

### 3.2.1 Overview: assumptions of the model and approach for finding the chain orientational distribution function

Prior to Leadbetter, the problem of determining the orientational distribution function and order parameters for systems of rodlike particles from scattering techniques was addressed by a number of researchers (for examples see Alexander and Michalik, 1959; de Vries, 1972; Pynn, 1975; Vainshtein, 1966). The general formulas derived were complicated and cumbersome to use. Leadbetter popularized a simplified model which has been widely applied to many mesogenic particles (Leadbetter, 1979; Leadbetter and Norris, 1979; Leadbetter and Wrighton, 1979; for a review see Davidson et al., 1995). Although the model is usually attributed to Leadbetter, it was used earlier by Levine and Wilkins to fit scattering data from fluid-phase egg lecithin/cholesterol mixtures (Levine, 1970; Levine and Wilkins, 1971).

Although we do not know the first source of the model, for simplicity we will refer to the model as the "Leadbetter model." In the model, the system is composed of straight rods of length $L$ separated by a mean distance $d_{rod}$, with $L>>d_{rod}$ (in our case $d_{rod}=d_{cc}$). Figure 3.1 is a schematic for the model, which defines angles and the coordinate system used for the derivation of the analytical equations for the scattering intensity. Note that the *x*-*y*-*z* coordinate system shown in Fig. 3.1 is with respect to the sample; we define the direction of the membrane normal, **n**, as $+\hat{z}$. The figure and

the theory are independent of the exact scattering geometry used. Later in the chapter (Section 3.2.6) we will relate the sample geometry to the scattering geometry used in the experiments presented in the thesis.

The model assumes that the sample is composed of different regions of rods ("grains") with a local director $\mathbf{n}_L$ which makes an angle $\beta$ with the $z$-axis. Locally, the rods are assumed to be well-correlated and rotationally symmetric about $\mathbf{n}_L$. Given these assumptions, scattering occurs only on a ring with $\mathbf{q}$ at right angles to $\mathbf{n}_L$ and for $q=2\pi/d_{rod}$ (see Fig. 3.1A). Across the sample, $\mathbf{n}_L$ can assume a distribution of orientations, which is described by the chain orientational distribution function, $f(\beta)$. The fraction of rods with a particular orientation is given by $f(\beta)\sin\beta d\beta d\chi$ (see Fig. 3.1C for the definition of angles). For a particular $\mathbf{q}$, the total scattering is a sum of the scattering contributions from grains with local directors $\mathbf{n}_L$ perpendicular to $\mathbf{q}$ (see Fig. 3.1B). Thus the scattering intensity $I(\phi_L)$ at an angle $\phi_L$ (see Fig. 3.1D) is a sum of the scattering from grains with tilt angles $\beta$ in the range: $\phi_L \le \beta \le \pi/2$. Note that our sample is rotationally symmetric about the $z$-axis; that is, the observed scattering intensity depends only on $\phi_L$ and is independent of the azimuthal angle. The following section develops a formula relating $I(\phi_L)$ to the chain orientational distribution function, $f(\beta)$.

Here we outline the strategy we followed for analysis of our x-ray scattering data based on the model described above:

1. As a starting point use a formula which relates $I(\phi_L)$ to $f(\beta)$, the chain orientational distribution function [Section 3.2.2].
2. Assume a particular functional form for $f(\beta)$ with one adjustable parameter $m$ related to the width of the orientational distribution. Insert this $f(\beta)$ into the general formula for $I(\phi_L)$ to determine a closed analytical expression for $I(\phi_L)$ [Section 3.2.4].

3. Fit the scattering data to obtain $f(\beta)$ with the best-fit value of the adjustable parameter $m$ [Section 3.3.1].
4. Calculate quantities involving average values of $\beta$, such as $S_{mol}$, from $f(\beta)$ [Section 3.3.3].

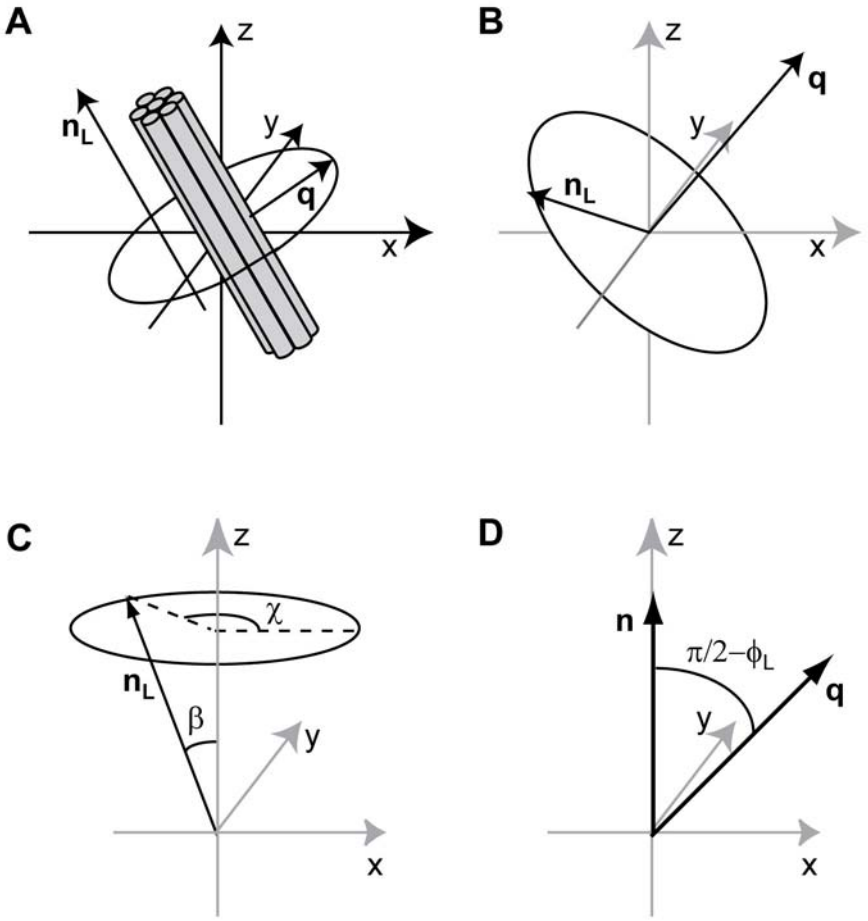


Figure 3.1. (A) In Leadbetter's model, long, thin rods are locally well-aligned along the local director $\mathbf{n}_L$. For each grain (group of rods) scattering is concentrated at right angles to $\mathbf{n}_L$. (B) The scattering intensity for a given $\mathbf{q}$ is the sum over all grains with directors lying on the ring $\mathbf{q}\cdot\mathbf{n}_L=0$. (C) The direction of $\mathbf{n}_L$ is described by the polar angle $\beta$ and the azimuthal angle $\chi$, the angle of the local director $\mathbf{n}_L$ projected on the $x$-$y$ plane. Across the sample, the local director $\mathbf{n}_L$ can assume a distribution of orientations. (D) The orientation of $\mathbf{q}$ with respect to the sample director $\mathbf{n}$ (in our case the membrane normal) is described by the angle $\phi_L$, the angle between the sample plane and $\mathbf{q}$, or more explicitly the angle complementary to the angle between $\mathbf{n}$ and $\mathbf{q}$. This figure is modified from Fig. 7 in Busch et al., 2007.

### 3.2.2 Corrected calculation of $I(\phi_L)$: the Toombes formula

We first present a corrected calculation for the scattering intensity for the system described above (the limit of infinitely straight rods which form differently aligned regions). The derivation is by G. E. S. Toombes. A shortened version of the derivation appears in Busch et al., 2007. As discussed above, scattering only occurs for $\mathbf{q} \perp \mathbf{n}_L$ and $q=q_0 \approx 2\pi/d_{rod}$. The scattering observed on the detector from a grain with local director $\mathbf{n}_L$ is given by:

$$I(\mathbf{q}) = I_T \frac{V^{2/3}}{2\pi q_0} \delta\left(\mathbf{q} \bullet \mathbf{n}_L V^{1/3}\right) \delta\left(\left(|\mathbf{q}| - q_0\right) V^{1/3}\right) \tag{3.1}$$

where $I_T$ is the total scattered intensity, $V$ is the volume, and $q_0$ is the radius of the scattering ring in reciprocal space ($q_0 \approx 2\pi / d_{rod}$). Using the geometry defined in Fig. 3.1, the scattering wavevector $\mathbf{q}$ is given by $\mathbf{q} = q_0\left(\cos\phi_L \hat{\mathbf{x}} + \sin\phi_L \hat{\mathbf{z}}\right)$ and the local director $\mathbf{n}_L$ is given by $\mathbf{n}_L = \sin\beta\cos\chi\hat{\mathbf{x}} + \sin\beta\sin\chi\hat{\mathbf{y}} + \cos\beta\hat{\mathbf{z}}$. Because the sample is rotationally symmetric with respect to the $z$-axis, the exact value of $q_x$ or $q_y$ in our calculation does not matter; we could have used $\mathbf{q} = q_0\left(\cos\phi_L \hat{\mathbf{y}} + \sin\phi_L \hat{\mathbf{z}}\right)$. We just need to allow for all possible values of $q_r = \sqrt{q_x^2 + q_y^2}$.

To obtain the total scattering from the collection of rodlike particles, we must integrate $I(\mathbf{q})$ over all possible local directors $\mathbf{n}_L$, weighting by the fraction of rods with a particular orientation, $f(\beta)\sin\beta d\beta d\chi$, where $f(\beta)$ is referred to as the chain orientational distribution function. The scattering is given by:

$$I(q,\phi_L) = \int_{\beta=0}^{\pi/2}\int_{\chi=0}^{2\pi}\int_{q=0}^{\infty} I_T \frac{V^{2/3}}{2\pi q_0} \delta\left(qV^{1/3}\left(\cos\phi_L \sin\beta\cos\alpha + \sin\phi_L \cos\beta\right)\right) \times \delta\left(\left(q - q_0\right)V^{1/3}\right) f(\beta)\sin\beta dq d\beta d\chi \tag{3.2}$$

Scattering is only possible for $q=q_0$. Integrating across the peak gives:

$$I(\phi_L) = \int_{\beta=0}^{\pi/2}\int_{\chi=0}^{2\pi} I_T \frac{V^{1/3}}{2\pi q_0} \delta\left(q_0 V^{1/3}\left(\cos\phi_L \sin\beta\cos\chi + \sin\phi_L \cos\beta\right)\right) f(\beta)\sin\beta d\beta d\chi \tag{3.3}$$

The delta function only contributes to the integration when

$$\cos\phi_L \sin\beta\cos\chi + \sin\phi_L \cos\beta = 0 \rightarrow \cos\chi = \frac{-\tan\phi_L}{\tan\beta} \rightarrow \sin\chi = \sqrt{1-\left(\frac{\tan\phi_L}{\tan\beta}\right)^2} \tag{3.4}$$

We now perform the following substitution:

$$\begin{aligned} u &= q_0 V^{1/3}\left(\cos\phi_L \sin\beta\cos\chi + \sin\phi_L \cos\beta\right) \\ du &= -q_0 V^{1/3} \cos\phi_L \sin\beta\sin\chi d\chi = q_0 V^{1/3} \cos\phi_L \sin\beta\sqrt{1-\left(\frac{\tan\phi_L}{\tan\beta}\right)^2} d\chi \end{aligned} \tag{3.5}$$

By inserting the results of Eq. 3.5 into Eq. 3.3, we obtain for the scattering:

$$I(\phi_L) = \int_\beta \int_u I_T \frac{V^{1/3}}{2\pi q_0} \delta(u) f(\beta) \sin\beta d\beta \frac{du}{q_0 V^{1/3} \cos\phi_L \sin\beta\sqrt{1-\left(\frac{\tan\phi_L}{\tan\beta}\right)^2}} \tag{3.6}$$

Noting that Equation 3.4 can only be true when $\beta \geq \phi_L$ (this makes sin$\chi$ a real number) and by integrating over *u* in Eq. 3.6, we obtain finally for the scattering as a function of $\phi_L$:

$$I(\phi_L) = \int_{\beta=\phi}^{\beta=\pi/2} \frac{I_T}{2\pi q_0^2} \frac{f(\beta)d\beta}{\cos\phi_L\sqrt{1-\left(\frac{\tan\phi_L}{\tan\beta}\right)^2}} \tag{3.7}$$

Finally, simplifying and combining constants gives:

$$I(\phi_L) = A\int_{\beta=\phi}^{\beta=\pi/2} \frac{\sec\phi_L f(\beta)\tan\beta d\beta}{\sqrt{\tan^2\beta - \tan^2\phi_L}} \tag{3.8}$$

where *A* is a constant, which is proportional to the amount of sample, the incident beam intensity, and the length of the exposure. We will refer to Eq. 3.8 as the "Toombes formula." This is our starting point for x-ray analysis in the strategy outlined at the end of Section 3.2.1.

### 3.2.3 Problems with Leadbetter's formula for $I(\phi_L)$

Leadbetter and Norris (1979) have derived a different formula for $I(\phi_L)$ using the same model and assumptions as described in Section 3.2.1. The formula (referred to in the thesis as the "Leadbetter formula") is:

$$I(\phi_L) = C \int_{\beta=\phi}^{\beta=\pi/2} \frac{\sec^2 \phi_L f(\beta) \sin \beta d\beta}{\sqrt{\tan^2 \beta - \tan^2 \phi_L}}. \quad (3.9)$$

Compared with the Toombes formula (Eq. 3.8), the Leadbetter formula (Eq. 3.9) is missing a factor of $\cos\phi_L/\cos\beta$. This factor comes from the angle at which each grain's diffraction ring intersects the Ewald sphere. The intensity of each grain's diffraction ring will depend on the orientation of the ring, which Leadbetter did not consider in his derivation. The Leadbetter formula was derived by considering all the possible values of the local grain director $\mathbf{n}_L$ and calculating where the diffraction ring would appear in reciprocal space (as a function of $\phi_L$). The scattering from all the grains was then added up to find the total $I(\phi_L)$. The step that Leadbetter is missing is to consider how the grain orientation affects the scattering intensity. By explicitly evaluating the delta function in the derivation of the Toombes formula, the effect of grain orientation on scattering intensity was not neglected.

Although Eq. 3.9 is often attributed to Leadbetter et al. (Leadbetter, 1979; Leadbetter and Norris, 1979; Leadbetter and Wrighton, 1979), it appears earlier in Levine's thesis (1970) without a derivation and without reference. Levine and Wilkins characterized chain orientational order in egg lecithin/cholesterol mixtures using Eq. 3.9 with different forms for $f(\beta)$ (Levine, 1970; Levine and Wilkins, 1971).

The most straightforward way of showing that the Leadbetter formula is incorrect is to consider explicit cases where the formula fails. In Appendix A, we show that the Leadbetter formula results in the incorrect calculation of the invariant (Roe, 2000, p.28-29):

$$\text{Invariant} = \int_V I(\mathbf{q}) d\mathbf{q} \tag{3.10}$$

Using the spherical coordinates shown in Fig. 3.1, the invariant can be written as (see Alexander, 1969, p. 243):

$$\text{Invariant} = \int_\chi \int_{\phi_L} \int_q I(q, \phi_L, \chi) q^2 \sin\left(\tfrac{\pi}{2} - \phi_L\right) dq d\phi_L d\chi \tag{3.11}$$

Note we are using the azimuthal angle $\chi$ to describe the orientation of the vector **q**, whereas in Section 3.2.2 it was used to describe the orientation of the vector $\mathbf{n}_L$. The most familiar form of Eq. 3.11 is the case of a powder sample, in which there is complete rotational symmetry:

$$\text{Invariant} = \int I(q) q^2 dq \tag{3.12}$$

In our case, there is rotational symmetry about the *z*-axis, and the invariant is:

$$\text{Invariant} = \int_{\phi_L} \int_q I(q, \phi_L) q^2 \sin\left(\frac{\pi}{2} - \phi_L\right) dq d\phi_L = \int_\phi \int_q I(q, \phi_L) q^2 \cos\phi_L dq d\phi_L \tag{3.13}$$

Since the model assumes that scattering occurs at only one value of $q=2\pi/d_{rod}$, the following equation should be true for $I(\phi_L)$:

$$\text{Constant} = \int_{\phi_L} I(\phi_L) \cos\phi_L d\phi_L \tag{3.14}$$

In Appendix A, we show that Eq. 3.14 is true for the Toombes formula (Eq. 3.8), but is not true for the Leadbetter formula (Eq. 3.9), implying a mistake in the Leadbetter derivation.

Another case where the Leadbetter formula fails is when all the rods have orientation $\beta=\pi/2$. In this case, the Leadbetter formula predicts the that $I(\phi_L)$ should be zero, whereas the Toombes formula gives a reasonable result (see Appendix A). This particular case is a very unlikely situation, especially for model membrane systems, which would mean all the chains were lying flat in the plane of the membrane.

By showing cases where the Leadbetter formula fails, our purpose is not to claim that there is anything wrong with the conclusions made from the liquid crystal

research done over the past 30 years using the Leadbetter formula. In most realistic situations with rods oriented at modest values of $\beta$ (closer to 0 than $\pi/2$), the Leadbetter formula is not unreasonable, especially if one is only interested in trends in the orientational distribution, or equivalently trends in the order parameters.

In some work, the average of grain orientations $\mathbf{n}_L$ over the azimuthal angle $\chi$ is neglected by assuming $I(\phi_L)=f(\beta)$ (for example see Özdilek et al., 2006). This is equivalent to assuming that scattering from a grain oriented with angle $\beta$ will only occur at the angle $\phi_L=\beta$. Again, if the main purpose of the work is to focus on trends in order parameters, this assumption should not drastically change the conclusions of the work. We used the Toombes formula because it seems to correctly predict $I(\phi_L)$ for the model described in Section 3.2.1.

### 3.2.4 Analytical form for scattering assuming the Maier-Saupe orientational distribution function

The Leadbetter formula (Eq. 3.9) has been inverted numerically (Leadbetter and Norris, 1979) or analytically (Deutsch, 1991) to obtain $f(\beta)$ from the measured $I(\phi_L)$. However, the inversion can be complicated and cumbersome to use. Instead, we chose to follow a commonly used approach in which an analytical expression for the scattering is derived by assuming a particular form for the distribution function $f(\beta)$, which has an adjustable parameter $m$ related to the width of the distribution. This expression can then be fit to the experimental data to obtain $f(\beta)$, from which order parameters and other quantities can be calculated (see Davidson et al, 1995 for a review of this approach).

The Maier-Saupe orientational distribution function has been applied in analysis of x-ray data to a number of nematic and smectic liquid crystalline systems (Davidson et al., 1995; Leadbetter and Norris, 1979; Oldenbourg et al., 1988; Özdilek,

2006). Jähnig (1979) has theoretically described the lipid gel to fluid transition using a Maier-Saupe mean-field approach. Because of the wide applicability of Maier-Saupe theory, we chose to assume the Maier-Saupe distribution function for the lipid chains. The Maier-Saupe distribution results from a mean-field model; it ignores the details of molecular structure and angular correlations between neighboring rods (Maier and Saupe, 1958, 1959, 1960; see de Gennes and Prost, 1993, p.66-70 for an explanation of the derivation in English). The final normalized form for the Maier-Saupe orientational distribution function is:

$$f(\beta) = \frac{1}{Z}\exp(m\cos^2\beta) \tag{3.15}$$

where $m$ is a parameter related to the width of the distribution which can take on any positive value and the normalization constant $Z$ satisfies:

$$\int_{\beta=0}^{\pi/2} f(\beta)\sin\beta d\beta = \frac{1}{4\pi}. \tag{3.16}$$

Satisfying the normalization condition (see Appendix B) gives:

$$\begin{aligned} Z &= 4\pi\int_0^1 \exp(mx^2)dx \\ &= 4\pi\frac{\exp(m)}{\sqrt{m}}D\left(\sqrt{m}\right) \end{aligned} \tag{3.17}$$

where $D$ is Dawson's integral.

Figure 3.2 plots the Maier-Saupe distribution function, $f(\beta)$, as well as $f(\beta)\sin\beta$ for two cases: $m$=3.69 and $m$=30.6. For larger $m$, the distribution is narrower, meaning that the rods are more likely to be oriented in a narrow range around $\beta$=0. The two values of $m$ chosen correspond to the sample, DOPC/DPPC + 15% cholesterol at 15˚C, which required an assumption of two Maier-Saupe distributions to fit the scattering data (for discussion see Section 3.3.1 and Figs. 3.6 and 3.8).

We have assumed that the distribution is centered about the angle $\beta_t$=0 (the same direction as the membrane normal); in the liquid-crystal literature, this type of

sample is referred to as smectic A. In smectic C liquid crystals, the distribution is centered around a nonzero angle $\beta_t$. For this situation, in Eq. 3.15 $\beta$ is replaced by $\beta$-$\beta_t$ (see Leadbetter and Norris, 1979 for further complications involving smectic C samples). We had no reason to believe that the samples we studied had an average tilt angle other than $\beta_t$=0, and so we did not include this complication in the analysis.

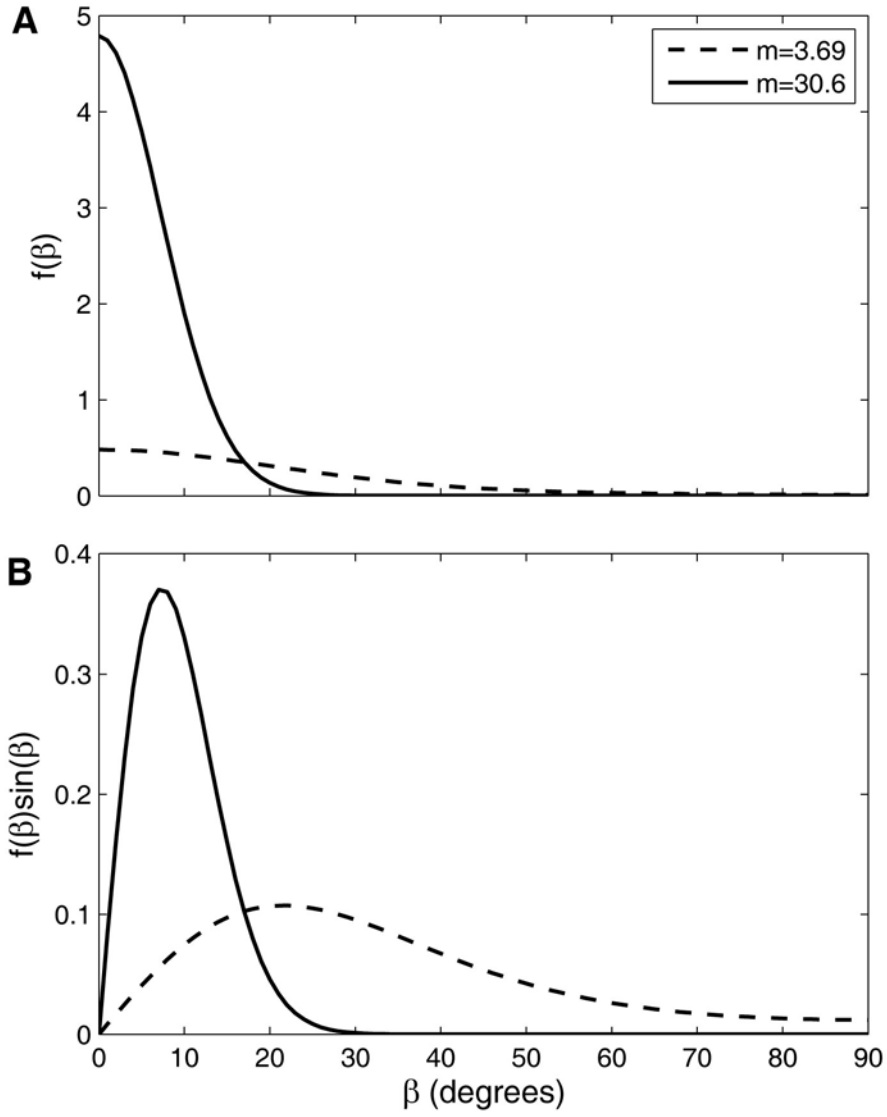


Figure 3.2. (A) Plot of Eq. 3.15, the Maier-Saupe orientational distribution function, $f(\beta)$ for two different values of $m$. (B) Plot of $f(\beta)\sin\beta$ for the same two values of $m$. Note that $f(\beta)\sin\beta$ is proportional to the fraction of rods oriented at the angle $\beta$.

Paranjpe and Kelkar were the first to derive a simple analytical equation for $I(\phi_L)$ using the Leadbetter formula (3.9) and the Maier-Saupe distribution (Kelkar and Paranjpe, 1987; Paranjpe and Kelkar, 1984). G. E. S. Toombes has derived a result for $I(\phi_L)$ using the Maier-Saupe distribution and the Toombes formula (unpublished). Inserting Eq. 3.15 into the Toombes formula (Eq. 3.8) gives (see Appendix B):

$$I(\phi_L) = \frac{A}{Z} \times \exp\left(\frac{m\cos^2\phi_L}{2}\right) \times \frac{\pi}{2} I_0\left(\frac{m\cos^2\phi_L}{2}\right) \tag{3.18}$$
$$= \frac{A}{8} \times \frac{\sqrt{m}}{\exp(m) D\left(\sqrt{m}\right)} \times \exp\left(\frac{m\cos^2\phi_L}{2}\right) \times I_0\left(\frac{m\cos^2\phi_L}{2}\right)$$

where $I_0$ is a modified Bessel function of the first kind (see Appendix B). Equation 3.18 is our starting equation for data fitting (see Section 3.3.1).

### 3.2.5 Problems with the analytical model

Fitting Eq. 3.18 to experimental $I(\phi_L)$ data is a simple way of obtaining the chain orientational distribution function, from which average values involving $\beta$, such as the molecular order parameter $S_{mol}$ (see Section 3.3.3), can be calculated. However, this approach makes several major assumptions, and so we cannot expect that the $f(\beta)$ found is the true orientational distribution function for the system.

We first consider problems independent of the exact form of the distribution function chosen (problems with the Leadbetter model and resulting Toombes formula, Eq. 3.8). The following two assumptions can introduce opposite errors in $f(\beta)$ (Leadbetter and Norris, 1979; Davidson et al., 1995):

1. The model assumes that the scattering intensity comes from a cluster of interfering particles. This assumption will result in a distribution function sharper than the true $f(\beta)$ or equivalently will tend to overestimate the order parameter.

2. The model assumes that the rods are infinitely long and thus neglects the form factor of the rods. The scattering due to a rod of finite length will contribute to the width of $I(\phi_L)$. Neglecting this effect results in a too broad distribution function, and thus a systematic underestimate of the order parameter.

For highly oriented phases (i.e. the lipid gel phase), the second effect of neglecting the form factor for a finite-sized rod is very important.

Figure 3.3 shows the scattering expected for rods of length $L$ with perfect orientation $\beta$=0˚ and packed into a hexagonal lattice.

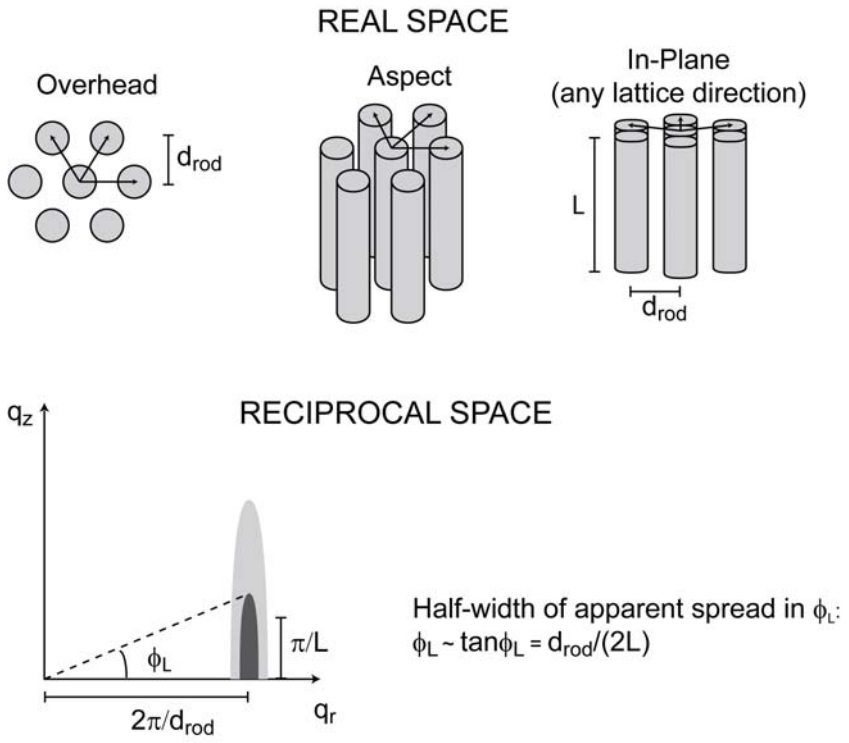


Figure 3.3. The top panel shows the perfect hexagonal packing of rods of length $L$ all oriented with $\beta$=0. The rods form rows with spacing $d_{rod}$. The bottom panel shows the scattering expected from such a system assuming rotational symmetry about the $z$-axis. The first diffraction spot will occur at $q_r = \sqrt{q_x^2 + q_y^2} = 2\pi / d_{rod}$. In the $q_z$ direction, the spot has a half-maximum intensity value at $q_z \approx \pi/L$ The apparent angular spread of the intensity is given by $\Delta\phi_L \approx d_{rod}/(2L)$. This figure was modified from a drawing by G. E. S. Toombes.

In general the scattering intensity from the sample depicted in Fig. 3.3 will depend on the Fourier transform of the electron density:

$$A(\mathbf{q}) = \int \rho(\mathbf{r}) \exp(-i\mathbf{q} \bullet \mathbf{r}) d^3 r \tag{3.19}$$

We can describe the electron density of the rod by a rectangular function:

$$\begin{aligned} \rho(z) &= \text{Const} \quad \text{for } |z| < L/2 \\ &= 0 \qquad \text{for } |z| > L/2 \end{aligned} \tag{3.20}$$

Since we assumed a perfect hexagonal lattice, scattering is only allowed for distinct values of $q_r$, the smallest value being $q_r = \sqrt{q_x^2 + q_y^2} = 2\pi / d_{\text{rod}}$. The scattering in the $q_z$ direction depends on the Fourier transform for the rectangular function (Guinier, 1963, p. 359):

$$A(q_z) = \int \rho(z) \exp(-iq_z z) dz = L \frac{\sin\left(\frac{q_z L}{2}\right)}{\left(\frac{q_z L}{2}\right)} = L \text{sinc}\left(\frac{q_z L}{2}\right) \tag{3.21}$$

where the sinc function is defined as:

$$\begin{aligned} \text{sinc}(t) &= \frac{\sin t}{t} \quad t \neq 0 \\ &= 1 \qquad t = 0 \end{aligned} \tag{3.22}$$

The scattering intensity is proportional to the square of $A(q_z)$:

$$I(q_z) \propto \left[A(q_z)\right]^2 \propto \left[\frac{\sin\left(\frac{q_z L}{2}\right)}{\left(\frac{q_z L}{2}\right)}\right]^2 = \text{sinc}^2\left(\frac{q_z L}{2}\right) \tag{3.23}$$

Figure 3.4 shows plots of $\text{sinc}(q_z L/2)$ and $\text{sinc}^2(q_z L/2)$. The half-maximum value of $I(q_z) \propto \text{sinc}^2(q_z L/2)$ is near $\pi/L$. The apparent angular spread is given by $\Delta\phi_L \approx d_{\text{rod}}/(2L)$, where $\Delta\phi_L$ refers to the half-width at half-maximum (see Fig. 3.3).

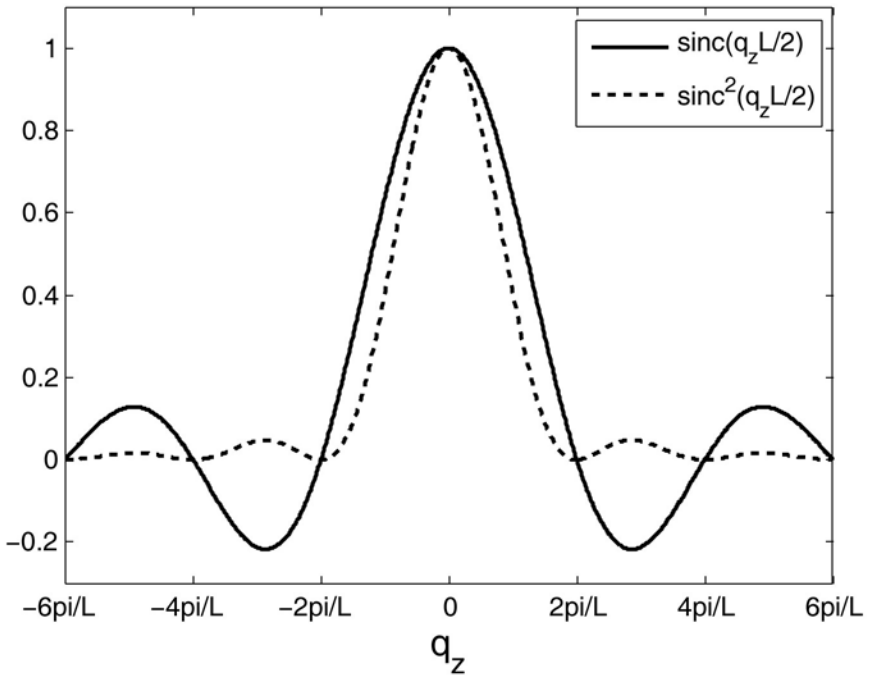


Figure 3.4. Plots of $\mathrm{sinc}(q_zL/2)$ and $\mathrm{sinc}^2(q_zL/2)$. For a rod of length $L$ with electron density described by a rectangular function along the $z$-axis, the Fourier transform $A(q_z) \propto \mathrm{sinc}(q_zL/2)$ and $I(q_z) \propto \mathrm{sinc}^2(q_zL/2)$.

We can provide a lower bound to the effect of the finite length of the lipid acyl chains on the angular spread of scattering using the measured length of a DPPC chain. The effective length depends on the phase that the chain is in (gel, Ld, or Lo). Table 3.1 shows calculations for $\Delta\phi_L$ using $L$ from the literature for DPPC chains in different phases.

Table 3.1. Apparent angular spread of scattering for finite rods with different effective lengths, $L$.

| **Phase** | $d_{rod}=d_{cc}$ **(Å)** | $L^*$ **(Å)** | $\Delta\phi_L \approx d_{rod}/(2L)$ |
|---|---|---|---|
| gel | ~4.2 | 18.75 (DPPC, all trans) | 0.11 rad=6.4˚ |
| Ld | ~4.5 | 11.6 (DPPC, 52˚C) | 0.19 rad=11˚ |
| Lo | ~4.6 | 14.9 (DPPC + 33% chol, 52˚C) | 0.15 rad=8.8˚ |

*The effective acyl chain lengths ($L$) come from Sankaram and Thompson, 1990.

According to Table 3.1, by neglecting the finite length of the rods, the Leadbetter model would overestimate the angular distribution of scattering due to a distribution of chain orientations by ~6-11˚. For more ordered samples, we can expect the model will begin to break down due to the neglect of the finite length of the rods because this effect, and not the orientational disorder, begins to dominate the $\phi$-width. Leadbetter and Norris (1979) found that the model begins to break down for order parameters ($S_{mol}$) greater than 0.8. de Vries (1972) has considered the effect of neglecting the finite size of the rods on the orientational distribution function and on the order parameters calculated from the x-ray diffraction data from liquid crystals. He concluded that although the errors on the calculated orientational distribution function can be large, the errors on the chain order parameters are not as large and the order parameters from the x-ray data are reasonable approximations. Since we are mainly interested in trends in order parameters as a function of temperature and composition, approximate values are sufficient.

For model membrane gel phases, the chains are well-ordered and the angular spread of scattering will be dominated by the apparent width $\Delta\phi_L \approx d_{cc}/(2L)$ due to the finite size of the acyl chains, an effect which the Leadbetter model does not consider (see Busch et al., 2007 for a model which explicitly considers the form factor for scattering from a rodlike polymer system). Although the model may be used to fit gel-phase data, we must be careful in any conclusions that we draw from the fits (this issue is further discussed in Ch. 5). In liquid phases (Ld or Lo), we do expect chain orientational disorder, which the Leadbetter approach is designed to model. Therefore, the model is more appropriate for liquid-phase lipids. Because chain tilts, lipid areas, etc. can be obtained from the gel phase diffraction data with simple models, this is not a major limitation (see Sun et al., 1994 and Tristram-Nagle et al., 1993 and the references therein). The value of the Leadbetter model as applied to

model membrane systems is that it provides a way of quantitatively analyzing the GIWAXS data from liquid-phase samples.

In many ways, the gel phase seems to be a better match to the assumptions of the model. For example, in the gel phase the acyl chains' conformation more closely resemble rods. Chains in the fluid phase are conformationally disordered. The chains in the liquid phase are often modeled with two divisions, one closer to the headgroup region and one closer to the middle of the bilayer. The methylene segments toward the middle of the bilayer have significantly more disorder than the segments closer to the surface (see Gennis, 1989, p. 52-55 and the references therein). In liquid phases, a model consisting of rigid rods with orientation described by the single angle $\beta$ is unrealistic. Levine and Wilkins (1971) point out that if we think of the scattering domains as segments of chains, then application of such a simple model is less problematic.

An improvement of the model would be to consider the rods as flexible (for examples of modification of Maier-Saupe mean-field theory for the situation of flexible rods see Jähnig, 1979 and Picken, 1989). Such a modification would require more fitting parameters. Since our data are well-fit by using a simple Maier-Saupe distribution for rigid rods, we could not distinguish between the simple model and a more complicated model on the basis of how well they fit the data. However, we may be able to re-interpret the fitting parameters in the context of a more complicated, and more realistic, model.

In our approach, we constrained ourselves to using the Maier-Saupe orientational distribution function. Assuming a form for $f(\beta)$ is convenient because it allows us to fit our data to an equation (Eq. 3.18) using a basic least-squares fitting routine (see Section 3.3.1). However, there are other simple models for the chain-orientational distribution function which may be more appropriate for our system; the

most appropriate form for $f(\beta)$ may depend on the lipid, temperature, and hydration level. For example, Levine and Wilkins (1971) found that they needed to assume different functional forms for the orientational distribution functions in order to fit their egg lecithin data at different levels of hydration. While the Maier-Saupe distribution function works well to describe the scattering from some liquid crystalline systems, other models are sometimes more appropriate (Purdy et al., 2003; Savenko and Dijkstra, 2004). As long as our focus is on trends in chain orientational order, the exact form of the chain orientational distribution function should not play a major role as long as it fits the data reasonably.

### 3.2.6 Relationship between the sample geometry and the experimental scattering geometry: the $\phi_L \approx \phi$ approximation

Figure 3.5 shows the experimental scattering geometry and shows how the angle $\phi_L$ is related to the angle $\phi$. The angle $\phi$ is the angle on the detector from the $x$-axis, while $\phi_L$ is the angle between **q** and the sample plane, more specifically the angle complementary to the angle between the membrane normal **n** and **q**. In the preceding sections, we have derived an equation relating the scattering intensity to $\phi_L$. The derivation of $I(\phi_L)$ is independent of the exact experimental scattering geometry used, and so the Toombes equation (Eq. 3.8) can be used for a variety of experimental setups. However, to produce the $I(\phi)$ plots, we integrated over constant $\phi$, not constant $\phi_L$ (See Section 2.3.7.3). In this thesis we make the approximation $\phi_L \approx \phi$. Leadbetter et al. always implicitly made this approximation (Leadbetter, 1979; Leadbetter and Norris, 1979; Leadbetter and Wrighton, 1979). As we will show below, this approximation is valid for our experiments, but the approximation begins to break down for scattering at wider angles. This is not a limitation of the model, as $I(\phi_L)$ instead of $I(\phi)$ can be calculated from the detector images (see Busch et al., 2007).

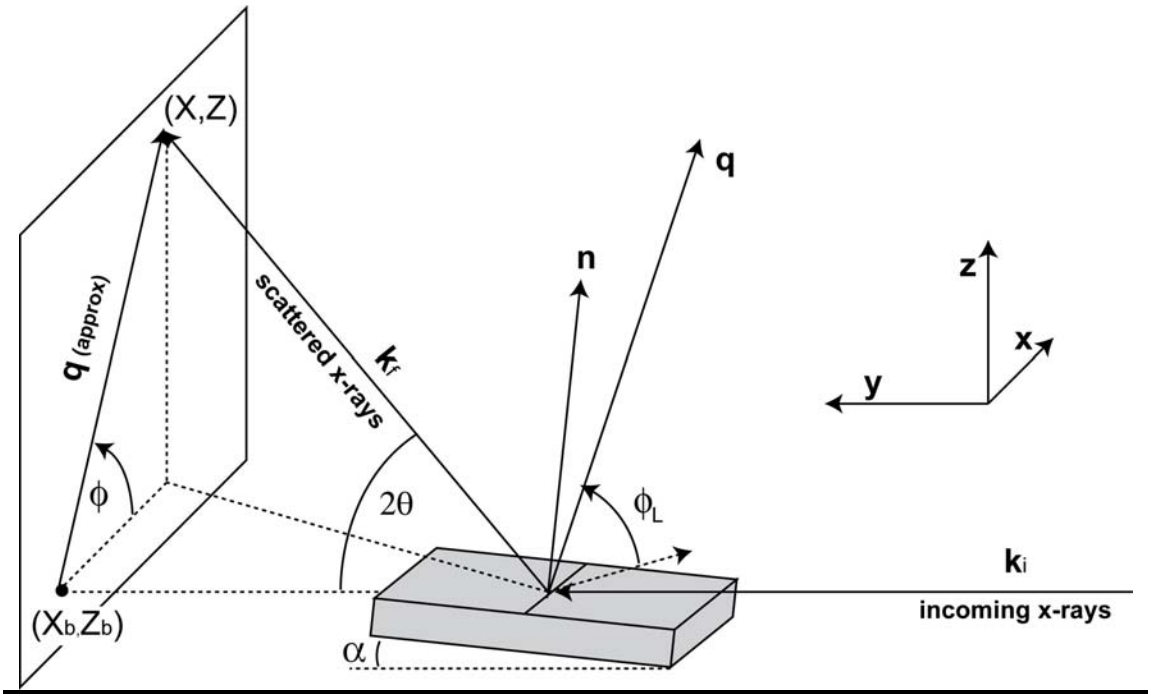


Figure 3.5. Experimental scattering geometry. Modified from Fig. 3 in Busch et al., 2007.

The following equation relates $\phi_L$ to $\phi$ (Busch et al., 2007):

$$\sin\phi_L = \sin\phi\cos\alpha\cos\theta + \sin\alpha\sin\theta. \tag{3.24}$$

In our experiments $\alpha$ is small (~0.15˚), and so the above equation simplifies to:

$$\sin\phi_L = \sin\phi\cos\theta. \tag{3.25}$$

For both the February and October 2006 setups, $\theta$~8˚ ($\cos\theta$=0.99) for $q$=1.4 Å$^{-1}$. Table 3.2 relates $\phi_L$ to $\phi$ using Eq. 3.25 with $\cos\theta$=0.99. Since even for the most orientationally disordered samples, the region of change in the $I(\phi)$ plot is over by $\phi$ ≈60˚, the approximation $\phi_L \approx \phi$ introduces negligible error. Note also that we cannot record on our detector the full range (0-90˚) of $\phi_L$ for a single sample orientation. Again, this is not important because the data do not change much for $\phi$ (or $\phi_L$)>60˚.

Table 3.2. Relationship between $\phi$ and $\phi_L$ using Eq. 3.25 with $\cos\theta$=0.99

| $\phi$ (degrees) | $\phi_L$ (degrees) |
|---|---|
| 0 | 0 |
| 10 | 9.9 |
| 20 | 19.8 |
| 30 | 29.7 |
| 40 | 39.5 |
| 50 | 49.3 |
| 60 | 59.0 |
| 70 | 68.5 |
| 80 | 77.2 |
| 90 | 81.9 |

### 3.2.7 Remark on the calculation of $I(\phi)$

Leadbetter's model assumes that the scattering peak has no width in reciprocal space; that is, scattering occurs only for $q=2\pi/d_{rod}$. In practice, the chain-chain scattering occurs over a range of $q$ values. Haase et al. (1988) have shown that $I(\phi)$ should be considered as the intensity integrated radially across the peak for a given $\phi$ rather than the peak intensity. Thus, to measure experimentally the angular dependence of the scattering, we integrated the data over the peak to obtain:

$$I(\phi) = \int_{q1=0.8}^{q2=1.8} I(\phi, q)dq \,. \tag{3.26}$$

The range of $q$=0.8-1.8 Å$^{-1}$ was chosen to be the widest possible considering experimental limitations. Considering the definition of the invariant (Eq. 3.13), it may be more appropriate to use the following equation (Busch et al., 2007):

$$I(\phi) = \int_{q_1}^{q_2} I(\phi, q)q^2 dq \,. \tag{3.27}$$

We tried both Eq. 3.26 and Eq. 3.27, and found that the differences in the fitting results were negligible. We decided to use Eq. 3.26 because Eq. 3.27 magnifies the problem if the data are not perfectly smooth. In Section 3.3.1 we will show how we

can obtain the orientational distribution function $f(\beta)$ by fitting the experimental data as obtained by Eq. 3.26 (described in Section 2.3.7.3) to Eq. 3.18, which combines the Maier-Saupe orientational distribution function (Eq. 3.15) with the Toombes formula (Eq. 3.8).

## 3.3 Data fitting

### 3.3.1 Fitting equations: Single and double order parameters

As a starting point for data fitting equations, we use Eq. 3.18, reproduced here:

$$I_{\text{chains}}(\phi) = \frac{A}{8} \times \frac{\sqrt{m}}{\exp(m) D\left(\sqrt{m}\right)} \times \exp\left(\frac{m \cos^2 \phi}{2}\right) \times I_0\left(\frac{m \cos^2 \phi}{2}\right) \tag{3.28}$$

Note in the above equation that we made the substitution of $\phi$ for $\phi_L$. This equation assumes that $I_{\text{chains}}(\phi)$ is only due to scattering from the chains. However, other sources can contribute to the scattering observed in the wide-angle region, most notably water, as discussed in Section 2.3.8.1. In some of the literature for liquid crystalline systems, a background was estimated based on the scattering intensity surrounding the region of the wide-angle peak (Davidson et al., 1995), while in other studies a constant background is included as a fitting parameter (Özdilek et al., 2006). Because of the difficulties in estimating a background intensity when water is involved, we chose to use the approach of including $I_{\text{back}}$ as a fitting parameter. We assumed that the background scattering was isotropic and so $I_{\text{back}}$ is a constant. Including $I_{\text{back}}$, the fitting equation assuming a single distribution of chains becomes:

$$I(\phi) = I_{\text{back}} + \frac{A}{8} \times \frac{\sqrt{m}}{\exp(m) D\left(\sqrt{m}\right)} \times \exp\left(\frac{m \cos^2 \phi}{2}\right) \times I_0\left(\frac{m \cos^2 \phi}{2}\right) \tag{3.29}$$

where the three fitting parameters are: (1) the constant background, $I_{\text{back}}$; (2) $A$, proportional to the amount of sample, beam intensity, and length of exposure; and (3) $m$, which describes the width of the Maier-Saupe distribution function, given by:

$$f_1(\beta) = \frac{1}{Z}\exp(m\cos^2\beta) \tag{3.30}$$

with

$$Z = 4\pi\frac{\exp(m)}{\sqrt{m}}D\left(\sqrt{m}\right)$$

For some samples, we might expect that one orientational distribution function would not describe the system. For example, if there is phase coexistence between a disordered and more ordered phase (i.e. Ld/Lo coexistence in ternary mixtures), the system may require two distribution functions in order to fit the data. In this case, we assume the total distribution function is a combination of two distributions:

$$f_2(\beta) = P_1\left[\frac{1}{Z_1}\exp(m_1\cos^2\beta)\right] + P_2\left[\frac{1}{Z_2}\exp(m_2\cos^2\beta)\right] \tag{3.31}$$

with

$$Z_1 = 4\pi\frac{\exp(m_1)}{\sqrt{m_1}}D\left(\sqrt{m_1}\right) \text{ and } Z_2 = 4\pi\frac{\exp(m_2)}{\sqrt{m_2}}D\left(\sqrt{m_2}\right)$$

$P_1$ and $P_2$ are the fraction of each phase. The fitting equation is:

$$I(\phi) = I_{\text{back}} + \frac{A_1}{8}\times\frac{\sqrt{m_1}}{\exp(m_1)D\left(\sqrt{m_1}\right)}\times\exp\left(\frac{m_1\cos^2\phi}{2}\right)\times I_0\left(\frac{m_1\cos^2\phi}{2}\right) \tag{3.32}$$
$$+\frac{A_2}{8}\times\frac{\sqrt{m_2}}{\exp(m_2)D\left(\sqrt{m_2}\right)}\times\exp\left(\frac{m_2\cos^2\phi}{2}\right)\times I_0\left(\frac{m_2\cos^2\phi}{2}\right)$$

where the five fitting parameters are the constant background $I_{\text{back}}$, $A_1$ and $m_1$ for phase 1, and $A_2$ and $m_2$ for phase 2. Note that we do not know $P_1$ and $P_2$ prior to the fit; they are rolled into the fitting parameters $A_1$ and $A_2$. The parameters $A_1$ and $A_2$ are proportional to the relative amounts of each phase (discussed in more detail in Section 3.3.3); that is $P_1=A_1/(A_1+A_2)$. In Ch. 4-6, we refer to Eq. 3.29 as the single order parameter fit and to Eq. 3.32 as the double order parameter fit. If the double order parameter fit is required to fit the data well, this is indirect evidence for phase coexistence (discussed in more detail in Section 3.4).

Figure 3.6 shows examples of fits to our data using Eq. 3.29 and Eq. 3.32. Figure 3.6A shows a situation where the data are well-fit by a single order parameter while Fig. 3.6B shows a situation where the double-order parameter fit is required to fit the data well. Table 3.3 shows the fitting parameters from the fits. For fitting, the built-in Matlab least-squares fitting function "lsqcurvefit" was used to fit the data. The results of the fits did not depend on the initial guess for the parameters, so long as the initial values of $m_1$ and $m_2$ were different in the double order parameter fit. The table also shows the 95% confidence intervals for the fitting parameters, calculated using the built-in Matlab function "nlparci". The goodness of fit quantities RMSE and $R^2$ are defined in Eq. 3.46 and Eq. 3.44.

One question is whether the fitted value for $I_{back}$ is reasonable. In Fig. 3.6B, the single order parameter fit has an $I_{back}$ which is larger than some of the data. This is clearly unreasonable and a reason for rejecting the single order parameter fit in favor of the double order parameter fit. Another way of judging whether $I_{back}$ is reasonable is to plot it on top of sector plots (see Fig. 3.7). The $I_{back}$ values seem reasonable, considering they represent an average background for all $q$ in the range 0.8 $Å^{-1}$ to 1.8 $Å^{-1}$.

Table 3.3. Results of single and double order parameter fits for the data shown in Fig. 3.6.

| **Sample** | **Type Fit** | $I_{back}$ | $A$ | $m$ | **RMSE** | $R^2$ |
|---|---|---|---|---|---|---|
| DOPC (25˚C) | Single | 441.5±18.0 | $A$ =2746±142 | $m$=1.71±0.09 | 3.38 | 0.9986 |
| | Double | NA | NA | $m_1$=$m_2$=1.71 | NA | NA |
| 1:1 DOPC/DPPC + 15% Chol (15˚C) | Single | 809.7±20.6 | $A$=2917±145 | $m$=11.6±1.1 | 68.9 | 0.9695 |
| | Double | 689.6±12.6 | $A_1$=2680±74<br>$A_2$=1341±50 | $m_1$=3.69±0.23<br>$m_2$=30.6±1.3 | 8.56 | 0.9995 |

*If "$m_1$=$m_2$" is listed, this means these parameters were the same to within ±0.01 units.

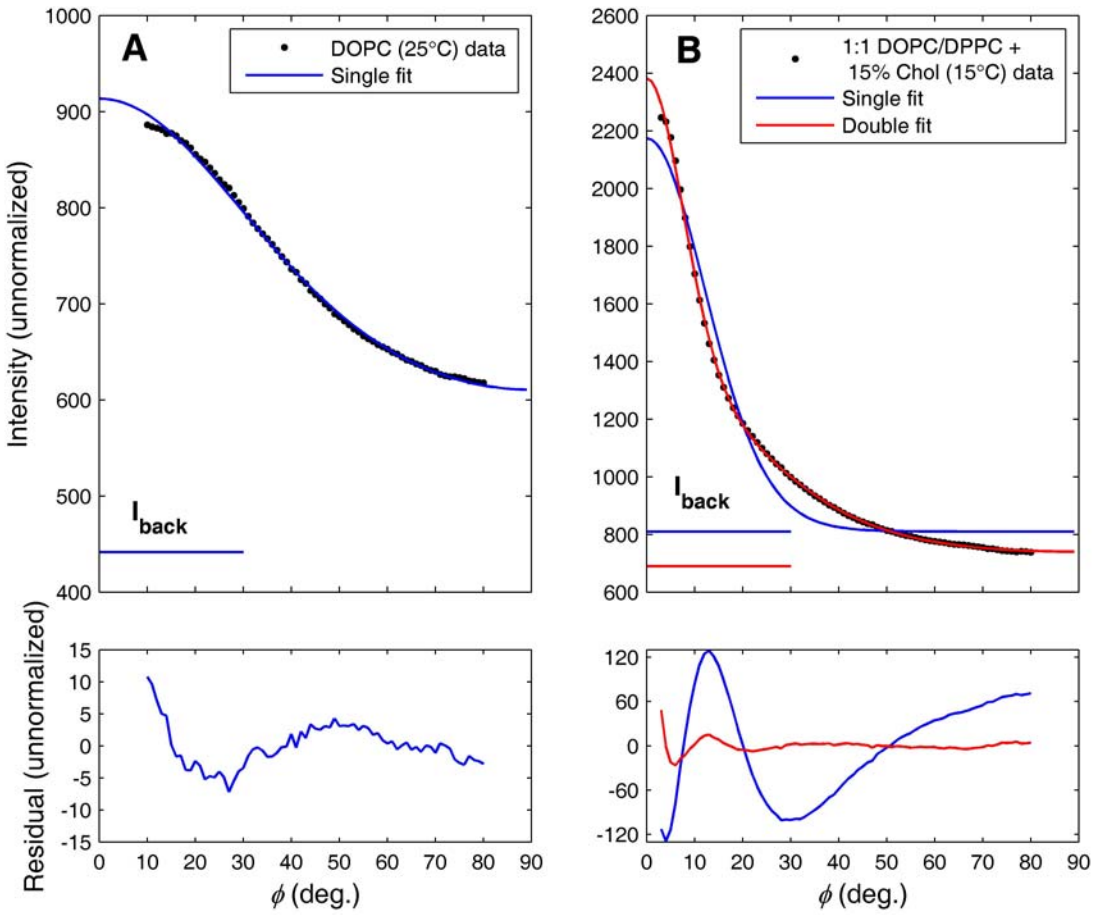


Figure 3.6. (A) $I(\phi)$ plot for DOPC ($T$=25˚C, $d_L$=60 Å, October 2006, G-1) with single order parameter fit (Eq. 3.29) shown in blue. The double order parameter fit resulted in $m_1$=$m_2$ and was therefore equivalent to the single order parameter fit. The residual is plotted beneath. (B) $I(\phi)$ plot for 1:1 DOPC/DPPC + 15% cholesterol ($T$=15˚C, October 2006, G-1) with a single order parameter fit (Eq. 3.29) in blue and the double order parameter fit (Eq. 3.32) in red. The residual plot underneath shows a clear improvement for the double order parameter fit over the single order parameter fit.

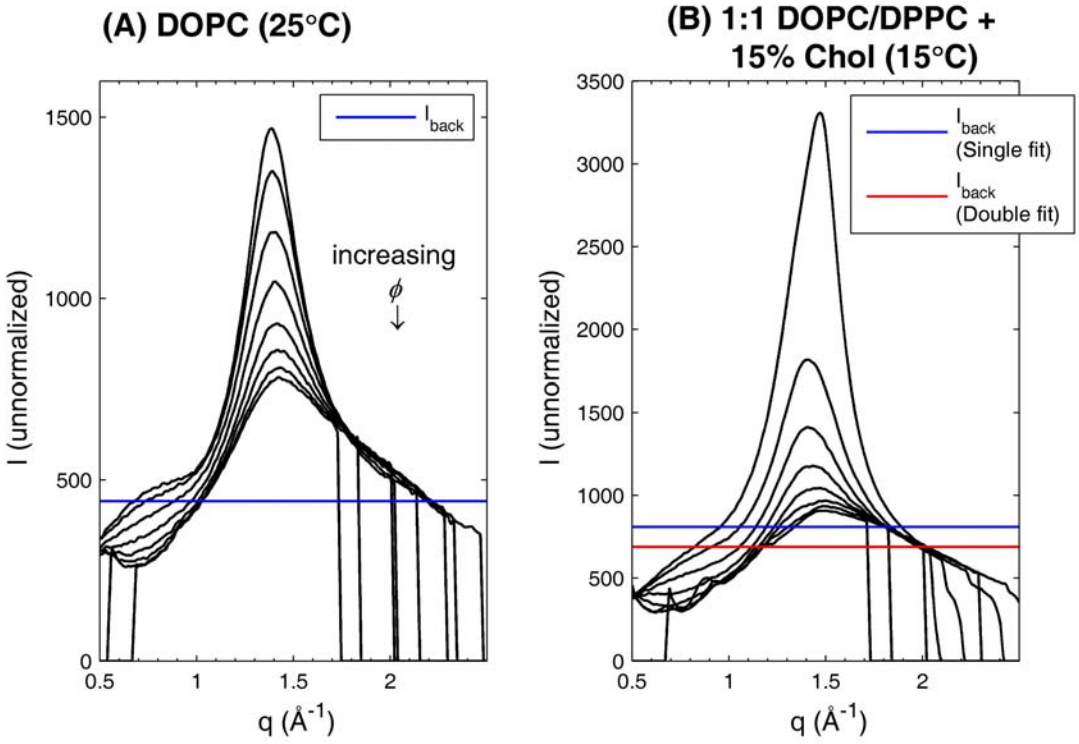


Figure 3.7. $I(q)$ sector plots (see Section 2.3.7.3) for (A) DOPC ($T$=25˚C, $d_L$=60 Å, October 2006, G-1) and (B) 1:1 DOPC/DPPC + 15% cholesterol ($T$=15˚C, October 2006, G-1). The results of the fitted background $I_{back}$ are shown.

### 3.3.2 Normalization

If we were only comparing two equations (the single and double order parameter fits) to a single set of data, the logical way to represent the data would be to plot the un-normalized data and fits on the same scale, as shown in Fig. 3.6B. However, in Ch. 4-6, we want to be able to compare many sets of data. We chose to normalize the data and the output fit as follows:

$$I_{\text{norm}}(\phi) = \frac{I(\phi) - I_{\text{back}}}{A_{\text{tot}}} \tag{3.33}$$

where $I(\phi)$ is the un-normalized experimental data or the un-normalized fit result, $I_{\text{back}}$ is the fitted constant background, and $A_{\text{tot}}=A$ for a single order parameter fit and $A_{\text{tot}}=A_1+A_2$ for a double order parameter fit.

Figure 3.8 shows the same data shown in Fig. 3.6, except normalized according to Eq. 3.33. Figure 3.8A plots the single order parameter fit for the DOPC data and 1:1 DOPC/DPPC + 15% cholesterol data, with the data and fit normalized using $I_{\text{back}}$ and $A_{\text{tot}}$ from the single order parameter fit. Figure 3.8B plots the double order parameter fit for 1:1 DOPC/DPPC + 15% cholesterol data, with the data and fit normalized using $I_{\text{back}}$ and $A_{\text{tot}}$ from the double order parameter fit. Note that in each case the fitting is performed on the un-normalized data. The data were normalized only for the purpose of presentation.

By normalizing to each fit separately, it is immediately obvious that for the single order parameter fit to the 1:1 DOPC/DPPC + 15% cholesterol data, $I_{\text{back}}$ is greater than $I(\phi)$ for the largest $\phi$ values: the normalized data go below zero. In Ch. 4-6, we normalize all the data in this way. The data are shown as stacked plots, each offset from the one below by a constant value, as in Fig. 3.8A.

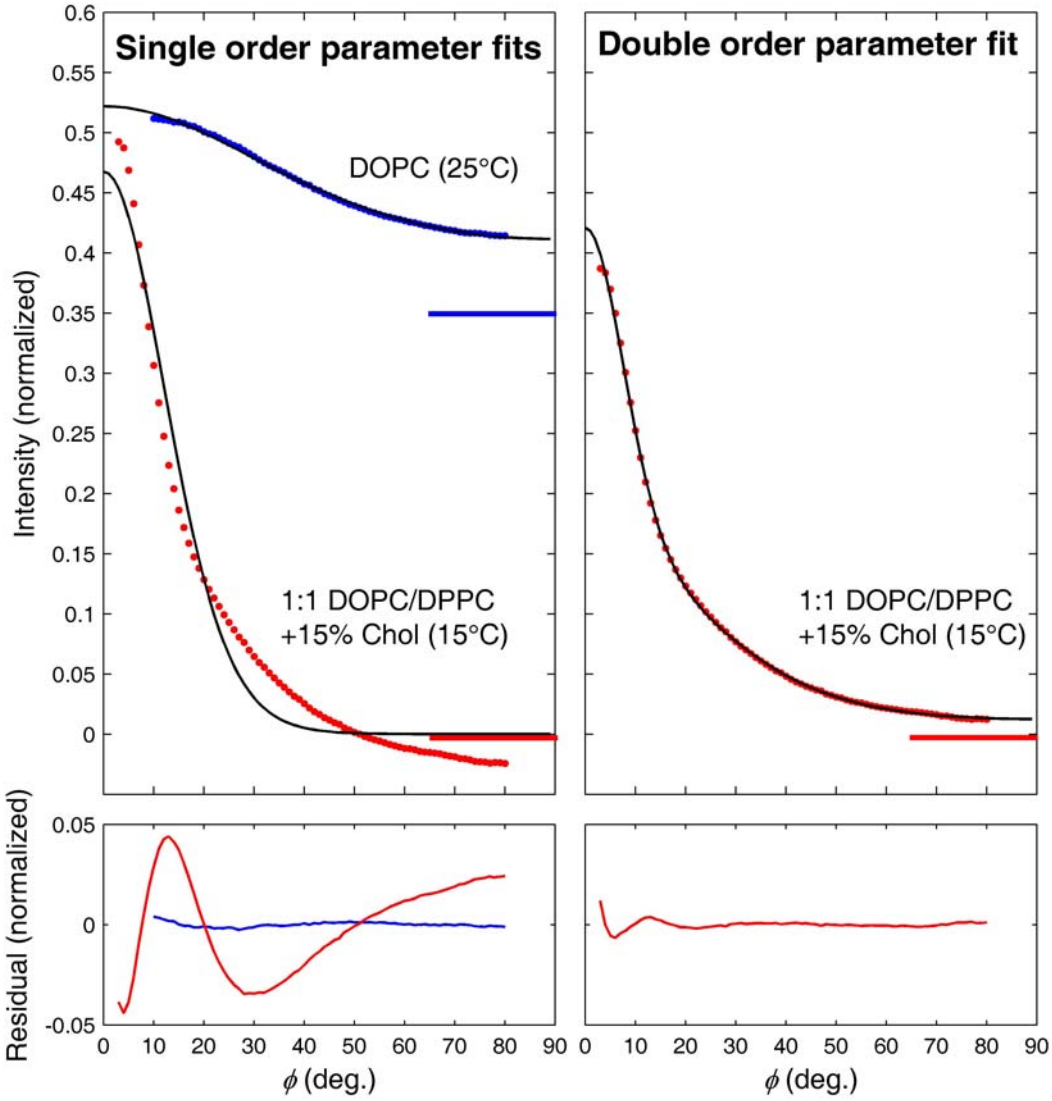


Figure 3.8. (A) $I(\phi)$ plots for DOPC, $T$=25˚C (blue) and 1:1 DOPC/DPPC + 15% cholesterol, $T$=15˚C (red) normalized according to Eq. 3.33 with single order parameter fits shown in black. Residuals are plotted below. (B) $I(\phi)$ plot for 1:1 DOPC/DPPC + 15% cholesterol, $T$=15˚C with the double order parameter fit shown in black. The colored bars show the zero offset for the corresponding plots. The same un-normalized data and fits are shown in Fig. 3.6. (All data from October 2006, G-1.)

Figure 3.9 plots the normalized double order parameter fit for 1:1 DOPC/DPPC +15% cholesterol ($T$=15˚C) as well as the two separate components of the fit. The scattering intensity for each component is weighted according to its phase fraction: $P_1=A_1/(A_1+A_2)$ and $P_2=A_2/(A_1+A_2)$.

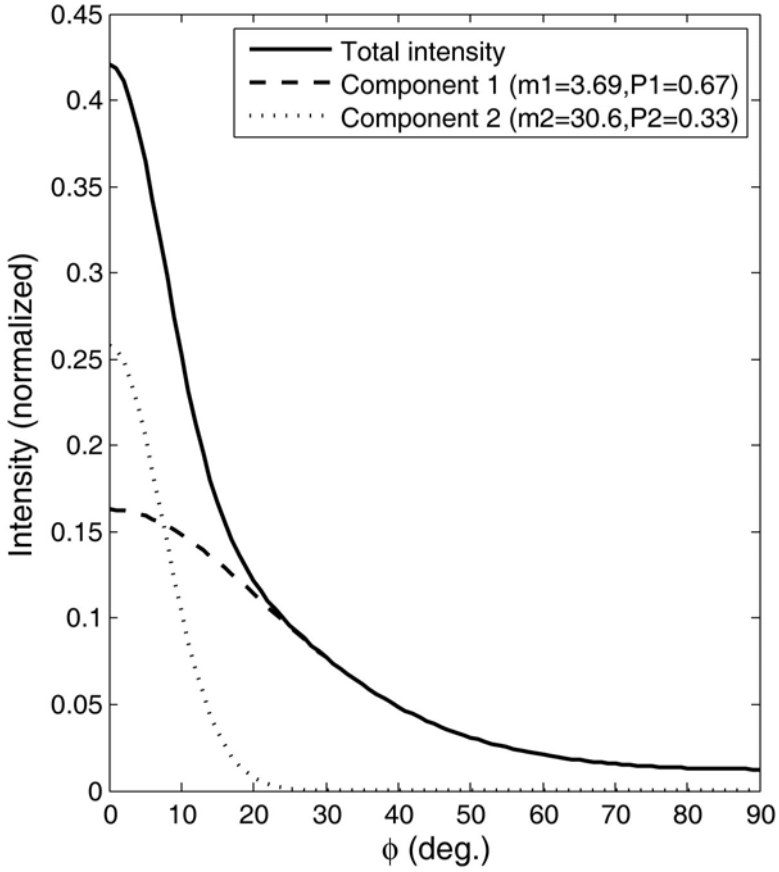


Figure 3.9. Normalized $I(\phi)$ plots showing the results of the double order parameter fit to 1:1 DOPC/DPPC + 15% cholesterol ($T$=15˚C). The black line shows the normalized total intensity. The dashed and dotted lines show the normalized scattering intensity from the less ordered and more ordered distributions, respectively.

### 3.3.3 Calculation of $S_{mol}$, phase fractions, and scattering fractions

Once we have fit the data to obtain $m$ and therefore know the chain-orientational distribution function, we can calculate quantities involving average values of the chain tilt angle $\beta$. For a function $X(\beta)$, the average value can be calculated as follows:

$$\langle X(\beta)\rangle = \frac{\int_{\beta=0}^{\beta=\pi/2} X(\beta) f(\beta) \sin\beta d\beta}{\int_{\beta=0}^{\beta=\pi/2} f(\beta)\sin\beta d\beta} \tag{3.34}$$

The molecular order parameter $S_{mol}$ (usually referred to simply as $S$ in the liquid crystal literature) is a common quantity used to describe the average orientational order in the system. $S_{mol}$ is calculated as follows:

$$S_{mol} = \frac{1}{2}\left(3\langle\cos^2\beta\rangle - 1\right) = \frac{\int_{\beta=0}^{\beta=\pi/2} \frac{1}{2}\left(3\cos^2\beta - 1\right) f(\beta)\sin\beta d\beta}{\int_{\beta=0}^{\beta=\pi/2} f(\beta)\sin\beta d\beta} \tag{3.35}$$

where we use for $f(\beta)$ the Maier-Saupe orientational distribution function, rewritten here for clarity:

$$f(\beta) = \frac{1}{Z}\exp(m\cos^2\beta) \tag{3.36}$$

with

$$Z = 4\pi\frac{\exp(m)}{\sqrt{m}} D\left(\sqrt{m}\right)$$

For the double-order parameter fits, there are two associated values of $S_{mol}$ (one for $m_1$ and one for $m_2$). Figure 3.10 shows a plot of $S_{mol}$ vs. $m$. While $m$ can take on any positive value, $S_{mol}$ can take on values of 0-1, with $S_{mol}$ =1 corresponding to perfect orientational order.

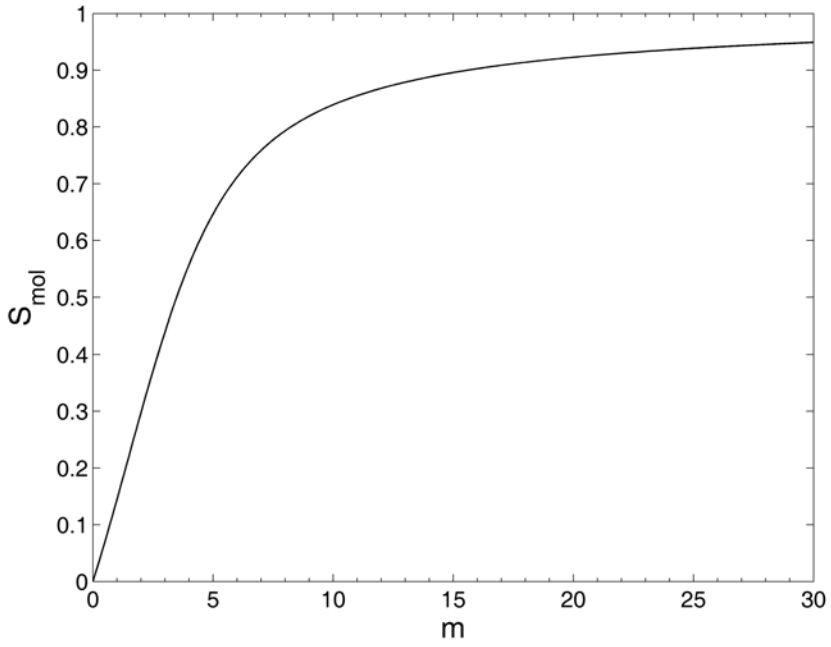


Figure 3.10. Plot of $S_{mol}$ vs. $m$. $S_{mol}$ was calculated numerically from Eq. 3.35.

Phase fractions can also be calculated from the double order parameter fits, as mentioned previously. The fraction of sample described by orientational distribution function #1, $P_1$(with associated parameters $A_1$ and $m_1$) is:

$$P_1 = \frac{A_1}{A_1 + A_2} \tag{3.37}$$

with an analogous equation for $P_2$. We believe that the phase fractions calculated in this way are prone to error and will not necessarily agree with phase fractions found from other methods (i.e. microscopy or NMR). A major problem with the model as applied to model membrane systems is that it assumes all of the wide-angle scattering is due to chain-chain interactions. In addition to phospholipid-phospholipid scattering, cholesterol-cholesterol and cholesterol-phospholipid scattering will also contribute to the total scattering observed. Even for simple chain-chain scattering in a single-

component phospholipid system, the model makes many assumptions and does not describe the true behavior of the system (see Section 3.2.5). When phases within the same sample have different amounts of cholesterol, we cannot expect the model to work equally well. For example, if cholesterol contributes less to the total scattering than the phospholipids, we would expect the phase fraction calculated for the phase with more cholesterol to be lower than the true value. Due to these complications, in this work we focus on trends in the data instead of on absolute values of parameters.

Using our fits, another quantity that we can calculate is the fraction of scattering observed on the detector in a certain $\phi$ range. For most samples, we did not make this calculation, but we did make the calculation for DOPC to compare to Spaar and Salditt (2003). The fraction of scattering observed on the detector in a range $\phi_1$ to $\phi_2$ is given by:

$$\text{Fract. Scattering}\,(\phi_1 \le \phi \le \phi_2) = \frac{\int_{\phi_1}^{\phi_2} \left(I(\phi) - I_{\text{back}}\right) d\phi}{\int_{\phi=0}^{\phi=\pi/2} \left(I(\phi) - I_{\text{back}}\right) d\phi} \tag{3.38}$$

$$= \frac{\int_{\phi_1}^{\phi_2} \left[ \frac{A}{8} \times \frac{\sqrt{m}}{\exp(m) D\left(\sqrt{m}\right)} \times \exp\left( \frac{m \cos^2 \phi}{2} \right) \times I_0\left( \frac{m \cos^2 \phi}{2} \right) \right] d\phi}{\int_{\phi=0}^{\phi=\pi/2} \left[ \frac{A}{8} \times \frac{\sqrt{m}}{\exp(m) D\left(\sqrt{m}\right)} \times \exp\left( \frac{m \cos^2 \phi}{2} \right) \times I_0\left( \frac{m \cos^2 \phi}{2} \right) \right] d\phi}$$

where the first line is a general formula and the second line is the explicit formula for a single order-parameter fit. Note that this is the fraction of scattering observed on the detector: we did not include the weighting factor $\cos\phi$ for purposes of comparing with Spaar and Salditt (for the comparison see Ch. 4).

Spaar and Salditt assumed that the fraction of chains tilted in the range $\beta_1 \le \beta \le \beta_2$ was given by the fraction of scattering observed on the detector in the same angular range for $\phi$. Even in the simple model of chains described by infinitely long rods,

these two quantities are not equal. The fraction of chains in the sample with orientation in the range $\beta_1 \le \beta \le \beta_2$ is:

$$\text{Fract.chains}\,(\beta_1 \le \beta \le \beta_2) = \frac{\int_{\beta_1}^{\beta_2} f(\beta)\sin\beta d\beta}{\int_{\beta=0}^{\beta=\pi/2} f(\beta)\sin\beta d\beta} \tag{3.39}$$

Table 3.4 compares the fraction of scattering on the detector for particular ranges of $\phi$ with the fraction of chains tilted in the same angular range $\beta$ for DOPC at 25˚C. These calculations were done numerically. Since $S_{mol}$ contains the information about the distribution of chains, in most cases we do not report the fraction of scattering or fraction of chains in various angular ranges.

Table 3.4. Results for the fraction of chains and fraction of scattering intensity in certain angular ranges for DOPC ($T$=25˚C, $d_L$=60.0 Å, October 2006, G-1). This sample is described by a Maier-Saupe distribution with $m$=1.71. For the fraction of scattering, the angular range corresponds to $\phi$. For the fraction of chains, the angular range corresponds to $\beta$.

| Angular range | Fract. scattering (Eq. 3.38) | Fract. chains (Eq. 3.39) |
|---|---|---|
| 0˚-30˚ | 0.48 | 0.29 |
| 60˚-90˚ | 0.21 | 0.29 |

### 3.3.4 Error propagation

The error (or confidence interval) can be calculated for $S_{mol}$ and the phase fractions from the error on the fitted parameters. We use these errors (particularly the error in $m$ and $S_{mol}$) as one of the criteria for accepting or rejecting a double order parameter fit versus a single order parameter fit.

The error in $S_{mol}$, $\sigma_S$, is found from the error in $m$, $\sigma_m$, as follows (see Bevington, 1969):

$$\sigma_S = \sigma_m \left( \frac{\partial S}{\partial m} \right) \tag{3.40}$$
$$= \sigma_m \frac{\left[ \int_{\beta=0}^{\pi/2} W(\beta) d\beta \right] \left[ \int_{\beta=0}^{\pi/2} C(\beta) W(\beta) P(\beta) d\beta \right] - \left[ \int_{\beta=0}^{\pi/2} W(\beta) P(\beta) d\beta \right] \left[ \int_{\beta=0}^{\pi/2} C(\beta) W(\beta) d\beta \right]}{\left[ \int_{\beta=0}^{\pi/2} W(\beta) d\beta \right]^2}$$

where we have abbreviated $S_{\text{mol}}$ as $S$ and for $\sigma_{\text{m}}$ we use the 95% confidence interval from Matlab. The functions $W(\beta)$, $P(\beta)$, and $C(\beta)$ are defined as follows:

$$\begin{aligned} W(\beta) &= \exp(m \cos^2 \beta) \sin \beta \\ P(\beta) &= \frac{1}{2}\left(3 \cos^2 \beta - 1\right) \\ C(\beta) &= \cos^2 \beta \end{aligned} \tag{3.41}$$

The error in the phase fractions $P_1$ and $P_2$ ($\sigma_{P1}$ and $\sigma_{P2}$ respectively) are found from the confidence intervals for $A_1$ and $A_2$ ($\sigma_{A1}$ and $\sigma_{A2}$ respectively) as follows:

$$\sigma_{P1} = \sqrt{\sigma_{A1}^2 \left( \frac{\partial P_1}{\partial A_1} \right)^2 + \sigma_{A2}^2 \left( \frac{\partial P_1}{\partial A_2} \right)^2} \tag{3.42}$$
$$\frac{\partial P_1}{\partial A_1} = \left(A_1 + A_2\right)^{-1} - A_1 \left(A_1 + A_2\right)^{-2}$$
$$\frac{\partial P_1}{\partial A_2} = -A_1 \left(A_1 + A_2\right)^{-2}$$

$$\sigma_{P2} = \sqrt{\sigma_{A1}^2 \left( \frac{\partial P_2}{\partial A_1} \right)^2 + \sigma_{A2}^2 \left( \frac{\partial P_2}{\partial A_2} \right)^2}$$
$$\frac{\partial P_2}{\partial A_1} = -A_2 \left(A_1 + A_2\right)^{-2}$$
$$\frac{\partial P_2}{\partial A_2} = \left(A_1 + A_2\right)^{-1} - A_2 \left(A_1 + A_2\right)^{-2}$$

Table 3.5 reports the values of $S_{\text{mol}}$ and the phase fractions with error for the example data we have been using: DOPC and 1:1 DOPC/DPPC + 15% cholesterol. Although $\sigma_{P1}$ and $\sigma_{P2}$ were usually small (less than 5%), we are cautious about interpretation of $P_1$ and $P_2$ for the reasons stated in Section 3.3.3.

Table 3.5. Order parameters and phase fractions according to the single and double order parameter fits for the data shown in Fig. 3.6 (fit results shown in Table 3.3).

| Sample | Type Fit | $S_{mol}$ | *Phase Fractions* |
|---|---|---|---|
| DOPC (25˚C) | Single | $S$= 0.25 ± 0.01 | NA |
| | Double | $S_1 = S_2 = 0.25$ | NA |
| 1:1 DOPC/DPPC + 15% Chol (15˚C) | Single | $S$= 0.86 ± 0.01 | NA |
| | Double | $S_1$= 0.52 ± 0.03<br>$S_2$= 0.95 ± 0.01 | $P_1$= 0.67 ± 0.01<br>$P_2$= 0.33 ± 0.01 |

*Note: If "$S_1$=$S_2$" is listed, this means these parameters were the same to within ±0.01.

### 3.3.5 Evaluation of goodness of fit

For each $I(\phi)$ plot generated, we compared the data to two related models: the single order parameter fit and the double order parameter fit. Since the double order parameter fit has more fitting parameters (5) compared with the single order parameter fit (3), the double order parameter fit will generally fit the data better. However, we do not always accept the double order parameter fit. For example, the confidence intervals on the best-fit parameters may be larger for the double order parameter model. In some cases, the decision of whether to accept of reject a fit is ambiguous. Motulsky and Christopoulos (2004) give a very readable introduction to the basics of curve-fitting. When deciding on whether to accept or reject a fit, they suggest asking the following questions in the order given:

1. Does the fit go reasonably close to the data? A residual plot can help evaluate the fit.
2. Are the best-fit parameters plausible?
3. Are the best-fit parameters known based on the confidence intervals?
4. What is the most appropriate model (in our case a single-order parameter fit versus a double order-parameter fit)? Statistical tests such as the "F test" can be used to compare models (see Ch. 22 in Motulsky and Christopoulos, 2004).

However, these statistical tests should only be used if both models are sensible and the more complicated model fits better (in other words, both models have passed questions 1-3). For example, if the best-fit parameters are not plausible or the confidence intervals are very wide for either model, then that model can be rejected without the need for a statistical test. For our data, questions 1-3 were sufficient for us to be able to decide on the most appropriate model.

#### 3.3.5.1 Residual plots

Plotting the residual is a good first test of whether a plot is reasonable or not. A residual plot clearly shows if the fit systematically deviates from the data. The data points should not be clustered below or above the fitted curve: whether each point is below or above the curve should be random. Figure 3.6B shows the data, fits, and residual plots for both single order parameter and double order parameter fits to a single data set (DOPC/DPPC + 15% cholesterol at 15˚C). The single order parameter fit clearly systematically deviates from the data. Fig. 3.8 shows the same data and fits, except normalized.

#### 3.3.5.2 Reasonableness of parameters and confidence intervals

One obvious problem with the single order parameter fit to the 1:1 DOPC/DPPC + 15% cholesterol data ($T$=25˚C) is that the data dip below the zero level (see Fig. 3.8). This means the $I_{back}$ parameter was larger than some of the un-normalized $I(\phi)$ values. This is an unphysical situation and serves as good reason to reject the single-order parameter fit in favor of the double-order parameter fit.

Even if a fit looks good and the fitting parameters are reasonable, the confidence intervals may be very wide (see the 1:1 DOPC/DPPC + 15% cholesterol, $T$=35˚C entry in Table 6.2). This serves as another reason for rejecting a fit. A fit was rejected if any of the fitting parameters ($I_{back}$, $m_1$, $m_2$, $A_1$, or $A_2$) had an error of greater

than 1/3 of the value of the parameter. This means the confidence interval was 2/3 the size of the parameter.

#### 3.3.5.3 Evaluation of overall goodness of fit: the $R^2$ parameter

The value $R^2$, sometimes referred to as the coefficient of determination, quantifies the overall goodness of fit. $R^2$ is defined as follows (Motulsky and Christopoulos, 2004):

$$R^2 = 1 - \frac{SSE}{SST} \tag{3.43}$$

where *SSE* is the summed squares of the residuals and *SST* is the sum of squares about the mean. The values *SSE* and *SST* are calculated as follows:

$$\begin{aligned} SSE &= \sum_i \left(y_i - f_i\right)^2 \\ SST &= \sum_i \left(y_i - \langle y \rangle\right)^2 \end{aligned} \tag{3.44}$$

where $y_i$ is the observed value, $f_i$ is the fitted value, and $\langle y \rangle$ is the mean value. In our case $y_i$ corresponds to the intensity $I(\phi)$. The value of $R^2$ is typically in the range 0-1, with a value closer to 1 indicating a better fit. If $R^2$=0.90, this means the fit explains 90% of the variation in the data about the average value. If $R^2$=0, this means the fit is no better than a horizontal line at the mean value. If the fit is worse than just fitting a horizontal line, then $R^2$ will be negative.

Because we are comparing models with a different number of fitted coefficients, in Ch. 4-6, we report the degrees of freedom adjusted $R^2$ (adj. R2). This quantity is defined as (MATLAB Help, version 7.1):

$$\text{adj. } R^2 = 1 - \frac{SSE(n-1)}{SST(\nu)} \tag{3.45}$$

where $n$ is the number of data points and $\nu$ is the degrees of freedom, equal to $n$ minus the number of fitting parameters, $m$ ($\nu$=$n$-$m$). In our case, $n$~70 and $m$ is either 3 (for

the single order-parameter fit) or 5 (for the double order-parameter fit), so the factor $(n\text{-}1)/\nu$ is very close to 1.

Another statistical parameter that is often reported is RMSE, the root mean square, defined as follows:

$$RMSE = \sqrt{\frac{SSE}{\nu}} \tag{3.46}$$

where $\nu$ is the degrees of freedom and *SSE* was defined in Eq. 3.44. We reported RMSE values in Table 3.3, but we only report $R^2$ in Ch. 4-6.

Motulsky and Christopoulos (2004) point out that when comparing the fit of two equations, comparing RMSE or $R^2$ values should not be the only or main criterion for accepting one fit as opposed to another. For our data, the $R^2$ values were always close to 1 for both the single and double order parameter fits (see Ch. 4-6). The fits were accepted or rejected based on other criteria (residual plots, plausibility of parameters, and confidence intervals).

Another common statistical test used to evaluate the goodness of fit is Chisquare ($\chi^2$), defined as follows:

$$\chi^2 = \sum_i \left( \frac{y_i - f_i}{\sigma_i} \right)^2 \tag{3.47}$$

where $y_i$ is the observed value, $f_i$ is the fitted value, and $\sigma_i$ is the error for that data point. Calculation of $\chi^2$ requires an independent estimate of the error $\sigma_i$. The best way to determine $\sigma_i$ is to repeat the same measurement many times and find the standard deviation in the different data sets (see Figure 3.11). In Ch. 4-6, we report the $R^2$ parameter because for most samples, we did not repeat the measurement enough times in order to estimate $\sigma_i$.

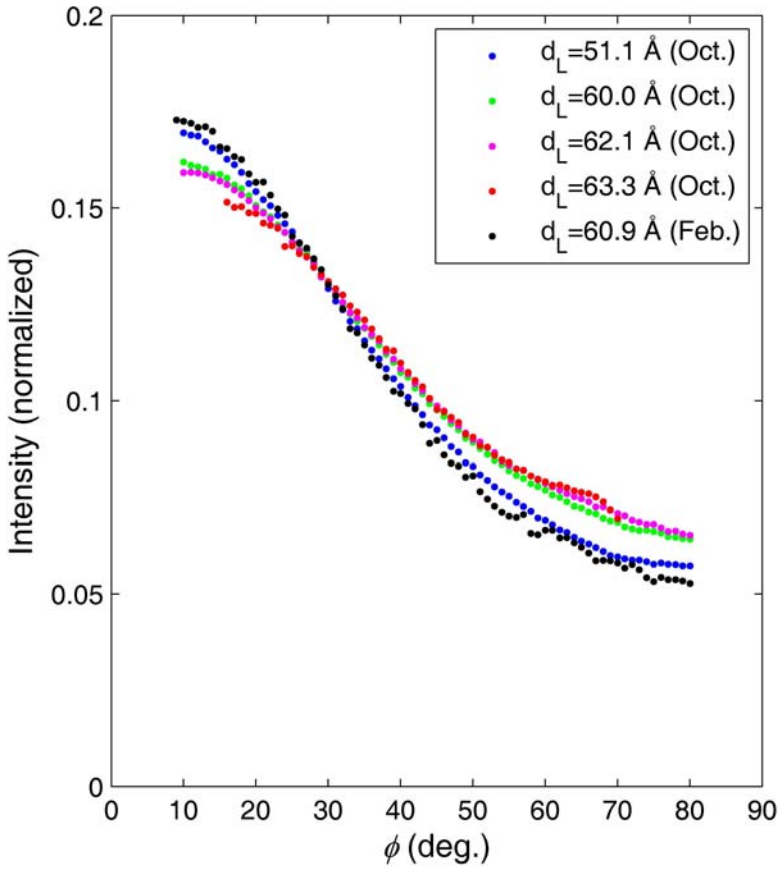


Figure 3.11. Normalized $I(\phi)$ plots for DOPC at 25˚C. Different levels of hydration and data taken with different samples on different beamlines (Oct.= October 2006 G-1 experiment; Feb.=February 2006 D-1 experiment).

## 3.4 Criteria for phase coexistence based on x-ray scattering data

In Section 3.3, we showed an example (1:1 DOPC/DPPC + 15% cholesterol at 15˚C) where an assumption of two Maier-Saupe distribution functions was required to fit the $I(\phi)$ data well. In contrast, another example (DOPC at 25˚C) required only one distribution to fit the $I(\phi)$ data. If an assumption of two order parameters is required to fit the $I(\phi)$ data, this provides indirect evidence of phase coexistence. In the case of 1:1 DOPC/DPPC + 15% cholesterol at 15˚C, the presence of phase coexistence agrees with microscopy and NMR data (Veatch and Keller, 2003b; Veatch et al., 2007b; discussed in detail in Ch. 6).

A much better fit using a double order parameter versus a single order parameter provides indirect evidence of phase coexistence. Before making a conclusion about the presence or absence of phase coexistence based on this criterion, it is important to compare the fit results to fits for other compositions and temperatures. A valid objection to the conclusion of phase coexistence based on a poor single order parameter fit is that the sample may be better described by a distribution function other than the Maier-Saupe form. We cannot disprove this objection, but we can make the following point: when the 1:1 DOPC/DPPC +15% cholesterol sample is heated above 30˚C, a single order parameter fit is sufficient to describe the $I(\phi)$ data. This behavior agrees with what is already known about the sample: below a certain temperature $T_{mix}$, Ld/Lo coexistence is present, while above this temperature the sample is in a single liquid phase (Veatch and Keller, 2003b; Veatch et al., 2007b; discussed in detail in Ch. 6).

In favorable cases, x-ray scattering can provide more direct evidence of phase coexistence. One example is the presence of two lamellar repeats ($d_L$ spacings). If two $d_L$ spacings are observed (and are reproducible and exhibit no thermal hysteresis), this is clear evidence of phase coexistence. However, the absence of two $d_L$ spacings

does not necessarily imply the absence of phase coexistence. To see two lamellar repeat spacings, the following conditions must be met:

1. The $d_L$-spacings must be different enough for the peaks to be resolvable.
2. The Lo (or Ld) domains must be aligned with the Lo (or Ld) domains in the neighboring bilayers (see Fig. 3.12). Gandhavadi et al. make the analogy to a stack of egg cartons (2002).

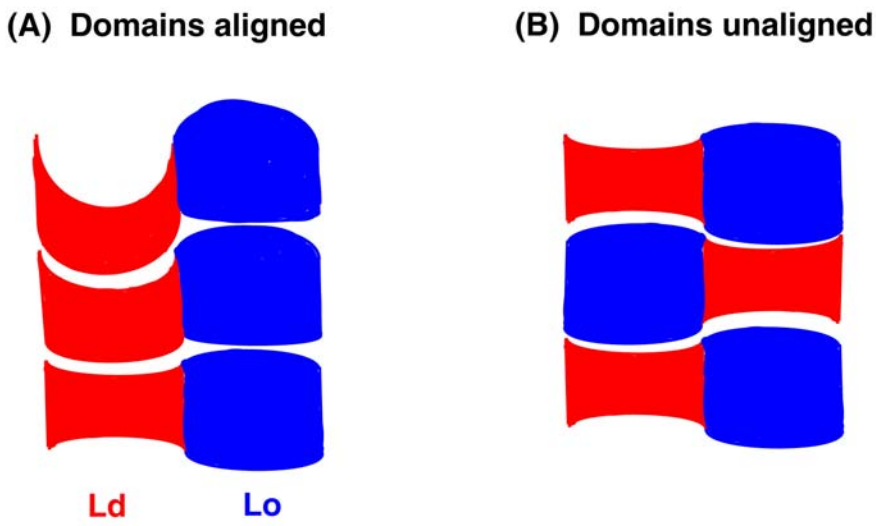


Figure 3.12. (A) Cartoon showing the Ld and Lo domains in alignment between neighboring bilayers. We assume the Ld phase has a smaller $d_L$-spacing. (B) The Lo (or Ld) domains are unaligned in neighboring bilayers. The colored areas represent a single lipid bilayer plus a water layer. The white spaces in between layers serve as a boundary between the layers.

Figure 3.12A shows that alignment of domains across many bilayers would present a problem, particularly if the two lamellar repeat spacings are very different. In order to observe two $d_L$ spacings, the domains must be aligned and the $d_L$ spacings must be different enough to resolve two lamellar peaks. In other words, the first condition for observing two $d_L$ values makes the second condition harder to satisfy.

The system could relieve strain by organizing as shown in Fig. 3.12B, in which case an average $d_L$-spacing would be observed. The real situation in a stack of oriented multilayers or MLVs is likely a mixture of the two situations, with patches of membrane in which the domains are aligned and patches in which they are not aligned.

In the case of wide-angle x-ray scattering from a sample with phase coexistence, domains in adjoining bilayers do not have to be in register in order to observe two chain-correlation ($d_{cc}$) spacings. However, the two peaks must be resolvable. In the case of gel-fluid coexistence, the gel peak is sharp (HWHM/$q_{cc}$<3% base on our oriented data and the powder data of Sun et al., 1994) and occurs at $q_{cc}$≈1.50 Å$^{-1}$ ($d_{cc}$~4.2 Å), while the fluid phase wide-angle band is broad (HWHM/$q_{cc}$~10%) and occurs at $q_{cc}$≈1.40 Å$^{-1}$ ($d_{cc}$≈4.5 Å). Therefore, we expect to be able to resolve two wide-angle bands in the case of gel-fluid coexistence, in a powder sample or oriented sample. However, in the case of Ld/Lo coexistence, the broad bands overlap, and analysis of the $I(\phi)$ distribution from oriented samples becomes useful.

Note that in the case of the Lβ' phase, two wide-angle peaks are present due to the distorted hexagonal lattice. However, we can distinguish this situation from gel-fluid coexistence, even in powder samples. Powder samples of Lβ'-phase DPPC consist of a very sharp (2,0) peak at $q_{20}$=1.48 Å$^{-1}$ ($d_{20}$=4.24 Å) and the broader (1,1) peak at $q_{11}$=1.50 Å$^{-1}$ ($d_{11}$=4.18 Å). This pattern is different in the following ways from scattering we expect from a sample with gel-fluid coexistence:

1. In the case of the DPPC Lβ' phase (at full hydration), the broader band is at a larger $q$-value but not necessarily for all Lβ'. The opposite is true for gel-fluid coexistence.
2. For a fluid phase band, HWHM/$q_{cc}$~10%. The (1,1) peak is much narrower, with HWHM/$q_{11}$~2.5% (Sun et al., 1994).

Therefore, the characteristic scattering from the Lβ' phase should not be mistaken for gel-fluid coexistence, even in powder samples.

The following list summarizes the criteria for phase coexistence in model membrane systems based on the x-ray scattering data:

1. Presence of two lamellar repeat spacings. If two $d_L$ spacings are present, this is clear evidence of phase coexistence.
2. Presence of two $d_{cc}$ spacings. In the case of gel/fluid phase coexistence, we would expect a broad band and narrow band in the wide angle pattern (for powder or oriented samples). However, in the case of Ld/Lo coexistence, we expect the broad wide-angle bands to overlap.
3. Poor fit of the $I(\phi)$ data by a single order parameter fit. This is a useful criteria for liquid/liquid coexistence. If gel phases are involved, we must be very careful with our interpretation of the fits because the Leadbetter model does not apply to well-ordered crystalline phases (see Section 3.2.5 and Ch. 5).
4. Change in $q_{cc}$ as a function of $\phi$ which is consistent with the presence of coexisting phases. This point is subtle and has not been discussed previously. It is discussed at length in relation to Ld/Lo coexistence in Ch. 6.

Note that the first two criteria are sufficient but not necessary for phase coexistence. This thesis will test the last two criteria for evaluating liquid-liquid phase coexistence.

# Chapter 4 - Cholesterol's effect on phospholipid chain order: GIWAXS results for DOPC/cholesterol

## 4.1 Introduction

To provide a framework for our investigation of ternary DOPC/DPPC/cholesterol mixtures (Ch. 6), we studied the binary mixtures DOPC/cholesterol and DPPC/cholesterol (Ch. 5). The literature suggests that DOPC/cholesterol does not phase-separate at any temperature or cholesterol composition (Filippov et al., 2003), whereas many reports suggest DPPC/cholesterol does phase-separate (see Ch. 5). DOPC/cholesterol is a simple system for calibrating the GIWAXS method for measuring chain order.

Although DOPC is a component in many studies of ternary phospholipid mixtures, cholesterol's effect on DOPC chain order is not well-studied in comparison with saturated lipids (such as DPPC and DMPC) and monounsaturated lipids (such as POPC). A major reason is that chain-perdeuterated DOPC is unavailable, making measurements of chain order by NMR difficult. Habiger et al. (1992) have made $^2$H NMR measurements on DOPC selectively deuterated at the *cis*-double bond position in each chain. Warschawski and Devaux (2005) have made NMR measurements on undeuterated DOPC. Both studies are in agreement that cholesterol causes a significant ordering of the DOPC chains. As another calibration of our GIWAXS measurements, we calculate lipid areas, which show that cholesterol causes a decrease in the DOPC area, consistent with an increase in chain orientational order.

This chapter presents our results for chain order parameters ($S_{mol}$) and lipid areas calculated from the GIWAXS data for mixtures of DOPC with cholesterol at 25˚C, well above the chain melting temperature of DOPC ($T_m \approx$-17˚C; Perly et al., 1985). We also discuss the effect of hydration on the DOPC wide angle scattering.

## 4.2 2D diffraction images: effect of cholesterol and hydration on the wide angle scattering from DOPC

Figure 4.1 shows the 2D diffraction images and $I(q)$ sector plots for DOPC at various levels of hydration. The high-$q$ water scattering begins to overwhelm the lipid scattering as the sample approaches full hydration. As discussed in Section 2.3.8.1, we believe that wide-angle data at 98% relative humidity (lamellar repeat~10 Å below full hydration) should be very similar to the data at full hydration. Sections 4.3 and 4.4 prove this assertion by quantifying the $q$- and $\phi$-widths of the wide-angle scattering.

A major assumption involved in our analysis is that we can separate the scattering from the chains from other sources of scattering in the sample, such as water, headgroups, etc. Because the wide-angle scattering for liquid-phase lipids is diffuse, this can be difficult. Even for gel-phase DPPC, much of the wide-angle scattering may be diffuse scattering due to sources other than chain-chain scattering (Sun et al., 1994).

A possible source of scattering in the wide-angle region is correlations between neighboring headgroups. Figure 4.2 shows two $I(q)$ slices for DOPC with $\phi$=5-10˚ compared with $\phi$=30-35˚. In the $\phi$=5-10˚ sector, a left shoulder is visible which is no longer apparent in the $\phi$=30-35˚ sector. Münster et al. (2000) have attributed a similar shoulder in their grazing incidence data for DMPC as possibly due to in-plane headgroup-headgroup correlations. Attempts have been made to separate out the various contributions of scattering (chain-chain correlations, headgroup-headgroup correlations, chain-headgroup correlations, etc.) using molecular dynamics simulations (Sega et al., 2007; Spaar and Salditt, 2003).

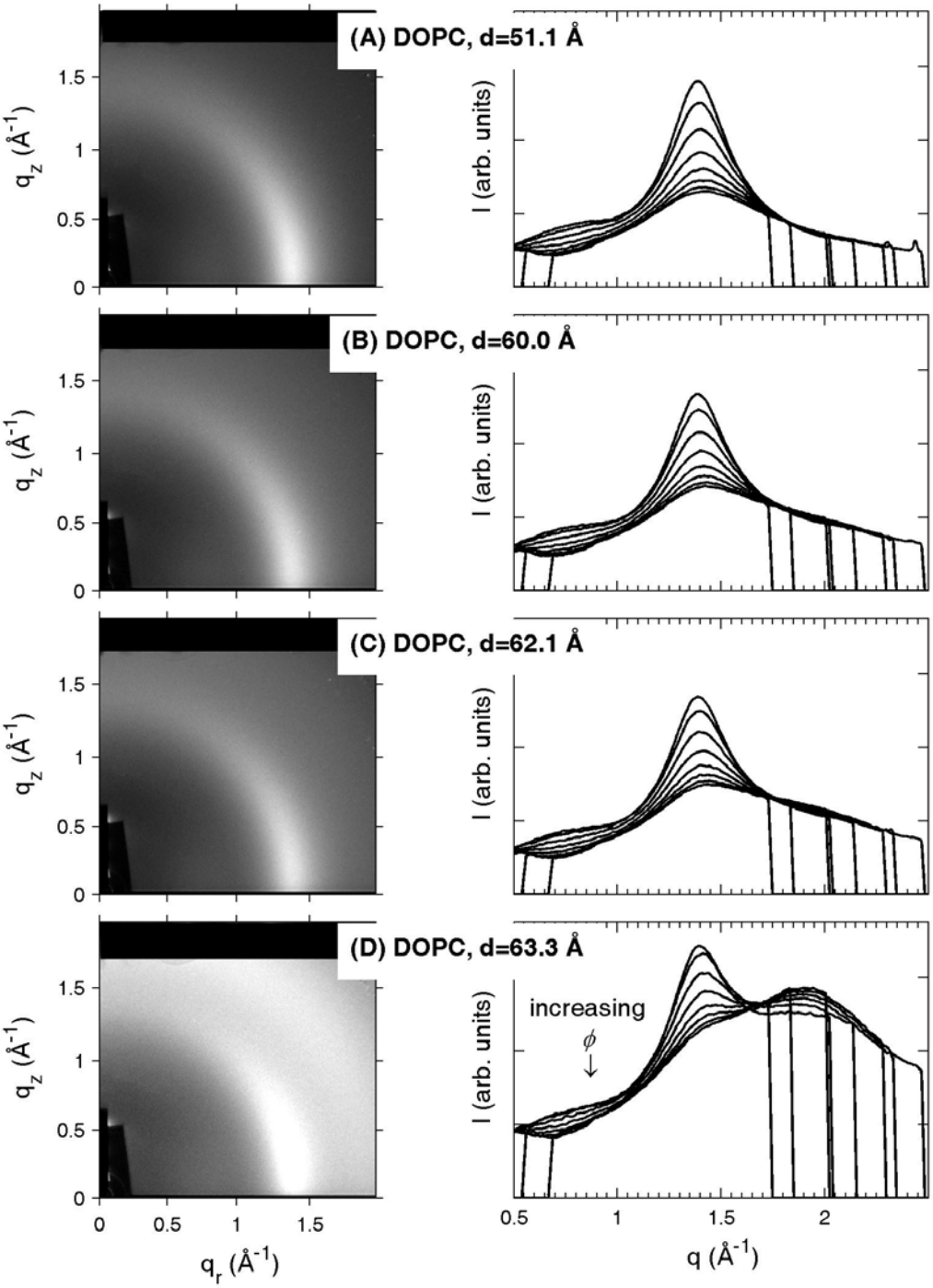


Figure 4.1. The left column shows 2D GIWAXS images for DOPC ($T$=25 ˚C) at different levels of hydration as measured by the lamellar repeat: (A) 51.1 Å, (B) 60.0 Å, (C) 62.1 Å, and (D) 63.3 Å. The right panel shows the corresponding $I(q)$ sector plots (see Section 2.3.7.3). The top trace corresponds to the smallest $\phi$ range. (October 2006, G-1)

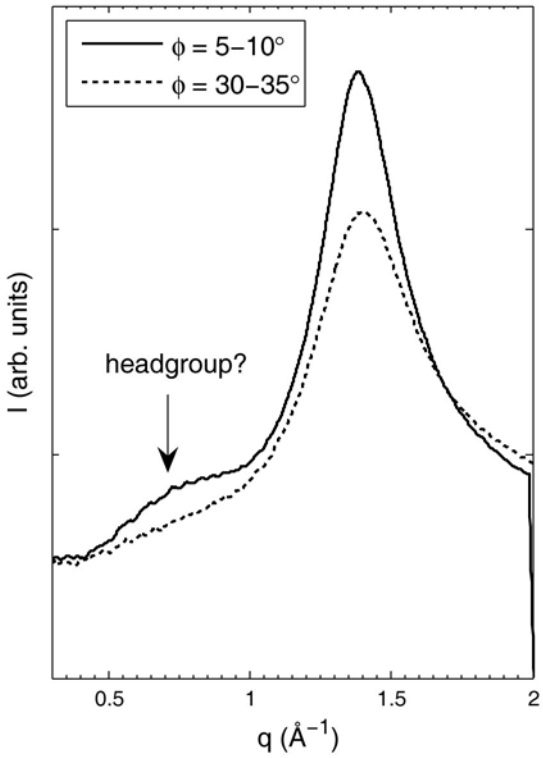


Figure 4.2. $I(q)$ sectors for DOPC at 25˚C ($d_L$=60.0 Å, 2D image shown in Fig. 4.1B). In the sector integrated over $\phi$=5-10˚ (solid line), a left shoulder, possibly due to headgroup-headgroup correlations, is visible. This shoulder has diminished in the $\phi$=30-35˚ sector (dashed line). (October 2006, G-1)

Figure 4.3 shows GIWAXS images and sector plots for DOPC, DOPC + 10% cholesterol, and DOPC + 40% cholesterol. The DOPC + 40% cholesterol sample has a much narrower angular distribution of scattering compared with pure DOPC and DOPC + 10% cholesterol. Note that the DOPC image and the DOPC + 40% cholesterol image have more high $q$ water scattering than the DOPC + 10% cholesterol image.

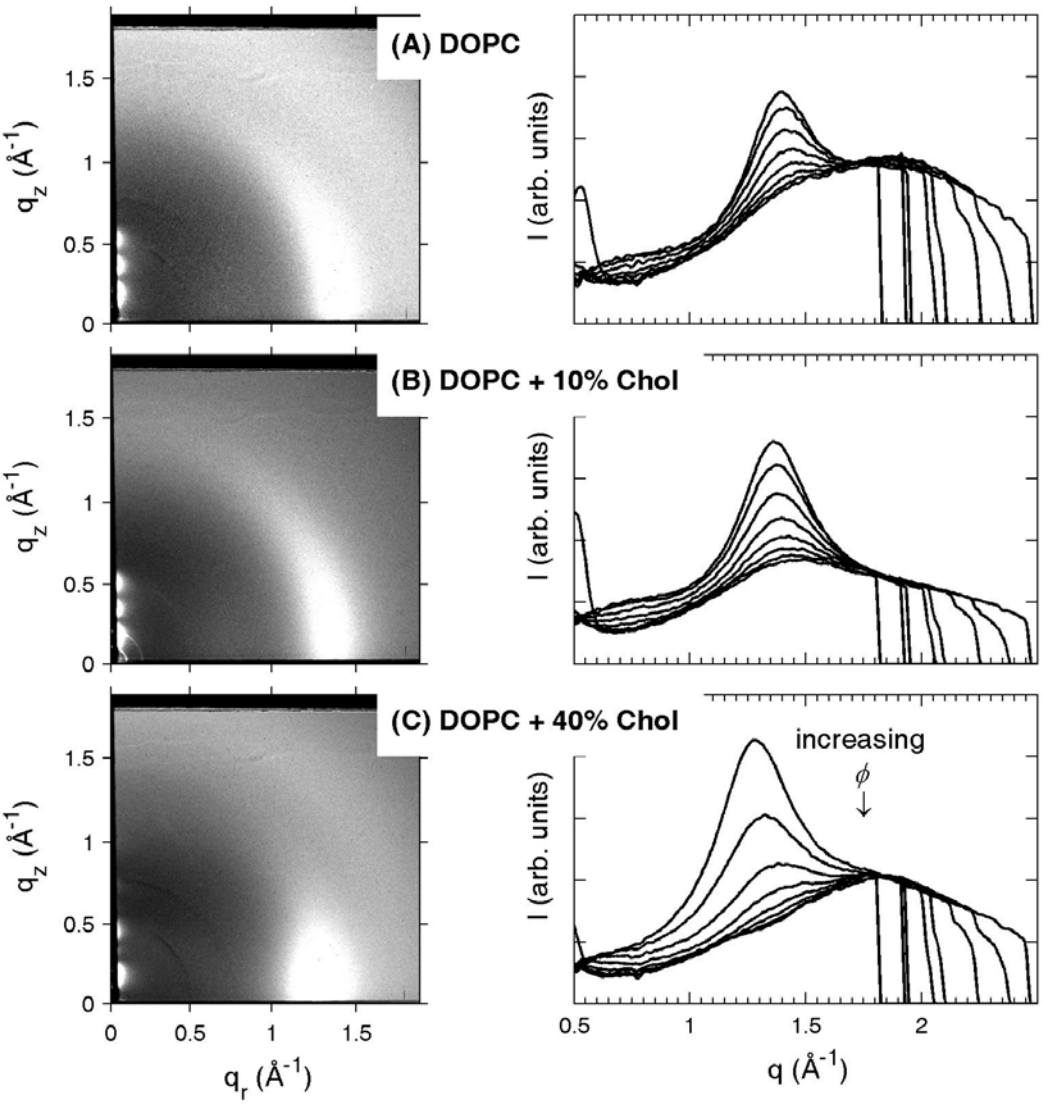


Figure 4.3. The left column shows 2D GIWAXS images taken at 25 ˚C for: (A) DOPC ($d_L$=60.9 Å), (B) DOPC + 10% cholesterol ($d_L$=60.0 Å), and (C) DOPC + 40% cholesterol ($d_L$=59.7 Å). The right column shows the corresponding $I(q)$ sector plots (see section 2.3.7.3). The top trace corresponds to the smallest $\phi$ range. (February 2006, D-1)

## 4.3 Lateral positional ordering for DOPC/cholesterol

GIWAXS data contain information about lateral positional ordering that will be important in our calculation of areas in Section 4.5. Figure 4.4 shows quantitative results obtained from the 2D diffraction images shown in Fig. 4.1. Figure 4.4A shows the scattering maximum, $q_{cc}$, as a function of the angle $\phi$. Note that for the fully hydrated sample ($d_L$=63.3 Å), $q_{cc}$ increases rapidly to a maximum of 1.7 Å$^{-1}$. This sample was flooded with excess water. At larger $\phi$ the high-$q$ water scattering, which is isotropic, begins to overwhelm the relatively weaker lipid scattering. Therefore, the value of $q_{cc}$ no longer corresponds to the maximum in the lipid scattering at large $\phi$.

Figure 4.4B shows the half width at half maximum (HWHM) as a function of $\phi$. Spaar and Salditt (2003) interpreted the increase in HWHM($\phi$) as an indication that the chain-chain scattering was less well correlated at larger $\phi$. The steep rise in the HWHM($\phi$) for the $d_L$ =63.3 Å plot is again due to water. If we only compare the data at low $\phi$, where the complications due to water scattering are not an issue, the position of the scattering maximum, $q_{cc}$ (~1.39 Å$^{-1}$), and the HWHM (~0.15 Å$^{-1}$) are relatively insensitive to hydration level for lamellar repeats of 51.1 Å to 63.3 Å.

Figures 4.4C and 4.4D convert the $q_{cc}(\phi)$ and HWHM($\phi$) information from reciprocal space to real space for DOPC ($d_L$ =60.0 Å). The chain-chain correlation spacing ($d_{cc}$ =2π/$q_{cc}$) is shown in Figure 4.4C. The decrease in $d_{cc}$ as a function of $\phi$ is likely due to drift of $q_{cc}$ to higher values as water scattering becomes relatively more prominent. The correlation length ($\xi$=1/HWHM) as a function of $\phi$ for DOPC at 25˚C is compared to Spaar and Salditt's data for DMPC at 45˚C (2003). Both samples are in the Ld phase. The DOPC $\xi(\phi)$ data is systematically larger than the DMPC data. Spaar and Salditt (2003) compared several Ld phase lipids, and did not report such a large difference. The difference may be a result in the different methods used to calculate HWHM (see Sections 2.3.7.5 and 2.3.8.2). Since it is difficult to determine

the baseline $I(q)$ value, the HWHM values we report are only estimates. Kaganer et al. (1999) point out that in the monolayer literature some groups report the correlation length as 1/HWHM while others use the Scherrer equation (Guinier, 1963, p. 121-124), which is larger by a factor of $0.94\pi$. Figure 4.4D shows $\xi$=1/HWHM in order to compare with Spaar and Salditt's data.

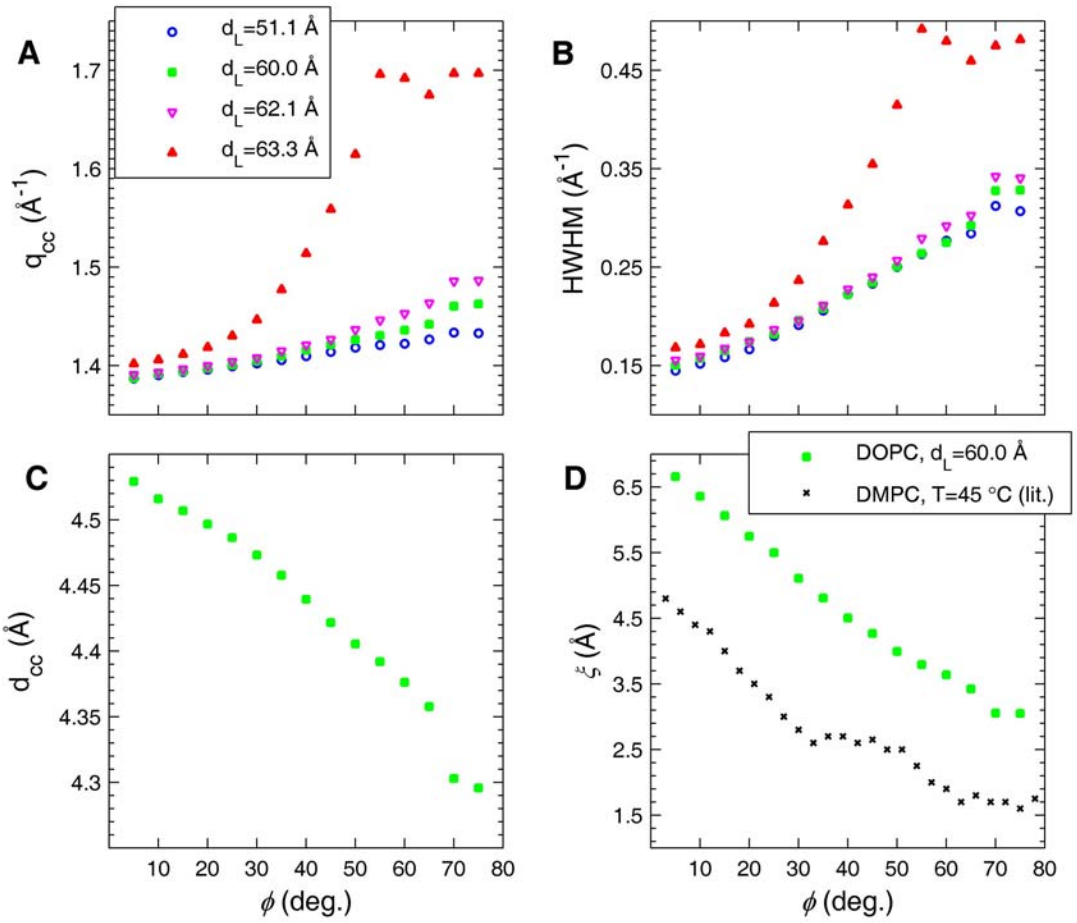


Figure 4.4. Lateral positional information from the wide-angle data for DOPC at different levels of hydration (see legend at top left). Plots (A) and (B) show the information in reciprocal space: (A) peak position, $q_{cc}(\phi)$ and (B) HWHM($\phi$). Plots (C) and (D) convert the information to real-space for the $d_L$=60.0 Å data: (C) chain-chain spacing, $d_{cc}(\phi)=2\pi/\ q_{cc}(\phi)$ and (D) correlation length, $\xi(\phi)$=1/HWHM($\phi$). Spaar and Salditt's $\xi(\phi)$ data for DMPC at 45˚C are shown in plot (D) for comparison (2003). (October 2006, G-1)

For gel-phase lipids, $d_{cc}=2\pi/q_{cc}$ can be interpreted as the average interchain spacing (note for the Lβ' phase there are two spacings: $d_{11}$ and $d_{20}$). As is well-known, $d_{cc}$ can be used to calculate the area per chain for gel-phase lipids (see Sun et al., 1994 and Tristram-Nagle et al., 1993 and the references therein). However, in the fluid phase the interpretation of $d_{cc}$ as the average interchain spacing is flawed because the chains are not well-ordered. In the fluid phase, the chains can even bend over themselves. Such a situation would double the area/chain but not affect $q_{cc}$. It also complicates the interpretation of correlation lengths. Spaar and Salditt (2003) and Sega et al. (2007) also point out the flaws in naively interpreting $d_{cc}=2\pi/q_{cc}$ as the interchain spacing for fluid-phase lipids. Based on comparison of scattering data to molecular dynamics simulations, Spaar and Salditt (2003) proposed a corrected relation for the interchain spacing, which we will call $a$:

$$a = \frac{9\pi}{4q_{cc}} = 1.125\frac{2\pi}{q_{cc}}. \tag{4.1}$$

Based on their simulations, Sega et al. (2007) find the following relation for $a$:

$$a = 1.2285\frac{2\pi}{q_{cc}}. \tag{4.2}$$

Although $d_{cc}$ and $\xi$ can easily be misinterpreted for the fluid phase, $d_{cc}$ is a useful number to report for comparison with other work. In the rest of this chapter and the following chapters, we will continue to use $d_{cc}=2\pi/q_{cc}$, but we will interpret it differently to obtain the lipid area in Section 4.5.

Table 4.1 lists $q_{cc}$, $d_{cc}$, and HWHM values (for a $\phi$=5-10˚ sector) for DOPC, DOPC + 10% cholesterol, and DOPC + 40% cholesterol. Cholesterol addition decreases $q_{cc}$ from 1.39 Å$^{-1}$ for DOPC to 1.28 Å$^{-1}$ for DOPC + 40% cholesterol. This corresponds to an increase in $d_{cc}$ with increasing cholesterol content, which has been observed for a variety of lipids (Finean, 1990). In general, this increase in $d_{cc}$ is interpreted as resulting from the cholesterol inserting between chains and increasing

the average interchain distance (see for example Maulik and Shipley, 1996a). However, Huey Huang has observed that the addition of peptide to phospholipid sometimes results in a decrease in $d_{cc}$ (personal communication); the same reasoning as applied to cholesterol then does not make sense. Resolution of this issue would require further investigation.

Table 4.1. Values of $q_{cc}$, $d_{cc}$ and HWHM for DOPC/cholesterol mixtures at 25˚C ($\phi$=5-10˚). (February 2006, D-1)

| mol% cholesterol | $q_{cc}$ (Å$^{-1}$) | $d_{cc}=2\pi/q_{cc}$ (Å) | HWHM (Å$^{-1}$) |
|---|---|---|---|
| 0 | 1.39 | 4.52 | 0.16 |
| 10 | 1.36 | 4.62 | 0.16 |
| 40 | 1.28 | 4.91 | 0.17 |

## 4.4 Quantifying chain order for DOPC/cholesterol: fits to $I(\phi)$

Figure 4.5 shows the single order parameter fits to the $I(\phi)$ data for DOPC at different levels of hydration. Due to noise in the data caused by water scattering, the $\phi$ range for the fits was considerably narrower for the fully hydrated ($d_L$=63.3 Å) data. The data are all well-fit by assuming a single Maier-Saupe distribution function. Note that Levine and Wilkins (1971) required different distribution functions to fit their $I(\phi)$ data depending on the hydration level of the egg lecithin. As described in Section 3.3.2, the data are normalized by subtracting the fitted background, $I_{back}$, and then dividing by the fitting parameter $A$ (proportional to the amount of sample, beam intensity, length of exposure). The colored bars on the graph show the zero offset for each normalized plot. According to the fits, the chain-chain scattering at $\phi$=90˚ is at least 25% of its maximum value at $\phi$=0˚. This may seem high, but Spaar and Salditt (2003) obtained a similar result for several lipids in the Ld phase.

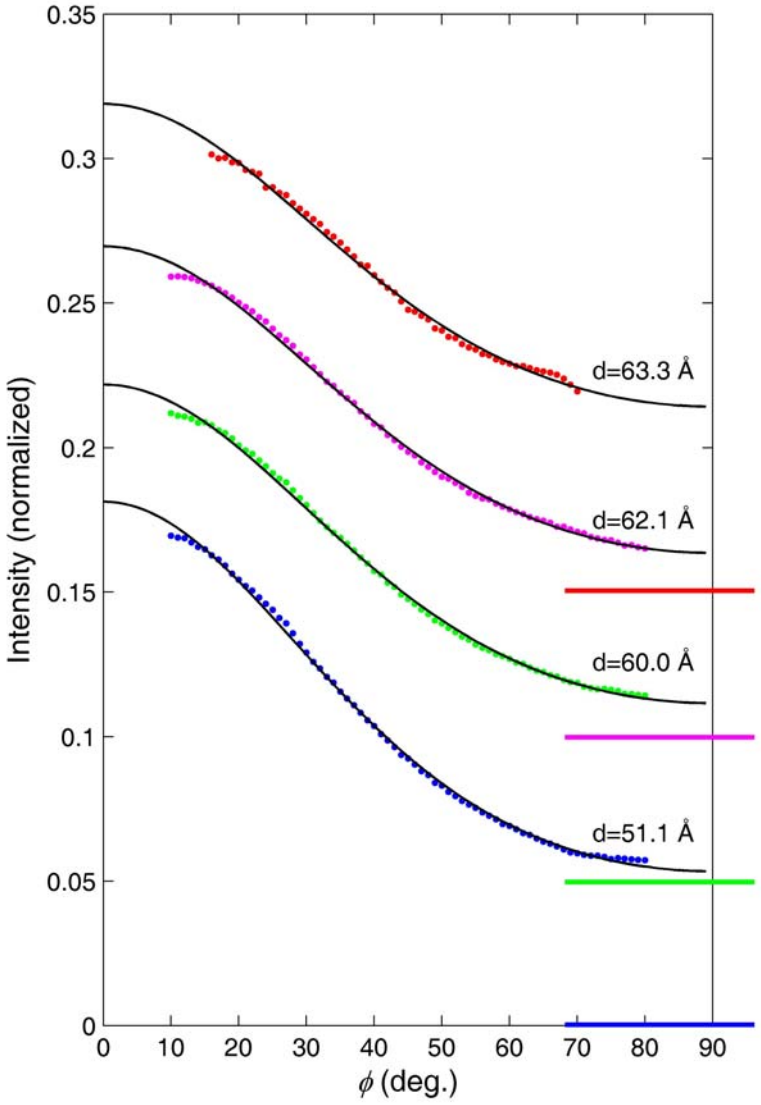


Figure 4.5. $I(\phi)$ plots at 25 ˚C for DOPC at various levels of hydration are shown by colored data points. Black lines are Maier-Saupe fits assuming one order parameter. The colored bars show the zero offset for the corresponding plots. (October 2006, G-1)

Figure 4.6 plots the value of $S_{mol}$, obtained by the fitted Maier-Saupe distribution function, as a function of hydration for DOPC. This figure combines data for different samples taken on different beamlines and different sample chambers. The variation in $S_{mol}$ between different samples (or beamlines) is larger than the variation in $S_{mol}$ due to hydration. This plot is further evidence that the chain scattering should be relatively insensitive to the level of hydration, at least at higher hydration levels. However, for the October 2006 NIH chamber data set, which was taken on a single sample, there is a trend of decreasing $S_{mol}$ with increasing hydration. This agrees with the expected trend of increasing lipid area with increasing hydration (Rand and Parsegian, 1989).

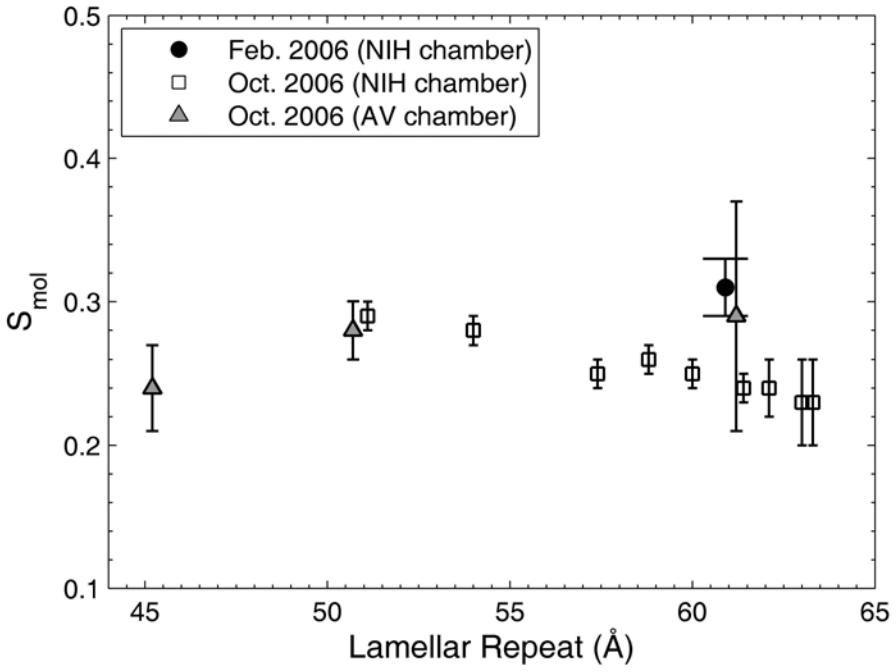


Figure 4.6. $S_{mol}$ vs. lamellar repeat for DOPC at 25˚C.

Figure 4.7 shows the single order parameter fits to the $I(\phi)$ data for DOPC, DOPC + 10% cholesterol, and DOPC + 40% cholesterol. The data are all described well by assuming a single Maier-Saupe distribution function. In comparison to DOPC, the angular distribution of scattering is much narrower for DOPC + 40% cholesterol. Also, according to the fit, the scattering intensity at $\phi$=90˚ is close to zero for DOPC + 40% cholesterol.

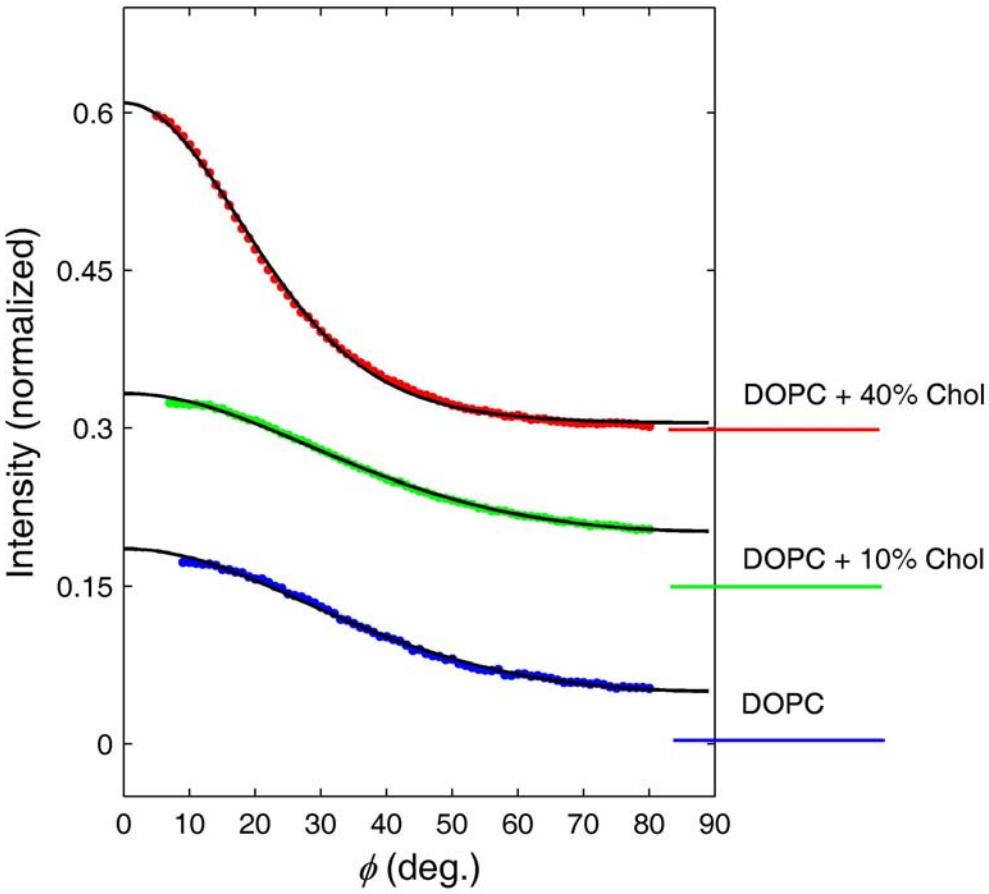


Figure 4.7. $I(\phi)$ plots at 25 ˚C for DOPC/cholesterol mixtures are shown by colored data points. Black lines are Maier-Saupe fits assuming one order parameter. The colored bars show the zero offset for the corresponding plots. (February 2006, D-1)

Table 4.2 summarizes the fit results for the DOPC/cholesterol mixtures at 25˚C. Spaar and Salditt's results (2003) for the fraction of the integrated scattering intensity in the range $0^\circ \le \phi \le 30^\circ$ and $60^\circ \le \phi \le 90^\circ$ for OPPC, DMPC, and DLPC (all in Ld phase at 45˚C) are given for comparison to DOPC. Since the scattering intensity fractions for the fluid phases are similar, this suggests that our method for subtracting the non-chain scattering ($I_{back}$ in Eq. 3.29) and Salditt's method of subtracting a linear background (see Section 2.3.8.2) give similar results. Note that the fraction of integrated scattering intensity in a certain $\phi$ range does not correspond to the fraction of chains tilted at an angle in that range according to the fitted Maier-Saupe distribution (see Section 3.3.3). Of course, in the real system, the chains are not straight rods, and so referring to a single tilt angle for each chain is highly simplified. Also, the model predicts that some of the chains lie parallel to the plane of the bilayer ($\beta$=90˚), which is exceedingly unlikely in the real system. Levine and Wilkins (1971) point out that if we think of the scattering domains as segments of chains, then we can avoid some of these difficulties in interpretation of the results of the simple model.

Table 4.2. Results of fits (Eq. 3.2.9) to $I(\phi)$ data for DOPC/cholesterol mixtures at 25˚C. The data are shown in Fig. 4.7.

| **Sample** | ***m*** | $\boldsymbol{S_{mol}}$ | $\mathbf{R^2}$ | **Fraction Scatter** | |
|---|---|---|---|---|---|
| | | | | $\mathbf{0^\circ \le \phi \le 30^\circ}$ | $\mathbf{60^\circ \le \phi \le 90^\circ}$ |
| DOPC | 2.10 ± 0.13 | 0.31 ± 0.02 | 0.9974 | 53% | 18% |
| DOPC + 10% Chol | 2.02 ± 0.08 | 0.30 ± 0.01 | 0.9988 | 52% | 18% |
| DOPC + 40% Chol | 5.52 ± 0.09 | 0.68 ± 0.01 | 0.9992 | 83% | 3% |
| OPPC* | | | | 52.2% | 19.3% |
| DMPC* | | | | 49.1% | 21.7% |
| DLPC* | | | | 46.1% | 23.7% |

*The OPPC, DMPC, and DLPC data (all at 45˚C) are from Spaar and Salditt (2003).

$S_{mol}$ more than doubles for DOPC + 40% cholesterol compared with pure DOPC. Information about average chain order, as measured by $^2$H NMR first moment data, is unavailable for DOPC. However, Habiger et al. (1992) have made $^2$H NMR measurements on DOPC selectively deuterated at the C-9 and C-10 positions, the *cis*-double bond. With 50% cholesterol content, the NMR quadrupole splittings almost double. Habiger et al. (1992) interpret this as evidence that at 50% cholesterol, the chain orientational order is high. Warschawski and Devaux (2005) have used NMR to measure $^1$H-$^{13}$C dipolar couplings for DOPC and DOPC + 30% cholesterol. This technique allows for the measurement of segmental order parameter profiles without deuteration. Their conclusion is that the addition of 30% cholesterol results in a "lipid state analogous to the Lo phase" with a substantial increase in chain orientational order.

A more indirect measure of the effect of cholesterol on chain order is the change in the membrane thickness, which can be calculated from electron density profile reconstruction from the lamellar diffraction data. As discussed in Ch. 1, the addition of cholesterol causes the chains to straighten, resulting in an increase in membrane thickness. Since the DOPC lipid volume does not change (Greenwood et al., 2006), an increase in membrane thickness results in a decrease in the lipid area, known as the cholesterol condensing effect. The thickening effect of cholesterol was reported by Levine and Wilkins (1971) for egg lecithin and has been measured for various lipids (see Hung et al., 2007 and the references therein). Hung et al. (2007) have shown that the bilayer thickness increases and the lipid area decreases substantially with the addition of cholesterol to DOPC. They report 72 Å$^2$ for DOPC at 30˚C and 54 Å$^2$ for DOPC + 40% cholesterol. Note that these measurements were taken at 98% relative humidity. The Nagle lab had earlier published an area of 72.4 Å$^2$ for DOPC (Liu and Nagle, 2004; Kučerka et al., 2005b; Tristram-Nagle et al.,

1998) and has recently obtained 64 Å$^2$ for the area of DOPC + 40% cholesterol (Mathai et al., 2007). These results are qualitatively consistent with the increase in $S_{mol}$ observed for addition of 40% cholesterol to DOPC. In the next section we show how areas for fluid-phase lipids can be calculated from combining information about the fitted chain orientational distribution with the lateral packing correlation distance, $d_{cc}$.

## 4.5 Calculation of lipid areas: combining chain orientational order and lateral ordering

Lipid area is an important structural parameter which helps define the molecular packing microstructure. Experimental lipid area measurements are often used to guide or to evaluate molecular dynamics simulations. However, experimental values of lipid areas, especially for the fluid phase, vary widely (see Nagle and Tristram-Nagle, 2000 and the references therein). Calculation of lipid areas from NMR and lamellar diffraction data can be complicated, but these methods make use of the simple relation:

$$\frac{A_L}{2} = \frac{V}{\langle L \rangle} \tag{4.3}$$

where $A_L$ is the area per lipid headgroup ($A_L/2$ is the area of a single chain in the plane of the bilayer), $V$ is the volume per chain, and $\langle L \rangle$ is the mean chain length. (See Petrache et al., 2000 for an alternative calculation of lipid areas using NMR data.) The volume $V$ is typically found from dilatometry (Nagle and Wilkinson, 1978). In the NMR method, $\langle L \rangle$ or equivalently the projected length of each chain segment along the membrane normal, is calculated from segmental order parameters (see references in: Brown et al., 2006; Nagle, 1993; Petrache et al., 2000). Lamellar diffraction can also be used to find $\langle L \rangle$. In the well-used Luzzati method, area is calculated from the lamellar spacing and a knowledge of the minimum water/lipid

ratio necessary to achieve full hydration (Luzzati, 1968), and then the volume of the hydrocarbon chain is used to obtain the chain length. Because not all of the water resides between the bilayers, lamellar scattering-based methods that involve calculating the hydrocarbon thickness from electron density profiles are preferred (for a review see Nagle and Tristram-Nagle, 2000).

For fully-extended, rigid gel-phase lipids, areas can be calculated entirely from the wide-angle diffraction data. The lipid area is calculated from the interchain spacing(s) and the chain tilt angle, which can be determined from powder or oriented WAXS data. For a calculation of the area for tilted chains in a distorted hexagonal lattice, see: Tristram-Nagle et al., 1993 and Sun et al., 1994. These papers show relationships between the real-space lattice spacings and the $q$ values of the scattering peaks for the Lβ' phase of DPPC.

Levine and Wilkins (1971) considered the fluid phase as an assembly of domains with almost fully extended chains packed in a hexagonal lattice. The domains can have different orientations, described by the angle $\beta$. Figure 4.8 is a schematic of how the lipid area can be calculated from the lattice spacing $d_{cc}$ for a chain tilted at an angle $\beta$. For simplicity we assume perfect hexagonal packing in the plane perpendicular to the axes of the chains (not the plane of the bilayer). Figure 4.8A shows a hexagonal lattice in a plane perpendicular to the axes of the chains. Figure 4.8B shows how the area per chain in the plane of the bilayer, $A_L(\beta)/2$, is related to $A_c$, the area per chain in the plane perpendicular to the chain.

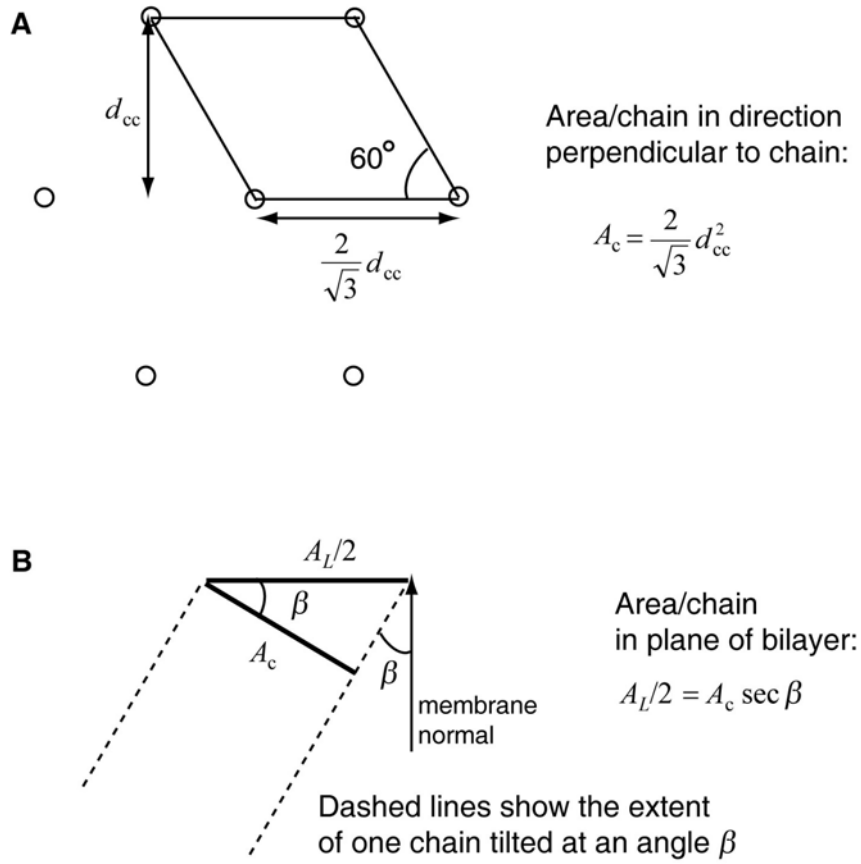


Figure 4.8. (A) Assumed hexagonal lattice in a plane perpendicular to the axes of the chains with interchain spacing $d_{cc}$. The unit cell is outlined. (B) Relationship between $A_c$, the area/chain in the plane perpendicular to the chain axis, and $A_L/2$, the area/chain in the plane of the bilayer.

As a check on the model used to fit the $I(\phi)$ data (see Ch. 3), we can calculate the areas from the wide-angle scattering data and compare to the literature. With the above assumptions, the area/chain in the plane of the bilayer for a chain tilted at an angle $\beta$ is given by:

$$\frac{A_L(\beta)}{2} = \frac{2}{\sqrt{3}} d_{cc}^2 \sec\beta \tag{4.4}$$

with $d_{cc}=2\pi/q_{cc}$. We assume $d_{cc}$ is independent of the angle $\beta$ (or equivalently $q_{cc}$ is independent of $\phi$) and use the value of $q_{cc}$ near $\phi=0$ (Note in Fig. 4.4C, the $d_{cc}$ value changes by ~5%). The chains have a variety of orientations, and so to calculate the average area per chain, we must average over all angles:

$$\frac{A_L}{2} = \frac{\langle A_L(\beta)\rangle}{2} = \frac{2}{\sqrt{3}} d_{cc}^2 \langle \sec\beta \rangle \tag{4.5}$$

Recall that the area per headgroup is given by $A_L$. The average $\langle \sec\beta \rangle$ cannot be computed because $\sec\beta$ becomes infinite as $\beta$ approaches 90˚. In our model, this would reflect the situation of an infinitely long chain lying in the surface of the bilayer; this situation obviously does not apply to the real physical system.

Levine and Wilkins (1971) point out this problem and do not attempt to approximate $\langle \sec\beta \rangle$. The same problem of calculating $\langle \sec\beta \rangle$ is encountered in a calculation of areas from NMR data. The following three approximations have been suggested (Petrache et al., 2000):

$$\langle \sec\beta \rangle \approx \langle \cos\beta \rangle^{-1} \tag{4.6}$$

$$\langle \sec\beta \rangle \approx \frac{\langle \cos^2\beta \rangle}{\langle \cos\beta \rangle^3}$$

$$\langle \sec\beta \rangle \approx 3 - 3\langle \cos\beta \rangle + \langle \cos^2\beta \rangle$$

The values $\langle\cos\beta\rangle$ and $\langle\cos^2\beta\rangle$ can be calculated from the chain orientational distribution function, using the generalized equation for average values, Eq. 3.34. Since none of these substitutions is strictly correct, we will calculate $A_L$ using all three and compare. Table 4.3 summarizes our area/headgroup ($A_L$) values calculated by combining the lateral positional information ($d_{cc}$) with the chain orientational information from our fits of $f(\beta)$. The two DOPC $S_{mol}$ values listed in the table reflect the entire range of $S_{mol}$ values measured for different DOPC samples, different levels of hydration, or different beamlines. We also show our results for DPPC at 45˚C (DPPC data discussed in Ch. 5). The GIWAXS results for the area per headgroup are compared with area values measured by the Nagle group using the diffuse scattering method.

Table 4.3. Area per headgroup calculations using Eq. 4.5 for DOPC/cholesterol (25˚C) and DPPC (45˚C).

| **Lipid** | $d_{cc}$ **(Å)** | $m$ | $S_{mol}$ | **Replacement for** $\langle\sec\beta\rangle$ | $A_L$ | **Literature** |
|---|---|---|---|---|---|---|
| DOPC (25˚C) | 4.52 | 1.53 | 0.23 | $\langle\cos\beta\rangle^{-1}$=1.58 | 74.6 | 71.2 ± 0.5 (25˚C) (Pan, 2007) |
| | | | | $\langle\cos^2\beta\rangle\langle\cos\beta\rangle^{-3}$=1.89 | 89.2 | |
| | | | | 3 - 3$\langle\cos\beta\rangle$ + $\langle\cos^2\beta\rangle$ =1.58 | 74.6 | |
| | | 2.10 | 0.31 | $\langle\cos\beta\rangle^{-1}$=1.46 | 68.8 | 72.4 ± 0.5 (30˚C) (Mathai et al., 2007) |
| | | | | $\langle\cos^2\beta\rangle\langle\cos\beta\rangle^{-3}$=1.69 | 79.8 | |
| | | | | 3 - 3$\langle\cos\beta\rangle$ + $\langle\cos^2\beta\rangle$=1.49 | 70.4 | |
| DOPC + 10% Chol (25˚C) | 4.62 | 2.02 | 0.30 | $\langle\cos\beta\rangle^{-1}$=1.48 | 72.8 | 71.4 ± 1.0 (30˚C) (Mathai et al., 2007) |
| | | | | $\langle\cos^2\beta\rangle\langle\cos\beta\rangle^{-3}$=1.72 | 84.6 | |
| | | | | 3 - 3$\langle\cos\beta\rangle$ + $\langle\cos^2\beta\rangle$=1.50 | 73.8 | |
| DOPC + 40% Chol (25˚C) | 4.91 | 5.52 | 0.68 | $\langle\cos\beta\rangle^{-1}$=1.14 | 63.4 | 64 ± 1.0 (30˚C) (Mathai et al., 2007) |
| | | | | $\langle\cos^2\beta\rangle\langle\cos\beta\rangle^{-3}$=1.17 | 65.0 | |
| | | | | 3 - 3$\langle\cos\beta\rangle$ + $\langle\cos^2\beta\rangle$=1.16 | 64.4 | |
| DPPC (45˚C) | 4.52 | 3.03 | 0.44 | $\langle\cos\beta\rangle^{-1}$=1.32 | 62.2 | 64.3 (50˚C) (Kučerka et al., 2006) |
| | | | | $\langle\cos^2\beta\rangle\langle\cos\beta\rangle^{-3}$=1.46 | 68.8 | |
| | | | | 3 - 3$\langle\cos\beta\rangle$ + $\langle\cos^2\beta\rangle$=1.36 | 64.2 | |

The areas calculated using 3 - 3⟨cos$\beta$⟩ + ⟨cos$^2\beta$⟩ as a substitution give the best agreement with the literature. Although this is unlikely to be the preferred way to calculate lipid areas, these calculations serve as a gauge of whether or not our model is reasonable. While we would not trust the exact values of the molecular areas for fluid-phase lipids calculated using Eq. 4.5 with ⟨sec$\beta$⟩ replaced by 3 - 3⟨cos$\beta$⟩ + ⟨cos$^2\beta$⟩, the areas calculated in this way should reproduce trends. For example, if two lipids are known to have significantly different molecular areas, an approximate calculation of the areas using the GIWAXS data should reproduce this trend, as was the case for DOPC and DPPC. Also, the calculation from the GIWAXS data shows a decrease in area when 40% cholesterol is added to DOPC, in agreement with other area measurements.

Spaar and Salditt (2003) give a general relation for the area per chain based on comparison to molecular dynamics simulations for POPC:

$$\frac{A_L}{2} \cong 1.32\left(\frac{9\pi}{4q_{cc}}\right)^2. \tag{4.7}$$

Spaar and Salditt simply state the relation without thorough explanation, but we attempt to explain their reasoning here. According to molecular dynamics simulations, the area per lipid chain for POPC is $A_L$=65.5 Å$^2$ (Heller et al., 1993) and the corresponding wide angle scattering maximum is $q_{cc}$=1.42 Å$^{-1}$. We believe Spaar and Salditt simply solved for $x$ in the following equation to obtain Eq. 4.7:

$$\frac{65.5}{2} \cong x\left(\frac{9\pi}{4*1.42}\right)^2. \tag{4.8}$$

Equation 4.7 for the area relies on a comparison to the POPC molecular dynamics data. It only takes into effect changes in the lateral positional correlations between chains, as described by $q_{cc}$. However, the changes in the chain orientational distribution should also be taken into consideration. Equation 4.7 predicts that if two

lipids have the same wide-angle scattering maximum, $q_{cc}$, they should have the same area even if their chain order (and thus $\langle \sec\beta \rangle$ ) differs. DOPC at 25˚C and DPPC at 45˚C do have the same $q_{cc}$, but different molecular areas. Although using Eq. 4.5 with an approximation for $\langle \sec\beta \rangle$ has obvious flaws, we believe this approach provides a better way of thinking about calculating areas for fluid phase lipids from the wide-angle data than Spaar and Salditt's Eq. 4.7.

## 4.6 Effect of undulation fluctuations on the angular distribution of scattering

In Chapters 2 and 3, we discussed sources of error which can affect our $S_{mol}$ values calculated from the x-ray data. These include:

1. Sample mosaicity (see Section 2.3.5.1)
2. Geometric broadening (see Section 2.3.5.2)
3. Absorption of x-rays: most problematic at small $\phi$ (see Section 2.3.7.4)
4. Use of the approximation $\phi_L = \phi$ (see Section 3.2.6)

These effects introduce an error in the angular distribution of scattering (or $S_{mol}$ values) of no more than 10%. These effects produce systematic errors, and so as long as we focus on trends in $S_{mol}$, these errors should not change our conclusions. More problematic are errors which are different for each sample. In addition to chain order, the amplitude of undulations in the bilayer can affect the angular distribution of scattering and thus our $S_{mol}$ values. The magnitude of the undulation fluctuations depends on the elastic properties of the bilayer, which are known to change as a function of temperature and lipid composition. For example, studies show that cholesterol stiffens fluid-phase phosphatidylcholine bilayers (Evans and Needham, 1986; Needham and Nunn, 1990; Henriksen et al., 2004). Thus, in general we can expect the undulation amplitude to be smaller for membranes in the Lo phase (higher

cholesterol content) than the Ld phase. Higher chain order and smaller undulation amplitude (both expected for samples with more cholesterol) would result in a decrease in the angular distribution of scattering. However, we will show that the undulations have a small effect in comparison with chain orientational order on the angular distribution of scattering.

A fluctuating bilayer can be divided into sections which are tilted at an angle $\beta_F$ with respect to the average membrane normal. This angle is different from $\beta$, the angle of each chain with respect to the membrane normal. Nagle and Tristram-Nagle (2000) have considered the effect of undulation fluctuations on calculations of membrane areas. The correction involves multiplying the calculated area by $\langle \sec \beta_F \rangle \approx \langle \cos\beta_F \rangle^{-1}$. They find that $\langle \cos\beta_F \rangle^{-1} \approx 1.01\text{-}1.02$ for fluid-phase lipids, which means a 1-2% correction to the area. We have found that $\langle \cos\beta \rangle^{-1} \approx 1.3\text{-}1.6$ for fluid-phase DOPC and DPPC, where $\beta$ refers to the orientation of a chain with respect to the membrane normal. Perhaps a more straightforward way of showing that we can ignore the effect of the fluctuations is by comparing $\langle \beta_F \rangle^{1/2}$, calculated from the membrane elastic properties, to $\langle \beta \rangle^{1/2}$, calculated from our fits of the Maier-Saupe orientational distribution function to the x-ray data. For DOPC at 30˚C, $\langle \beta_F \rangle^{1/2} \approx 10^\circ$ (Nagle and Tristram-Nagle, 2000). In comparison, from the fitted Maier-Saupe distribution function, we calculate $\langle \beta \rangle^{1/2} \approx 50^\circ$ for DOPC at 25˚C. Our analysis of the angular distribution of scattering does not distinguish between $\beta$ and $\beta_F$, but the undulations are a small effect. Thus, the large changes we observe in the angular distribution of scattering with addition of cholesterol to DOPC are due in most part to changes in the chain orientational order.

## 4.7 Conclusion

For all the DOPC/cholesterol mixtures studied, the $I(\phi)$ data are well fit by a single Maier-Saupe distribution function. Our analysis of the GIWAXS data shows a significant increase in $S_{mol}$ when cholesterol is added to DOPC, in agreement with the available literature NMR data. The areas calculated from the GIWAXS data are also in agreement with the literature, showing that the simplified model of hexagonally-packed straight rods can reproduce trends such as the decrease in area with the addition of cholesterol. Level of hydration of DOPC had only a small effect on our values for $S_{mol}$ and the lateral positional ordering, as measured by $q_{cc}$ and the HWHM of the wide-angle peak.

# Chapter 5 - X-ray scattering results for the controversial DPPC/cholesterol system

## 5.1 Introduction

Although the DPPC/cholesterol system has been much studied, there is no definitive phase diagram for this system or other similar systems (other saturated phospholipids and cholesterol). Some experiments suggest gel/liquid phase coexistence at low temperatures and liquid/liquid phase coexistence at high temperatures, while other experiments suggest no evidence of phase coexistence in this system. In this chapter, we will evaluate our x-ray data for DPPC cholesterol using the criteria for phase coexistence discussed in Section 3.4. We will compare our DPPC/cholesterol GIWAXS data to 1:1 DOPC/DPPC, a mixture for which fluorescence microscopy clearly shows macroscopic liquid/gel phase separation. We will also compare our x-ray results to those reported in the literature for DPPC/cholesterol and other similar systems.

In addition to an examination of phase behavior, our DPPC/cholesterol measurements provide a test of the analytical model for chain scattering (see Ch. 3) as applied to model membranes. Although there is disagreement about the presence of phase coexistence in binary mixtures of phospholipids and cholesterol, there are points of agreement in the literature, which were outlined in Section 1.5. Most researchers are in agreement that DPPC + 40% cholesterol is in the Lo phase, both below and above the $T_m$ for DPPC (41.4˚C). The trends in DPPC chain order as a function of cholesterol content are well-established by NMR and other techniques. Comparison to these measurements, along with the lipid area calculations in Ch. 4, serve as calibration of our method. We will also discuss cases in which the model should not be applied.

## 5.2 Proposed DPPC/cholesterol phase diagrams: summary of discrepancies in the literature

Figure 5.1 shows the phase diagram for DPPC/cholesterol, based on NMR and DSC, published by Vist and Davis in 1990. This phase diagram was not the first that proposed phase coexistence in binary phospholipid/cholesterol mixtures, but it is the most cited. At low temperature ($T<T_m$; DPPC $T_m = 41.4^{\circ}C$), gel and Lo phases coexist; the NMR spectra are a superposition of characteristic gel and Lo spectra and DSC thermograms are a superposition of two peaks. At high temperature ($T>T_m$), Lo and Ld phases coexist; however, the evidence for the liquid-liquid coexistence is indirect, as the $^2H$ NMR spectra cannot be represented as a superposition of Ld and Lo spectra. A triple point, a line in which gel, Ld, and Lo phases all exist at a single temperature, separates the gel-fluid and fluid-fluid coexistence regions.

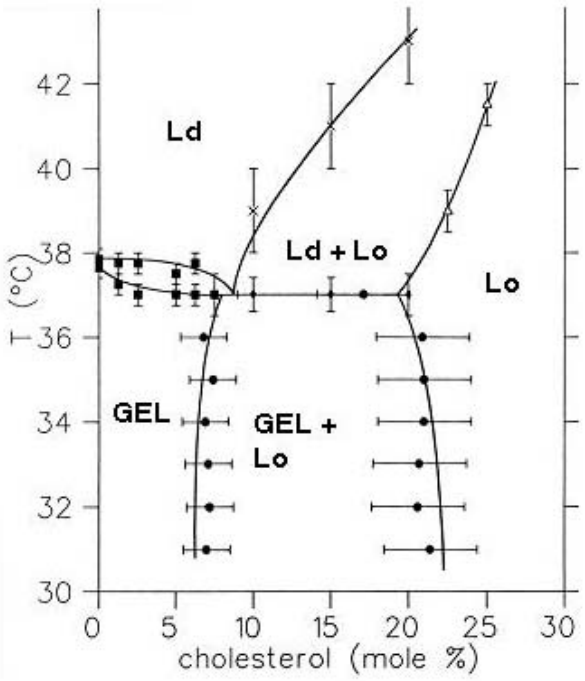


Figure 5.1. The Vist and Davis phase diagram for DPPC/cholesterol shows gel/liquid coexistence at low temperature and liquid/liquid coexistence at high temperature for ~7.5-22% cholesterol (modified from Vist and Davis, 1990).

Similar phase diagrams have been published for DMPC (Almeida et al., 1992; Recktenwald and McConnell, 1981). Although most phase diagrams for binary lipid/cholesterol mixtures are for saturated phospholipids or sphingomyelin, solid-liquid and liquid-liquid coexistence have also been reported for monounsaturated phospholipids, such as POPC (de Almeida et al., 2003; Thewalt and Bloom, 1992). Phase diagrams of the type in Fig. 5.1 have also been modeled theoretically (Ipsen et al., 1987).

A common reason stated for the discrepancies in the literature is that different experimental methods probe different time and length scales. When domains are small, assignment of phases can be difficult (Bloom and Thewalt, 1995). Fluorescence microscopy images of GUVs are uniform at all temperatures for DPPC/cholesterol and other binary phospholipid/cholesterol mixtures (Veatch and Keller, 2005b); therefore, phase-separation, if it exists in binary phospholipid/cholesterol systems, must consist of domains less than one micron in diameter. Techniques sensitive to smaller scale heterogeneities, including NMR (Vist and Davis, 1990), ESR (Sankaram and Thompson, 1991; Shimshick and McConnell, 1973) , fluorescence polarization (de Almeida et al., 2003), and x-ray diffraction (Engelman and Rothman, 1972), suggest that phospholipid/cholesterol mixtures do form phase-separated domains. $^2$H NMR, with a time scale of $10^{-5}$ s, probes domains with intermediate sizes of 20 nm or more (Bloom and Thewalt, 1995). ESR and fluorescence polarization, with very fast time scales of $10^{-8}$ s, are sensitive to domains as small as 1 nm (Bloom and Thewalt, 1995). Time scales are converted to distance scales on the basis of how far the lipid molecules diffuse away on the spectroscopic time scale. For example, for fluid phases a typical value for the lateral diffusion coefficient, $D$, is $4 \times 10^{-12}$ m$^2$/s and a typical value for the $^2$H NMR timescale, $\tau_{NMR}$, is $2 \times 10^{-5}$ s; this gives a distance scale of $L_{NMR}=(4D\,\tau_{NMR})^{1/2}$=20 nm (Bloom and

Thewalt, 1995). The time it takes for an x-ray scattering event to occur is rapid in comparison with diffusion of lipid molecules. Diffusion of the molecules does not significantly affect the scattering pattern, and so even very small domains should be detectable by x-ray scattering.

Differences in time and distance scales of different techniques do not fully account for the discrepancies in the literature. Even researchers using the same techniques as Vist and Davis (DSC and NMR) disagree with their phase diagram, especially the high temperature liquid-liquid coexistence region. Based on DSC measurements, McMullen and McElhaney (1995) have proposed a phase diagram for DPPC/cholesterol which does include solid-liquid phase coexistence at low temperature and liquid-liquid phase coexistence at high temperature; however, their diagram includes no triple point and has different phase boundaries than the Vist and Davis diagram. Also, the diagram distinguishes between several types of gel phase and two types of Lo phase (one more fluid-like and one more gel-like). Using NMR, Huang et al. (1993) published phase diagrams for DPPC/cholesterol and DSPC/cholesterol which do have a solid-liquid coexistence region at low temperature but do not have a liquid-liquid coexistence region at high temperature. The gel/fluid coexistence region reported by Huang et al. (1993) extends to much higher cholesterol concentrations than the ~22% cholesterol boundary in the Vist and Davis phase diagram. Huang et al. (1993) are careful to note that it is problematic to discuss their spectroscopic measurements in terms of a phase diagram because NMR is sensitive to heterogeneities (at least 10's of nanometers in size, but do not have to be macroscopic) which are not necessarily thermodynamic phases. Thewalt and Bloom (1992) do not attempt to assign phases in the high-temperature region of their POPC/cholesterol phase diagram because $^{2}H$ NMR measurements do not give direct evidence of liquid-liquid phase coexistence. Based on molecular volume data, Heerklotz and

Tsamaloukas (2006) suggest POPC/cholesterol mixtures are neither phase-separated nor ideal one-phase mixtures, but instead highly nonideal mixtures.

X-ray diffraction studies on binary phospholipid/cholesterol mixtures also give conflicting results. Some report evidence of solid-liquid coexistence at low temperature (Engelman and Rothman, 1972), while others report no evidence of any type of phase separation at any temperature or cholesterol content (Hui and He, 1983; Ladbrooke et al., 1968). Most of the evidence of phase coexistence from the x-ray literature concern gel-fluid coexistence (observation of either two $d_L$ or two $d_{cc}$ spacings below $T_m$). However, Petrache et al. (2005) claim that their lamellar repeat versus % cholesterol data for DMPC/cholesterol mixtures above $T_m$, which shows a sudden decline in $d_L$ spacing values at 30% cholesterol, provide evidence of Ld/Lo phase coexistence. This evidence is indirect, as Petrache et al. (2005) observed only a single $d_L$ spacing. To our knowledge, there are no reports of two $d_L$ or two $d_{cc}$ spacings in binary lipid/cholesterol mixtures at high temperature which would provide direct evidence of Ld/Lo coexistence.

## 5.3 2D diffraction images for DPPC/cholesterol mixtures compared to DOPC/DPPC

Figure 5.2 shows the 2D diffraction images and sector plots for DPPC, DPPC + 10% cholesterol, DPPC + 25% cholesterol, and DPPC + 40% cholesterol at 25˚C. Cholesterol causes a significant broadening ($q$-width) of the wide-angle scattering. Also, we observe no off-equatorial peak (indicative of no Lβ' phase) for DPPC + 10% cholesterol, consistent with previous results that the Lβ' phase disappears at ~7.5% cholesterol (Ladbrooke et al., 1968). The most obvious change in the data is the increase in the $q$-width. Since the $\phi$-width remains narrow, this indicates a change from the gel to Lo for DPPC + 40% cholesterol, in agreement with the literature.

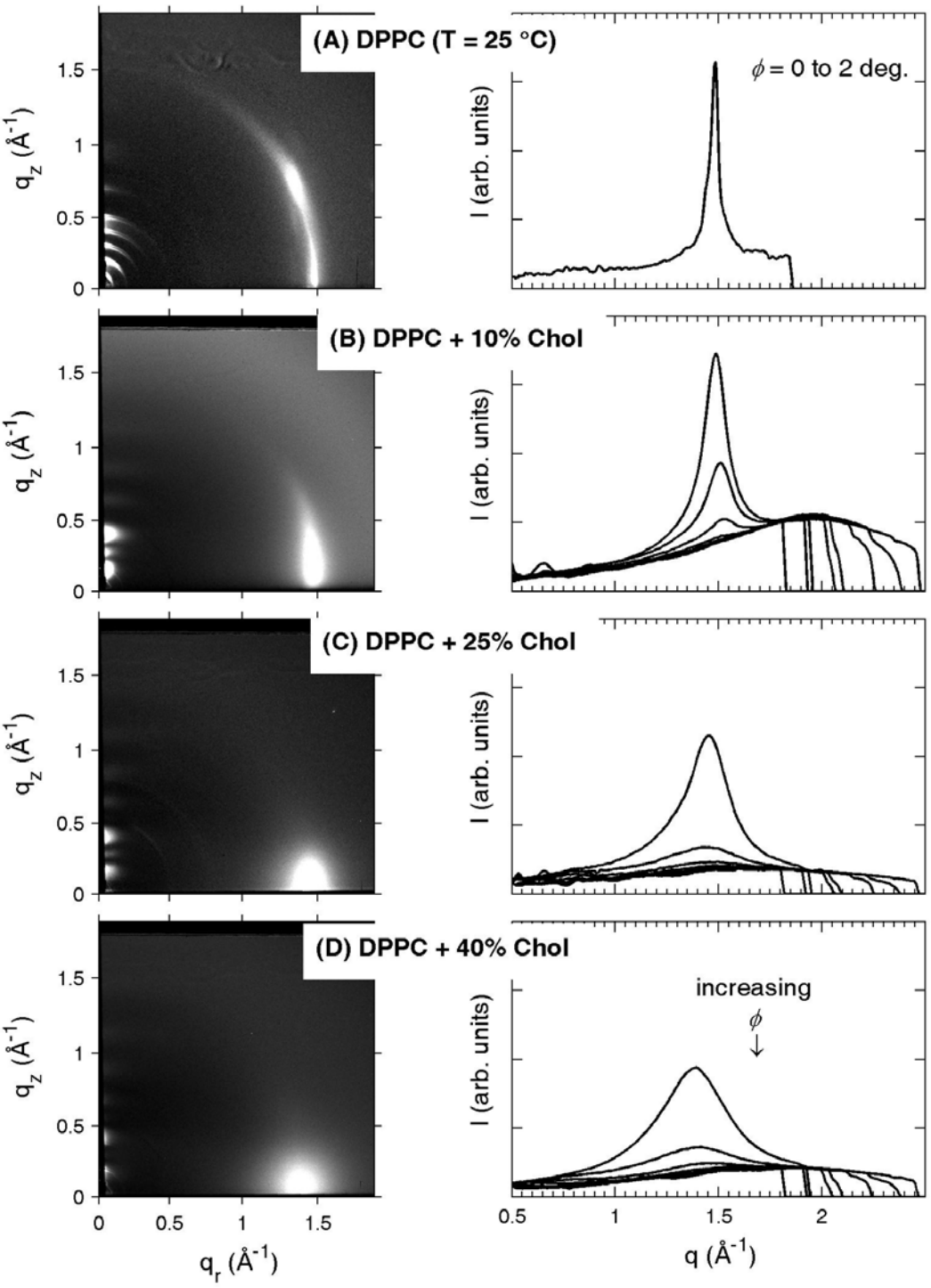


Figure 5.2. Left column shows 2D GIWAXS images taken at 25˚C for DPPC plus: (A) 0% cholesterol; (B) 10% cholesterol; (C) 25% cholesterol; (D) 40% cholesterol. The right column shows the corresponding $I(q)$ sector plots (see Section 2.3.7.3). The top trace corresponds to the smallest $\phi$ range. (February 2006, D-1)

Figure 5.3 shows 2D GIWAXS images and sector plots for DPPC + 15% cholesterol and 1:1 DOPC/DPPC at 25˚C. According to Vist and Davis, DPPC + 15% cholesterol is in the middle of a two-phase gel/Lo coexistence region. While GUV images at 25˚C of binary DPPC/cholesterol mixtures are uniform (Feigenson and Buboltz, 2001; Veatch, 2004; Veatch and Keller, 2003b), images of GUVs show coexisting gel and fluid domains of greater than one micron in size for 1:1 DOPC/DPPC at 25˚C (Veatch and Keller, 2003b). For 1:1 DOPC/DPPC, two separate peaks, one broad and one narrow, are evident in the $I(q)$ plots at small $\phi$ (Fig. 5.3b). The narrow peak is characteristic of gel phase with $q_{cc}$=1.50 Å$^{-1}$ and $d_{cc}$=4.19 Å. For large $\phi$, we observe only one broad peak. The gel phase (corresponding to the sharp peak) has high orientational order, and thus the angular distribution of scattering should be narrower, explaining the disappearance of the narrow peak at larger $\phi$.

Although there is agreement that there is a large region of gel/fluid coexistence in the DOPC/DPPC system, the phase boundaries are not clearly defined in the literature. (For instance, the phase diagram published by Lentz et al., 1976 is confusing.) From recent FRET measurements, the gel/fluid phase coexistence region is in the following range at 25˚C: 35%-95% DPPC (J. T. Buboltz, personal communication). The 1:1 DOPC/DPPC sample is therefore 75% fluid phase and 25% gel phase.

We do not observe an off-equatorial peak in the GIWAXS image for 1:1 DOPC/DPPC cholesterol, indicating that the gel phase is Lβ and not Lβ' as in pure DPPC at 25˚C. Since the choice of grayscale can affect judgment, we also compare $I(\phi)$ plots for 1:1 DOPC/DPPC and DPPC at 25˚C (Fig. 5.4). In contrast to 1:1 DOPC/DPPC, the (1,1) peak from the Lβ' gel phase appears in the $I(\phi)$ plots as a maximum near $\phi$~30˚ for DPPC. Note that in another binary phospholipid mixture, 1:1 DOPC/DSPC, we have observed the coexistence of Lβ' and Ld phases at 25˚C by

both GIWAXS on oriented samples and powder WAXS. (Oriented data were taken on this system in May 2005 at D1-station and powder data were taken in October 2005 on the Gruner rotating anode. The powder data appears in Zhao et al., 2007a). It is important that we established that Lβ, not Lβ', is coexisting with a fluid phase in 1:1 DOPC/DPPC because we want to use the GIWAXS pattern for 1:1 DOPC/DPPC as a control for fluid/Lβ coexistence. In Vist and Davis' proposed gel/Lo coexistence region for DPPC/cholesterol, there is no evidence of tilted chains in the gel phase.

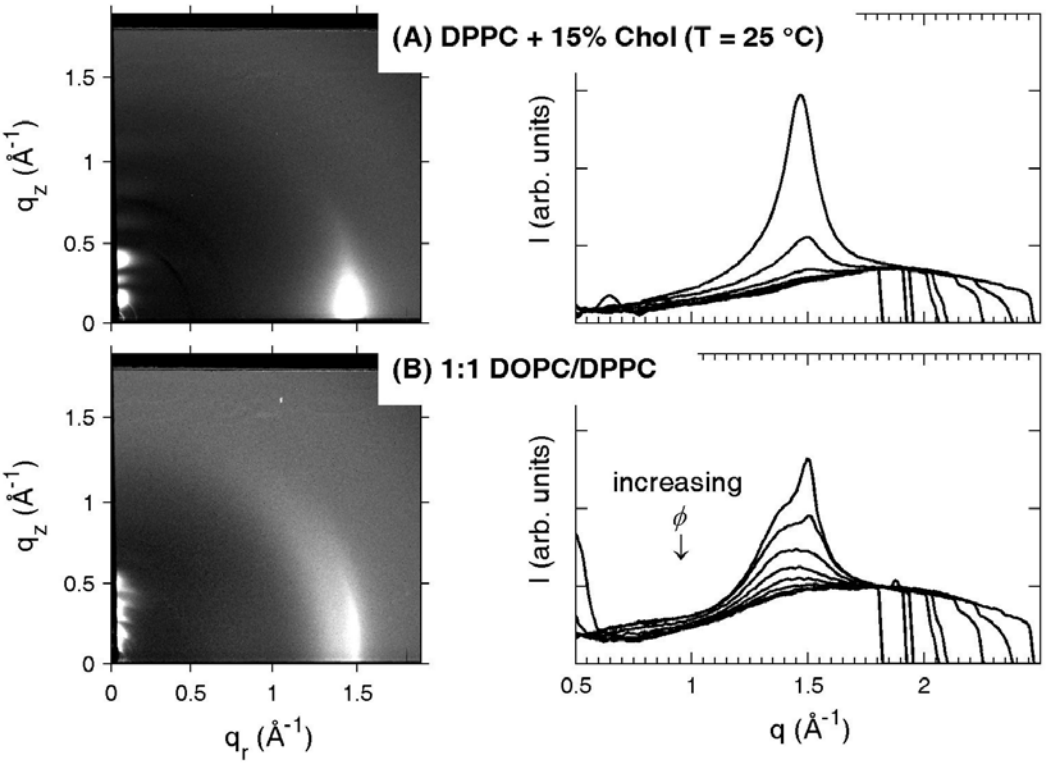


Figure 5.3. Left column shows 2D GIWAXS images taken at 25˚C for (A) DPPC + 15% cholesterol and (B) 1:1 DOPC/DPPC. The right column shows the corresponding $I(q)$ sector plots (see Section 2.3.7.3). The top trace corresponds to the smallest $\phi$ range. (February 2006, D-1)

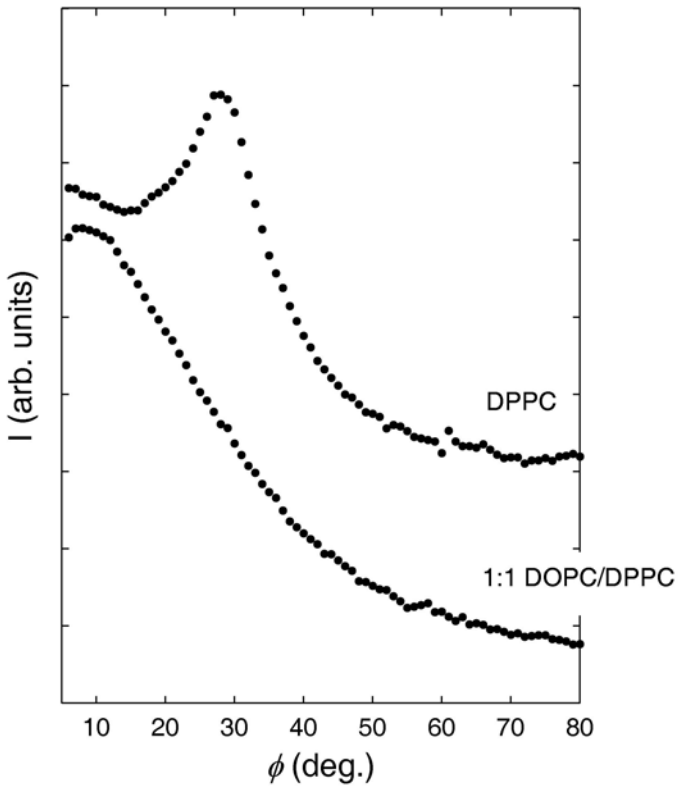


Figure 5.4. $I(\phi)$ plots for DPPC and 1:1 DOPC/DPPC. The peak at $\phi$~30˚ in the DPPC plot is indicative of the Lβ' phase. (February 2006, D-1)

In contrast to 1:1 DOPC/DPPC, we do not observe two peaks in the $I(q)$ curves for DPPC + 15 % cholesterol (Fig. 5.3A), or any other concentration of cholesterol at 25˚C (Fig. 5.2). The literature is in disagreement concerning the wide-angle scattering data for DPPC/cholesterol mixtures. Ladbrooke et al. (1968) studied MLV mixtures of DPPC with 0%, 5%, 7.5%, 12.5%, 20%, 32%, and 50% cholesterol at 25˚C. In agreement with our results, they observed only a single wide-angle peak for cholesterol concentrations of 7.5%-50%, which continuously changes from a sharp peak at 7.5% ($d_{cc}$=4.2 Å) to a broad band at 50% cholesterol ($d_{cc}$ =4.45 Å). Below

7.5% cholesterol, two wide-angle bands, corresponding to the Lβ' phase, were observed in agreement with our GIWAXS data and earlier higher compositional resolution data on MLV samples taken by the Feigenson lab (see Fig. 5.10A). Engelman and Rothman (1972) studied mixtures of DPPC with 0%, 20%, 25%, 30%, 33%, 36%, and 42% cholesterol at 20˚C. In contrast to our results, for mixtures containing 20%-33% cholesterol, they observed two wide-angle diffraction bands, one sharp line ($d_{cc}$=4.15 Å) and one diffuse band ($d_{cc}$ =4.7 Å), which they interpret as evidence of gel/fluid phase coexistence.

Figure 5.5 shows the 2D diffraction images and sector plots for DPPC with 0%, 10%, 25%, and 40% cholesterol at 45˚C. The diffuse wide-angle scattering shows that all of these samples are in a fluid phase. The angular distribution of scattering ($\phi$-width) becomes narrower with the addition of cholesterol. Despite the disagreement over the presence of liquid-liquid phase coexistence in DPPC/cholesterol mixtures with $T>T_m$, there is general agreement that DPPC + 40% cholesterol forms a single Lo phase at 45˚C. We do not observe two wide-angle peaks for any of the cholesterol concentrations we examined: 10%, 15% (data not shown), 25%, and 40% cholesterol. Even if there were fluid-fluid coexistence, we would not expect to observe two peaks in the wide angle data because the diffuse scattering from Ld and Lo phases would overlap. Instead, we will evaluate the angular distribution of scattering ($I(\phi)$ plots) to determine if the data are well fit by assuming one order parameter or two order parameters (see Section 5.5).

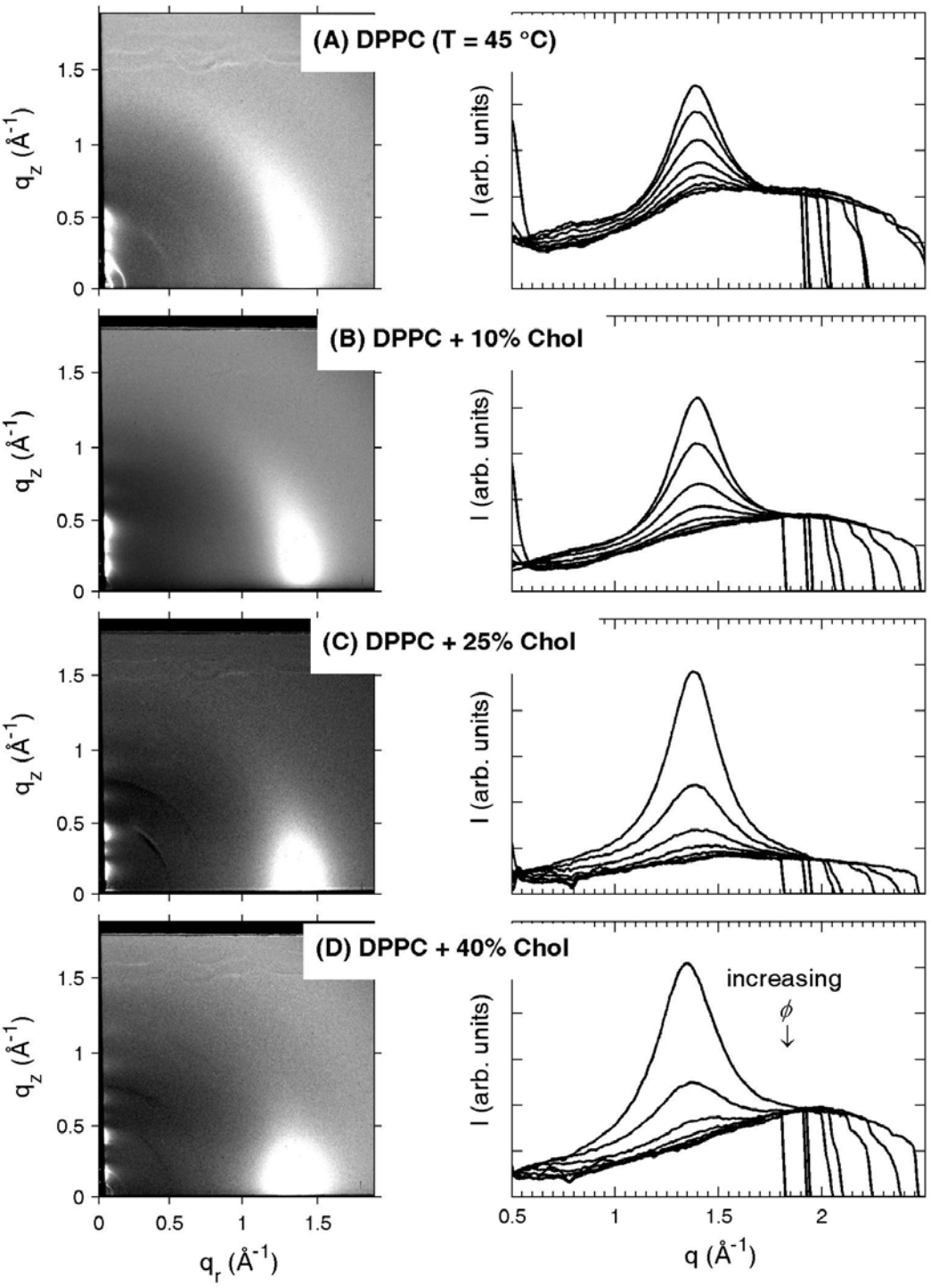


Figure 5.5. Left column shows 2D GIWAXS images taken at 45˚C for DPPC plus (A) 0% cholesterol; (B) 10% cholesterol; (C) 25% cholesterol; (D) 40% cholesterol. The right column shows the corresponding $I(q)$ sector plots (see Section 2.3.7.3). The top trace corresponds to the smallest $\phi$ range. (February 2006, D-1)

## 5.4 Lateral positional ordering: $q_{cc}$ and HWHM data

For most of the DPPC/cholesterol mixtures, the scattering falls off rapidly as a function of $\phi$. For such well-ordered samples, it is difficult to determine a peak position ($q_{cc}$) and half-width (HWHM) for the larger $\phi$ values by the method described in Section 2.3.7.5. Instead of showing $q_{cc}(\phi)$ and HWHM($\phi$) plots, values of $q_{cc}$, $d_{cc}$, and HWHM (for a $\phi$=5-10˚ sector) are listed in Table 5.1.

Table 5.1. Values of $q_{cc}$, $d_{cc}$ and HWHM data for DPPC/cholesterol mixtures ($\phi$=5-10˚). (February 2006, D-1)

| T (˚C) | mol% cholesterol | $q_{cc}$ (Å$^{-1}$) | $d_{cc}=2\pi/q_{cc}$ (Å) | HWHM (Å$^{-1}$) |
|---|---|---|---|---|
| 25 | 10 | 1.48 | 4.25 | 0.08 |
| | 15 | 1.46 | 4.30 | 0.09 |
| | 25 | 1.45 | 4.33 | 0.12 |
| | 40 | 1.38 | 4.55 | 0.18 |
| 45 | 0 | 1.39 | 4.52 | 0.15 |
| | 10 | 1.39 | 4.52 | 0.15 |
| | 15 | 1.37 | 4.59 | 0.14 |
| | 25 | 1.38 | 4.55 | 0.14 |
| | 40 | 1.35 | 4.65 | 0.16 |

At 25˚C, the HWHM increases as a function of cholesterol content, indicating that cholesterol is causing disorder in the tight packing of the DPPC chains. The HWHM more than doubles for 40% cholesterol compared with 10% cholesterol. At 45˚C, where all compositions are in a fluid phase, the HWHM is relatively constant (~0.15 Å$^{-1}$) as a function of cholesterol content. As with DOPC, the addition of cholesterol to DPPC causes a decrease in $q_{cc}$ (increase in $d_{cc}$), indicating the chain segments are further apart on average.

## 5.5 Fits to $I(\phi)$ plots: one order parameter or two?

Figure 5.6 shows $I(\phi)$ plots as well as fits assuming one chain order parameter compared with fits assuming two order parameters for DPPC/cholesterol mixtures at 25˚C. For cholesterol concentrations of 15%, 25%, and 40%, the $I(\phi)$ data are well-fit in the steeply changing low-$\phi$ region, but the fits are poorer at large $\phi$ when compared with fits to the DOPC/cholesterol data (see Ch. 4).

Figure 5.6 also shows the fit to the 1:1 DOPC/DPPC data at 25˚C, our control for gel/fluid phase coexistence. Although two peaks were clear in the $I(q)$ sector plots for 1:1 DOPC/DPPC at 25˚C (Fig. 5.3B), the $I(\phi)$ data are well-fit by assuming only one order parameter. In fact, the double order parameter fit returns the same value (to within 0.01 units) for both $m_1$ and $m_2$. We have written "NA" in the "$R^2$" and "Accept fit?" columns for the double order parameter fits because they are equivalent to the single order parameter fits. See Table 5.2, which also includes the fit results for the 45˚C data for 1:1 DOPC/DPPC (data not shown).

Table 5.2. Results of fits to $I(\phi)$ data for 1:1 DOPC/DPPC at 25˚C and 45˚C.

| T (˚C) | $m$* | $S_{mol}$* | $R^2$ | Accept fit? |
|---|---|---|---|---|
| 25 | m= 3.61 ± 0.06 | S= 0.51 ± 0.01 | 0.9994 | YES |
| | m1=m2 | S1=S2= 0.51 | NA | NA |
| 45 | m= 1.99 ± 0.12 | S= 0.29 ± 0.02 | 0.9977 | YES |
| | m1=m2 | S1=S2= 0.29 | NA | NA |

* If only one order parameter is given, the fit is to Eq. 3.29. If two order parameters are listed, the fit is to Eq. 3.32. If "m1=m2" or "S1=S2" are listed, this means these parameters were the same to within ±0.01.

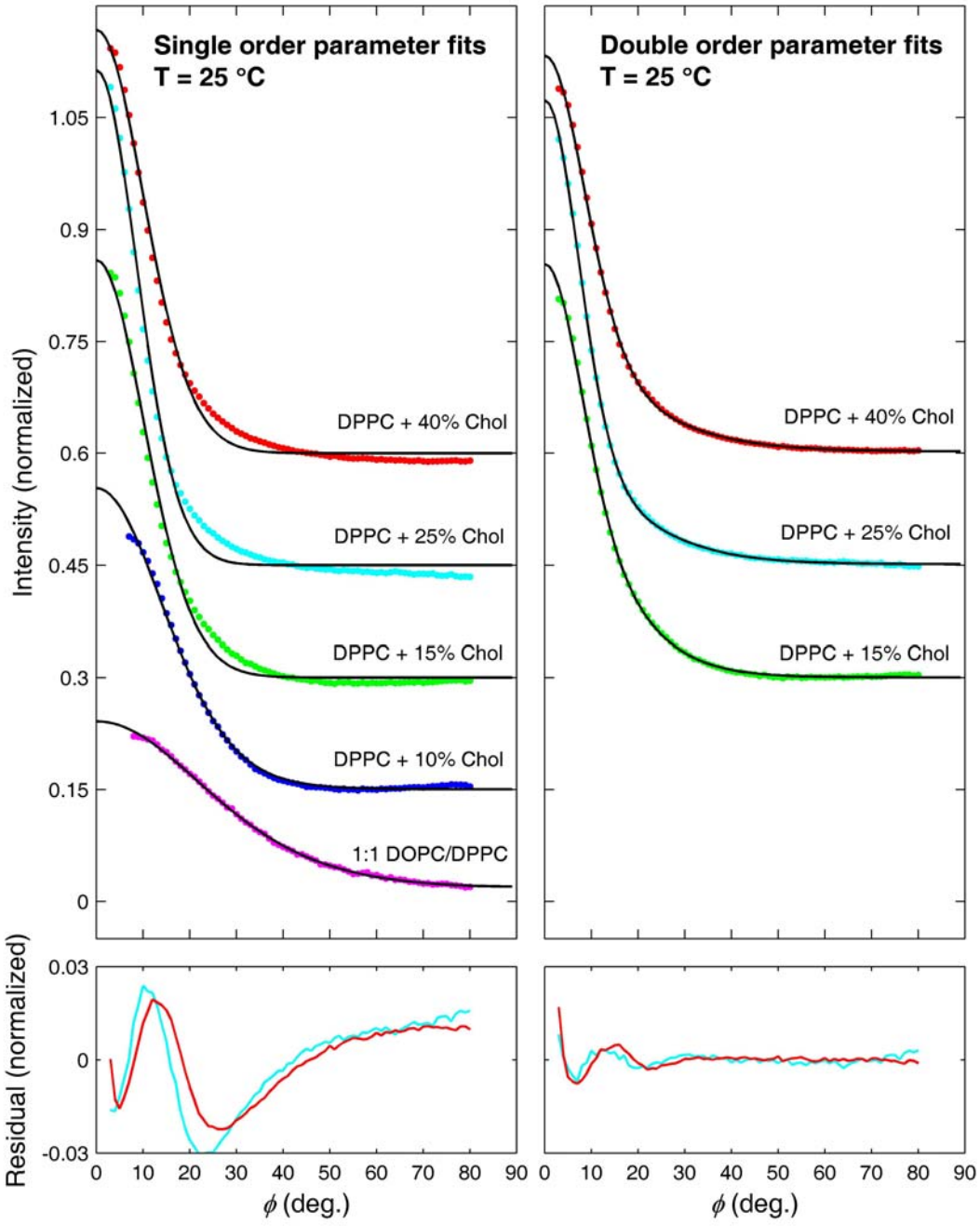


Figure 5.6. $I(\phi)$ plots at 25˚C for 1:1 DOPC/DPPC and DPPC/cholesterol mixtures are shown by colored data points. Black lines are Maier-Saupe fits assuming one order parameter (left panel) and two order parameters (right panel) with representative residual plots for the fits to the DPPC + 25% cholesterol (cyan) and DPPC + 40% cholesterol (red) data shown beneath. Each plot is offset from the one below by 0.15 normalized intensity units. If the double order parameter fit is not shown, it gave the same value (to within 0.01 units) for both order parameters.

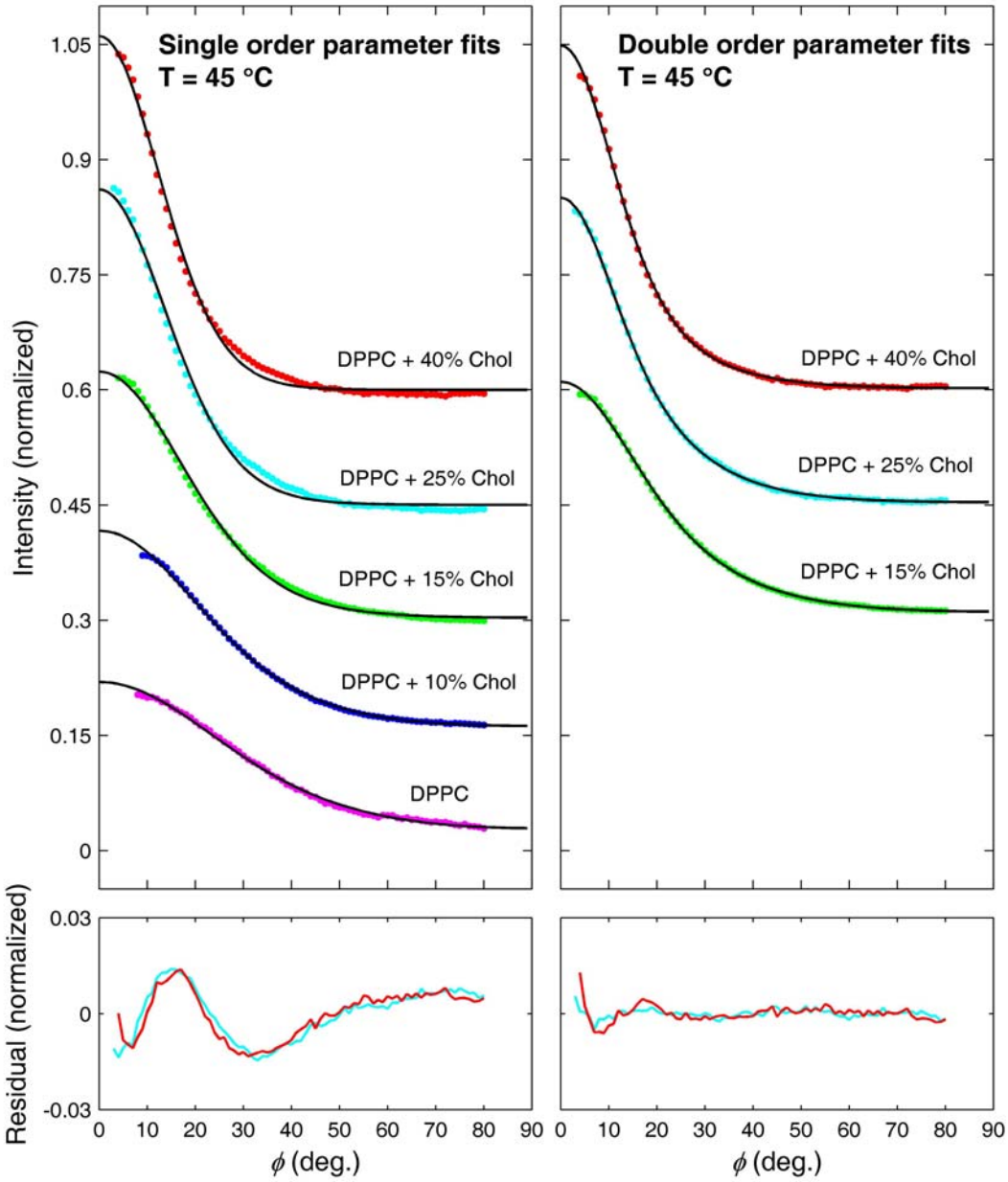


Figure 5.7. $I(\phi)$ plots at 45˚C for DPPC/cholesterol mixtures are shown by colored data points. Black lines are Maier-Saupe fits assuming one order parameter (left panel) and two order parameters (right panel) with representative residual plots for the fits to the DPPC + 25% cholesterol (cyan) and DPPC + 40% cholesterol (red) data shown beneath. Each plot is offset from the one below by 0.15 normalized intensity units. If the double order parameter fit is not shown, it gave the same value (to within 0.01 units) for both order parameters. (February 2006, D-1)

We will first attempt to explain why only one order parameter is necessary to fit the data for 1:1 DOPC/DPPC at 25˚C. Consideration of the flaws of the model as applied to coexisting gel and fluid phases will help with interpretation of the DPPC/cholesterol data. The Leadbetter model was developed to interpret the $I(\phi)$ data based on chain orientational disorder (Ch. 3). In gel phases, chain orientational order is high. The finite size of the chains will lead to an apparent angular spread, which dominates the $\phi$-width for the gel phase; however, the model neglects the form factor resulting from the finite size of the chains (see Section 3.2.5). Since the model is not applicable to highly ordered gel phases, we should not be surprised if the results of the fits to the $I(\phi)$ data are puzzling when the model is applied to a sample containing gel phase.

The DPPC/cholesterol data at 25˚C should be interpreted with caution because the $q$-widths of the wide angle scattering becomes significantly larger with the addition of cholesterol (see Table 5.1). This suggests a change from gel-like packing at low cholesterol contents to liquid-like packing at high cholesterol content. Although the Lo phase is more highly ordered than the Ld phase, there is still orientational disorder, particularly toward the ends of the chains (see Section 1.4.2). Therefore, the Leadbetter model is still applicable to the Lo phase (higher cholesterol content) but may not be applicable to the low-cholesterol (gel-phase) data.

Table 5.3 summarizes the results of the fits for the DPPC/cholesterol data. The DPPC + 10% cholesterol data are well fit by assuming a single order parameter. For cholesterol concentrations of 15%, 25%, and 40%, the data are not as well fit by assuming a single order parameter as for the DOPC/cholesterol data (see Ch. 4). However, the single order parameter fit does describe the data well in the steeply-changing low $\phi$ region (see Fig. 5.6), and the error on the $S_{mol}$ values are reasonable (<2% relative error; see Table 5.3). Similar fitting to $I(\phi)$ data using the Maier-Saupe

orientational distribution function has been observed for highly ordered smectic polymer liquid crystals. For $S_{mol}$>0.8, the fit to the polymer data is reasonable in the steeply changing low $\phi$ region, but underestimates the data at medium $\phi$ values and overestimates the data at large $\phi$ values (see Fig.7d in Davidson et al., 1995).

Table 5.3. Results of fits to $I(\phi)$ data for DPPC/cholesterol mixtures at 25˚C and 45˚C.

| T (˚C) | Mol% Chol | *m** | $S_{mol}$* | Phase Fractions | $R^2$ | Accept fit? |
|---|---|---|---|---|---|---|
| 25 | 10 | m= 8.79 ± 0.18 | S= 0.81 ± 0.01 | | 0.9985 | YES |
| | | m1=m2 | S1=S2=0.81 | NA | NA | NA |
| | 15 | m= 16.25 ± 0.72 | S= 0.90 ± 0.01 | | 0.9937 | ? |
| | | m1= 7.98 ± 0.77<br>m2= 28.9 ± 2.4 | S1= 0.79 ± 0.02<br>S2= 0.95 ± 0.01 | P1= 0.53 ± 0.04<br>P2= 0.47 ± 0.04 | 0.9994 | NO |
| | 25 | m= 22.7 ± 1.2 | S= 0.93 ± 0.01 | | 0.9911 | ? |
| | | m1= 5.80 ± 0.42<br>m2= 32.9 ± 0.8 | S1= 0.70 ± 0.02<br>S2= 0.95 ± 0.01 | P1= 0.37 ± 0.01<br>P2= 0.63 ± 0.01 | 0.9998 | NO |
| | 40 | m= 16.8 ± 0.8 | S= 0.91 ± 0.01 | | 0.9934 | ? |
| | | m1= 5.01 ± 0.73<br>m2= 23.8 ± 1.1 | S1= 0.65 ± 0.06<br>S2= 0.94 ± 0.01 | P1= 0.38 ± 0.02<br>P2= 0.62 ± 0.02 | 0.9995 | NO |
| 45 | 0 | m= 3.03 ± 0.11 | S= 0.44 ± 0.01 | | 0.9982 | YES |
| | | m1=m2 | S1= S2=0.44 | NA | NA | NA |
| | 10 | m= 4.29 ± 0.06 | S= 0.59 ± 0.01 | | 0.9995 | YES |
| | | m1= m2 | S1=S2=0.59 | NA | NA | NA |
| | 15 | m= 5.97 ± 0.13 | S= 0.71 ± 0.01 | | 0.9984 | YES |
| | | m1= 3.93 ± 0.57<br>m2= 10.5 ± 1.6 | S1= 0.55 ± 0.06<br>S2= 0.85 ± 0.03 | P1= 0.70 ± 0.08<br>P2= 0.30 ± 0.08 | 0.9998 | NO |
| | 25 | m= 9.11 ± 0.32 | S= 0.82 ± 0.01 | | 0.9957 | YES |
| | | m1= 5.28 ± 0.30<br>m2= 17.5 ± 1.1 | S1= 0.67 ± 0.02<br>S2= 0.91 ± 0.01 | P1= 0.65 ± 0.03<br>P2= 0.35 ± 0.03 | 0.9999 | NO |
| | 40 | m= 11.26 ± 0.37 | S= 0.86 ± 0.01 | | 0.9964 | YES |
| | | m1= 5.49 ± 0.87<br>m2= 17.0 ± 1.5 | S1= 0.68 ± 0.06<br>S2= 0.91 ± 0.01 | P1= 0.47 ± 0.05<br>P2= 0.53 ± 0.05 | 0.9995 | NO |

* If only one order parameter is given, the fit is to Eq. 3.29. If two order parameters are listed, the fit is to Eq. 3.32. If "m1=m2" or "S1=S2" are listed, this means these parameters were the same to within ±0.01.

In general, there is agreement in the literature that DPPC + 40% cholesterol is in a single Lo phase at 25˚C, and yet the single order parameter fit to these data are just as poor as the fits to the 15% and 25% cholesterol data (see the left residual plot in Fig. 5.6). DPPC + 15% cholesterol is in the middle of most phase diagrams claiming

gel/fluid coexistence. In the Vist and Davis two-phase region, 25% cholesterol is just outside the gel/fluid two-phase region, while the two-phase region extends to 30% cholesterol or more according to other researchers (Scheidt et al., 2005 and Huang et al., 1993).

Despite the imperfect single order parameter fits, we rejected the inferences from the good double order parameter fits for DPPC + 15%, 25%, and 40% cholesterol at 25˚C for the following two reasons:

1. Based on the polymer literature, we do not expect the single order parameter fits to work perfectly, particularly in the larger $\phi$ region, for very well-ordered systems ($S_{mol}$>0.8).
2. We should be cautious in interpreting data when the sample may contain gel phase.

In Table 5.3, "?" was put in the "Accept Fit?" column for DPPC + 15%, 25%, and 40% cholesterol because the model works poorly for well-ordered ($S_{mol}$>0.8) systems. Although we should be cautious in making quantitative comparisons, we can safely conclude that at 25˚C, DPPC chain orientational order is high at all cholesterol concentrations.

Figure 5.7 shows $I(\phi)$ plots as well as fits assuming one chain order parameter compared with fits assuming two order parameters for DPPC/cholesterol mixtures at 45˚C. The HWHM values are similar (~0.15 $Å^{-1}$) for all of these mixtures at 45˚C; therefore, these samples are liquid phases and the model is more applicable to these high-temperature data. In general, the data are better fit by assuming a single order parameter than at 25˚C. For the 25% and 40% cholesterol data, the fitted $S_{mol}$ values are high (0.82 and 0.86, respectively), and so we should not expect a perfect fit: these data are well fit in the low $\phi$ region but not as well in the high $\phi$ region. DPPC + 40% cholesterol and DPPC + 25% cholesterol are both in a single Lo phase at 45˚C

according to the Vist and Davis phase diagram, but DPPC + 25% cholesterol may be in the Ld/Lo two-phase region according to some phase diagrams (Scheidt et al., 2005). The DPPC + 15% cholesterol $I(\phi)$ data is well-fit by assuming a single order parameter. Although the phase diagrams of Vist and Davis (1990) and McMullen and McElhaney (1995) are very different, DPPC + 15% cholesterol at 45˚C is within the Ld/Lo phase coexistence region according to both diagrams. Fits to the $I(\phi)$ plots give no conclusive evidence of phase separation at 45˚C for the DPPC/cholesterol mixtures we examined.

An important test of the GIWAXS method for quantifying chain order is to reproduce the well-studied trend in chain order for DPPC/cholesterol as a function of cholesterol content. Ipsen et al. (1990) have calculated $S_{\text{mol}}$ from the Vist and Davis NMR average quadrupolar splitting ($M_1$, first moment data) using the following equation (Davis, 1979):

$$S_{\text{mol}} = 2\left\langle \left| S_{CD} \right| \right\rangle = 2 \times \frac{3\sqrt{3}}{4\pi} \frac{M_1}{\delta\nu_{\max}}, \tag{5.1}$$

where $2\delta\nu_{\max}$ is the maximum value of the quadrupolar coupling constant for a deuteron on a CH bond ($\delta\nu_{\max}$=125 kHz). Figure 5.8 compares the $S_{\text{mol}}$ values from GIWAXS with $S_{\text{mol}}$ values from a recent $^2$H NMR study which included a higher range of cholesterol concentrations than the study by Vist and Davis (Scheidt et al., 2005). At 45˚C, $S_{\text{mol}}$ increases monotonically as a function of cholesterol content and stops increasing rapidly at ~25% cholesterol. This high temperature behavior for chain order as a function of sterol concentration has also been observed for DPPC/ergosterol (Hsueh et al., 2005) and has been modeled theoretically for general sterol-phospholipid mixtures (McConnell and Radhakrishnan, 2006).

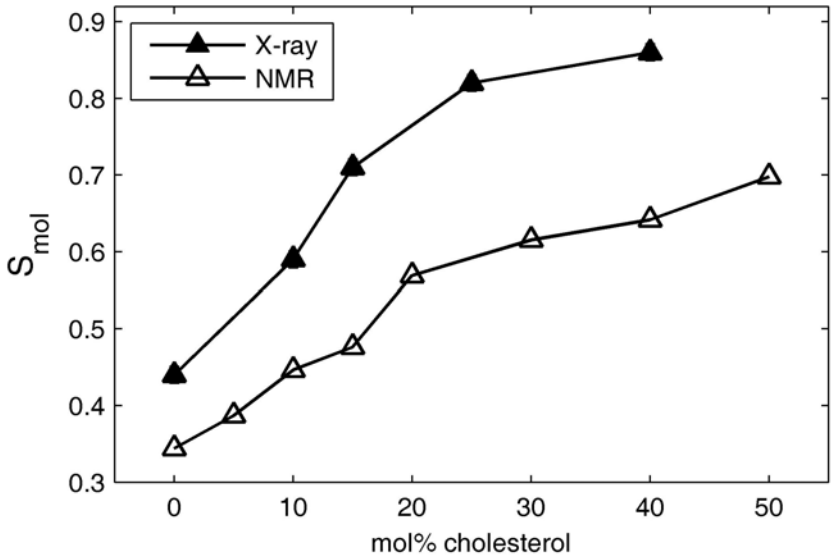


Figure 5.8. Comparison of x-ray and NMR order parameter data for DPPC/cholesterol mixtures: $S_{mol}$ vs. mol% cholesterol at 45˚C. NMR data are from Scheidt et al., 2005. The error bars for the x-ray $S_{mol}$ are all ± 0.01, and are covered by the symbols.

The trends in the data are in agreement, but the x-ray order parameters are higher compared with the NMR $S_{mol}$. The two methods make very different assumptions, and so this disparity in the $S_{mol}$ values is not surprising. A major difference between the two methods is that the x-ray analysis makes the assumption that the chains are infinitely long straight rods. In NMR, separate segmental order parameters are measured and then averaged.

At 25˚C (below $T_m$), changes in the angular distribution of scattering are small in comparison with those at 45˚C (above $T_m$) as the chains remain orientationally well-ordered as cholesterol is added at low temperatures. Although the effect is small, most studies agree that below $T_m$, cholesterol causes a decrease in phospholipid chain conformational and orientational order [Cortijo et al., 1982 (uses IR); Haberkorn et al., 1977 (uses $^2$H NMR)]. The first moment data of Scheidt et al. (2005) also indicate a

small decrease in DPPC chain order with the addition of cholesterol as the bilayer transitions from gel to Lo. Using NMR, Huang et al. (1993) report almost no change in DPPC chain orientational order as a function of cholesterol below $T_m$. Although chain orientational order remains high, the lateral positional order changes from gel-like to liquid-like, as shown by the increase in the $q$-width of the WAXS peak (see Fig. 5.2 and Table 5.1). However, the chains must remain orientationally well-ordered so that the phospholipid head groups can protect the cholesterol from water (see discussion of the "umbrella model" in Huang and Feigenson, 1999). We are hesitant to compare the x-ray $S_{mol}$ values for different cholesterol contents at 25˚C because the model may not apply to the lower cholesterol samples (gel phase), but our data indicate the chains remain orientationally well-ordered as a function of cholesterol content at 25˚C, in agreement with other studies.

## 5.6 Effects of hydration on DPPC/cholesterol phase behavior

The recent work of Karmakar et al. using x-ray diffraction on oriented DPPC/cholesterol multilayers shows that caution must be taken in comparing phase diagrams for fully-hydrated systems with those for systems below full hydration. In their first reports of DPPC/cholesterol phase behavior, the phase diagram includes a region of Lβ' phase coexisting with a ripple phase (see Fig. 5.9a and Karmakar and Raghunathan, 2003, 2005; Karmakar et al., 2005). This new Pβ phase is distinct from the ripple phase (Pβ') found in pure DPPC (and with small amounts of cholesterol) for a narrow temperature range just below $T_m$. (See Katsaras et al., 2000 for a discussion of ripple phases.) The researchers identified the Pβ phase from the off-$q_z$ axis "satellite" reflections in the lamellar repeat data, and they identify the region of Lβ'/Pβ coexistence by the appearance of two lamellar repeat peaks (Fig. 5.9B).

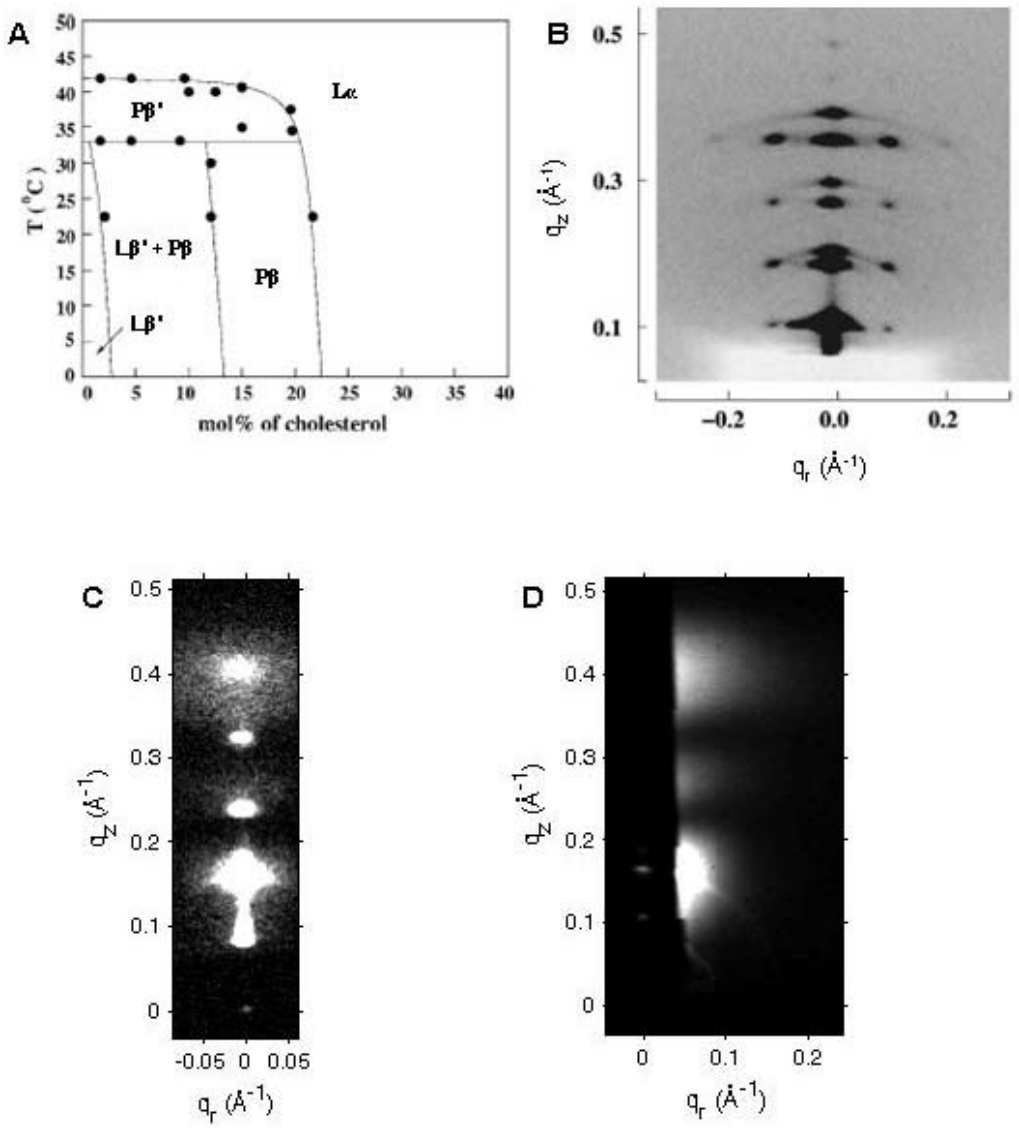


Figure 5.9. Comparison of our oriented sample data for DPPC/cholesterol with that of Karmakar et al. (A) Phase diagram for DPPC/Cholesterol at 98% relative humidity (RH) (Fig. 1a in Karmakar and Raghunathan, 2005). (B) Lamellar repeat diffraction data showing the coexistence of Lβ' and Pβ for DPPC + 10% cholesterol at 10˚C and 98% RH (Fig. 4a in Karmakar and Raghunathan, 2005). (C) Our DPPC + 10% cholesterol data at 25˚C has only one lamellar repeat. (D) No off-$q_z$ axis peaks are visible in our DPPC + 10% cholesterol data. (C) and (D) are scattering from the same sample but (C) is a short exposure to focus on the strong lamellar orders and (D) is a long exposure to focus on the weak off-specular reflections.

In contrast, we observed no evidence of two lamellar repeat spacings in our oriented data for DPPC + 10% cholesterol at 25˚C, in the Lβ'/Pβ coexistence region reported by Karmakar et al. (see Fig. 5.9C). Also, we did not observe off-$q_z$ axis reflections at any cholesterol concentration. In Fig. 5.9D, which covers the $q$ range where Karmakar et al. observed the off-$q_z$ axis reflections (q~0.1 $Å^{-1}$), only diffuse scattering is observed. Also, for cholesterol concentrations of 10% and above, we observed no evidence of the Lβ' phase. Figure 5.10 shows lamellar repeat data and wide-angle data for fully-hydrated MLVs at room temperature, ~25˚C (Unpublished data from the Feigenson lab taken at CHESS by J. T. Buboltz, J. Huang, and G. W. Feigenson). These powder data, taken at higher compositional resolution, confirm our results for oriented samples. The sharp peak at 1.48 $Å^{-1}$, characteristic of the Lβ' phase, disappears by 7% cholesterol (Fig. 5.10A). Only one lamellar repeat spacing was observed at all cholesterol concentrations (Fig. 5.10B), in agreement with Ladbrooke et al. (1968). The lamellar repeat increases dramatically at low concentrations, which has been explained by thickening of the bilayer due to the loss of chain tilt and increased hydration (Ladbrooke et al., 1968; McIntosh, 1978).

Although their data were taken at 98% relative humidity (RH), Karmakar et al. compared their phase diagram with the Vist and Davis phase diagram for fully hydrated DPPC/cholesterol mixtures (Karmakar and Raghunathan, 2003, 2005; Karamakar et al., 2005). They attempt to explain why the Pβ phase was not observed previously. In their most recent paper on this system, Karmakar et al. (2006) report results for DPPC/cholesterol mixtures at 100% RH, which agree with our findings: their x-ray diffraction measurements do not show any evidence of phase separation (only one lamellar repeat) and the Lβ' phase disappears by ~5 mol% cholesterol. This is a good example of the caution that must be taken in comparing phase diagrams for systems at different levels of hydration.

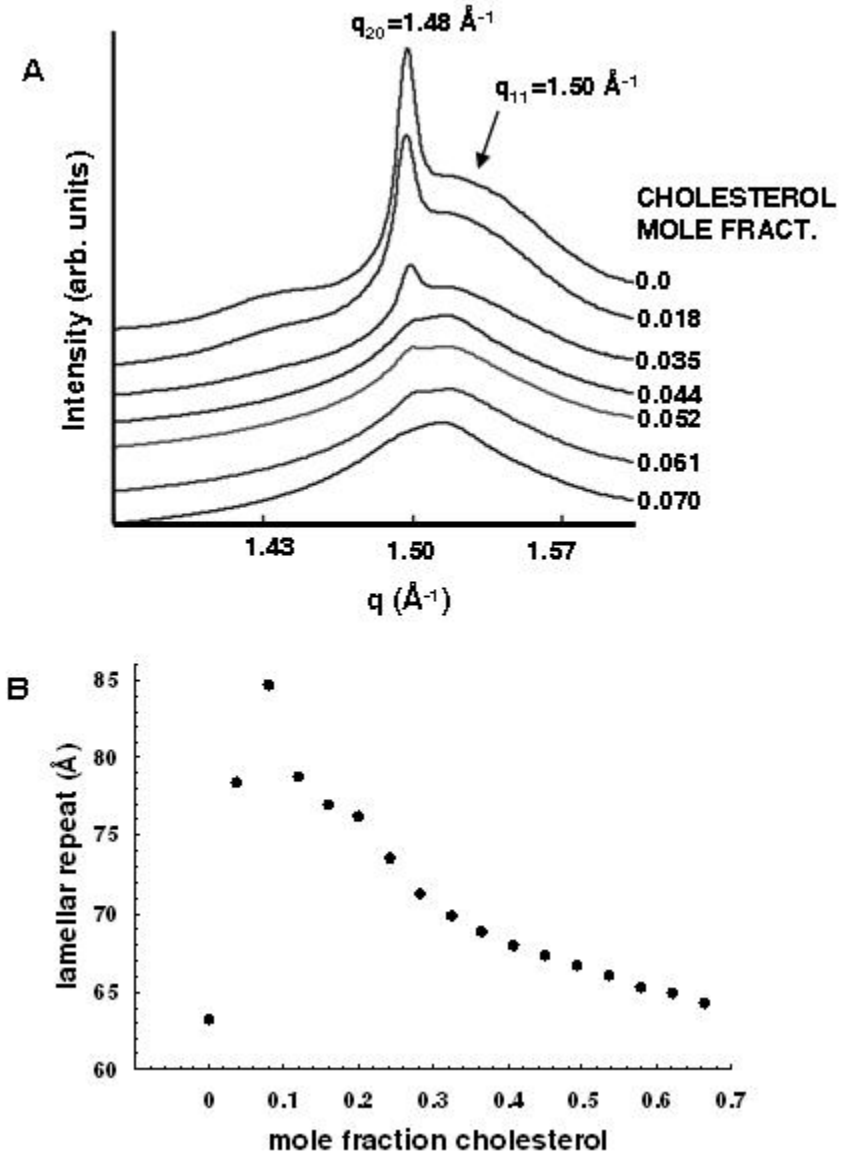


Figure 5.10. (A) Wide-angle $I(q)$ data for MLV samples of DPPC/cholesterol mixtures showing the disappearance of the characteristic scattering from Lβ'. (B) Lamellar repeat data for DPPC/cholesterol MLV samples as a function of the mole fraction of cholesterol. These are unpublished data collected by J. T. Buboltz, J. Huang, and G. W. Feigenson.

## 5.7 Effect of equilibration on DPPC/cholesterol phase behavior

In addition to hydration, temperature equilibration time can have a large effect on lipid phase behavior, especially when gel phases, with slow lateral diffusion, are involved. For example, Mortensen et al. (1988) observed very different low-temperature phase behavior for deuterated DMPC/cholesterol mixtures after storage at 5˚C for months compared with the phase behavior observed just after preparation and after annealing at 30˚C.

Figure 5.11 shows our x-ray lamellar diffraction data for DPPC/cholesterol MLV samples. After annealing the bulk sample at high temperature and then loading into a capillary (see Section 2.4.1), a small second first order peak was observed at 25˚C in the DPPC + 10% cholesterol sample (Fig. 5.11A). The diffuse scattering between rings could be due to etiher incomplete equilibration or stacking disorder due to frustrated packing of the MLVs. At 45˚C, only one lamellar repeat with sharp rings was observed (Fig. 5.11B). After the capillary was cooled back down to 25˚C, the diffuse scattering remained but the second peak disappeared (Fig. 5.11C). For DPPC + 25% cholesterol (Fig. 5.11E), the second order lamellar peak was split even after cycling the temperature to 45˚C twice. Only one lamellar repeat was observed for DPPC + 15% cholesterol and DPPC + 40% cholesterol (Fig. 5.11D and F). The diffuse scattering between rings in the DPPC + 10% cholesterol and 25% cholesterol data at 25˚C is evidence that these samples were not completely equilibrated despite annealing of the bulk sample and temperature cycling of the capillary (see Fig. 5.11A,C, and E). These temperature-dependent observations were reproduced with a second set of MLV samples. In contrast to the powder sample data, we only observed a single lamellar repeat for all the DPPC/cholesterol oriented samples. The data show that thermal history and sample preparation have large effects on equilibration of DPPC/cholesterol mixtures at low temperature.

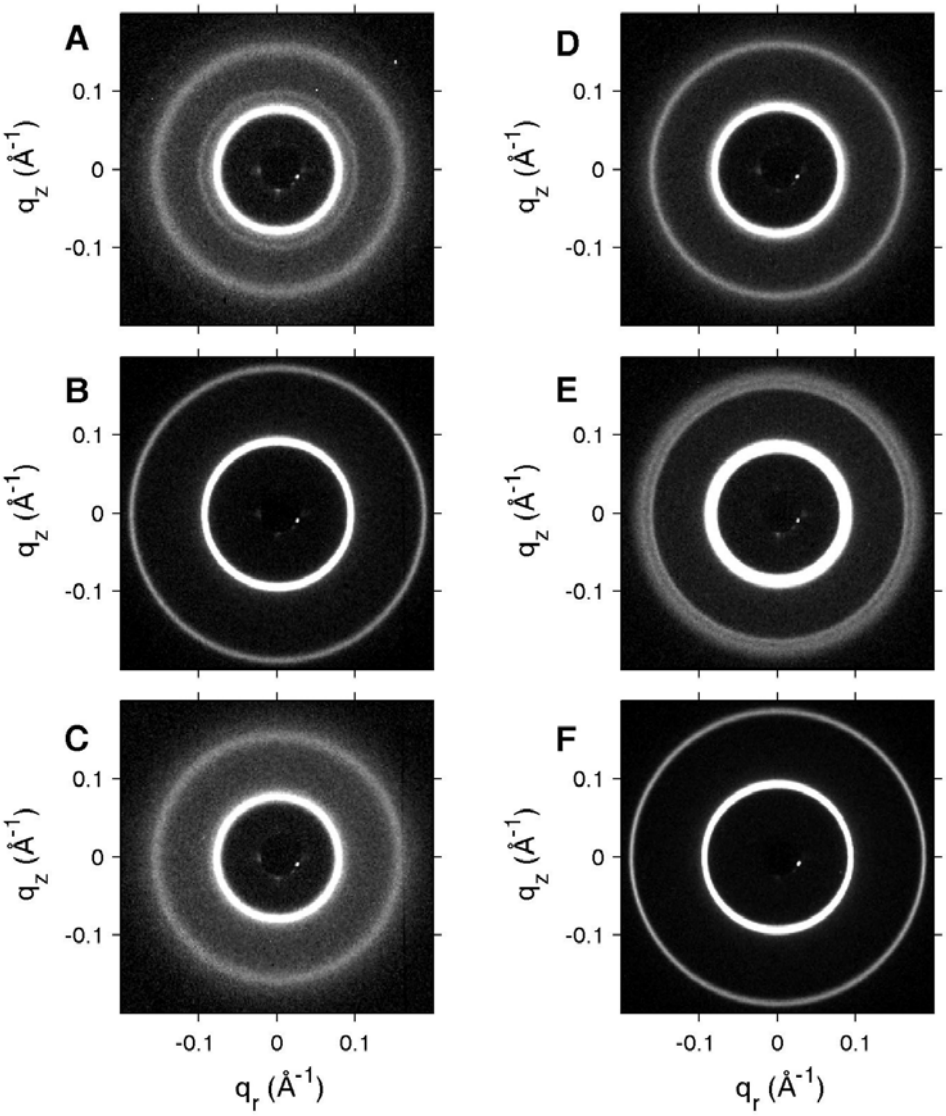


Figure 5.11. Lamellar diffraction data from capillary MLV DPPC/cholesterol mixtures showing the first two orders of diffraction (data taken on rotating anode). (A) DPPC + 10% cholesterol at 25˚C after loading into the capillary (the bulk sample was annealed from high temperature); the two lamellar repeats are 80.7 Å (strong) and 63.8 Å (weak). (B) DPPC + 10% cholesterol at 45˚C; the single lamellar repeat is 67.4 Å. (C) DPPC + 10% cholesterol at 25˚C after the capillary was cooled down from 45˚C; the lamellar repeat is 80.5 Å and the second weak first order ring visible in (A) is gone. (D) DPPC + 15% cholesterol at 25˚C after loading into the capillary; the single lamellar repeat is 78.1 Å. (E) The second order diffraction from DPPC + 25% cholesterol has two rings even after cycling the temperature to 45˚C twice; the repeat spacings are 72.6 Å and 77.1 Å. (F) DPPC + 40% cholesterol at 25˚C immediately after loading into the capillary; the single lamellar repeat is 67.4 Å.

In previous x-ray measurements made in the Feigenson lab, rapid solvent exchange (RSE) or low-temperature trapping (lyophilization from chloroform) was used to prepare MLV samples (Huang et al., 1999). The data presented in Fig. 5.10B were from samples prepared by rapid solvent exchange. For these samples, only a single lamellar repeat was observed at 25˚C for DPPC with 0-66% cholesterol (66% is the solubility limit of cholesterol in DPPC). Rapid solvent exchange and low-temperature trapping are advantageous because they give reproducible results for the maximum solubility of cholesterol in lipid bilayers, evidence that there is thorough mixing of the cholesterol and phospholipid. Complete mixing of components is often a problem with other methods, such as adding excess water to a dried lipid film followed by freeze/thaw (the method used for the MLV data presented in Fig. 5.11). However, we chose to use the freeze/thaw method instead of rapid solvent exchange because this technique is only suitable for low lipid:water ratios (~1 mg/mL). Although DPPC can be concentrated by ultracentrifugation, mixtures containing DOPC (low density lipid) and pure water cannot be concentrated; we wanted to use the same method for all of our MLV samples.

Some reports indicate two lamellar repeats for DPPC/cholesterol mixtures at low cholesterol concentration and at low temperature. Rand et al. (1980) report two lamellar repeat spacings for DPPC with ~3-10% cholesterol at temperatures below 30˚C. Meyer et al. (1997) report similar behavior for DPPC/cholesterol mixtures annealed at 4˚C for weeks to months. Interestingly, the observation of double lamellar repeat spacings is in the single phase (pure gel) portion of the Vist and Davis phase diagram. In most of the Vist and Davis two-phase coexistence region (~7.5-22% cholesterol), Rand et al. (1980) and Meyer et al. (1997) observed a single lamellar repeat.

Although Karmakar et al. do not observe two lamellar repeat spacings for DPPC/cholesterol bilayers in excess water, they do report coexisting gel and fluid domains in fluorescence micrographs of GUVs of DPPC with 5-10% cholesterol at 23˚C; they only observe domains when the GUVs are less than 20 μm in size (Karmakar et al., 2005). According to other reports, GUVs composed of binary mixtures of DPPC and cholesterol are uniform (Veatch and Keller, 2003b; Feigenson and Buboltz, 2001). Fluorescence microscopy of GUVs can be problematic when gel phases are involved, especially if only one dye is used, the case with the data of Karmakar et al. In two-dye imaging of two-component mixtures (e.g. DLPC/DPPC or DOPC/DSPC), the Feigenson lab has on occasion observed three domains, in violation of the Gibbs phase rule (G. W. Feigenson and J. Zhao, personal communication). In such pictures, two of the domains are bright (one labeled by a gel-preferring probe and the other labeled by an Ld-preferring probe) and one domain is black. G. W. Feigenson believes the black domains are kinetic artifacts. If only a single, Ld-preferring probe is used, the black domains cannot be distinguished from the dark gel phase domains. In what appears to be a violation of the Gibbs phase rule if the samples were at equilibrium, Li and Cheng (2006) have interpreted three coexisting domains (one black and two fluorescently labeled) as evidence of two types of gel phase coexisting with the Ld phase for binary DOPC/DPPC or DLPC/DPPC mixtures.

Such observations from x-ray diffraction and fluorescence microscopy show that caution must be taken in interpreting results for lipid systems in which gel phases are involved. Kinetic artifacts and changes in phase behavior after long equilibration can make comparing the data from different experiments problematic.

## 5.8 What can we learn about DPPC/cholesterol phase behavior from x-ray experiments?

As with other techniques, there are many discrepancies in the x-ray literature concerning binary mixtures of phospholipids and cholesterol. We have made the following observations concerning DPPC/cholesterol phase behavior:

1. Two $d_L$-spacings were not observed at any cholesterol concentration in oriented samples. The lamellar repeat spacing data for MLV samples at low temperature were dependent on thermal history.
2. Two $d_{cc}$-spacings were not observed in the GIWAXS data at any cholesterol concentration at either 25˚C or 45˚C.
3. At 45˚C, the $I(\phi)$ data can be described by a single order parameter fit. Because our model should not be applied to cases of gel/fluid coexistence, we cannot make conclusions about the $I(\phi)$ data at 25˚C.

Based on our x-ray data, we observe no evidence of phase coexistence in DPPC/cholesterol mixtures.

There are discrepancies in the x-ray diffraction literature for temperatures below $T_m$ (discussed earlier and summarized here). There are some reports of phase coexistence below $T_m$ based on the observation of two lamellar repeat spacings or two chain-chain correlation ($d_{cc}$) spacings. Meyer et al. (1997) and Rand et al. (1980) report two lamellar repeat spacings for DPPC with 3-10% cholesterol, in a range assigned to a single gel phase by Vist and Davis (1990). For mixtures containing 20%-33% cholesterol at 20˚C, Engelman and Rothman (1972) observed two wide-angle diffraction bands, one sharp line ($d_{cc}$=4.15 Å) and one diffuse band ($d_{cc}$=4.7 Å), which they interpret as evidence of gel/fluid phase coexistence.

In other reports, there is no evidence of phase separation based on the lamellar repeat or wide angle x-ray data. For DPPC with 0%-50% cholesterol at 25˚C,

Ladbrooke et al. (1968) only observed a single lamellar repeat spacing. In the wide-angle region, Ladbrooke et al. observed only a single wide-angle peak for cholesterol concentrations of 7.5%-50%, which continuously changes from a sharp peak at 7.5% ($d_{cc}$ =4.2 Å) to a broad peak at 50% cholesterol ($d_{cc}$ =4.45 Å). For their measurements on DPPC/cholesterol oriented samples at full hydration, Karmakar et al. (2006) report no evidence of phase separation from x-ray diffraction. They conclude that they did not observe a gel/fluid coexistence region because their steps along the composition axis were coarse (~2.5% cholesterol). This reasoning makes no sense because the postulated two-phase region is much larger than their compositional steps (~7.5%-22% cholesterol according to Vist and Davis, 1990). Many experiments reporting phase coexistence, including Vist and Davis, use even fewer data points. Hui and He (1983), Needham et al. (1988), and Finean (1990) observed only one lamellar repeat and one wide-angle band for DMPC/cholesterol mixtures, which are thought to have similar phase behavior to DPPC/cholesterol. Although they do not observe evidence of phase coexistence, Hui and He (1983) and Finean (1990) observe a change in behavior of the lamellar repeat data at 20%-30% cholesterol, where the spacings above and below $T_m$ merge. Researchers have also observed abrupt changes in other physical properties at 20% cholesterol, including the lateral diffusion coefficients (Rubenstein et al., 1979). Hui and He (1983) and Finean (1990) interpret their x-ray data in terms of complex formation instead of phase separation. We cannot comment on the abrupt change at 20% cholesterol because our data were not taken at high enough temperature and compositional resolution.

Our null results based on x-ray measurements for phase coexistence in DPPC/cholesterol mixtures are important in the context of other mixtures, where we do observe evidence of gel/fluid or fluid/fluid phase coexistence. In 1:1 DOPC/DPPC, we observed two wide-angle diffraction bands, one broad (fluid-like) and one narrow

(gel-like). In the next chapter, we report data for ternary mixtures of DOPC, DPPC, and cholesterol. In a region of known fluid-fluid coexistence, these mixtures have two lamellar repeat spacings (reproducible with no thermal hysteresis). In addition, the $I(\phi)$ data is best described by a two-order parameter fit for the ternary mixtures (see Ch. 6). In contrast to DPPC/cholesterol mixtures, for which fluorescence images of GUVs are uniform, fluorescence microscopy shows direct evidence of gel/fluid coexistence in binary DOPC/DPPC mixtures and fluid/fluid coexistence in ternary mixtures (Veatch and Keller, 2003b).

If mixtures of DPPC/cholesterol do phase-separate, why are the experimental observations so different from other cases of gel/fluid (e.g. binary DOPC/DPPC mixtures) or fluid/fluid (e.g. ternary DOPC/DPPC/cholesterol mixtures) phase coexistence? In the case of gel/fluid coexistence, we could make the argument that phase behavior is very dependent on equilibration time and that is why we did not observe evidence of gel/fluid coexistence in DPPC/cholesterol mixtures. Yet, gel/fluid coexistence was clear in the GIWAXS data for 1:1 DOPC/DPPC, which underwent the same annealing and equilibration steps as the DPPC/cholesterol mixtures.

Evidence from other methods (DSC, NMR, ESR, FRET, etc.) indicate that DPPC/cholesterol, and other binary phospholipid/cholesterol mixtures, do not behave as ideal mixtures (see Section 5.1). While phase coexistence is a popular interpretation of the experimental observations, other models have been proposed for DPPC/cholesterol interactions. McConnell et al. explain the high-temperature spectroscopic data by the formation of condensed complexes between phospholipids and cholesterol (McConnell and Radhakrishnan, 2006; McConnell and Vrljic, 2003). Based on the umbrella model of microscopic interactions of cholesterol with phospholipids (Huang and Feigenson, 1999), G. W. Feigenson and J. Huang have

postulated that cholesterol causes small-scale defects in the bilayer in which the physical properties of the phospholipids neighboring the cholesterol are changed (unpublished manuscript entitled "Continuous phase changes: a new picture of cholesterol/dipalmitoylphosphatidylcholine mixing in aqueous bilayers"). The region affected by Huang and Feigenson's cholesterol defects or McConnell's condensed complexes would have different spectroscopic signals than the surrounding region, explaining why the NMR or ESR data appears to be a superposition of two signals.

Consideration of the interactions between phospholipids and cholesterol naturally leads to the following question: if phase separation exists in binary phospholipid/cholesterol mixtures, what is the driving force? The umbrella model emphasizes the repulsive nature of cholesterol-cholesterol interactions. Cholesterol has too small a headgroup to cover its hydrophobic part, and so cholesterol would prefer to be neighboring phospholipids than other cholesterol molecules. The condensed complex model emphasizes an attractive interaction between cholesterol and saturated lipids. Both models predict nonideal mixing for phospholipid/cholesterol mixtures because cholesterol disrupts the phospholipid packing.

In both the umbrella model and the condensed complex model, it is unclear why a cholesterol-rich phase would form. In binary mixtures of DOPC (a low melting lipid) and DPPC (a high melting lipid), like-like interactions are favorable, explaining why these mixtures phase separate into a DOPC-rich liquid phase and a DPPC-rich gel phase below the $T_m$ of DPPC. In ternary mixtures of DOPC, DPPC, and cholesterol, several interactions are important: the unfavorable interaction between DOPC and DPPC, the unfavorable interaction between cholesterols, and the preferential interaction between cholesterol and DPPC (saturated phospholipid). In order to model liquid-liquid immiscibility in ternary mixtures, Radhakrishnan and McConnell (2005)

needed to add the unfavorable DOPC-DPPC interaction to the condensed complex model. If cholesterol-DPPC interactions are more favorable than cholesterol-cholesterol interactions, true for both the condensed complex model and umbrella model, it is unclear why DPPC and cholesterol would phase-separate. In order for the mixture to phase-separate, other interactions must be important: Ipsen et al. (1987) have modeled phase separation in DPPC-cholesterol by treating the system as a pseudoternary mixture of cholesterol, chain-disordered DPPC, and chain-ordered DPPC. Sankaram and Thompson (1990) propose a similar model in which the length mismatch between the cholesterol and phospholipid lead to two populations of chains, one shorter and one longer.

Models and experiments all point to the complicated nature of cholesterol-phospholipid interactions: if binary lipid/cholesterol mixtures were simple and well-behaved, there would be agreement. Discrepancies in the x-ray literature concern the low temperature region of the phase diagram. If any more experiments were to be done in this portion of the phase diagram, powder samples, not oriented samples, should be used for the following reasons:

1. If gel-fluid phase coexistence is present, there should be two reproducible wide-angle peaks in the powder x-ray $I(q)$ data.
2. Keeping oriented samples at full hydration for long time periods (days-months) is difficult. As described in Section 5.7, the low temperature region is particularly problematic because gel phases, which require long equilibration times, are involved. If further experiments were done to explain the x-ray literature discrepancies, they should involve a careful investigation of the effects of equilibration time.

In addition to equilibration time, experimental factors of possible importance are hydration and temperature cycling (annealing protocol). Much powder x-ray data,

especially wide-angle data, are taken on samples with a 1:1 (v/v) water/lipid ratio, which is close to the minimum required for full hydration (Lecuyer and Dervichian, 1969). In our experience, mixing is very difficult in such highly viscous samples; incomplete mixing, which affects hydration, may help explain some of the discrepancies. Systematically separating out the effects of these experimental variables (equilibration time, hydration, annealing protocol, etc.) would require great patience, and may not fully explain all the discrepancies in the literature.

## 5.9 Conclusion

We have evaluated our x-ray data in terms of the following criteria for phase coexistence: observation of two wide-angle spacings, observation of two lamellar repeats, or necessity of two chain order parameters to fit the $I(\phi)$ data. We observed no evidence of phase coexistence in DPPC/cholesterol mixtures below or above the DPPC $T_m$ using x-ray diffraction. Below $T_m$, there are discrepancies in the x-ray literature: some report evidence of solid-liquid coexistence (Engelman and Rothman, 1972), while others report no evidence of phase separation (Ladbrooke et al., 1968). Because of the difficulties in equilibration when gel phases are involved, sorting out these discrepancies would be a difficult undertaking.

Our null result for phase coexistence in DPPC/cholesterol is interesting in comparison to other mixtures, where we do find evidence of phase coexistence in the x-ray scattering data. In 1:1 DOPC/DPPC at 25˚C, two wide-angle peaks are evidence of gel/fluid coexistence. In ternary DOPC/DPPC/cholesterol mixtures (see Ch. 6) known to phase separate into coexisting Ld and Lo domains, we observed two lamellar repeats and a double order parameter fit was required to fit the $I(\phi)$ data. Unlike DPPC/cholesterol, in these systems phase coexistence has been previously observed by fluorescence microscopy (Veatch and Keller, 2003b).

We also used our DPPC/cholesterol data to calibrate our method for quantifying chain order in model membranes using GIWAXS and the fitting model presented in Ch. 3. The trends in $S_{mol}$ calculated from the x-ray data agree well with trends in chain order measured by $^2$H NMR for DPPC/cholesterol mixtures at 45˚C. Also, we have determined that the model for fitting the $I(\phi)$ data should not be applied (or at least very cautiously interpreted) if gel phase may be present. As gel/fluid coexistence should be evident by two non-overlapping wide angle peaks (in oriented or powder samples), this is not a major limitation.

# Chapter 6 - A new approach using GIWAXS for studying Ld/Lo phase coexistence

## 6.1 Introduction

In 2002 Gandhavadi et al. reported a single lamellar repeat spacing in MLVs composed of 1:1:1 DOPC/brain sphingomyelin (BSM)/cholesterol; they concluded that their x-ray scattering results showed no evidence of three-dimensional phase separation in this mixture. Since Dietrich et al. (2001) reported macroscopic liquid-liquid coexistence in this same mixture using fluorescence microscopy imaging of GUVs, many experimenters have used microscopy to examine Ld/Lo phase coexistence in model membrane systems. The discrepancy between the x-ray work of Gandhavadi et al. and the fluorescence microscopy results of Dietrich et al. is particularly relevant at this time because of recent work documenting the artifacts with fluorescent probes in model membrane systems (Ayuyan and Cohen, 2006; Veatch et al., 2007a; Zhao et al., 2007b).

Since x-ray scattering requires no probe, evidence of liquid-liquid coexistence using this technique could be particularly illuminating, even for a well-studied mixture like DOPC/DPPC/cholesterol. Our GIWAXS experiments on oriented samples and lamellar repeat spacing measurements on MLVs both indicate the presence of phase coexistence for mixtures of DOPC/DPPC/cholesterol previously shown to exhibit Ld/Lo coexistence by fluorescence microscopy and NMR (Veatch and Keller, 2003b; Veatch et al., 2004; Veatch et al., 2007b). This chapter is devoted to these x-ray results and a comparison to the NMR and fluorescence microscopy results of Veatch et al.

## 6.2 GIWAXS results for ternary mixtures

In Chapters 4 and 5, we showed that GIWAXS on oriented lipid samples, unlike powder WAXS, can be used to distinguish the Lo phase from the Ld phase. The Lo phase has a narrower angular ($\phi$) distribution of scattering. We also showed that we can quantitatively relate the angular distribution of scattering to the chain orientational distribution to obtain the average chain order parameter, $S_{mol}$, for model membrane systems. This section presents our GIWAXS data for ternary mixtures of DOPC/DPPC/cholesterol. For these mixtures at low temperatures, two distributions of chains (two values of $S_{mol}$) are needed to fit the GIWAXS data, providing evidence of phase coexistence. Also, the order parameters give physical information about the coexisting phases.

### 6.2.1 2D diffraction images: liquid-liquid coexistence not visually apparent

Figures 6.1-6.4 show 2D diffraction data for the four ternary mixtures we studied which are in a liquid-liquid coexistence region at low temperature (1:1 DOPC/DPPC + 15%, 20%, 25%, and 30% cholesterol). From the diffraction data, as the temperature is increased, the angular ($\phi$) distribution of scattering widens. Fluorescence microscopy and NMR results indicate that the miscibility transition temperature, $T_{mix}$, for these mixtures is near 30˚C (Veatch and Keller, 2003b). Below this temperature, there are coexisting Ld and Lo phases. However, the presence of two coexisting phases is not obvious from the GIWAXS images taken at 15˚C and 25˚C. This result is expected, as scattering from coexisting Ld and Lo phases is likely to overlap. In Section 6.2.3, we will show that the GIWAXS data for these mixture at 15˚C and 25˚C can be deconvolved into scattering from two different distributions of chains.

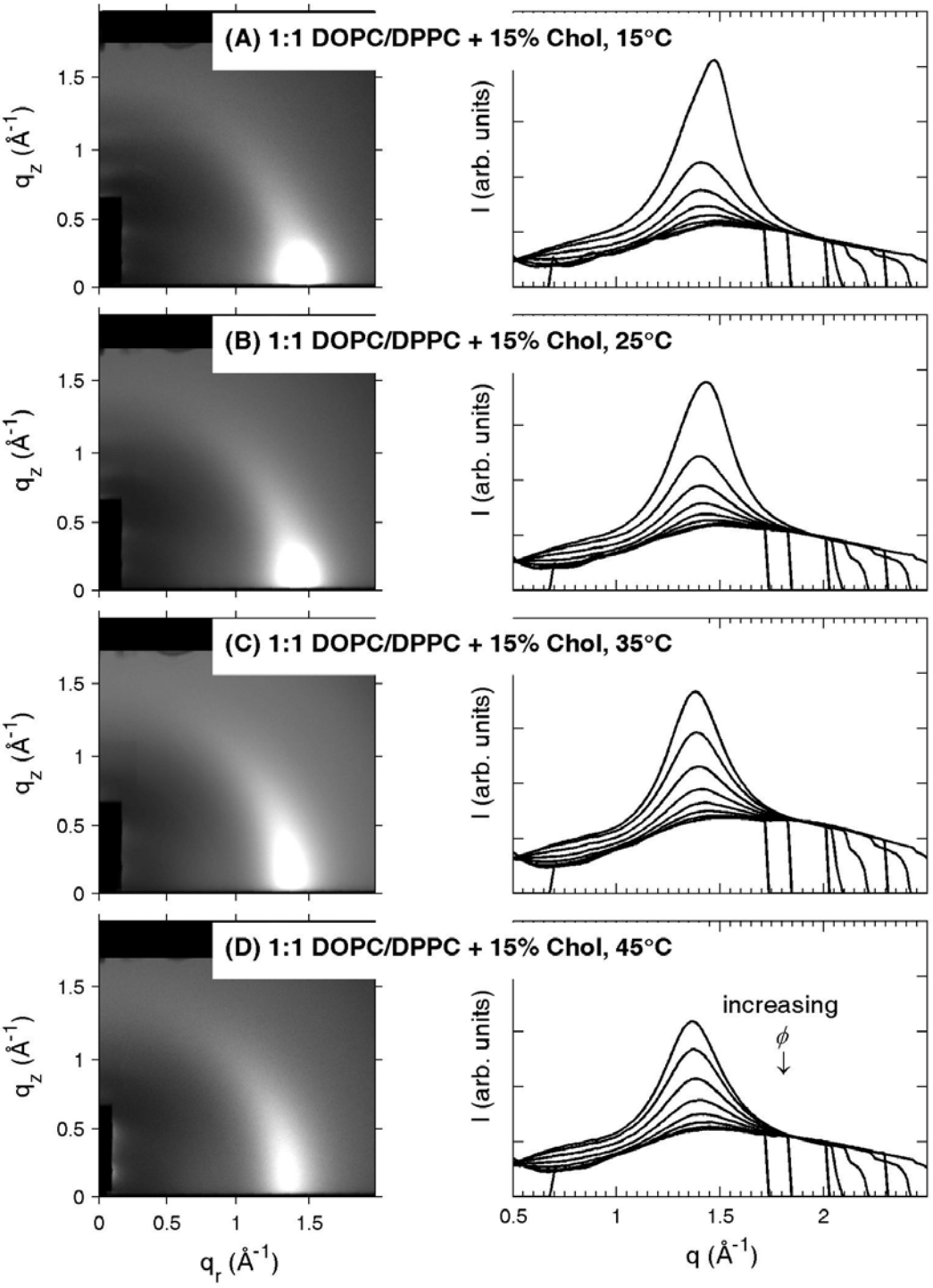


Figure 6.1. Left column shows 2D GIWAXS images for 1:1 DOPC/DPPC + 15% cholesterol at the following temperatures: (A) 15˚C; (B) 25˚C; (C) 35˚C; (D) 45˚C. The right column shows the corresponding $I(q)$ sector plots (see Section 2.3.7.3). The top trace corresponds to the smallest $\phi$ range. (October 2006, G-1)

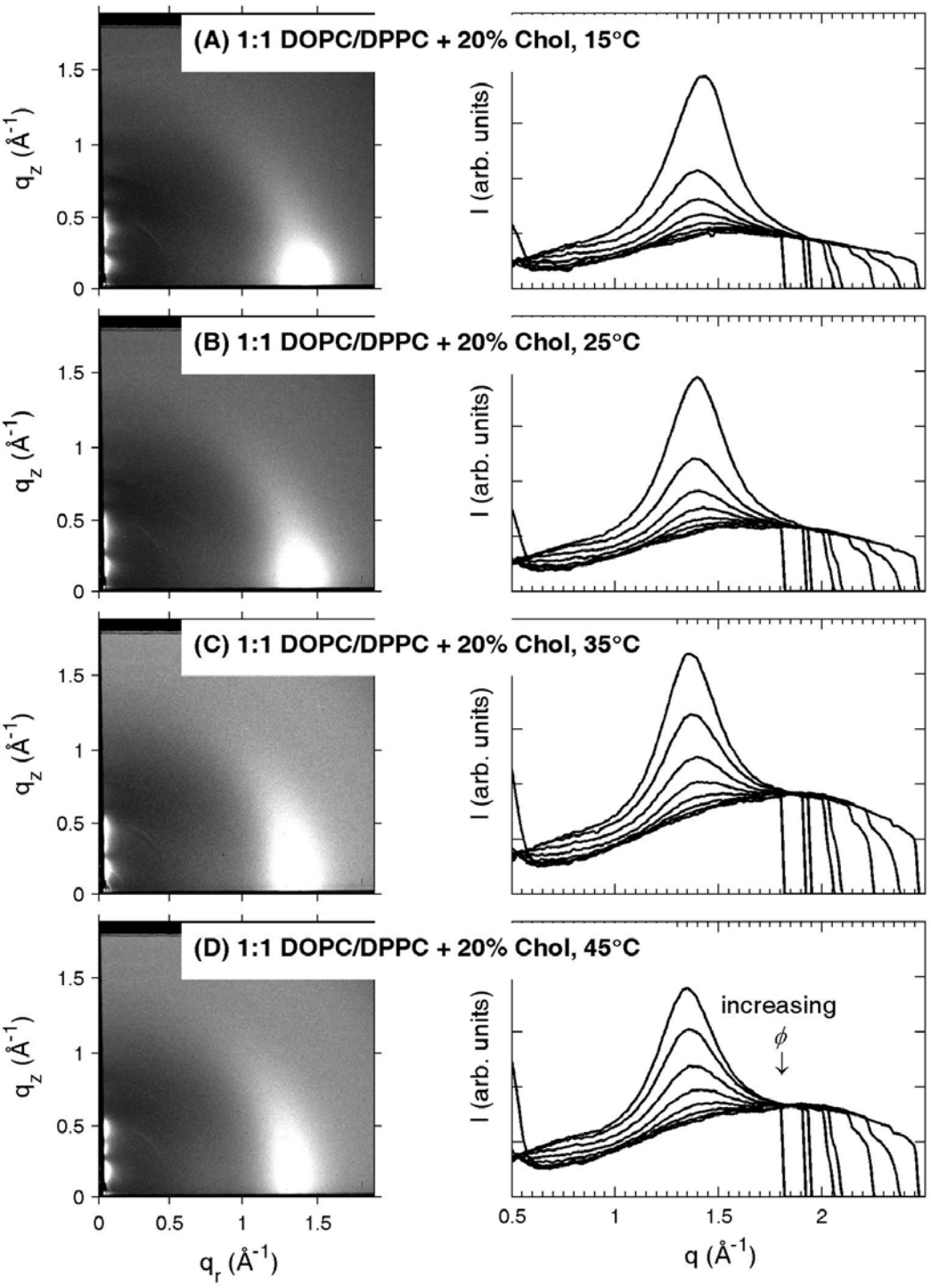


Figure 6.2. Left column shows 2D GIWAXS images for 1:1 DOPC/DPPC + 20% cholesterol at the following temperatures: (A) 15˚C; (B) 25˚C; (C) 35˚C; (D) 45˚C. The right column shows the corresponding $I(q)$ sector plots (see Section 2.3.7.3). The top trace corresponds to the smallest $\phi$ range. (February 2006, D-1)

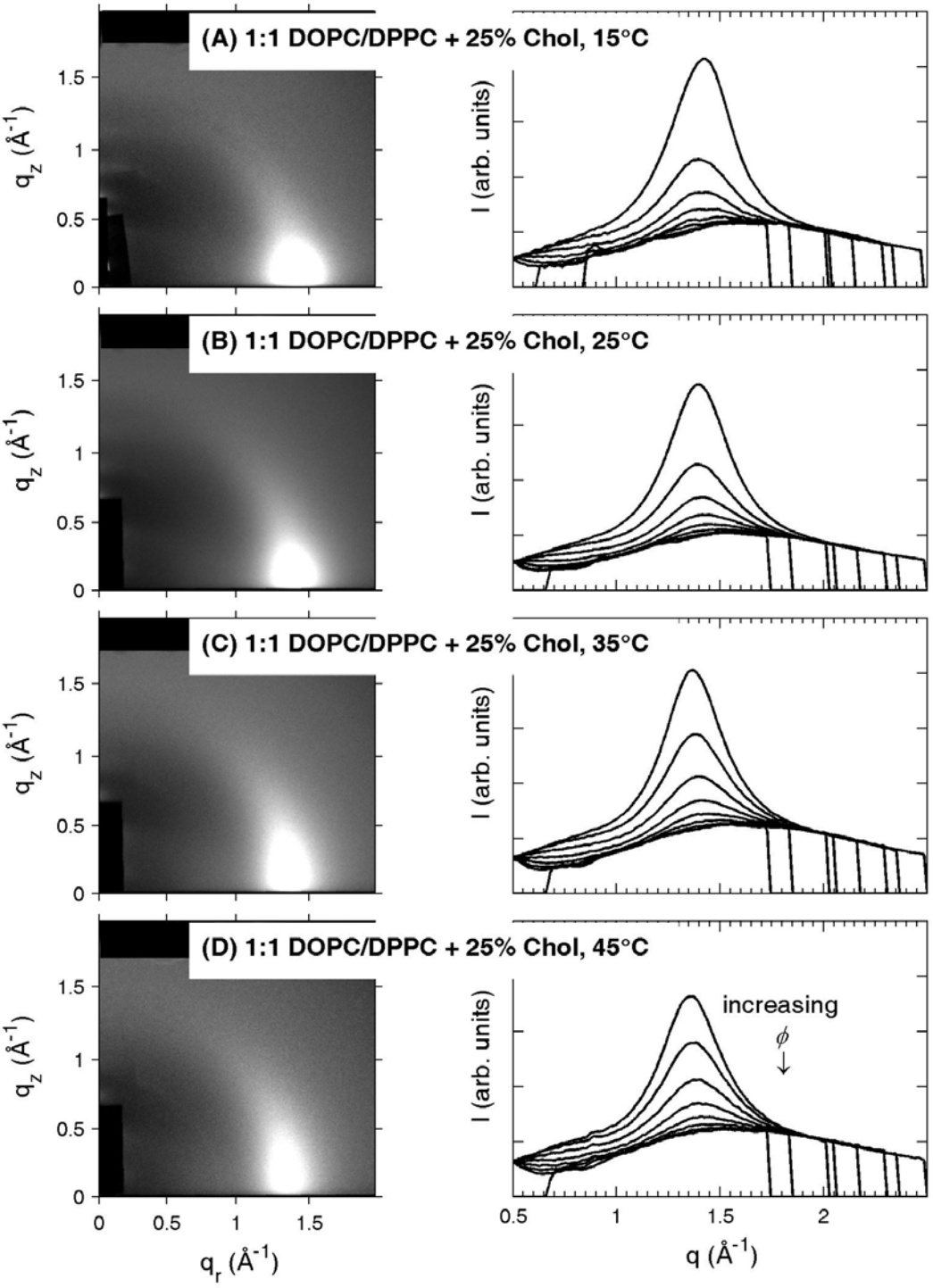


Figure 6.3. Left column shows 2D GIWAXS images for 1:1 DOPC/DPPC + 25% cholesterol at the following temperatures: (A) 15˚C; (B) 25˚C; (C) 35˚C; (D) 45˚C. The right column shows the corresponding $I(q)$ sector plots (see Section 2.3.7.3). The top trace corresponds to the smallest $\phi$ range. (October 2006, G-1)

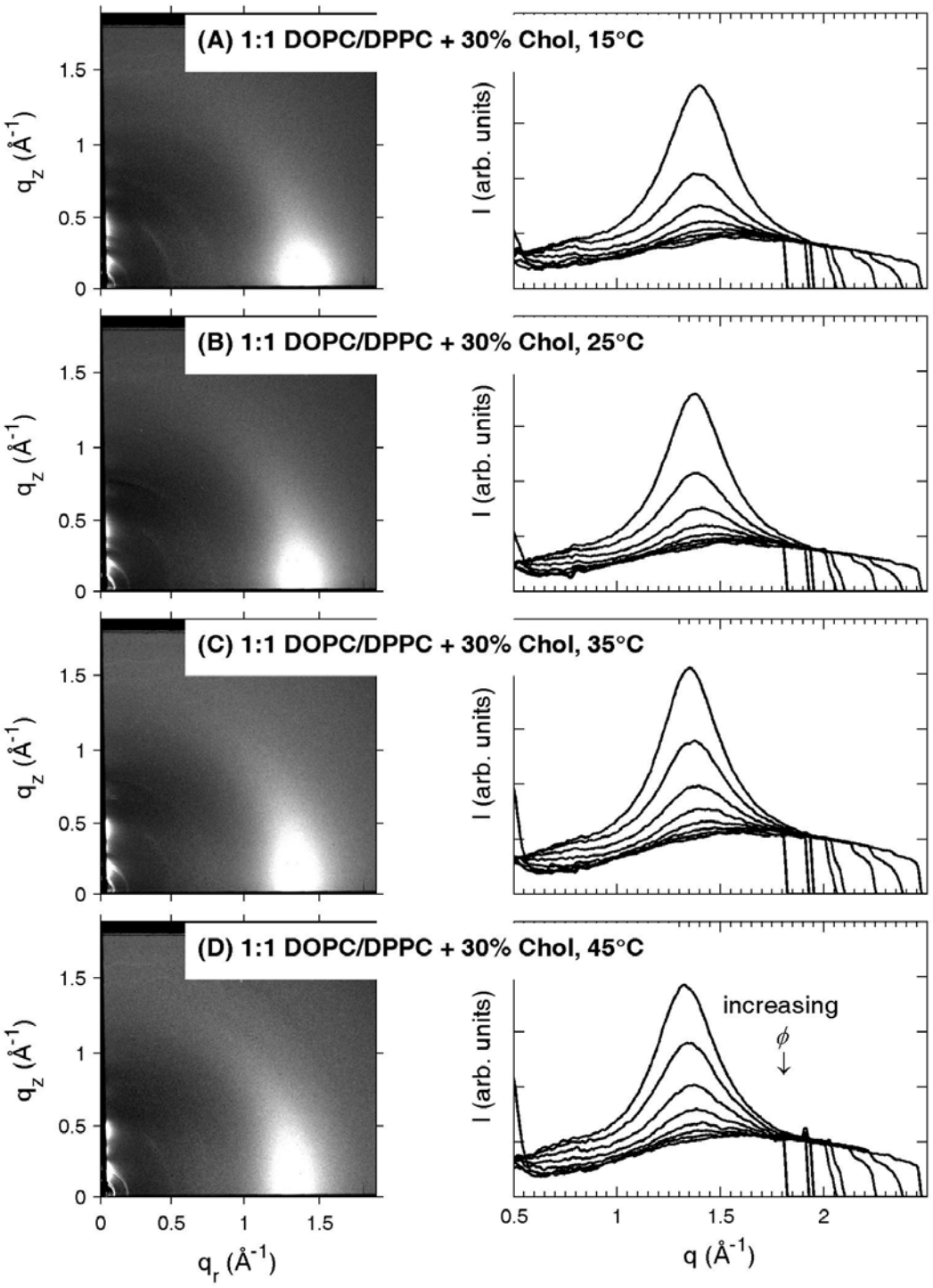


Figure 6.4. Left column shows 2D GIWAXS images for 1:1 DOPC/DPPC + 30% cholesterol at the following temperatures: (A) 15˚C; (B) 25˚C; (C) 35˚C; (D) 45˚C. The right column shows the corresponding $I(q)$ sector plots (see Section 2.3.7.3). The top trace corresponds to the smallest $\phi$ range. (February 2006, D-1)

### 6.2.2 Lateral positional ordering

Although the peak position, $q_{cc}$, and HWHM for the $I(q)$ plots can be misleading for large $\phi$ due to water scattering (see Section 2.3.7.5 and Section 4.3), we present these plots here because of an interesting trend in the data only observed for the ternary mixtures at low temperature (see Figs. 6.5-6.8). For most samples, there is a monotonic increase in the peak position as a function of $\phi$ angle, probably because the isotropic high $q$ water peak is a more significant fraction of the scattering at larger $\phi$. However, for the ternary mixtures, at temperatures of 30˚C and below, $q_{cc}$ decreases as a function of $\phi$ up to $\phi$~20˚, and then begins to increase. This trend is also detectable in the sector plots (Fig. 6.1-6.4). At high temperatures, the peak position is monotonically increasing as a function of $\phi$.

A possible explanation for this trend is that as $\phi$ increases, the Ld phase begins to dominate the wide-angle scattering. If $q_{cc}$ is smaller for the Ld phase in comparison with the Lo phase, this would explain the dip in the $q_{cc}(\phi)$ plot. Although we do not have x-ray data for the endpoints of the tie lines, we can determine if this is a reasonable explanation based on our $q_{cc}$ values for DOPC/cholesterol and DPPC/cholesterol mixtures. Table 6.1 shows the $q_{cc}$ and $d_{cc}$ values for DOPC/cholesterol and DPPC/cholesterol mixtures at 25˚C. For 1:1 DOPC/DPPC + 15% cholesterol at 25˚C, the compositions of the coexisting phases (the tie line endpoints) are: Ld = 57% DOPC / 34% DPPC / 9% Chol and Lo = 16% DOPC / 58% DPPC / 26% Chol (Veatch et al., 2007b). If we assume the $q_{cc}$ value for the Ld composition is close to that of DOPC + 10% cholesterol ($q_{cc}$=1.36 Å$^{-1}$) and the $q_{cc}$ value for the Lo composition is close to that of DPPC + 25% cholesterol ($q_{cc}$=1.45 Å$^{-1}$), the above explanation makes sense.

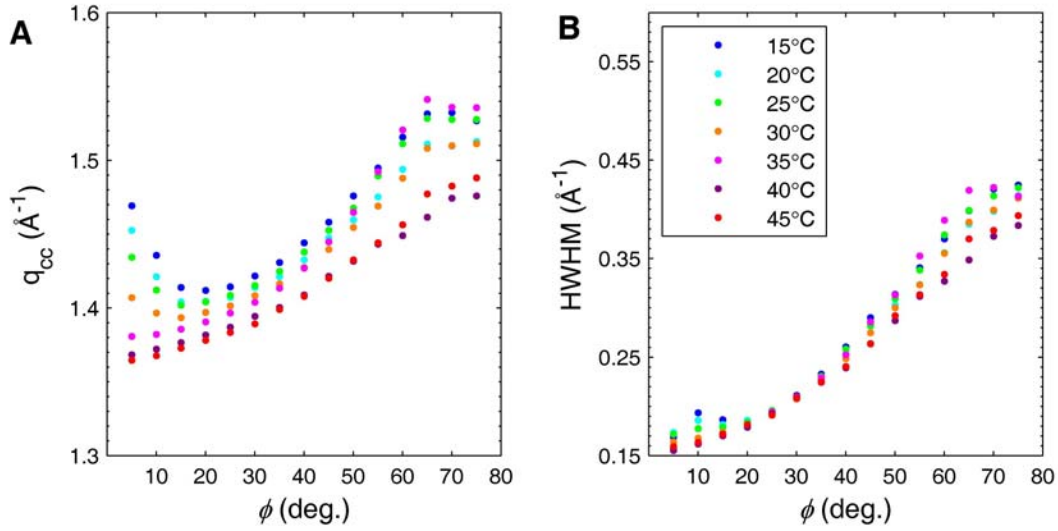


Figure 6.5. Wide-angle peak position, $q_{cc}(\phi)$, and HWHM($\phi$) plots for 1:1 DOPC:DPPC + 15% cholesterol at different temperatures.

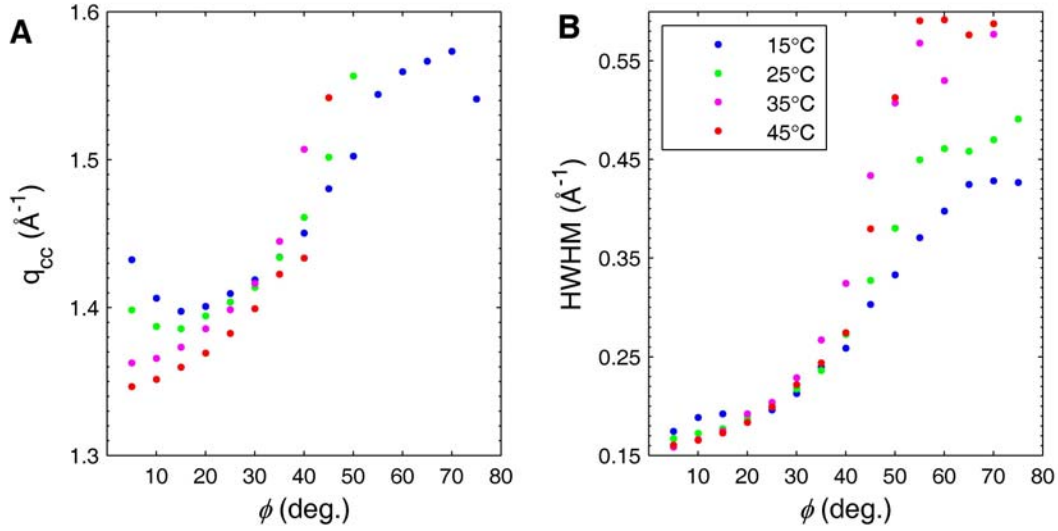


Figure 6.6. Wide-angle peak position, $q_{cc}(\phi)$, and HWHM($\phi$) plots for 1:1 DOPC:DPPC + 20% cholesterol at different temperatures.

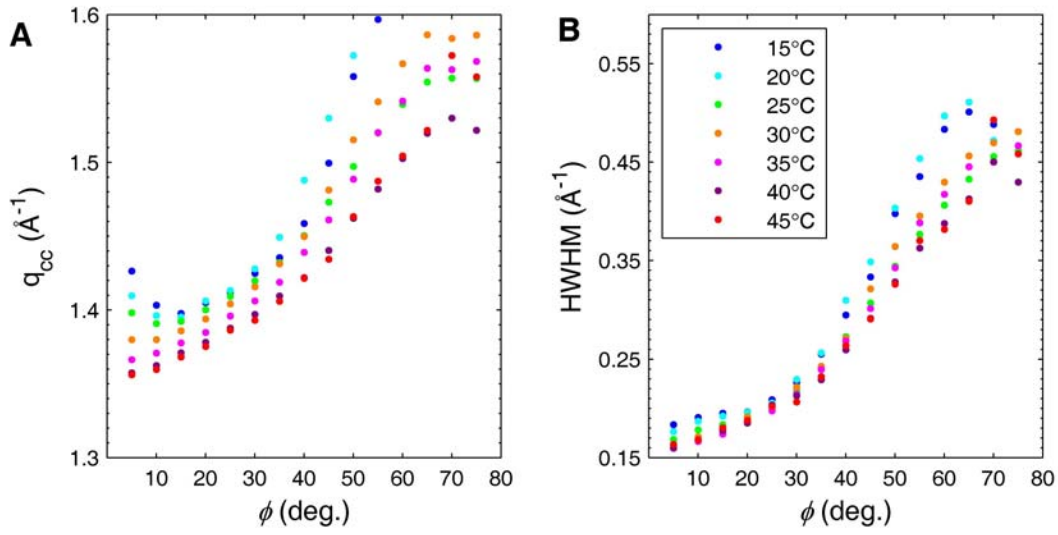


Figure 6.7. Wide-angle peak position, $q_{cc}(\phi)$, and HWHM($\phi$) plots for 1:1 DOPC:DPPC + 25% cholesterol at different temperatures.

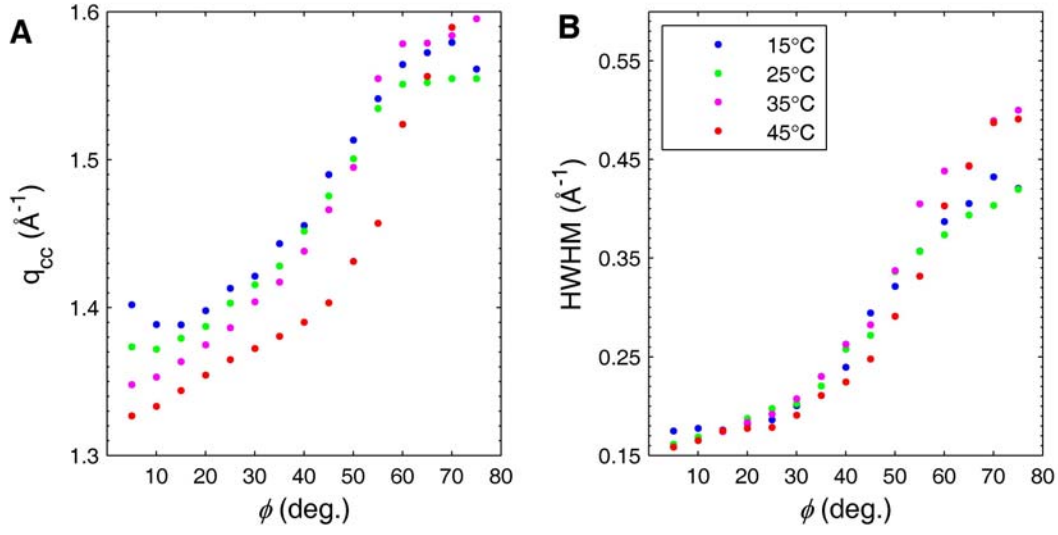


Figure 6.8. Wide-angle peak position, $q_{cc}(\phi)$, and HWHM($\phi$) plots for 1:1 DOPC:DPPC + 30% cholesterol at different temperatures.

Table 6.1. Values of $q_{cc}$ and $d_{cc}$ for DPPC/cholesterol and DOPC/cholesterol mixtures at 25˚C ($\phi$=5-10˚).

| | **mol% cholesterol** | $q_{cc}$ (Å$^{-1}$) | $d_{cc}=2\pi/q_{cc}$ (Å) |
|---|---|---|---|
| DPPC | 10 | 1.48 | 4.25 |
| | 15 | 1.46 | 4.30 |
| | 25 | 1.45 | 4.33 |
| | 40 | 1.38 | 4.55 |
| DOPC | 0 | 1.39 | 4.52 |
| | 10 | 1.36 | 4.62 |
| | 40 | 1.28 | 4.91 |

A larger $q_{cc}$ value for the Lo phase (more cholesterol) in comparison with the Ld phase (less cholesterol) may seem counterintuitive based on our knowledge of binary mixtures of phospholipid and cholesterol. For binary mixtures of phospholipid and cholesterol, we have observed that $q_{cc}$ decreases as a function of cholesterol concentration (see Table 6.1). Based on the NMR tie line data, the ternary mixtures at low temperature separate into an Ld phase (lower cholesterol content) and an Lo phase (higher cholesterol content). We might expect the Lo phase, not the Ld phase, to have a smaller $q_{cc}$. However, the Ld and Lo phases have different amounts of DOPC and DPPC, which appear to dominate the relative $q_{cc}$ values.

The wide-angle HWHM values are very similar for the different mixtures and for different temperatures: at low $\phi$, the HWHM is about 0.16 Å$^{-1}$. This agrees with our DOPC/cholesterol and DPPC/cholesterol data, for which we observed that the fluid phases, no matter whether they are orientationally ordered or disordered, have a similar distribution of nearest neighbor distances as measured by HWHM. Thus, the $q$-widths are not a criterion for distinguishing the different liquid phases.

### 6.2.3 Fits to $I(\phi)$ data: one order parameter or two?

To our knowledge, no one has reported fitting $I(\phi)$ data for a liquid crystal known to have coexisting phases using the method described in Ch. 3. If the chain ordering in the two phases is different, then a combination of two chain orientational distribution functions may be necessary to describe the system. We have found that this is indeed the case for the DOPC/DPPC/cholesterol mixtures we studied.

Figures 6.9-6.12 show the $I(\phi)$ plots with fits assuming one order parameter (Eq. 3.29) and two order parameters (Eq. 3.32) for the mixtures 1:1 DOPC + 15%, 20%, 25%, and 30% cholesterol. For all the mixtures, for temperatures of 35˚C and above, the data were well-fit with one order parameter. For temperatures below 35˚C, we needed two different order parameters in order to fit the data well. Later in the chapter (see Fig. 6.18), we plot the GIWAXS order parameter data as well as NMR order parameter data and lamellar repeat data for these mixtures.

Note that at temperatures below 35˚C, the single order parameter fits miss the data for all values of $\phi$ (the residual has structure instead of being randomly positive or negative). This differs with the imperfect single order parameter fits to the DPPC + cholesterol data, where the fit and data matched fairly well in the steeply changing low-$\phi$ region (see Fig. 5.7). As mentioned in Ch. 5, the fits to the DPPC + cholesterol data look like fits to $I(\phi)$ for a very well-ordered liquid crystal. Another reason to reject the single order parameter fits below 35˚C is that the normalized data go below the zero offset, meaning the $I_{back}$ parameter is larger than the high-$\phi$ data. For some of the DPPC + cholesterol data, the choice between the single and double order parameter fits was not clear-cut. In contrast, the choice of accepting the two-order parameter fit for the ternary mixtures below 35˚C is more clear-cut.

The double order parameter fit always fits the data as well as or better than the single order parameter fit. The double order parameter fit was rejected if the following two conditions were met (see also Section 3.3.5):

1. The single order parameter fit was reasonable. The single order parameter fit was judged as reasonable if the residual plot was fairly random and the normalized data fell above the zero offset.
2. Any of the double order parameter fitting parameters ($I_{back}$, $m_1$, $m_2$, $A_1$, or $A_2$) had error of greater than 1/3 of the value of the parameter. This means the confidence interval was 2/3 the size of the parameter.

We interpret the poor single-order parameter fit as evidence of phase coexistence at low temperature. A criticism of this interpretation is that the form of the distribution function may change as a function of temperature. For example, the sample may be in a single phase, but the chain orientational distribution may no longer be well-described by the Maier-Saupe form. Levine and Wilkins (1971) required two different models, each describing a single distribution of chains, in order to describe their egg lecithin $I(\phi)$ data at two different levels of hydration. We cannot disprove the possibility that the system may be described well by a completely different distribution function for a single population of chains at low temperature. However, our interpretation of the fitting results as evidence for phase coexistence at low temperature is consistent with microscopy and NMR (see Section 6.4).

Furthermore, since the wide-angle scattering is diffuse for all of these mixtures (large HWHM~0.16 $Å^{-1}$), the coexisting phases must both be liquids. The two different $S_{mol}$ values tell us about chain order in the two phases. Thus, the GIWAXS data give information about phase coexistence and physical information about the coexisting phases. Table 6.2 summarizes the fitting data for all of the mixtures. Phase fractions are listed, but there are caveats about phase fractions (see Section 3.3.3).

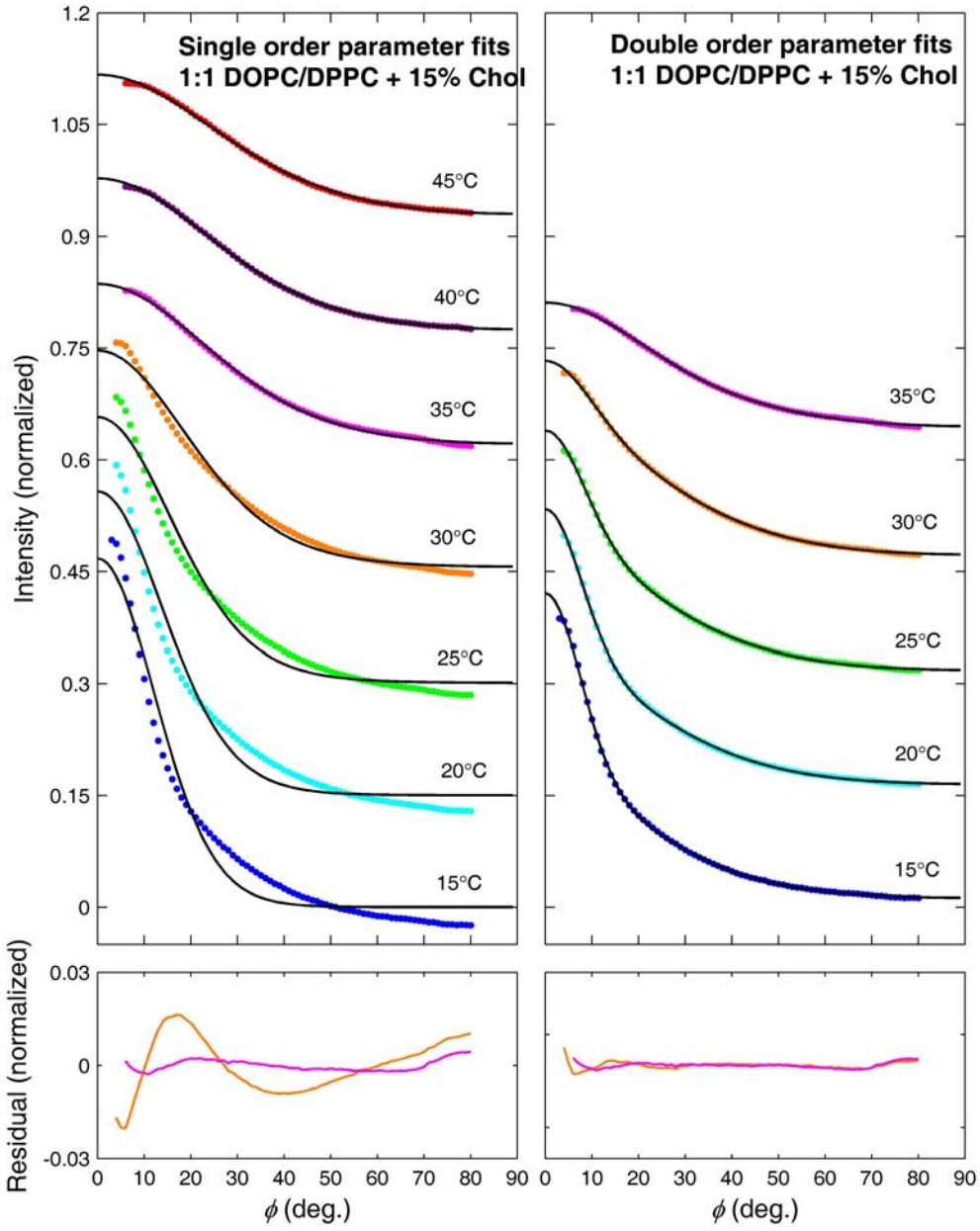


Figure 6.9. $I(\phi)$ plots at different temperatures for 1:1 DOPC/DPPC + 15% cholesterol are shown by colored data points. Black lines are Maier-Saupe fits assuming one order parameter (left panel) and two order parameters (right panel) with representative residual plots for the fits to the 30˚C (orange) and 35˚C (magenta) data shown beneath. Each plot is offset from the one below by 0.15 normalized intensity units. For temperatures of 35˚C and above, the data were well-fit with one order parameter. For temperatures of 30˚C and below, two order parameters were needed to obtain a good fit. The double order parameter fits are not shown for 40˚C and 45˚C because they gave the same value (within 0.01 units) for both order parameters.

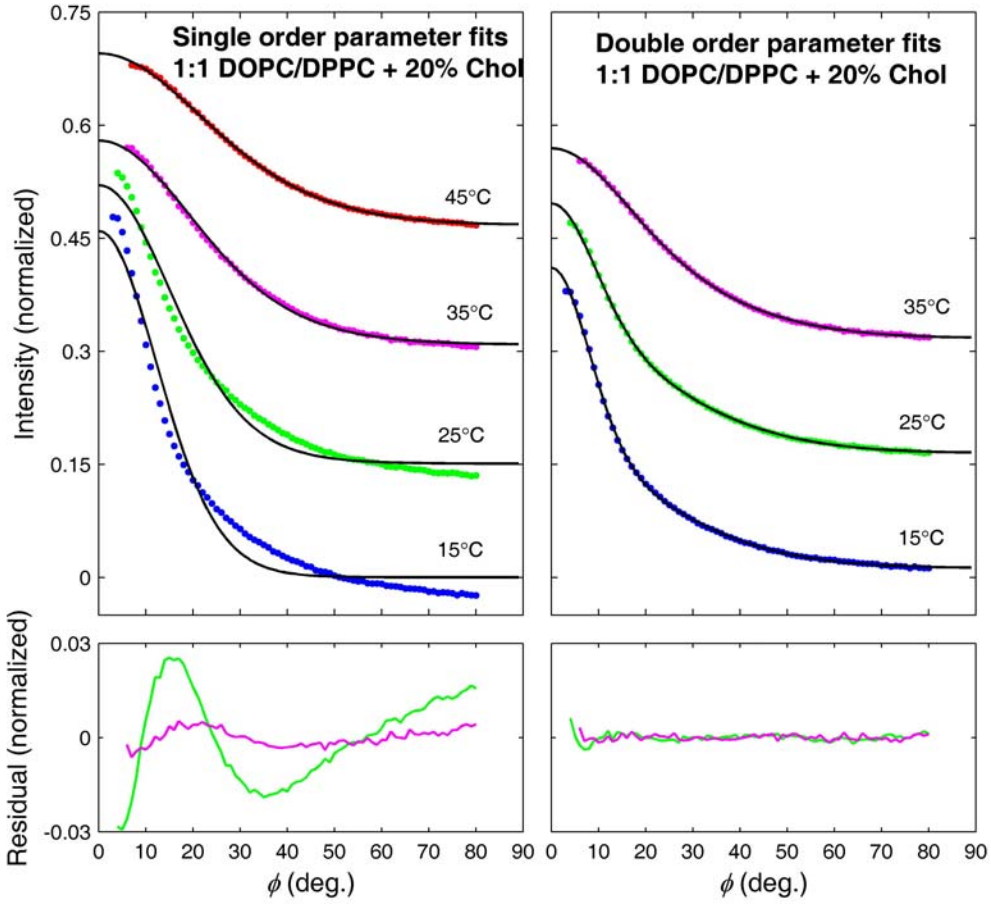


Figure 6.10. $I(\phi)$ plots at different temperatures for 1:1 DOPC/DPPC + 20% cholesterol are shown by colored data points. Black lines are Maier-Saupe fits assuming one order parameter (left panel) and two order parameters (right panel) with representative residual plots for the fits to the 25˚C (green) and 35˚C (magenta) data shown beneath. Each plot is offset from the one below by 0.15 normalized intensity units. For temperatures of 35˚C and above, the data were well-fit with one order parameter. For temperatures of 25˚C and below, two order parameters were needed to obtain a good fit. The double order parameter fit is not shown for the 45˚C data because it gave the same value (within 0.01 units) for both order parameters.

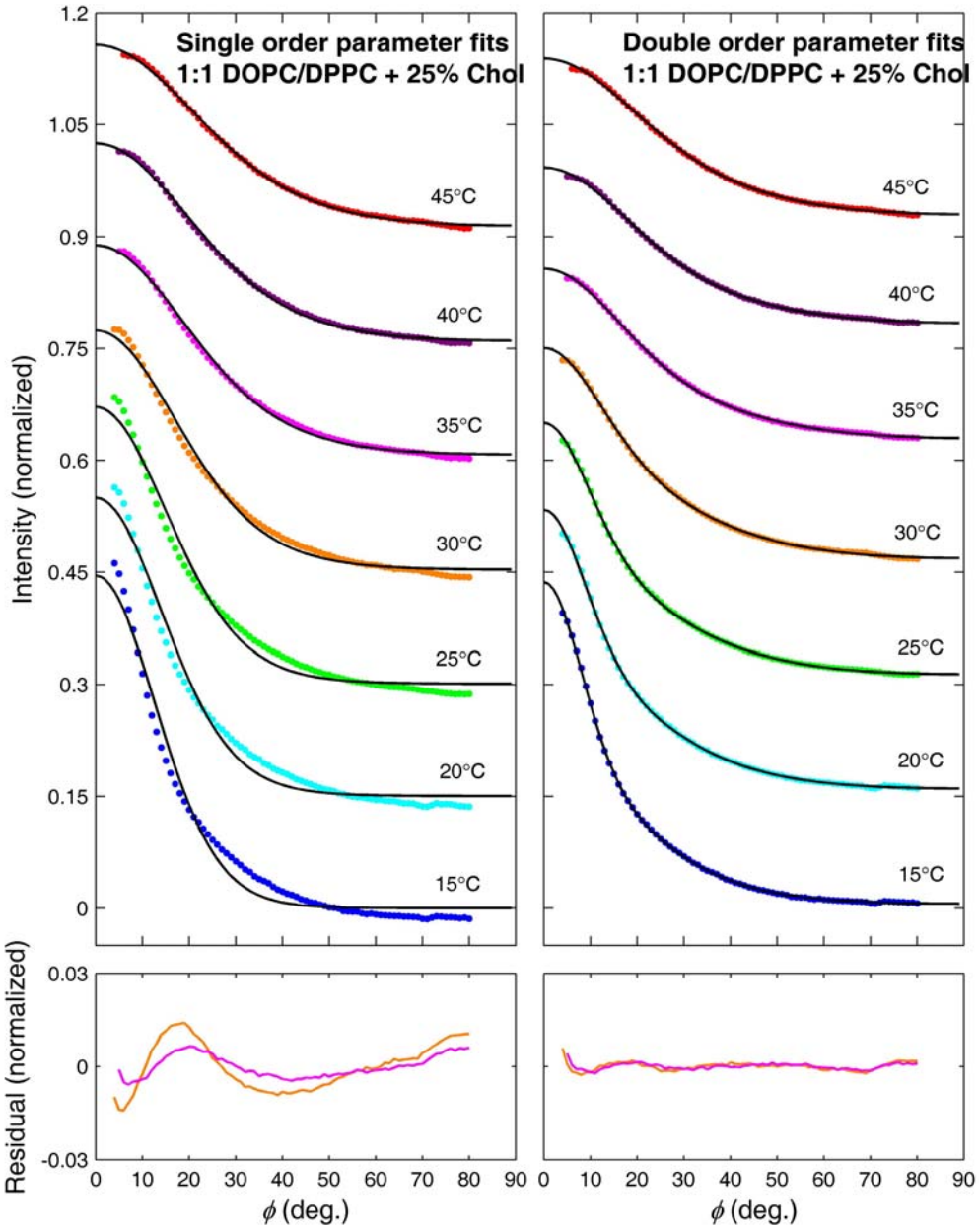


Figure 6.11. $I(\phi)$ plots at different temperatures for 1:1 DOPC/DPPC + 25% cholesterol are shown by colored data points. Black lines are Maier-Saupe fits assuming one order parameter (left panel) and two order parameters (right panel) with representative residual plots for the fits to the 30˚C (orange) and 35˚C (magenta) data shown beneath. Each plot is offset from the one below by 0.15 normalized intensity units. The double order parameter fit was rejected for the 35˚C data because of the large error in the fitted parameters (the error in $m_1$ was greater than 1/3 of $m_1$) despite the clear improvement in the residual when two order parameters are assumed. For temperatures of 30˚C and below, two order parameters were required to fit the data.

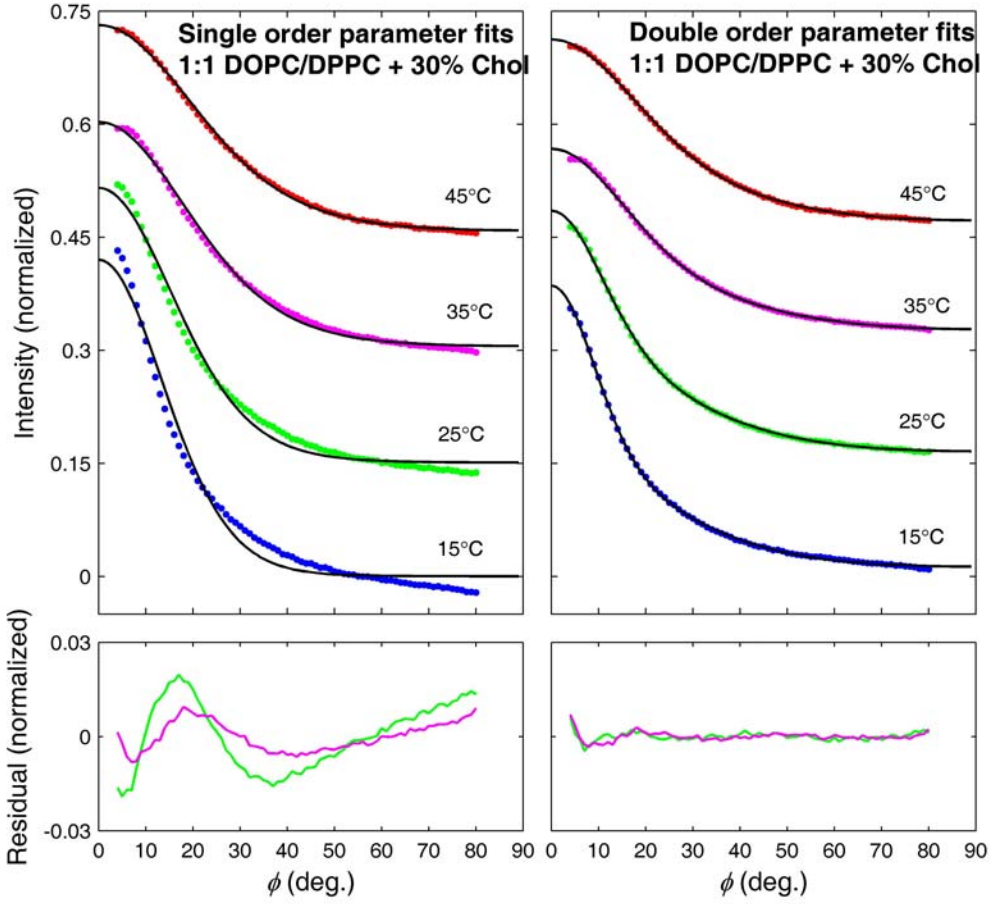


Figure 6.12. $I(\phi)$ plots at different temperatures for 1:1 DOPC/DPPC + 30% cholesterol are shown by colored data points. Black lines are Maier-Saupe fits assuming one order parameter (left panel) and two order parameters (right panel) with representative residual plots for the fits to the 25˚C (green) and 35˚C (magenta) data shown beneath. Each plot is offset from the one below by 0.15 normalized intensity units. The double order parameter fit was rejected for the 35˚C data because of the large error in the fitted order parameters (the error in $m_1$ was greater than 1/3 of $m_1$) despite the clear improvement in the residual when two order parameters are assumed. For temperatures of 35˚C and above, the data were well-fit with one order parameter. For temperatures of 25˚C and below, two order parameters were needed to obtain a good fit.

Table 6.2. Results of fits to $I(\phi)$ data for 1:1 DOPC/DPPC with varying amounts of cholesterol.

| Mol% Chol | T (˚C) | *m** | $S_{mol}$* | Phase Fractions | $R^2$ | Accept fit? |
|---|---|---|---|---|---|---|
| 15 | 15 | m= 11.5 ± 1.1 | S= 0.86 ± 0.01 | | 0.9695 | NO |
| | | m1= 3.69 ± 0.23<br>m2= 30.6 ± 1.3 | S1= 0.52 ± 0.03<br>S2= 0.95 ± 0.01 | P1= 0.67 ± 0.01<br>P2= 0.33 ± 0.01 | 0.9995 | YES |
| | 20 | m= 8.96 ± 0.86 | S= 0.82 ± 0.02 | | 0.9693 | NO |
| | | m1= 3.48 ± 0.12<br>m2= 29.8 ± 0.9 | S1=0.50 ± 0.01<br>S2= 0.95 ± 0.01 | P1= 0.72 ± 0.01<br>P2= 0.28 ± 0.01 | 0.9998 | YES |
| | 25 | m= 7.08 ± 0.58 | S= 0.76 ± 0.02 | | 0.9782 | NO |
| | | m1= 3.34 ± 0.14<br>m2= 25.7 ± 1.1 | S1= 0.48 ± 0.02<br>S2= 0.94 ± 0.01 | P1= 0.77 ± 0.01<br>P2= 0.23 ± 0.01 | 0.9998 | YES |
| | 30 | m= 5.15 ± 0.29 | S= 0.66 ± 0.02 | | 0.9910 | NO |
| | | m1= 3.16 ± 0.14<br>m2= 20.1 ± 1.5 | S1= 0.46 ± 0.02<br>S2= 0.92 ± 0.01 | P1= 0.85 ± 0.01<br>P2= 0.15 ± 0.01 | 0.9998 | YES |
| | 35 | m= 3.47 ± 0.07 | S= 0.50 ± 0.01 | | 0.9993 | YES |
| | | m1= 1.43 ± 3.52<br>m2= 4.61 ± 2.01 | S1= 0.21 ± 0.56<br>S2= 0.61 ± 0.18 | P1= 0.58 ± 0.36<br>P2= 0.42 ± 0.36 | 0.9997 | NO |
| | 40 | m= 3.25 ± 0.04 | S= 0.47 ± 0.01 | | 0.9998 | YES |
| | | m1=m2 | S1=S2=0.47 | NA | NA | NA |
| | 45 | m= 2.96 ± 0.05 | S= 0.43 ± 0.01 | | 0.9995 | YES |
| | | m1=m2 | S1=S2=0.43 | NA | NA | NA |
| 20 | 15 | m= 11.2 ± 1.0 | S= 0.86 ± 0.01 | | 0.9747 | NO |
| | | m1= 3.61 ± 0.25<br>m2= 27.6 ± 1.2 | S1= 0.51 ± 0.03<br>S2= 0.94 ± 0.01 | P1= 0.66 ± 0.01<br>P2= 0.34 ± 0.01 | 0.9995 | YES |
| | 25 | m= 7.54 ± 0.53 | S= 0.78 ± 0.02 | | 0.9837 | NO |
| | | m1= 3.48 ± 0.17<br>m2= 21.6 ± 1.0 | S1= 0.50 ± 0.02<br>S2= 0.93 ± 0.01 | P1= 0.73 ± 0.01<br>P2= 0.27 ± 0.01 | 0.9998 | YES |
| | 35 | m= 4.65 ± 0.09 | S= 0.62 ± 0.01 | | 0.9989 | YES |
| | | m1= 3.43 ± 0.38<br>m2= 9.80 ± 1.92 | S1= 0.49 ± 0.05<br>S2= 0.83 ± 0.04 | P1= 0.82 ± 0.07<br>P2= 0.18 ± 0.07 | 0.9998 | NO |
| | 45 | m= 3.71 ± 0.04 | S= 0.53 ± 0.01 | | 0.9998 | YES |
| | | m1=m2 | S1=S2=0.53 | NA | NA | NA |

* If only one order parameter is given, the fit is a one order parameter fit (Eq. 3.29). If 2 order parameters are listed, the fit assumes 2 order parameters (Eq. 3.32). If "m1=m2" or "S1=S2" are listed, this means these parameters were the same to within ±0.01.

Table 6.2 (continued)

| Mol% chol | T (°C) | *m** | $S_{mol}$* | Phase Fractions | $R^2$ | Accept fit? |
|---|---|---|---|---|---|---|
| 25 | 15 | m= 10.6 ± 0.8 | S= 0.85 ± 0.01 | | 0.9811 | NO |
| | | m1= 4.71 ± 0.16<br>m2= 28.3 ± 0.9 | S1= 0.62 ± 0.01<br>S2= 0.95 ± 0.01 | P1= 0.66 ± 0.01<br>P2= 0.34 ± 0.01 | 0.9998 | YES |
| | 20 | m= 8.65 ± 0.60 | S= 0.81 ± 0.02 | | 0.9836 | NO |
| | | m1= 4.05 ± 0.18<br>m2= 23.8 ± 1.1 | S1= 0.56 ± 0.02<br>S2= 0.94 ± 0.01 | P1= 0.70 ± 0.01<br>P2= 0.30 ± 0.01 | 0.9998 | YES |
| | 25 | m= 7.58 ± 0.47 | S= 0.78 ± 0.02 | | 0.9876 | NO |
| | | m1= 3.68 ± 0.15<br>m2= 20.4 ± 0.8 | S1= 0.52 ± 0.02<br>S2= 0.92 ± 0.01 | P1= 0.72 ± 0.01<br>P2= 0.28 ± 0.01 | 0.9993 | YES |
| | 30 | m= 5.98 ± 0.26 | S= 0.71 ± 0.01 | | 0.9868 | NO |
| | | m1= 3.29 ± 0.28<br>m2= 14.1 ± 1.2 | S1= 0.48 ± 0.04<br>S2= 0.89 ± 0.01 | P1= 0.75 ± 0.02<br>P2= 0.25 ± 0.02 | 0.9999 | YES |
| | 35 | m= 4.90 ± 0.12 | S= 0.64 ± 0.01 | | 0.9943 | YES |
| | | m1= 2.30 ± 0.77<br>m2= 7.85 ± 1.0 | S1= 0.34 ± 0.11<br>S2= 0.79 ± 0.03 | P1= 0.65 ± 0.07<br>P2= 0.35 ± 0.07 | 0.9997 | NO |
| | 40 | m= 4.52 ± 0.09 | S= 0.61 ± 0.01 | | | YES |
| | | m1= 1.79 ± 1.8<br>m2= 6.13 ± 1.2 | S1= 0.27 ± 0.28<br>S2= 0.72 ± 0.06 | P1= 0.56 ± 0.14<br>P2= 0.44 ± 0.14 | | NO |
| | 45 | m= 4.03 ± 0.06 | S= 0.56 ± 0.01 | | | YES |
| | | m1= 2.02 ± 4.0<br>m2= 5.16 ± 2.3 | S1= 0.30 ± 0.59<br>S2= 0.66 ± 0.17 | P1= 0.51 ± 0.44<br>P2= 0.49 ± 0.44 | | NO |
| 30 | 15 | m= 9.47 ± 0.67 | S= 0.83 ± 0.01 | | 0.9828 | NO |
| | | m1= 3.61 ± 0.23<br>m2= 21.9 ± 0.9 | S1= 0.51 ± 0.03<br>S2= 0.93 ± 0.01 | P1= 0.65 ± 0.01<br>P2= 0.35 ± 0.01 | 0.9997 | YES |
| | 25 | m= 7.37 ± 0.39 | S= 0.77 ± 0.01 | | 0.9904 | NO |
| | | m1= 3.38 ± 0.25<br>m2= 16.4 ± 0.9 | S1= 0.49 ± 0.03<br>S2= 0.91 ± 0.01 | P1= 0.69 ± 0.02<br>P2= 0.31 ± 0.02 | 0.9998 | YES |
| | 35 | m= 5.33 ± 0.15 | S= 0.67 ± 0.01 | | 0.9975 | YES |
| | | m1= 2.37 ± 0.92<br>m2= 8.60 ± 1.23 | S1= 0.35 ± 0.13<br>S2= 0.81 ± 0.03 | P1= 0.65 ± 0.07<br>P2= 0.35 ± 0.07 | 0.9996 | NO |
| | 45 | m= 4.70 ± 0.07 | S= 0.62 ± 0.02 | | 0.9994 | YES |
| | | m1= 2.64 ± 1.49<br>m2= 6.61 ± 1.53 | S1= 0.39 ± 0.21<br>S2= 0.74 ± 0.07 | P1= 0.59 ± 0.19<br>P2= 0.41 ± 0.19 | 0.9998 | NO |

* If only one order parameter is given, the fit is a one order parameter fit (Eq. 3.29). If 2 order parameters are listed, the fit assumes 2 order parameters (Eq. 3.32). If "m1=m2" or "S1=S2" are listed, this means these parameters were the same to within ±0.01.

## 6.3 Double lamellar repeat spacings: is seeing (in reciprocal space) believing?

Fluorescence microscopy has a major advantage over other techniques for detecting phase coexistence: seeing is believing. Fitting to a model is not required to determine if there are two coexisting phases from a GUV image with clear-cut domains. Other methods for detecting phase coexistence, such as NMR, FRET, and GIWAXS, are less direct. For these methods, extensive analysis including comparison to models and data for other samples may be required to determine if a sample has phase-separated. Observation of two resolvable peaks in the x-ray diffraction data is a direct criterion to determine that a mixture has phase-separated; however, observation of only a single lamellar repeat does not necessarily imply the absence of phase coexistence (see Section 3.4).

Figure 6.13 shows our lamellar repeat spacing data for fully-hydrated MLV (powder) samples for mixtures of DOPC/DPPC/cholesterol known to exhibit liquid-liquid coexistence at low temperatures. Figures 6.14-6.17 show the same data on a larger scale. For 1:1 DOPC:DPPC + 15% cholesterol (Fig. 6.13A), two first order and two second order peaks are clearly visible for temperatures of 25˚C and below. At 30˚C, two second order peaks are visible, but two peaks are not resolvable on the first order. For the other mixtures (Fig. 6.13B-D), the first order is not clearly separated into two peaks at any temperature, but at low temperatures there is a shoulder on the first order. We relied on the second order to calculate lamellar repeat spacings which are summarized in the next section (see Fig. 6.18).

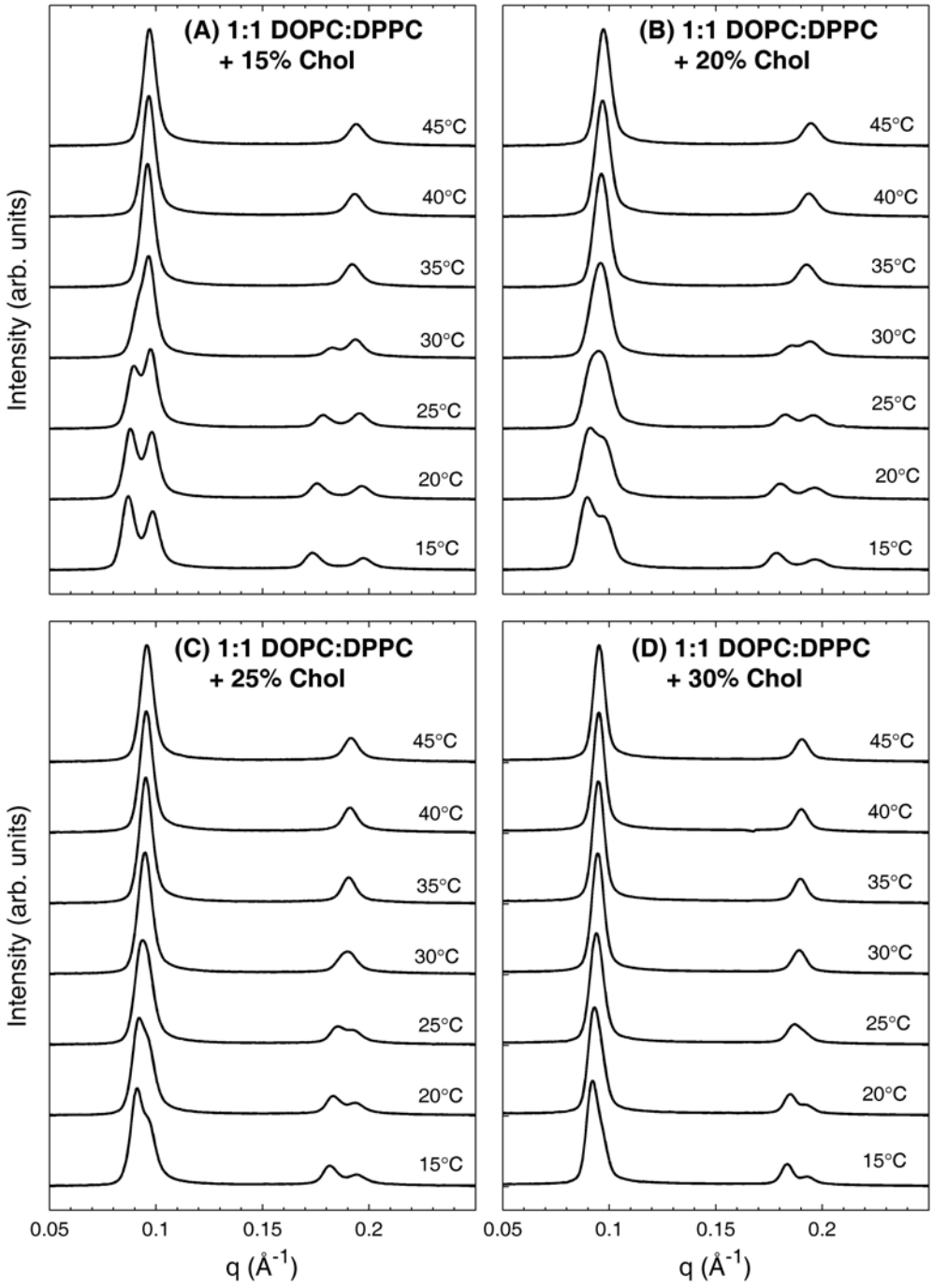


Figure 6.13. *I*(*q*) plots for MLV samples of 1:1 DOPC/DPPC + varying amounts of cholesterol: (A) 15%; (B) 20%; (C) 25%; (D) 30%. The first order and second order lamellar peaks are visible. (Rotating anode measurement)

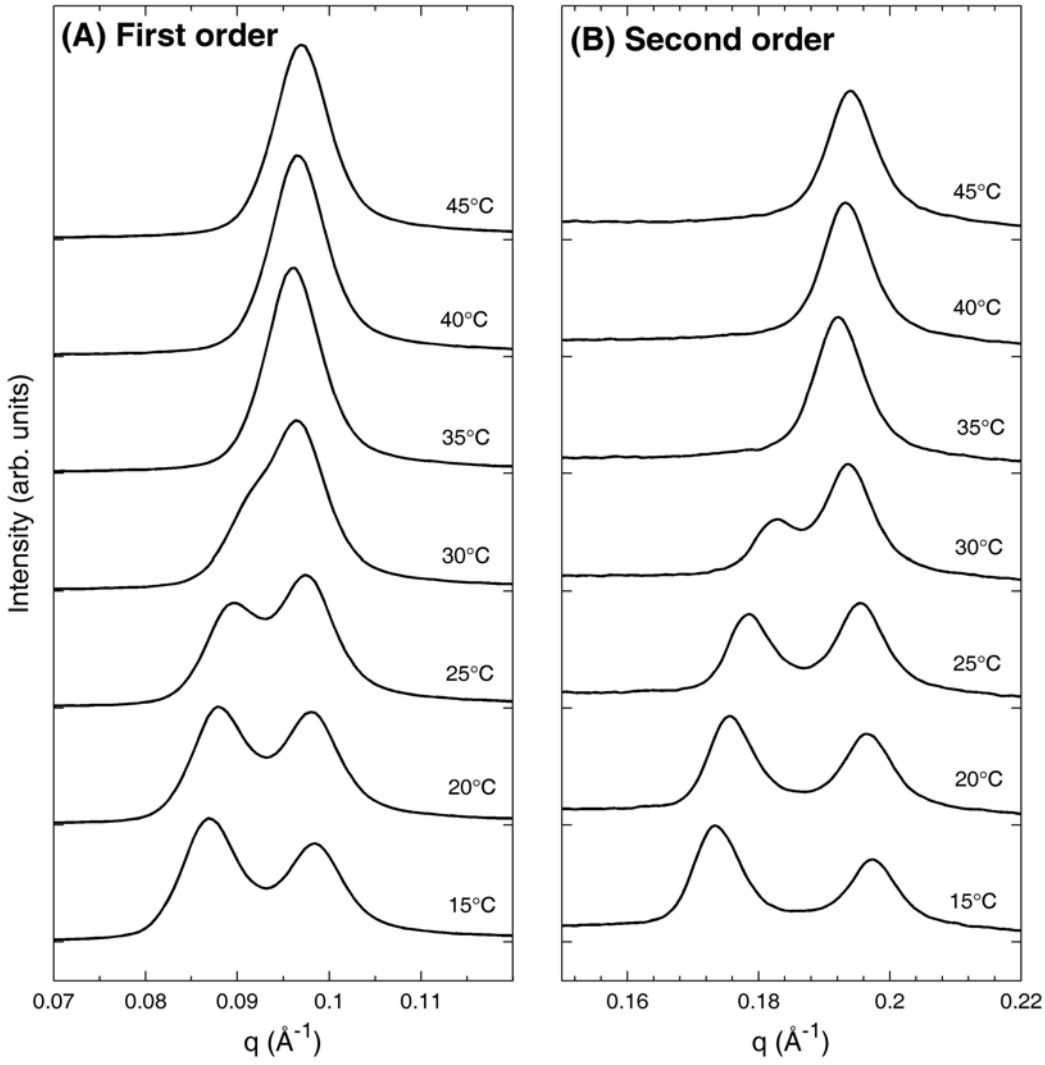


Figure 6.14. (A) First order lamellar diffraction peaks and (B) second order lamellar diffraction peaks for MLV samples of 1:1 DOPC/DPPC + 15% cholesterol. The vertical scale in (B) is 4 times larger than the scale in (A).

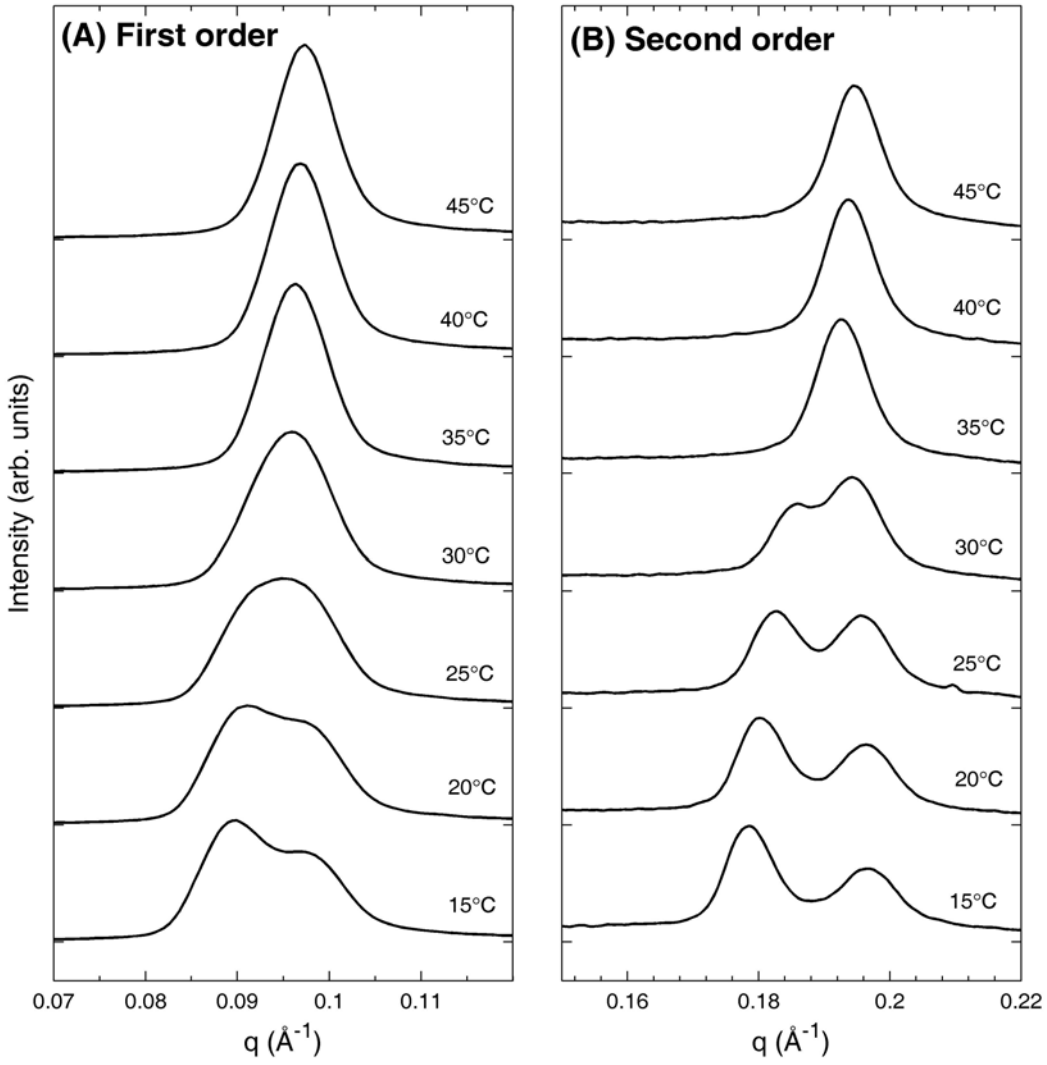


Figure 6.15. (A) First order lamellar diffraction peaks and (B) second order lamellar diffraction peaks for MLV samples of 1:1 DOPC/DPPC + 20% cholesterol. The vertical scale in (B) is 4 times larger than the scale in (A).

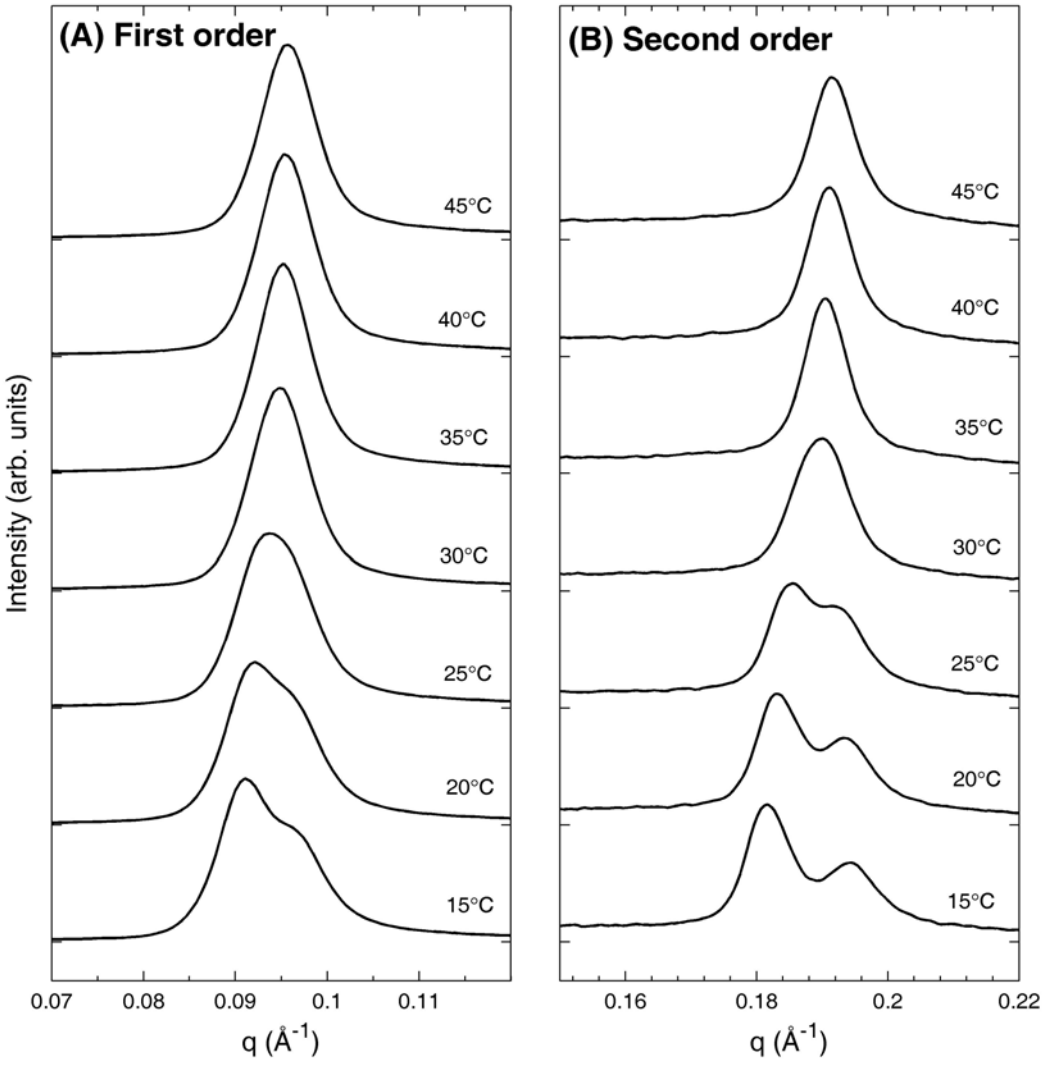


Figure 6.16. (A) First order lamellar diffraction peaks and (B) second order lamellar diffraction peaks for MLV samples of 1:1 DOPC/DPPC + 25% cholesterol. The vertical scale in (B) is 4 times larger than the scale in (A).

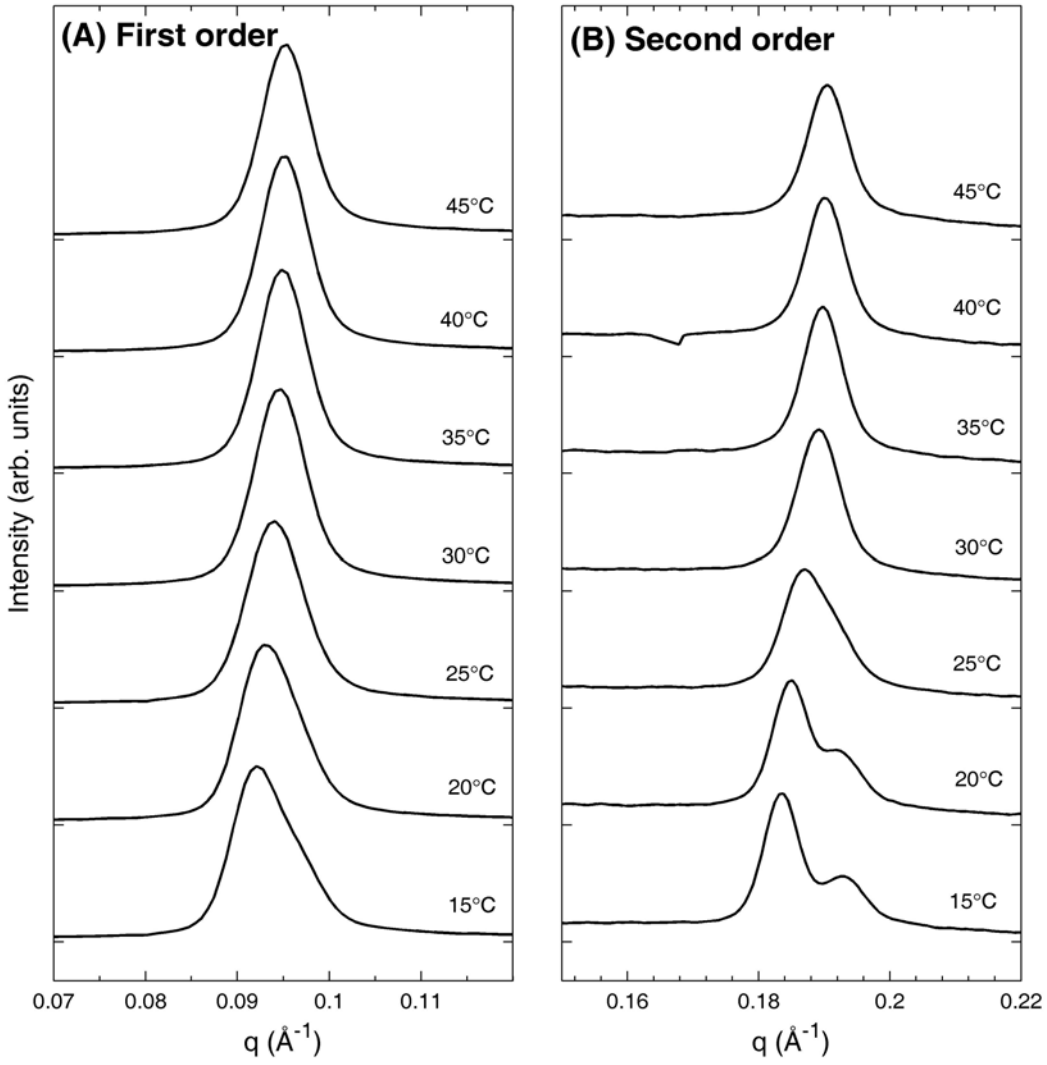


Figure 6.17. (A) First order lamellar diffraction peaks and (B) second order lamellar diffraction peaks for MLV samples of 1:1 DOPC/DPPC + 30% cholesterol. The vertical scale in (B) is 4 times larger than the scale in (A).

The existence of two lamellar repeats is evidence of two coexisting phases, but insufficient time for hydration and temperature equilibration can cause temporary double lamellar repeats. As described in Section 2.4.1, the samples were hydrated in a large excess of water (5:1 to 10:1 (v/v) water: lipid) and taken through temperature cycling before being loaded into capillaries. After mounting in the rotating anode apparatus, the capillary samples were equilibrated for at least 30 minutes at each temperature before data collection. After the samples were heated to 45˚C, where there is clearly only one $d_L$-spacing, the samples were cycled back down in temperature to determine if the double $d_L$-spacings were reproducible. In all cases, after cooling the samples, the double $d_L$-spacings were reproducible. The values of the $d_L$-spacings varied by no more than 0.3 Å between the heating and cooling cycles. Since the samples were well-hydrated and did not exhibit thermal hysteresis, we are confident that the double $d_L$-spacings are due to phase separation.

Gandhavadi et. al. (2002) observed only one lamellar repeat spacing for 1:1:1 DOPC/BSM/cholesterol, a mixture which has been called the "canonical raft mixture". Veatch and Keller (2003a) point out that this mixture is very close to a phase boundary. A small error in the lipid ratio could have caused the mixture to be outside the two-phase region. Veatch and Keller (2003a) suggest that 1:1 DOPC/BSM + 20% cholesterol is a better choice for experiments because it is well within a two-phase region at 25˚C. Our x-ray scattering results for an MLV sample of 1:1 DOPC/BSM + 20% cholesterol indicate only one lamellar repeat spacing of 69.7 Å at 25˚C.

Even more puzzling is our observation of only one lamellar repeat spacing for 1:1 DOPC/DPPC at 25˚C ($d_L$=63.2 Å), in both the fully hydrated MLV sample and the oriented sample. This mixture is known to exhibit gel/fluid coexistence; in addition, our GIWAXS data clearly show two wide-angle peaks for this sample (see Fig. 5.3B). On the other hand, Gandhavadi et al. observed two lamellar repeat spacings for 1:1

DOPC/BSM at 25˚C, also known to be separated into a gel and fluid phase. Clearly, relying on lamellar repeat spacings to determine the absence or presence of phase coexistence can be misleading.

As discussed in Section 3.4, to see two lamellar repeat spacings, the following conditions must be met:

1. The $d_L$-spacings must be different enough for the peaks to be resolvable.
2. The Lo (or Ld) domains must be aligned with the Lo (or Ld) domains in the neighboring bilayers. Gandhavadi et al. (2002) make the analogy to a stack of egg cartons.

In principle, we could calculate the correlation length in the direction of the membrane normal by using the Scherrer equation (Warren, 1969):

$$\xi = \frac{0.94\lambda}{\mathrm{FWHM}_{\mathrm{rad}} \cos\theta}, \tag{6.1}$$

where $\xi$ is the correlation length, $2\theta$ is the standard scattering angle, $\lambda$ is the x-ray wavelength, and $\mathrm{FWHM}_{\mathrm{rad}}$ is the full width in radians of the powder pattern peak at half maximum intensity The Scherrer equation applies to Gaussian-shaped scattering peaks. Converting to $q$ from radians, the Scherrer equation can be approximated as :

$$\xi \approx \frac{2\pi}{\mathrm{FWHM}_{\mathrm{q}}}, \tag{6.2}$$

where $\mathrm{FWHM}_{\mathrm{q}}$ is the full width at half maximum in reciprocal angstroms ($q$). For a Gaussian the $\mathrm{FWHM}_{\mathrm{q}}$ can be found from the measured value, $\mathrm{FWHM}_{\mathrm{mes}}$, and the instrumental resolution, $\mathrm{FWHM}_{\mathrm{res}}$ using the following formula (Kaganer et al., 1999):

$$\mathrm{FWHM}_{\mathrm{q}}^2 = \mathrm{FWHM}_{\mathrm{mes}}^2 - \mathrm{FWHM}_{\mathrm{res}}^2. \tag{6.3}$$

The size of the beam was not measured for the rotating anode setup, so we do not have a direct measure of $\mathrm{FWHM}_{\mathrm{res}}$. The beam size is usually near 0.7 mm, so we used this number to estimate $\mathrm{FWHM}_{\mathrm{res}}$ for the 1:1 DOPC/DPPC + 15% cholesterol data at 15˚C

presented in Fig. 6.14. Converting to $q$ (with sample to detector distance of 386 mm and $\lambda$=1.542 Å), a 0.7 mm beam size gives a $FWHM_{res}$ of 0.007 $Å^{-1}$. Unfortunately, $FWHM_{mes}$ is approximately 0.008 $Å^{-1}$ for either of the first order peaks shown in Fig. 6.14, and so we are resolution-limited. However, we can put a lower limit on the correlation length by using $FWHM_q$=0.008 $Å^{-1}$ in Eq. 6.2. This gives $\xi \geq$785 Å, i.e. ~13 lipid bilayers in correlated stacks.

Lipid type, lipid purity, and sample preparation may all affect whether the two conditions are met. Pure DOPC and pure DPPC have very similar lamellar repeat spacings at 25˚C ($d_L$~63-64 Å). We may have only observed one lamellar repeat for 1:1 DOPC/DPPC because the two lamellar peaks were not resolvable. Brain sphingomyelin (BSM) is a naturally occurring mixture of sphingomyelins with different chain lengths and degrees of unsaturation. Such a mixed system may make alignment of the domains across bilayers more sensitive to the exact sample preparation conditions. This would explain why we and Gandhavadi et al. (2002) do not observe two lamellar repeat spacings for mixtures of DOPC, BSM, and cholesterol and yet Nicolini et al. (2004) report that the domains are aligned in 1:1:1 DOPC/BSM/cholesterol based on small-angle neutron scattering experiments.

Karmakar et al. (2006) have reported the observation of double lamellar repeat spacings in oriented samples composed of DOPC, DPPC, and cholesterol. We also observed two lamellar repeat spacings in our oriented samples, but equilibration in oriented samples can be problematic (see Section 2.3.4.2) . Although lamellar repeat spacings can be misleading, the observation of two spacings is intriguing. For the DOPC/DPPC/cholesterol system, the observation of two lamellar repeats appears to be a robust, reproducible phenomenon. The observation in one system and not in another leads to many questions. What interactions cause the domains to align across stacks of bilayers? What factors can disrupt these interactions?

As pointed out by Gandhavadi et al. (2002), the second condition (aligning of domains across bilayers) means that the sample must be phase-separated in three dimensions in order to see two lamellar repeat spacings. On the other hand, the chain-chain correlation peak results from ordering within a single bilayer; thus, GIWAXS can detect two-dimensional phase separation within single bilayers. Fitting to the GIWAXS data is not as straightforward as observation of two lamellar repeats, but the GIWAXS method may be more reliable for detecting liquid-liquid phase coexistence by giving fewer false negatives.

## 6.4 How do the GIWAXS and lamellar repeat data compare with NMR and fluorescence microscopy?

Figure 6.18 compares our values of $S_{mol}$ from GIWAXS to $^2$H NMR data (Veatch et al., 2007b) for mixtures known by fluorescence microscopy to exhibit Ld/Lo phase coexistence. Lamellar repeats for fully hydrated MLV samples are also shown. For a given temperature, two different values of $S_{mol}$ or two lamellar repeats indicate phase coexistence. The larger $S_{mol}$ corresponds to the Lo phase and the smaller $S_{mol}$ corresponds to the Ld phase. We based the assignment of the larger lamellar repeat value to the Lo phase based on the trend in lamellar repeat spacings for binary mixtures of DPPC + cholesterol and DOPC + cholesterol and on the nearly horizontal direction of tie lines in the liquid-liquid coexistence region (see Fig. 1.7). The miscibility transition temperatures, $T_{mix}$, from $^2$H NMR (Veatch et al., 2007b) and fluorescence microscopy (Veatch and Keller, 2003b) are indicated on the plots. $^2$H NMR first moments ($M_1$) were converted to $S_{mol}$ using Eq. 5.1. We assumed that substitution of DPPC by DPPC-d62 reduces the $^2$H NMR temperatures by 2.5˚C (Veatch et al., 2004). An offset of 2.5˚C has already been added to the $^2$H NMR temperatures.

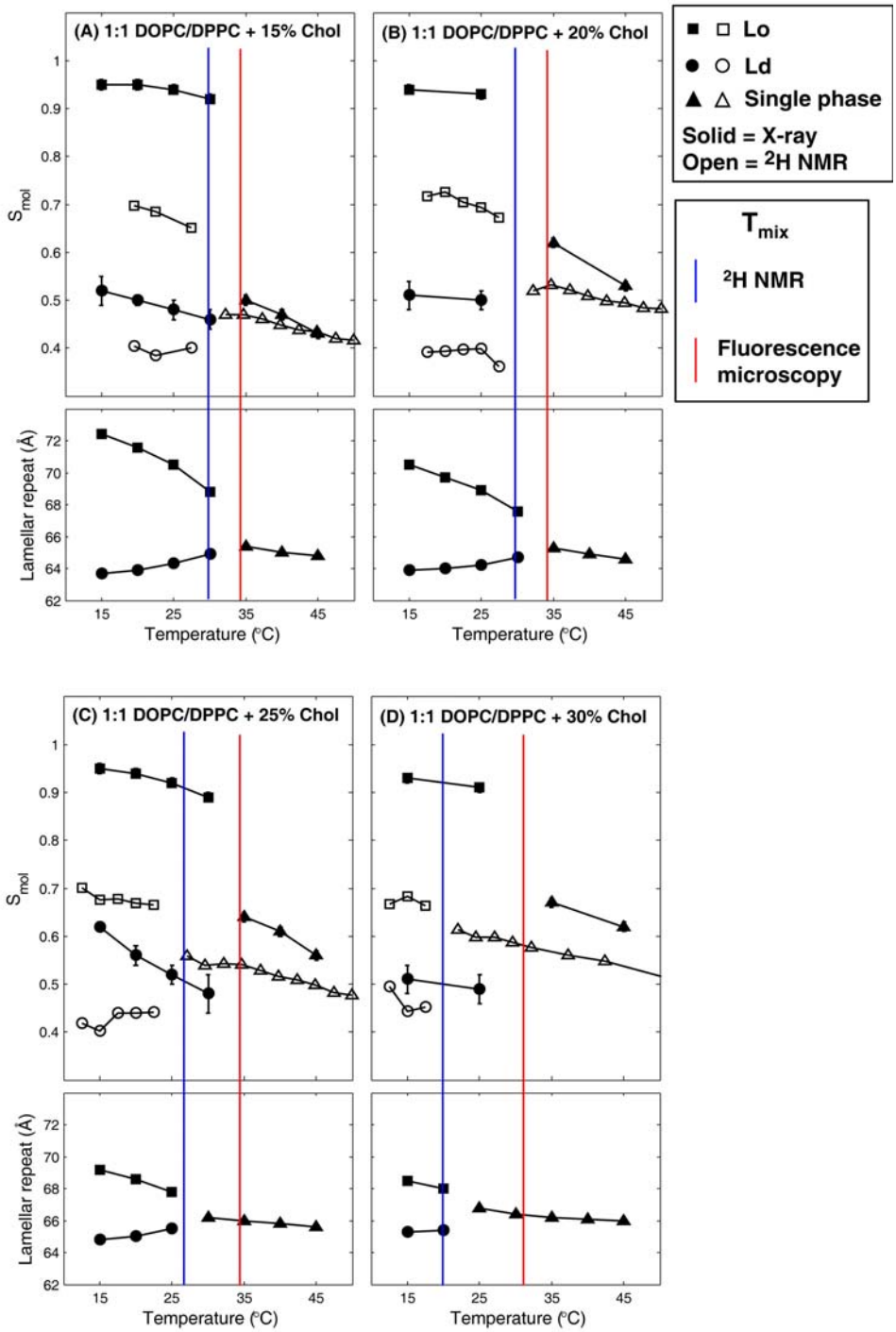


Figure 6.18. Top plots show $S_{mol}$ vs. temperature (from GIWAXS and NMR) and bottom plots show lamellar repeat (for MLV samples) vs. temperature for 1:1 DOPC/DPPC + varying amounts of cholesterol: (A) 15%; (B) 20%; (C) 25%; (D) 30%. The NMR data are from Veatch et al., 2007b. The fluorescence microscopy $T_{mix}$ temperatures are from Veatch et al., 2004.

Errors on $T_{mix}$ as determined by $^2$H NMR are $\pm$ 2˚C. Errors on $T_{mix}$ as determined by fluorescence microscopy are more complicated. Without considering the effects of dye, the uncertainty is at most 5˚C (Veatch and Keller, 2003b). However, Veatch et al. have shown that dye impurities may significantly shift $T_{mix}$ values and phase boundaries (2007a). The effect of the dye has been to increase $T_{mix}$ and expand the region of Ld/Lo coexistence.

Since the Leadbetter model (Ch. 3) has not been used to examine phase coexistence in model membranes, we will compare the x-ray data with the NMR and fluorescence microscopy data to calibrate the GIWAXS method. Using Figure 6.18, we can compare trends in $S_{mol}$ values as determined by GIWAXS and NMR. Also, we can determine if the x-ray data are in agreement with $T_{mix}$ values as determined by fluorescence microscopy and NMR.

**Comparison of $S_{mol}$ values.** When there is two phase coexistence, the two $S_{mol}$ values as determined by GIWAXS are always significantly larger than the two $S_{mol}$ values as determined by $^2$H NMR. This was also the case for mixtures of DPPC and cholesterol (see Fig. 5.8). The two $S_{mol}$ values do not reflect the same physical quantity because of the different assumptions made in the two different methods. The most obvious difference is that the GIWAXS fits make the assumption that the chains are infinitely long straight rods. NMR does not make this assumption: the order parameter is determined for each methylene chain segment separately and then averaged. At high temperatures with a single $S_{mol}$ value, the NMR and GIWAXS values are in better agreement. We believe this is an accident caused by two competing effects. First, we have observed that the GIWAXS $S_{mol}$ values are consistently higher that the NMR values. Second, the NMR $S_{mol}$ reports on chain order for only the deuterated DPPC, whereas the GIWAXS $S_{mol}$ is an average order

parameter for all the lipids. The saturated DPPC chains are likely to be more ordered than the unsaturated DOPC chains.

The $S_{mol}$ values for the coexisting Lo and Ld phases are not very sensitive to temperature or composition. In the ternary mixtures at low temperature, the GIWAXS $S_{mol}$ values for the Ld phases were close to 0.5 and the Lo $S_{mol}$ values were all near 0.9. The mixtures we studied with GIWAXS only varied in cholesterol concentration. Since we know the tie lines are roughly horizontal with an upward slope toward higher DPPC concentration (see Fig. 1.7), we can be confident that these mixtures do not fall on the same tie line. Therefore, our observation that the $S_{mol}$ values for the Ld and Lo phases are very similar as a function of temperature and composition suggests that chain orientational order is similar for different Lo phase (or Ld phase) compositions as we move along the liquid-liquid phase boundary.

We are not at all suggesting that the Lo (or Ld) phase has a single set of properties. This is a common misconception, which Clarke et al. (2006) have shown to be untrue by studying properties of the Lo phase using NMR and powder WAXS in systems of DPPC and cholesterol for a variety of temperatures and compositions. Also, mixtures of DOPC and cholesterol are not considered to phase-separate at any temperature (Filippov et al., 2003), and yet our GIWAXS measurements show that the addition of 40% cholesterol significantly orders the chains. At least for the DOPC/cholesterol system, the liquid phase has a continuum of properties, from Ld to more Lo-like.

If the $S_{mol}$ values for each phase changed significantly as a function of temperature or composition for the samples in the Ld/Lo coexistence region, we could possibly determine tie lines from the GIWAXS data. To do so, we would compare the $S_{mol}$ values determined for a mixture in the Ld/Lo region to the $S_{mol}$ values along the

two-phase boundary to determine which compositions could make up endpoints of a tie line through the given mixture. Our data suggest this is not possible.

**Comparison of miscibility transition temperatures ($T_{mix}$).** In the following discussion, $T_{mix}^{NMR}$ is the NMR $T_{mix}$ temperature, $T_{mix}^{Fluor}$ is the fluorescence microscopy $T_{mix}$ temperature, $T_{mix}^{WAXS}$ refers to the temperature break between single and double $S_{mol}$ values as determined by GIWAXS, and $T_{mix}^{LAXS}$ refers to the temperature break between the observation of double and single lamellar repeat spacings. For 1:1 DOPC:DPPC + 15% cholesterol and 1:1 DOPC:DPPC + 20% cholesterol, $T_{mix}^{WAXS}$ and $T_{mix}^{LAXS}$ agree with $T_{mix}^{NMR}$ and $T_{mix}^{Fluor}$ to within the 5˚C resolution of the x-ray experiments (see Fig. 6.18A and B). For the higher cholesterol concentrations, 25% and 30%, there is agreement between $T_{mix}^{Fluor}$ and $T_{mix}^{WAXS}$ (see Fig. 6.18C and D). However, the other data are not in complete agreement. First of all, there is a single lamellar repeat at temperatures with two $S_{mol}$ values as determined by GIWAXS. Lamellar repeat spacings can be misleading. As discussed in Section 6.3, the absence of two lamellar repeats does not necessarily imply a single phase. Second, $T_{mix}^{NMR}$ is lower than the 5˚C $T_{mix}^{WAXS}$ range. However, this discrepancy is not large and could be accounted for by a +5˚C relative shift of $T_{mix}^{NMR}$. This is not unreasonable given the assumptions and uncertainties associated with both methods. Determination of $T_{mix}^{NMR}$ involves deciding when the $^2$H NMR spectrum is composed of two overlapping $\phi$ distributions. Similarly, determination of $T_{mix}^{WAXS}$ involves deciding if the GIWAXS data is described by one or two overlapping peaks. For the 25% and 30% cholesterol samples, the third and largest discrepancy is between $T_{mix}^{NMR}$ and $T_{mix}^{Fluor}$. By comparing $T_{mix}^{NMR}$ values for samples with and without fluorescent dye, Veatch et al. (2007a) have shown that the effect of dye is to increase $T_{mix}^{NMR}$, which helps explain this discrepancy.

The disagreement between $T_{mix}^{NMR}$ and $T_{mix}^{WAXS}$ at the higher cholesterol concentrations makes sense because the higher cholesterol concentations (25% and

30%) are closer to the critical point (Sarah Veatch, personal communication). Thus, the tie lines are shorter and we would expect the Ld and Lo phases to have more similar properties, making deconvolution of the NMR or x-ray data more challenging and error-prone.

In order to make $T_{mix}^{WAXS}$ agree with $T_{mix}^{NMR}$ for 1:1 DOPC/DPPC with 25% and 30% cholesterol, we would have to change our criteria for rejecting the double order parameter fits. The current criteria (see also 6.2.3) are that the double order parameter fit is rejected if any of the double order parameter fitting parameters ($I_{back}$, $m_1$, $m_2$, $A_1$, or $A_2$) had error of greater than 1/3 of the value of the parameter. In order to make the x-ray and NMR data agree for 1:1 DOPC/DPPC + 25% cholesterol, we would have to reject the double order parameter fit at 30˚C, requiring an error cutoff of 1/10 of the parameter value instead of 1/3. In order to make the x-ray and NMR data agree for 1:1 DOPC/DPPC + 30% cholesterol, we would have to reject the double order parameter fit at 25˚C, requiring an error cutoff of 1/20 of the parameter value instead of 1/3. In both cases, we would also have to accept a single order parameter fit with negative normalized data at high $\phi$.

When comparing $T_{mix}$ values, it is intriguing to consider the effect of differences in averaging between $^2$H NMR and x-ray methods. A GIWAXS image is a spatial average of very fast snapshots of the system. The $^2$H NMR data are time-averaged for each molecule on a microsecond time scale, so if molecules diffuse into coexisting domains faster than that, the data will indicate only one phase. If the domains are macroscopic, GIWAXS and NMR should both report phase coexistence. If the domains are smaller than 20 nm, the $^2$H NMR signal will be averaged (Bloom and Thewalt, 1995). On the other hand, in an x-ray experiment, the scattering from a small domain with different chain ordering properties is recorded faster than the lipids can diffuse away. Arguing along these lines, we might expect the GIWAXS method

to give a higher $T_{mix}$ than NMR because the domains must be larger before NMR can detect them. For our data, this was indeed the case. Domains must be greater than the diffraction limit of light, ~0.5 microns, before being detectable with optical microscopy. If distance scale sensitivity were the only factor affecting $T_{mix}$, $T_{mix}^{Fluor}$ should be the lowest. However, as discussed above, the presence of fluorescent dye may tend to increase $T_{mix}^{Fluor}$.

## 6.5 Conclusion

Fits to the GIWAXS $I(\phi)$ data suggest the presence of liquid-liquid coexistence in ternary mixtures of DOPC, DPPC, and cholesterol. Our results are in relatively good agreement with $^2$H NMR and fluorescence microscopy, suggesting that our method of determining if two order parameters are necessary to fit the chain-chain scattering data is a valid way of deciding if a mixture is phase-separated into two fluid phases. On the other hand, while the presence of double lamellar repeat spacings in well-equilibrated samples is proof of phase separation, their absence is inconclusive.

Many methods used to examine liquid-liquid phase coexistence use a potentially perturbing probe. Given the recent experiments showing that fluorescent dye can have a large effect on phase behavior (Ayuan and Cohen, 2006; Veatch et al., 2007a; Zhao et al., 2007b), the availability of another probe-independent method for examining liquid-liquid phase coexistence in model membranes is useful. Our data add to the evidence that liquid-liquid phase separation does indeed occur in probe-free model membrane mixtures.

Veatch et al. have shown that NMR can be a useful complement to fluorescence microscopy experiments. Our GIWAXS method provides another way of examining model membrane phase behavior and characterizing coexisting Ld and Lo phases. Both GIWAXS and NMR can be used to determine $T_{mix}$ temperatures and

the chain ordering properties in the different coexisting phases. In addition, Filippov et al. (2004) and Polozov and Gawrisch (2006) have shown how NMR techniques can be used to measure diffusion coefficients in the coexisting phases. Although x-ray scattering cannot be used to measure the dynamic property of diffusion, GIWAXS provides a direct measurement of lateral positional ordering (chain packing), which is not directly observable from NMR. Thus, NMR and x-ray scattering are complementary techniques for examining lipid physical properties. Clarke et al. (2006) have shown that a combination of powder WAXS and NMR data is useful for characterizing Lo phase properties. In the future, interesting observations from microscopy experiments on model membranes may warrant more careful investigation of the physical properties of the system with techniques such as GIWAXS.

# Chapter 7 - Conclusion

## 7.1 Summary of results

The angular ($\phi$) distribution of scattering intensity in a GIWAXS image can give information about the chain orientational order in liquid phases which is not available from powder samples. In order to calculate the chain orientational distribution function $f(\beta)$ and chain order parameter $S_{mol}$ from $I(\phi)$ data, we used the Leadbetter model, which assumes that the chains are infinitely long rods. This analysis approach has been applied to a number of liquid crystal systems, but to our knowledge has not been applied to model membrane systems since Levine and Wilkins' studies of egg lecithin/cholesterol mixtures (Levine, 1970; Levine and Wilkins, 1971).

Using this analysis approach, we were able to reproduce the reported trends in NMR order parameters as a function of cholesterol content for DOPC/cholesterol (25˚C) and DPPC/cholesterol (45˚C). In both these systems, the addition of 40% cholesterol more than doubles $S_{mol}$, and yet the lateral positional order remains low as indicated by the large $q$-width of the WAXS peak. This decoupling of chain orientational order and lateral positional order is characteristic of the Lo phase.

In addition to calculating $S_{mol}$ values, we combined information about $f(\beta)$ (chain orientational order) with $d_{cc}$ (lateral positional order) to calculate areas for lipids in the liquid phase, based entirely on the GIWAXS data. Although WAXS data is often used to calculate areas for gel phases (Tristram-Nagle et al., 1993, 2002), most x-ray methods for calculating liquid-phase lipid areas are based on combining lamellar repeat data with volume measurements (Nagle and Tristram-Nagle, 2000). Our calculations for lipid areas from the GIWAXS data agree to within 5% with the Nagle group's area measurements based on LAXS data. This is reasonable agreement,

especially considering the large discrepancies in the literature for areas of liquid phase lipids (Nagle and Tristram-Nagle, 2000). We reproduced the trend of decreasing area as a function of cholesterol content for DOPC/cholesterol mixtures, showing that our approach for calculating areas from the GIWAXS data is reasonable.

In addition to calibrating the GIWAXS method based on comparisons to literature values for areas and NMR order parameters, we extended the method to study Ld/Lo phase coexistence in ternary mixtures of 1:1 DOPC/DPPC + cholesterol (15%, 20%, 25%, and 30%). In these ternary systems at low temperatures, the $I(\phi)$ data were best fit by assuming two distributions of chains (two order parameters), while at high temperature the data were well fit by assuming a single order parameter. In addition, we observed two lamellar repeat spacings in these mixtures, providing further evidence of phase coexistence. Our $T_{mix}$ values based on x-ray work agree reasonably (to within the 5-10˚C steps used) with the $T_{mix}$ values based on the NMR and fluorescence microscopy work of Veatch et al. (Veatch and Keller, 2003b; Veatch et al., 2004; Veatch et al., 2007b).

While liquid-liquid coexistence in ternary mixtures such as DOPC, DPPC, and cholesterol is well-established by a variety of techniques (microscopy, NMR, FRET), phase coexistence in binary mixtures of DPPC and cholesterol is controversial. Although fluorescence microscopy indicates neither liquid-liquid nor gel-liquid coexistence in DPPC/cholesterol mixtures (Veatch and Keller, 2005b), other methods such as NMR indicate the presence of phase coexistence (gel/liquid at low temperature and liquid/liquid at high temperature) in this system (Vist and Davis, 1990). We observed no conclusive evidence of phase coexistence in DPPC/cholesterol based on x-ray scattering. This null result is interesting in the context of control samples for which fluorescence microscopy images contain macroscopic domains (showing either gel-liquid or liquid-liquid coexistence). For 1:1 DOPC/DPPC (25˚C), we observed

two WAXS peaks (one broad and one narrow in $q$-width), in agreement with the observation of gel-liquid coexistence by fluorescence microscopy (Veatch and Keller, 2003b). For ternary mixtures of DOPC/DPPC/cholesterol known to separate into macroscopic Ld and Lo domains, we observed two lamellar repeats and found that the $I(\phi)$ data were best fit by assuming two order parameters. Our null result for phase coexistence in the DPPC/cholesterol system adds to a long list of conflicting literature for this system. At low temperature, some of the discrepancies in the literature may result from slow equilibration when slowly diffusing gel phases are involved.

We have shown that GIWAXS can be useful for studying chain order and liquid-liquid phase coexistence in model membranes. We have compared our data to $^2$H NMR, another probe-free method for order parameter determination and phase coexistence identification. These two techniques are complementary. Compared with x-ray scattering, NMR provides much more detailed information about chain orientational order as order parameters can be measured for each chain segment and for phospholipids and cholesterol separately. Although GIWAXS provides only global information about chain orientational order, it provides a direct measurement of lateral chain packing, a property which NMR can measure only indirectly.

## 7.2 Future directions

### 7.2.1 Other systems of interest

Now that we have characterized the GIWAXS method for studying chain orientational order in a well-studied system, there are many possible interesting applications. The following are suggestions for other systems to study.

**(1) Other outer leaflet models.** POPC/sphingomyelin/cholesterol is a more realistic model for the outer leaflet of the cell membrane than DOPC/DPPC/cholesterol. POPC/SM/cholesterol would have been a poor choice for a

test system because the previously reported observation of liquid-liquid coexistence in this system (Veatch and Keller, 2005a) may be an artifact due to fluorescence probe oxidation effects (Zhao et al., 2007b). The fact that a small amount of impurity in this system can cause large-scale demixing into two liquid phases suggests that POPC/SM/cholesterol may be a highly nonideal mixture (Veatch et al., 2007a). A comparison of GIWAXS data for this mixture to our DOPC/DPPC/cholesterol data would be of interest.

**(2) Inner leaflet lipids.** Much lipid work has focused on phosphatidylcholines (PCs). The inner leaflet contains a large amount of phosphatidylethanolamines (PEs) and charged lipids such as phosphatidylserines (PSs). An investigation of the structural properties of these lipids is particularly interesting because inner leaflet models do not phase-separate into two liquid domains (Wang and Silvius, 2001). The PE headgroup is much smaller than the PC headgroup, and so pure DLPE (and other PEs) form an Lβ gel phase rather than Lβ' (McIntosh and Simon, 1986). In the fluid phase, NMR measurements show that POPE chains are more ordered than POPC chains, and that the addition of 45% cholesterol results in a smaller increase in the POPE order parameter in comparison to POPC (Lafleur et al., 1990; Paré and Lafleur, 1998). It has been proposed that the small PE headgroup restricts the conformational freedom of the acyl chains (Lafleur et al., 1990). This is the same line of reasoning as the umbrella model (Huang and Feigenson, 1999): the chains must straighten in both the gel phase (untilted chains in the Lβ phase instead of Lβ') and the fluid phase in order to be covered by the PE headgroup. We hypothesize that angular ($\phi$) distribution of scattering in a GIWAXS image would be much lower for POPE compared with POPC.

**(3) Mixtures with different sterols.** Cholesterol is the major sterol found in mammalian membranes, but other molecules can function like cholesterol. In fact,

viable cholesterol-free mice (with desmosterol replacing cholesterol) have been genetically engineered (Wechsler et al., 2003). Ergosterol, found in fungal cells, and the plant sterols sitosterol and stigmasterol have been found to function similarly to cholesterol in model systems (Xu et al., 2001). The increase in chain NMR order parameters as a result of incorporation of sterol into fluid phase bilayers depends on the type of sterol: cholesterol, lanosterol, ergosterol, and others (Urbina et al., 1995). The effect of sterol on the ability of the chains to form an ordered, tightly packed state has been linked to their effect on Lo domain formation; some sterols inhibit domains while others, like cholesterol, promote domain formation (Wang et al., 2004; Xu and London, 2000; Xu et al., 2001).

**(4) Lipid/ceramide mixtures.** Ceramides, lipids formed by conversion of sphingomyelins by sphingomyelinase, have been reported to displace cholesterol from liquid ordered domains (Megha and London, 2004). Because of its small headgroup, ceramide can take on the structural role of cholesterol and cause ordering of acyl chains; however, a ceramide-rich ordered phase is thought to have different properties than a cholesterol-rich ordered phase (Megha and London, 2004). Rapid increase in ceramide levels due to sphingomyelinase action has been postulated to play a role in the formation of transient ordered domains (rafts) in the cell membrane (Feigenson, 2006).

**(5) Membranes with peptides.** The Salditt group has studied lipid/peptide interactions using experimental and simulated GIWAXS data (Spaar et al., 2004). Currently, the Nagle lab is studying cholesterol-sequestering peptides using both WAXS (chain-chain scattering) and LAXS (scattering from lamellae); they plan to investigate the effect of these peptides on chain order by analysis of the GIWAXS data using the approach described in this thesis. One question is whether these cholesterol-sequestering peptides induce domains in the membrane (Epand, 2006).

### 7.2.2 Correlation between chain order and other structural properties

The correlation between increased chain order (straighter chains) and increased hydrophobic thickness or decreased area is direct and easily explained (Petrache et al., 2000), but the relationships between chain order and other physical properties are not as clear-cut. Recently, Henriksen et al. (2006) have explored the relationship between chain order and elastic properties. They observed a linear relationship between the bending modulus and NMR first moment ($M_1$) for POPC mixed with several different sterols; they called the correlation between bending modulus and chain order "universal." The Nagle lab has measured the bending modulus of DOPC/cholesterol mixtures using their diffuse scattering method; the addition of 40% cholesterol to DOPC causes a negligible change in the bending modulus (Tristram-Nagle et al., 2007; see Liu and Nagle, 2004 for methodology). However, we have shown in this thesis that chain orientational order in DOPC + 40% cholesterol is almost double that in DOPC (see Ch. 4). This suggests that the correlation between bending modulus and chain order observed by Henriksen et al. (2006) is not universal.

Tristram-Nagle and Nagle (2007) have reported that HIV fusion peptide dramatically increases the bending modulus of DOPC; the Nagle lab has also observed a change in the elastic properties of DOPC with alamethicin addition (unpublished). It would be interesting to see if these peptides cause changes in chain order (both orientational and lateral positional order) using GIWAXS.

The Nagle lab is particularly well-situated to investigate the correlation between chain order (using GIWAXS) and elastic properties (using LAXS). The same sample can be used for both measurements; at CHESS we frequently switched between the GIWAXS setup and the Nagle lab's LAXS setup over the course of an experiment.

### 7.2.3 Comparison to molecular dynamics simulations

In this thesis, we have applied a simple analytical model to study chain orientational order. Spaar and Salditt (2003) have demonstrated the value of comparing experimental GIWAXS data to GIWAXS images constructed from the Fourier transforms of molecular dynamics (MD) simulations. The simple Leadbetter model has advantages, in that it can be applied to a large set of data and to ternary mixtures, for which simulations are time-consuming and costly. However, a comparison to simulations allows for more detailed interpretations on the molecular level. In addition, GIWAXS data provide another way to check MD simulations against experimental data. [Lipid areas, NMR order parameter profiles, and electron density profiles can all be calculated from MD simulations and compared to experimental data (for example see Smondyrev and Berkowitz, 1999).] J. Sachs and A. Grossfield are collaborating with the Nagle group to produce GIWAXS images from DOPC/cholesterol MD simulations for comparison to the data presented in this thesis.

# APPENDIX A
# Examples of failures of the Leadbetter formula

## A.1 Summary

The purpose of this appendix is to show two situations where the Leadbetter formula for $I(\phi_L)$ fails and the Toombes formula gives the correct behavior:

1. The Leadbetter formula results in an incorrect invariant.
2. The Leadbetter formula fails when all the rods are oriented at $\beta = \pi/2$.

The appendix also gives examples where both the Leadbetter formula and Toombes formula give reasonable results:

1. Both give a reasonable result in the case of a powder sample.
2. Both formulas give a reasonable result when all the rods are oriented with angle $\beta_0 < \pi/2$.

The calculations shown in this appendix were done by G. E. S. Toombes (unpublished). The Leadbetter formula and Toombes formula were discussed in Ch. 3 and are repeated here for clarity. The Leadbetter formula (Leadbetter and Norris, 1979) is:

$$I(\phi_L) = C \int_{\beta=\phi_L}^{\beta=\pi/2} \frac{\sec^2 \phi_L f(\beta) \sin \beta d\beta}{\sqrt{\tan^2 \beta - \tan^2 \phi_L}}. \quad \text{(A.1)}$$

The Toombes formula (Busch et al., 2007) is:

$$I(\phi_L) = A \int_{\beta=\phi_L}^{\beta=\pi/2} \frac{\sec \phi_L f(\beta) \tan \beta d\beta}{\sqrt{\tan^2 \beta - \tan^2 \phi_L}}. \quad \text{(A.2)}$$

## A.2 Calculation of the invariant

The first test is determining if the two equations yield the correct invariant for the scattering. Assuming rotational symmetry about the $z$ axis, the following equation in general must hold true (see Ch.3 for discussion):

$$Const = \int_{\phi_L} \int_{q} I(q,\phi_L) q^2 \sin\left(\frac{\pi}{2} - \phi_L\right) dq d\phi_L = \int_{\phi_L} \int_{q} I(q,\phi_L) q^2 \cos\phi_L \, dq d\phi_L \qquad \text{(A.3)}$$

Equation A.3 states that the total scattering in all of **q** space for all sample orientations is a conserved quantity. Since Leadbetter's theory and the modification presented above both assume that all of the chain scattering occurs at only one value of $q$, the equation we need to test is:

$$Const \stackrel{?}{=} \int_{\phi_L=0}^{\phi_L=\pi/2} I(\phi_L) \cos\phi_L \, d\phi_L \qquad \text{(A.4)}$$

Note that Deutsch (1991) and Davidson et al. (1995) assume that the following equation should hold:

$$Const = \int_{\phi_L=0}^{\phi_L=\pi/2} I(\phi_L) d\phi_L \qquad \text{(A.5)}$$

Davidson et al. (1995) state: "As already implicitly noted [by Deutsch], no solid angle correction...needs to be made to calculate the integrated intensity because it is directly included in $I(\phi_L)$ by the solid angle of the detector itself." This statement is false because $I(\phi_L)$ is supposed to represent only the scattering measured by the detector for a particular orientation of the sample. In our case and the case of Leadbetter's model, sample orientations are averaged with respect to rotation about the z-axis. Unlike a powder sample for which the $\cos\phi_L$ term in the invariant calculation is unnecessary, our samples are not rotationally averaged with respect to the *x*-*y* axes. The solid angle must be taken into account when calculating the total scattering over all sample orientations (Alexander, 1969).

The following calculation will show that Eq. A.5 is indeed true for Leadbetter's formula; thus, the correct invariant, Eq. A.4, is not constant, evidence that Leadbetter's formula is faulty. We wish to solve the following integral:

$$\int_{\phi_L=0}^{\phi_L=\pi/2} I(\phi_L) d\phi_L = \int_{\phi_L=0}^{\phi_L=\pi/2} d\phi_L \int_{\beta=\phi_L}^{\beta=\pi/2} \frac{\sec^2\phi_L f(\beta) \sin\beta d\beta}{\sqrt{\tan^2\beta - \tan^2\phi_L}}. \qquad \text{(A.6)}$$

Switching the order of integration gives:

$$\int_{\phi_L=0}^{\phi_L=\pi/2} I(\phi_L)d\phi_L = \int_{\beta=0}^{\beta=\pi/2} f(\beta)\sin\beta \int_{\phi_L=0}^{\phi_L=\beta} \frac{d\phi_L}{\cos^2\phi_L\sqrt{\tan^2\beta-\tan^2\phi_L}}d\beta. \quad \text{(A.7)}$$

The inner integral can be solved by making the following substitutions:

$$\tan\phi_L = \tan\beta\sin\Omega \quad \text{where } \Omega = 0 \text{ to } \frac{\pi}{2} \quad \text{(A.8)}$$

$$\frac{d\tan\phi_L}{d\Omega} = \sec^2\phi_L\frac{d\phi_L}{d\Omega} = \tan\beta\cos\Omega$$

$$\frac{d\phi_L}{\cos^2\phi_L} = \tan\beta\cos\Omega d\Omega$$

$$\int_{\phi_L=0}^{\phi_L=\beta} \frac{d\phi_L}{\cos^2\phi_L\sqrt{\tan^2\beta-\tan^2\phi_L}} = \int_{\Omega=0}^{\Omega=\pi/2} \frac{\tan\beta\cos\Omega d\Omega}{\sqrt{\tan^2\beta-\tan^2\beta\sin^2\Omega}}$$

$$= \int_{\Omega=0}^{\Omega=\pi/2} \frac{\tan\beta\cos\Omega d\Omega}{\sqrt{\tan^2\beta(1-\sin^2\Omega)}}$$

$$= \frac{\pi}{2}$$

The outer integral in Eq. A.7 is equal to $1/(4\pi)$ from the normalization condition for $f(\beta)$. Inserting the results of A.8 into Eq. A.7, we obtain for the invariant using Leadbetter's equation for $I(\phi_L)$:

$$\int_{\phi_L=0}^{\phi_L=\pi/2} I(\phi_L)d\phi_L = \frac{1}{4\pi}\times\frac{\pi}{2} = \frac{1}{8}. \quad \text{(A.9)}$$

This is the same result reported in the literature for Leadbetter's model (Davidson et al., 1995), but as stated above, this integral should not yield a constant if $I(\phi_L)$ were derived correctly.

Now we will show that the Toombes' formula (Eq. A.2) does satisfy the correct formula for the invariant (Eq. A.4). Substituting Eq. A.2 into Eq. A.4 gives:

$$\int_{\phi_L=0}^{\phi_L=\pi/2} I(\phi_L)\cos\phi_L d\phi_L = \int_{\phi_L=0}^{\phi_L=\pi/2}\int_{\beta=\phi}^{\beta=\pi/2} \frac{\sec\phi_L f(\beta)\tan\beta d\beta}{\sqrt{\tan^2\beta-\tan^2\phi_L}}\cos\phi_L d\phi_L \quad \text{(A.10)}$$

$$= \int_{\phi_L=0}^{\phi_L=\pi/2}\int_{\beta=\phi}^{\beta=\pi/2} \frac{f(\beta)\tan\beta d\beta}{\sqrt{\tan^2\beta-\tan^2\phi_L}}d\phi_L$$

Switching the order of integration and pulling out a sin$\beta$ in order to make use of the normalization condition for $f(\beta)$, we obtain:

$$\int_{\phi_L=0}^{\phi_L=\pi/2} I(\phi_L)\cos\phi_L d\phi_L = \int_{\beta=0}^{\beta=\pi/2} f(\beta)\sin\beta d\beta \int_{\phi_L=0}^{\phi_L=\beta} \frac{1}{\cos\beta\sqrt{\tan^2\beta-\tan^2\phi_L}} d\phi_L \qquad \text{(A.11)}$$

The integral over $\phi_L$ can be simplified as follows to a form where clever substitution will help solve the integral:

$$\begin{aligned}
&\int_{\phi_L=0}^{\phi_L=\beta} \frac{1}{\cos\beta\sqrt{\tan^2\beta-\tan^2\phi_L}} d\phi_L \qquad \text{(A.12)}\\
&= \int_{\phi_L=0}^{\phi_L=\beta} \frac{1}{\cos\beta\sqrt{\tan^2\beta-\tan^2\phi_L}} \times \frac{\cos\phi_L\cos\beta}{\sqrt{\cos^2\phi_L\cos^2\beta}} d\phi_L\\
&= \int_{\phi_L=0}^{\phi_L=\beta} \frac{\cos\phi_L}{\sqrt{\sin^2\beta\cos^2\phi_L-\sin^2\phi_L\cos^2\beta}} d\phi_L\\
&= \int_{\phi_L=0}^{\phi_L=\beta} \frac{\cos\phi_L}{\sqrt{\sin^2\beta(1-\sin^2\phi_L)-\sin^2\phi_L\cos^2\beta}} d\phi_L\\
&= \int_{\phi_L=0}^{\phi_L=\beta} \frac{\cos\phi_L}{\sqrt{\sin^2\beta-\sin^2\phi_L}} d\phi_L
\end{aligned}$$

We now make the following substitutions to solve the integral over $\phi_L$:

$$\begin{aligned}
\sin\phi_L &= \sin\beta\sin\psi \quad \text{where } \psi = 0 \text{ to } \frac{\pi}{2} \qquad \text{(A.13)}\\
\cos\phi_L d\phi_L &= \sin\beta\cos\psi d\psi\\
\sqrt{\sin^2\beta-\sin^2\phi_L} &= \sqrt{\sin^2\beta-\sin^2\beta\sin^2\psi} = \sin\beta\cos\psi\\
\int_{\phi_L=0}^{\phi_L=\beta} \frac{1}{\cos\beta\sqrt{\tan^2\beta-\tan^2\phi_L}} d\phi_L &= \int_{\phi_L=0}^{\phi_L=\beta} \frac{\cos\phi_L}{\sqrt{\sin^2\beta-\sin^2\phi_L}} d\phi_L\\
&= \int_{\psi=0}^{\psi=\pi/2} \frac{\sin\beta\cos\psi}{\sin\beta\cos\psi} d\psi = \frac{\pi}{2}
\end{aligned}$$

Inserting the results of Eq. A.13 into Eq. A.11, we obtain for the Toombes formula for $I(\phi_L)$:

$$\int_{\phi_L=0}^{\phi_L=\pi/2} I(\phi_L)\cos\phi_L d\phi_L = \int_{\beta=0}^{\beta=\pi/2} f(\beta)\sin\beta d\beta \int_{\phi_L=0}^{\phi_L=\beta} \frac{1}{\cos\beta\sqrt{\tan^2\beta - \tan^2\phi_L}} d\phi_L \qquad (A.14)$$

$$= \frac{1}{4\pi}\times\frac{\pi}{2} = \frac{1}{8}.$$

The correct equation for the invariant is indeed a constant for the Toombes formula, while Leadbetter's formula does not result in the correct invariant calculation. This suggests an error in Leadbetter's formula.

## A.3 Results for Leadbetter's formula and the modified form for three cases

In order to further test the validity of Leadbetter's original equation and the modified form, the following discussion will consider three cases for the distribution of rods, or chains in the sample: (1) a powder sample; (2) a sample where all the rods have the same tilt angle $\beta = \beta_0$; and (3) a sample where all rods are tilted at the angle $\beta = \pi/2$. Both Leadbetter's original formula and the modified form give reasonable results for the first two cases (when $\beta_0 < \pi/2$), but Leadbetter's original formula does not give a reasonable result for the third case.

### A.3.1 Case 1: Powder sample

In the case of a powder sample, all orientations are equally likely and the chain orientational distribution function is a constant:

$$f(\beta) = \frac{1}{4\pi} \qquad (A.15)$$

The constant value satisfies the normalization condition:

$$\int_{\beta=0}^{\pi/2} f(\beta)\sin\beta d\beta = \frac{1}{4\pi} \qquad (A.16)$$

In the case of a powder pattern:

$$I(\phi_L) = \text{constant}. \qquad (A.17)$$

We will check that Eq. A.17 is valid for the Toombes formula and the Leadbetter formula. Using $f(\beta)$ (Eq. A.15) in the Leadbetter formula (Eq. A.1) gives:

$$I(\phi_L) = C\frac{1}{4\pi}\int_{\beta=\phi_L}^{\beta=\pi/2}\frac{\sec^2\phi_L \sin\beta d\beta}{\sqrt{\tan^2\beta - \tan^2\phi_L}} \tag{A.18}$$

$$= \frac{C}{4\pi}\int_{\beta=\phi_L}^{\beta=\pi/2}\frac{\sec^2\phi_L \sin\beta d\beta}{\sqrt{\tan^2\beta - \tan^2\phi_L}} \times \frac{\cos\beta}{\cos\beta}$$

$$= \frac{C}{4\pi}\int_{\beta=\phi_L}^{\beta=\pi/2}\frac{\sec^2\phi_L \sin\beta\cos\beta d\beta}{\sqrt{\sin^2\beta - \cos^2\beta\tan^2\phi_L}}$$

$$= \frac{C}{4\pi}\int_{\beta=\phi_L}^{\beta=\pi/2}\frac{\sec^2\phi_L \sin\beta\cos\beta d\beta}{\sqrt{1-(1+\tan^2\phi_L)\cos^2\beta}}$$

$$= \frac{C}{4\pi}\int_{\beta=\phi_L}^{\beta=\pi/2}\frac{\sec^2\phi_L \sin\beta\cos\beta d\beta}{\sqrt{1-\sec^2\phi_L\cos^2\beta}}$$

Making the substitutions $u = \sec^2\phi_L\cos^2\beta$ and $du = -2\sec^2\phi_L\cos\beta\sin\beta d\beta$ with limits on $u$=1 to 0 gives:

$$I(\phi_L) = \frac{C}{4\pi}\int_{u=1}^{u=0}\frac{-du}{2\sqrt{1-u}} \tag{A.19}$$

$$= \frac{C}{4\pi}\sqrt{1-u}\Big|_1^0 = \frac{C}{4\pi}$$

The Leadbetter formula gives a constant for $I(\phi_L)$ as expected.

Using $f(\beta)$ (Eq. A.15) in the Toombes formula (Eq. A.2) gives:

$$I(\phi_L) = A\frac{1}{4\pi}\int_{\beta=\phi_L}^{\beta=\pi/2}\frac{\sec\phi_L \tan\beta d\beta}{\sqrt{\tan^2\beta - \tan^2\phi_L}} \tag{A.20}$$

$$= \frac{A}{4\pi}\int_{\beta=\phi_L}^{\beta=\pi/2}\frac{\sec\phi_L \tan\beta d\beta}{\sqrt{\tan^2\beta - \tan^2\phi_L}} \times \frac{\cos\beta}{\cos\beta}$$

$$= \frac{A}{4\pi}\int_{\beta=\phi_L}^{\beta=\pi/2}\frac{\sec\phi_L \sin\beta d\beta}{\sqrt{\sin^2\beta - \cos^2\beta\tan^2\phi_L}}$$

$$= \frac{A}{4\pi}\int_{\beta=\phi_L}^{\beta=\pi/2}\frac{\sec\phi_L \sin\beta d\beta}{\sqrt{1-\sec^2\phi_L\cos^2\beta}}$$

Making the substitutions $u = \sec\phi_L \cos\beta$ and $du = -\sec\phi_L \sin\beta d\beta$ with limits on $u$=1 to 0 gives:

$$I(\phi_L) = \frac{A}{4\pi}\int_{u=1}^{u=0} \frac{-du}{\sqrt{1-u^2}} \tag{A.21}$$
$$= \frac{-A}{4\pi}\sin^{-1} u\Big|_1^0 \quad \text{using integral table}$$
$$= \frac{A}{8}$$

The Toombes formula also gives the expected result for the powder sample case.

### A.3.2 Case 2: Rods all have $\beta = \beta_0$.

In this case, the distribution function takes on the following form:

$$f(\beta) = C_0\delta(\beta - \beta_0), \tag{A.22}$$

where the constant $C_0$ is found by satisfying:

$$\int_{\beta=0}^{\pi/2} C_0\delta(\beta - \beta_0)\sin\beta d\beta = \frac{1}{4\pi} \tag{A.23}$$

Solving for $C_0$ we obtain finally for f(β):

$$f(\beta) = \frac{1}{4\pi\sin\beta_0}\delta(\beta - \beta_0), \tag{A.24}$$

The Toombes formula (Eq. A.2) becomes with the above $f(\beta)$:

$$I(\phi_L) = A \int_{\beta=\phi_L}^{\beta=\pi/2} \frac{1}{4\pi \sin\beta_0} \delta(\beta-\beta_0) \frac{\sec\phi_L \tan\beta d\beta}{\sqrt{\tan^2\beta - \tan^2\phi_L}} \tag{A.25}$$

$$= 0 \quad \text{for } \phi_L > \beta_0$$

$$= \text{Const} \times \frac{1}{\sin\beta_0} \frac{1}{\cos\phi_L} \frac{\tan\beta_0}{\sqrt{\tan^2\beta_0 - \tan^2\phi_L}} \quad \text{for } 0 \le \phi_L \le \beta_0$$

$$= \text{Const} \times \frac{1}{\cos\phi_L} \frac{\cos\beta_0}{\sqrt{\tan^2\beta_0 - \tan^2\phi_L}}$$

$$= \text{Const} \times \frac{1}{\cos\phi_L} \frac{1}{\sqrt{\sin^2\beta_0 - \cos^2\beta_0 \tan^2\phi_L}}$$

$$= \text{Const} \times \frac{1}{\sqrt{\sin^2\beta_0 \cos^2\phi_L - \cos^2\beta_0 \sin^2\phi_L}}$$

$$= \text{Const} \times \frac{1}{\sqrt{\sin^2\beta_0 (1-\sin^2\phi_L) - \cos^2\beta_0 \sin^2\phi_L}}$$

$$= \text{Const} \times \frac{1}{\sqrt{\sin^2\beta_0 - \sin^2\phi_L}}$$

In summary for $I(\phi_L)$ or the Toombes formula in the case of all rods oriented with $\beta=\beta_0$ we obtain:

$$I(\phi_L) = 0 \quad \text{for } \phi_L > \beta_0$$

$$= \text{Const} \times \frac{1}{\sqrt{\sin^2\beta_0 - \sin^2\phi_L}} \quad \text{for } 0 \le \phi_L \le \beta_0 \tag{A.26}$$

With the distribution function described by Eq. A.24, the Leadbetter formula (Eq. A.1) becomes:

$$I(\phi_L) = C \int_{\beta=\phi}^{\beta=\pi/2} \frac{1}{4\pi \sin\beta_0} \delta(\beta-\beta_0) \frac{\sec^2\phi_L \sin\beta d\beta}{\sqrt{\tan^2\beta - \tan^2\phi_L}} \tag{A.27}$$

$$= 0 \quad \text{for } \phi_L > \beta_0$$

$$= \text{Const} \times \frac{1}{\sin\beta_0} \frac{1}{\cos^2\phi_L} \frac{\sin\beta_0 d\beta}{\sqrt{\tan^2\beta_0 - \tan^2\phi_L}} \quad \text{for } 0 \le \phi_L \le \beta_0$$

$$= \text{Const} \times \frac{\cos\beta_0}{\cos\phi_L} \frac{1}{\sqrt{\sin^2\beta_0 - \sin^2\phi_L}}$$

In the last line the same steps as shown in Eq. A.25 were followed. In summary for $I(\phi_L)$ or the Leadbetter formula in the case of all rods oriented with $\beta=\beta_0$ we obtain:

$$\begin{aligned} I(\phi_L) &= 0 \quad \text{for } \phi_L > \beta_0 \\ &= \text{Const} \times \frac{\cos\beta_0}{\cos\phi_L} \frac{1}{\sqrt{\sin^2\beta_0 - \sin^2\phi_L}} \quad \text{for } 0 \le \phi_L \le \beta_0 \end{aligned} \tag{A.28}$$

Figure A.1 shows plots of the results of Eq. A.26 and Eq. A.28. Both plots are reasonable for $\beta<\pi/2$.

### A.3.3 Case 3: Rods all have $\beta= \pi/2$

The case of all rods with orientation $\beta=\pi/2$ is a special case of the one described in the previous section. For any given grain direction ($\chi$, $\beta= \pi/2$), scattering is concentrated on a circle through the poles (+$z$ and -$z$ axes). Since there is rotational symmetry about the z-axis, $I(\phi_L)d\phi_L$ should be proportional to $1/A_{ring}$, where $A_{ring}$ is the area of a ring in reciprocal space with $\phi_L$ between $\phi_L$ and $\phi_L+d\phi_L$: $A_{ring}=2\pi\sin(\pi/2-\phi_L)d\phi_L=2\pi\cos\phi_L d\phi_L$. The scattering intensity is given by:

$$I(\phi_L) \propto \frac{1}{A_{ring}} \propto \frac{1}{\cos\phi_L}. \tag{A.29}$$

Another way to think about this case is that the total intensity for any range $d\phi_L$ should be proportional to the size of the angular range. That is,

$$\int_{\phi_L}^{\phi_L+d\phi_L} I(\phi_L)\cos\phi_L d\phi_L \sim d\phi_L. \tag{A.30}$$

$I(\phi_L)\propto 1/\cos\phi_L$ is the scaling factor needed to produce the same intensity integrated over any range $d\phi_L$.

For the Toombes formula, Eq. A.26 with $\beta_0=\pi/2$ gives the expected result:

$$I(\phi_L) = \text{Const} \times \frac{1}{\sqrt{\sin^2\frac{\pi}{2} - \sin^2\phi_L}} = \text{Const} \times \frac{1}{\cos\phi_L}. \tag{A.31}$$

For the Leadbetter formula, Eq. A.28 with $\beta_0=\pi/2$ gives:

$$I(\phi_L) = \text{Const} \times \frac{\cos\frac{\pi}{2}}{\cos\phi_L} \frac{1}{\sqrt{\sin^2\frac{\pi}{2} - \sin^2\phi_L}} = 0 \qquad \text{(A.32)}$$

The Leadbetter formula does not yield a reasonable result in the case of rods all oriented with $\beta_0=\pi/2$. In our system, this corresponds to the case of all the chains lying in the plane of the membrane, an unphysical situation. In fact, this is an unlikely situation for all the systems studied in the liquid crystal literature with the Leadbetter formula, and so the distribution functions found using the Leadbetter formula are still reasonable, especially since much of the work in the literature was concerned with trends. Figure A.1 summarizes the results of the last two sections with a plot of $I(\phi_L)$ with three specific values of $\beta_0$.

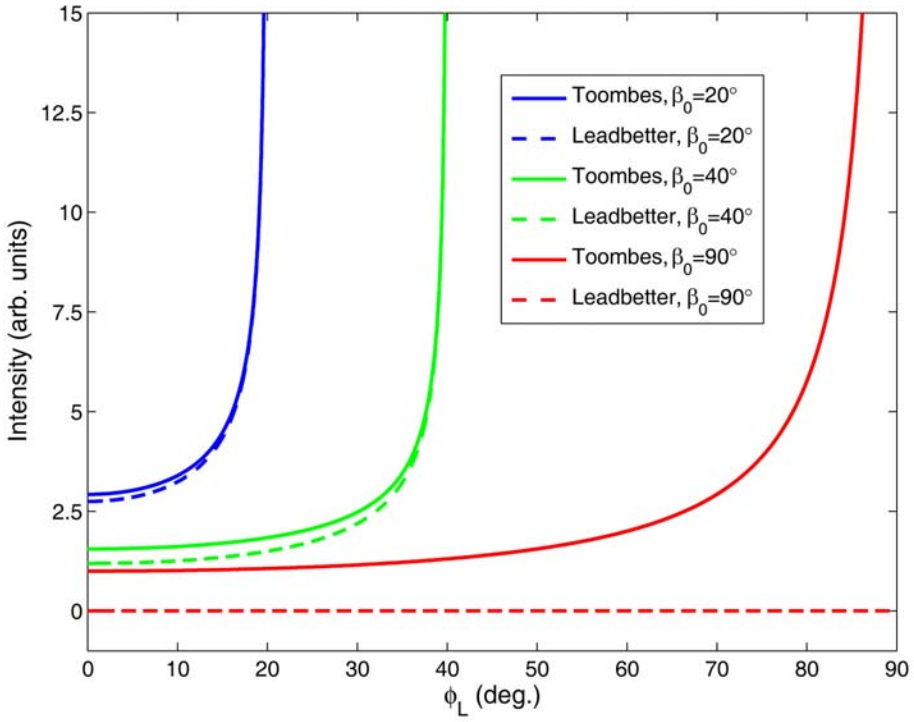


Figure A.1. Plot of $I(\phi_L)$ in the case that all rods are oriented with angle $\beta=\beta_0$ for three values of $\beta_0$: 20˚, 40˚, and 90˚. For this case, both the Leadbetter formula (Eq. A.28) and the Toombes formula (A.26) give reasonable results for $\beta_0<90$˚, while the Leadbetter result in unreasonable for $\beta_0=90$˚.

# APPENDIX B
# Calculation of $I(\phi_L)$ using the Maier-Saupe orientational distribution function

## B.1 Summary

In this appendix, we show the calculation of $I(\phi_L)$ using the Maier-Saupe orientational distribution function in the Toombes formula for $I(\phi_L)$. The first section explains the normalization of the Maier-Saupe distribution. The second section derives a formula for $I(\phi_L)$ using the normalized Maier-Saupe $f(\beta)$. For clarity we repeat the Toombes formula for $I(\phi_L)$ here (Busch et al., 2007; see full derivation in Ch. 3):

$$I(\phi_L) = A \int_{\beta=\phi}^{\beta=\pi/2} \frac{\sec\phi_L f(\beta)\tan\beta d\beta}{\sqrt{\tan^2\beta - \tan^2\phi_L}} \tag{B.1}$$

## B.2 Normalization of the Maier-Saupe distribution function

The final normalized form for the Maier-Saupe orientational distribution function is (Maier and Saupe, 1958, 1959, 1960; see de Gennes and Prost, 1993, p.66-70 for an explanation of the derivation in English):

$$f(\beta) = \frac{1}{Z}\exp(m\cos^2\beta) \tag{B.2}$$

where $m$ is a parameter which can take on any positive value and

the normalization constant $Z$ can be solved for with the normalization condition:

$$\int_{\beta=0}^{\pi/2} f(\beta)\sin\beta d\beta = \frac{1}{4\pi} \tag{B.3}$$

$$\int_{\beta=0}^{\pi/2} \frac{1}{Z}\exp(m\cos^2\beta)\sin\beta d\beta = \frac{1}{4\pi}$$

Substituting $x = \cos\beta$ gives:

$$Z = 4\pi\int_0^1 \exp(mx^2)dx\,. \tag{B.4}$$

Note in general:

$$\int \exp(au^2)du = \frac{\sqrt{\pi}}{2\sqrt{a}} erfi\left(u\sqrt{a}\right) \tag{B.5}$$

and

$$erfi(v) = \frac{2}{\sqrt{\pi}} \exp(v^2) D(v),$$

where *erfi* is the imaginary error function and *D* is Dawson's integral. Using Eq. B.5 in Eq. B.4, we get for *Z*:

$$\begin{aligned} Z &= 4\pi \frac{\sqrt{\pi}}{2\sqrt{m}} erfi\left(\sqrt{m}\right) \\ &= 4\pi \frac{\exp(m)}{\sqrt{m}} D\left(\sqrt{m}\right) \end{aligned} \tag{B.6}$$

## B.3 Calculation of $I(\phi_L)$ using the Maier-Saupe distribution function in the Toombes formula

The following derivation was done by G. E. S. Toombes and is unpublished. Inserting the Maier-Saupe orientational distribution function (Eq. B.2) into the Toombes formula (Eq. B.1) gives:

$$I(\phi_L) = \frac{A}{Z} \int_{\beta=\phi}^{\beta=\pi/2} \frac{\exp(m\cos^2\beta)\tan\beta d\beta}{\cos\phi_L \sqrt{\tan^2\beta - \tan^2\phi_L}} \tag{B.7}$$

The integral in Eq. B.7 can be solved by converting to a more convenient form:

$$\begin{aligned} I(\phi_L) &= \frac{A}{Z} \int_{\beta=\phi_L}^{\beta=\pi/2} \frac{\exp(m\cos^2\beta)\tan\beta d\beta}{\cos\phi_L \sqrt{\tan^2\beta - \tan^2\phi_L}} \times \frac{\cos\beta}{\cos\beta} \\ &= \frac{A}{Z} \int_{\beta=\phi_L}^{\beta=\pi/2} \frac{\exp(m\cos^2\beta)\sin\beta d\beta}{\cos\phi_L \sqrt{\sin^2\beta - \tan^2\phi_L \cos^2\beta}} \\ &= \frac{A}{Z} \int_{\beta=\phi_L}^{\beta=\pi/2} \frac{\exp(m\cos^2\beta)\sin\beta d\beta}{\cos\phi_L \sqrt{1 - (\tan^2\phi_L + 1)\cos^2\beta}} \\ &= \frac{A}{Z} \int_{\beta=\phi_L}^{\beta=\pi/2} \frac{\exp(m\cos^2\beta)\sin\beta d\beta}{\cos\phi_L \sqrt{1 - \dfrac{\cos^2\beta}{\cos^2\phi_L}}} \end{aligned} \tag{B.8}$$

The following substitutions can simplify the above equation:

$$\begin{aligned}
&\cos\beta = \cos\phi_{\mathrm{L}}\cos\psi \\
&\psi = 0 \to \frac{\pi}{2} \Rightarrow \beta = \phi_{\mathrm{L}} \to \frac{\pi}{2} \\
&\sqrt{1-\frac{\cos^2\beta}{\cos^2\phi}} = \sqrt{1-\cos^2\psi} = \sin\psi \\
&d(\cos\beta) = -\sin\beta d\beta = -\cos\phi_{\mathrm{L}}\sin\psi d\psi
\end{aligned} \tag{B.9}$$

Inserting the above substitutions into Eq. B.8 and simplifying gives:

$$I(\phi_{\mathrm{L}}) = \frac{A}{Z}\int_{\psi=0}^{\psi=\pi/2}\exp\left(m\cos^2\phi_{\mathrm{L}}\cos^2\psi\right)d\psi \tag{B.10}$$

We now convert Eq. B.10 into a form which can be found in an integral table by using the double angle formula $\cos^2 A = (\cos 2A + 1)/2$. Letting $a = m\cos^2\phi_{\mathrm{L}}$, Eq. B.10 becomes:

$$\begin{aligned}
I(\phi_{\mathrm{L}}) &= \frac{A}{Z}\int_{\psi=0}^{\psi=\pi/2}\exp\left(a\left(\frac{\cos 2\psi + 1}{2}\right)\right)d\psi \\
&= \frac{A}{Z}\exp\left(\frac{a}{2}\right)\int_{\psi=0}^{\psi=\pi/2}\exp\left(\frac{a\cos 2\psi}{2}\right)d\psi \\
&= \frac{A}{Z}\exp\left(\frac{a}{2}\right)\int_{y=0}^{y=\pi}\exp\left(\frac{a\cos y}{2}\right)\frac{dy}{2} \\
&= \frac{A}{Z}\exp\left(\frac{a}{2}\right)\int_{y=0}^{y=2\pi}\exp\left(\frac{a\cos y}{2}\right)\frac{dy}{4} \\
&= \frac{A}{Z}\exp\left(\frac{a}{2}\right)\int_{y=0}^{y=2\pi}\exp\left(\frac{a\sin y}{2}\right)\frac{dy}{4}
\end{aligned} \tag{B.11}$$

where in the last three lines we have substituted $y = 2\psi$, changed the upper limit of integration from $\pi$ to $2\pi$, and changed a cosine to a sine. The general form for this integral can be found in an integral table:

$$I_0(x) = \frac{1}{2\pi}\int_{Q=0}^{2\pi}\exp(x\sin Q)dQ \tag{B.12}$$

where $I_0(x)$ is a modified Bessel function of the first kind (Spiegel, 1998). Re-substituting $a = m\cos^2\phi_{\mathrm{L}}$, we obtain

$$I(\phi_L) = \frac{A}{Z} \times \exp\left(\frac{m\cos^2\phi_L}{2}\right) \times \frac{\pi}{2} I_0\left(\frac{m\cos^2\phi_L}{2}\right) \quad \text{(B.13)}$$

Inserting normalization constant $Z$ (Eq. B.6) into Eq. B.13 results in the final equation for $I(\phi_L)$:

$$I(\phi_L) = \frac{A}{8} \times \frac{\sqrt{m}}{\exp(m) D\left(\sqrt{m}\right)} \times \exp\left(\frac{m\cos^2\phi_L}{2}\right) \times I_0\left(\frac{m\cos^2\phi_L}{2}\right) \quad \text{(B.14)}$$

We used Eq. B.14 as a starting point for the data fitting equations.

# REFERENCES


Alexander, L. E. 1969. X-ray diffraction methods in polymer science. John Wiley and Sons, New York.

Alexander, L. E., and E. R. Michalik. 1959. X-ray diffraction by assemblages of line scatterers with application to linear polymers. *Acta Cryst.* 12: 105-108.

Almeida, P. F. F., W. L. C. Vaz, and T. E. Thompson. 1992. Lateral diffusion in the liquid phases of dimyristoylphosphatidylcholine/cholesterol lipid bilayers: a free volume analysis. *Biochemistry*. 31: 6739-6747.

Almeida, P. F. F., W. L. C. Vaz, and T. E. Thompson. 1993. Percolation and diffusion in three-component lipid bilayers: effect of cholesterol on an equimolar mixture of two phosphatidylcholines. *Biophys. J.* 64: 399-412.

Als-Nielsen, J., and D. McMorrow. 2001. Elements of modern x-ray physics. Wiley, New York.

Arndt, U. W. 1984. Optimum x-ray wavelength for protein crystallography. *J. Appl. Cryst.* 17: 118-119.

Ashcroft, N. W., and N. D. Mermin. 1976. Solid state physics. Rinehart and Winston, New York.

Ayuyan, A. G., and F. S. Cohen. 2006. Lipid peroxides promote large rafts: effects of excitation of probes in fluorescence microscopy and electrochemical reactions during vesicle formation. *Biophys. J.* 80: 2172-2183.

Barna, S. L., M. W. Tate, S. M. Gruner, and E. F. Eikenberry. 1999. Calibration procedures for charge-coupled device x-ray detectors. *Rev. Sci. Instrum.* 70: 2927-2934.

Baumgart, T., S. T. Hess, and W. W. Webb. 2003. Imaging coexisting fluid domains in biomembrane models coupling curvature and line tension. *Nature.* 425: 821-824.

Bevington, P. R. 1969. Data reduction and error analysis for the physical sciences. McGraw-Hill, New York.

Bloom, M., and J. L. Thewalt. 1995. Time and distance scales of membrane domain organization. *Mol. Membr. Biol.* 12: 9-13.

Brown, D. A., and E. London. 1997. Structure of detergent-resistant membranes: does phase separation occur in biological membranes? *Biochem. Biophys. Res. Commun*. 240: 1-7.

Brown, M. F., S. Lope-Piedrafita, G. V. Martinez, and H. I. Petrache. 2006. Solid-state deuterium NMR spectroscopy of membranes. *In* Handbook of Modern Magnetic Resonance. G. A. Webb, ed. Kluwer Academic Publishers, Dordrecht.

Buboltz, J.T., and G. W. Feigenson. 1999. A novel strategy for the preparation of liposomes: rapid solvent exchange. *Biochim. Biophys. Acta.* 1417: 232-245.

Busch, P., S. Krishnan, M. Paik, G. E. S. Toombes, D.-M. Smilgies, S. M. Gruner, and C. K. Ober. 2007. Surface induced tilt propagation in thin films of semifluorinated liquid crystalline side chain block copolymers. *Macromolecules.* 40: 81-89.

Caffrey, M. 1984. X-radiation damage of hydrated lecithin membranes detected by real-time x-ray diffraction using wiggler-enhanced synchrotron radiation as the ionizing radiation source. *Nucl. Instr. and Meth. in Phys. Res.* 222: 329-338.

Chiang, Y.-W., J. Zhao, J. Wu, Y. Shimoyama, J. H. Freed, and G. W. Feigenson. 2005. New method for determining tie-lines in coexisting membrane phases using spin-label ESR. *Biochim. Biophys. Acta.* 1668: 99-105.

Chiras, D. D. 1999. Human biology. Jones and Bartlett, Sudbury.

Chu, N., N. Kučerka, Y. Liu, S. Tristram-Nagle, and J. F. Nagle. 2005. Anomalous swelling of lipid bilayer stacks is caused by softening of the bending modulus. *Phys. Rev. E.* 71:041904.

Clarke, J. A., A. J. Heron, J. M. Seddon, and R. V. Law. 2006. The diversity of the liquid ordered (Lo) phase of phosphatidylcholine/cholesterol membranes: a variable temperature multinuclear solid-state NMR and x-ray diffraction study. *Biophys. J.* 90: 2383-2393.

Cortijo, M., A. Alonso, J. C. Gomez-Fernandez, and D. Chapman. 1982. Intrinsic protein-lipid interactions: infrared spectroscopic studies of gramicidin A, bacteriorhodopsin, and $Ca^{2+}$-ATPase in biomembranes and reconstituted systems. *J. Mol. Biol.* 157: 597-618.

Davidson, P., D. Petermann, and A. M. Levelut. 1995. The measurement of the nematic order parameter by x-ray scattering reconsidered. *J. Phys. II France*. 5: 113-131.

Davis, J. H. 1979. Deuterium magnetic resonance study of the gel and liquid crystalline phases of dipalmitoyl phosphatidylcholine. *Biophys. J.* 27: 339-358.

de Almeida, R. F. M., A. Fedorov, and M. Prieto. 2003. Sphingomyelin/phosphatidylcholine/cholesterol phase diagram: boundaries and composition of lipid rafts. *Biophys. J.* 85: 2406-2416.

de Gennes, P. G., and J. Prost. 1993. The physics of liquid crystals. Clarendon Press, Oxford.

Deutsch, M. 1991. Orientatonal order determination in liquid crystals by x-ray diffraction. *Phys. Rev. A*. 44: 8264-8270.

de Vries, A. 1972. On the calculation of the molecular cylindrical distribution function and the order parameter from x-ray diffraction data of liquid crystals. *J. Chem. Phys.* 56: 4489-4495.

Dietrich, C., L. A. Bagatolli, Z. N. Volovyk, N. L. Thompson, M. Levi, K. Jacobson, and E. Gratton. 2001. Lipid rafts reconstituted in model membranes. *Biophys. J.* 80: 1417-1428.

Douliez, J.-P., A. Léonard, and E. J. Dufourc. 1995. Restatement of order parameters in biomembranes: calculation of C-C bond order parameters from C-D quadrupolar splittings. *Biophys. J.* 68: 1727-1739.

Dumas, F., M. C. Lebrun, and J.-F. Tocanne. 1999. Is the protein/lipid hydrophobic matching principle relevant to membrane organization and function? *FEBS Letters.* 458: 271-277.

Edidin, M. 2003. The state of lipid rafts: from model membranes to cells. *Annu. Rev. Biophys. Biomol. Struct.* 32: 257-283.

Ege, C., M. Ratajczak, J. Majewski, K. Kjaer, and K. Y. C. Lee. 2006. Evidence for lipid/cholesterol ordering in model lipid membranes. *Biophys. J.* 91: L01-L03.

Engelman, D. M., and J. E. Rothman. 1972. The planar organization of lecithin-cholesterol bilayers. *J. Biol. Chem.* 247: 3694-3697.

Epand, R. M. 2006. Cholesterol and the interaction of proteins with membrane domains. *Prog. Lipid Res.* 45: 279-294.

Estep, T. N., D. B. Mountcastle, R. L. Biltonen, and T. E. Thompson. 1978. Studies on the anomalous thermotropic behavior of aqueous dispersions of dipalmitoylphosphatidylcholine-cholesterol mixtures. *Biochemistry*. 17: 1984-1989.

Evans, E. and Needham, D. 1986. Giant vesicle bilayers composed of mixtures of lipids, cholesterol and polypeptides. *Faraday Discuss. Chem. Soc.* 81: 267-280.

Feigenson, G. W. 2006. Phase behavior of lipid mixtures. *Nature Chem. Biol.* 2: 560-563.

Feigenson, G. W., and J. T. Buboltz. 2001. Ternary phase diagram of dipalmitoyl-PC/dilauroyl-PC/cholesterol: nanoscopic domain formation driven by cholesterol. *Biophys. J.* 80: 2775-2788.

Filippov, A., G. Orädd, and G. Lindblom. 2003. The effect of cholesterol on the lateral diffusion of phospholipids in oriented bilayers. *Biophys. J.* 84: 3079-3086.

Filippov, A., G. Orädd, and G. Lindblom. 2004. Lipid lateral diffusion in ordered and disordered phases in raft mixtures. *Biophys. J.* 86: 891-896.

Finean, J. B. 1990. Interaction between cholesterol and phospholipid in hydrated bilayers. *Chem. Phys. Lipids.* 54: 147-156.

Finegold, L., and M. A. Singer. 1993. Cholesterol/phospholipid interactions studied by differential scanning calorimetry: effect of acyl chain length and role of the C(17) sterol side group. *In* Cholesterol in Membrane Models. L. Finegold, ed. CRC Press, Boca Raton.

Fung, B. K.-K., and L. Stryer. 1978. Surface density determination in membranes by fluorescence energy transfer. *Biochemistry.* 17: 5241-5248.

Gandhavadi, M., D. Allende, A. Vidal, S. A. Simon, and T. J. McIntosh. 2002. Structure, composition, and peptide binding properties of detergent soluble bilayers and detergent resistant rafts. *Biophys. J.* 82: 1469-1482.

Gennis, R. B. 1989. Biomembranes: molecular structure and function. Springer-Verlag, New York.

Greenwood, A. I., S. Tristram-Nagle, and J. F. Nagle. 2006. Partial molecular volumes of lipids and cholesterol. *Chem. Phys. Lipids.* 143: 1-10.

Gruner, S. M., M. W. Tate, G. L. Kirk, P. T. C. So, D. C. Turner, and D. T. Keane. 1988. X-ray diffraction study of the polymorphic behavior of n-methylated dioleoylphosphatidylethanolamine. *Biochemistry.* 27: 2853-2866.

Guinier, A. 1963. X-ray diffraction in crystals, imperfect crystals, and amorphous bodies. W. H. Freeman and Company, San Francisco.

Haase, W., Z. X. Fan, and H. J. Müller. 1988. Order parameter and packing studies in nematic and smectic A phases by x-ray diffraction. *J. Chem. Phys.* 89: 3317-3322.

Haberkorn, R. A., R. G. Griffin, M. D. Meadows, and E. Oldfield. 1977. Deuterium nuclear magnetic resonance investigation of the dipalmitoyl lecithin-cholesterol-water system. *J. Am. Chem. Soc.* 99: 7353-7355.

Habiger, R. G. K., J. M. Cassal, H. J. M. Kempen, and J. Seelig. 1992. Influence of stigmastanol and stigmastanyl-phosphorylcholine, two plasma cholesterol lowering substances, on synthetic phospholipid membranes. A $^{2}$H- and $^{31}$P-NMR study. *Biochim. Biophys. Acta.* 1103: 69-76.

Hajduk, D. A. 1994. Morphological transitions in block copolymers. Ph. D. Thesis, Princeton University.

Hancock, J. F. 2006. Lipid rafts: contentious only from simplistic standpoints. *Nature Reviews Mol. Cell Bio.* 7: 456-462.

Heberle, F. A., J. T. Buboltz, D. Stringer, and G. W. Feigenson. 2005. Fluorescence methods to detect phase boundaries in lipid bilayer mixtures. *Biochim. Biophys. Acta.* 1746: 186-192.

Heerklotz, H. 2002. Triton promotes domain formation in lipid raft mixtures. *Biophys. J.* 83: 2693-2701.

Heerklotz, H., and A. Tsamaloukas. 2006. Gradual change or phase transition: characterizing fluid lipid-cholesterol membranes on the basis of thermal volume changes. *Biophys. J.* 91: 600-607.

Heller, H., M. Schaefer, and K. Schulten. 1993. Molecular dynamics simulation of a bilayer of 200 lipids in the gel and in the liquid-crystal phases. *J. Phys. Chem.* 97: 8343-8360.

Henriksen, J., A. C. Rowat, E. Brief, Y. W. Hsueh, J. L. Thewalt, M. J. Zuckermann, and J. H. Ipsen. 2006. Universal behavior of membranes with sterols. *Biophys. J.* 90: 1639-1649.

Henriksen, J., A. C. Rowat, and J. H. Ipsen. 2004. Vesicle fluctuation analysis of the effects of sterols on membrane bending rigidity. *Eur. Biophys. J.* 33: 732-741.

Holowka, D., J. A. Gosse, A. T. Hammond, X. Han, P. Sengupta, N. L. Smith, A. Wagenknecht-Wiesner, M. Wu, R. M. Young, and B. Baird. 2005. Lipid segregation and IgE receptor signaling: a decade of progress. *Biochim. Biophys. Acta*. 1746: 252-259.

Hsueh, Y.-W., K. Gilbert, C. Trandum, M. Zuckermann, and J. Thewalt. 2005. The effect of ergosterol on dipalmitoylphosphatidylcholine bilayers: a deuterium NMR and calorimetric study. *Biophys. J.* 88: 1799-1808.

Huang, J., J. T. Buboltz, and G. W. Feigenson. 1999. Maximum solubility of cholesterol in phosphatidylethanolamine bilayers. *Biochim. Biophys. Acta.* 1417: 89-100.

Huang, J., and G. W. Feigenson. 1999. A microscopic interaction model of maximum solubility of cholesterol in lipid bilayers. *Biophys. J.* 76: 2142-2157.

Huang, T.-H., C. W. B. Lee, S. K. Das Gupta, A. Blume, and R. G. Griffin. 1993. A $^{13}C$ and $^{2}H$ nuclear magnetic resonance study of phosphatidylcholine/cholesterol interactions: characterization of liquid-gel phases. *Biochemistry.* 32: 13277-13287.

Hui, S. W., and N.-B. He. 1983. Molecular organization in cholesterol-lecithin bilayers by x-ray and electron diffraction measurements. *Biochemistry.* 22: 1159-1164.

Hung, W.-C., M.-T. Lee, F.-Y. Chen, and H. W. Huang. 2007. The condensing effect of cholesterol in lipid bilayers. *Biophys. J.* 92: 3960-3967.

Hura, G., J. M. Sorenson, R. M. Glaeser, and T. Head-Gordon. 2000. A high-quality x-ray scattering experiment on liquid water at ambient conditions. *J. Chem. Phys.* 113: 9140-9148.

Ipsen, J. H., G. Karlström, O. G. Mouritsen, H. Wennerström, and M. J. Zuckermann. 1987. Phase equilibria in the phosphatidylcholine-cholesterol system. *Biochim. Biophys. Acta.* 905: 162-172.

Ipsen, J. H., O. G. Mouritsen, and M. Bloom. 1990. Relationships between lipid membrane area, hydrophobic thickness, and acyl-chain orientational order. *Biophys. J.* 57: 405-412.

Israelachvili, J. N. 1985. Intermolecular and surface forces: with applications to colloidal and biological systems. Academic Press, London.

Jähnig, F. 1979. Molecular theory of lipid membrane order. *J. Chem. Phys.* 70: 3279-3290.

Jähnig, F. 1981. Critical effects from lipid-protein interaction in membranes. *Biophys. J.* 36: 329-345.

Janiak, M. J., D. M. Small, and G. G. Shipley. 1976. Nature of the thermal pretransition of synthetic phospholipids: dimyristoyl- and dipalmitoyllecithin. *Biochemistry*. 15: 4575-4580.

Kaganer, V. M., H. Möhwald, and P. Dutta. 1999. Structure and phase transitions in Langmuir monolayers. *Rev. Mod. Phys.* 71: 779-819.

Karmakar, S., and V. A. Raghunathan. 2003. Cholesterol-induced modulated phase in phospholipid membranes. *Phys. Rev. Lett.* 91: 098102.

Karmakar, S., and V. A. Raghunathan. 2005. Structure of phospholipid-cholesterol membranes: an x-ray diffraction study. *Phys. Rev. E.* 71: 061924.

Karmakar, S., V. A. Raghunathan, and S. Mayor. 2005. Phase behaviour of dipalmitoyl phosphatidylcholine (DPPC)-cholesterol membranes. *J. Phys.: Condens. Matter.* 17: S1177-S1182.

Karmakar, S., B. R. Sarangi, and V. A. Raghunathan. 2006. Phase behaviour of lipid-cholesterol membranes. *Solid State Comm.* 139: 630-634.

Katsaras, J. 1997. Highly aligned lipid membrane systems in the physiologically relevant "excess water" condition. *Biophys. J.* 73: 2924-2929.

Katsaras, J., S. Tristram-Nagle, Y. Liu, R. L. Headrick, E. Fontes, P. C. Mason, and J. F. Nagle. 2000. Clarification of the ripple phase of lecithin bilayers using fully hydrated, aligned samples. *Phys. Rev. E.* 61: 5668-5677.

Katsaras, J. and M. J. Watson. 2000. Sample cell capable of 100% relative humidity for x-ray diffraction of aligned lipid multibilayers. *Rev. Sci. Inst.* 71: 1737-1739.

Kelkar, V. K., and A. S. Paranjpe. 1987. Orientational order parameter of liquid-crystals by x-ray diffraction- a simple approach. *Mol. Cryst. Liq. Cryst. Lett.* 4: 139-144.

Kingsley, P. B., and G. W. Feigenson. 1979. The sysnthesis of a perdeuterated phospholipid: 1,2-dimyristoyl-sn-glycero-3-phosphocholine-d72. *Chem. Phys. Lipids.* 24: 135-147.

Kittel, C. 1957. Introduction to solid state physics. John Wiley and Sons, New York.

Kodati, V. R., and M. Lafleur. 1993. Comparison between orientational and conformational orders in fluid lipid bilayers. *Biophys. J.* 64: 163-170.

Korlach, J., P. Schwille, W. W. Webb, and G. W. Feigenson. 1999. Characterization of lipid bilayer phases by confocal microscopy and fluorescence correlation spectroscopy. *Proc. Natl. Acad. Sci. U. S. A.* 96: 8461-8466.

Kučerka, N., Y. Liu, N. Chu, H. I. Petrache, S. Tristram-Nagle, and J. F. Nagle. 2005a. Structure of fully hydrated fluid phase DMPC and DLPC lipid bilayers using x-ray scattering from oriented multilamellar arrays and from unilamellar vesicles. *Biophys. J.* 88: 2626-2637.

Kučerka, N., S. Tristram-Nagle, and J. F. Nagle. 2005b. Structure of fully hydrated fluid phase lipid bilayers with monounsaturated chains. *J. Membrane Biol.* 208: 193-202.

Kučerka, N., S. Tristram-Nagle, and J. F. Nagle. 2006. Closer look at structure of fully hydrated fluid phase DPPC bilayers. *Biophys. J.* 90: L83-L85.

Kusumi, A., and K. Suzuki. 2005. Toward understanding the dynamics of membrane-raft-based molecular interactions. *Biochim. Biophys. Acta.* 1746: 234-251.

Ladbrooke, B. D., R. M. Williams, and D. Chapman. 1968. Studies on lecithin-cholesterol-water interactions by differential scanning calorimetry and x-ray diffraction. *Biochim. Biophys. Acta.* 150: 333-340.

Lafleur, M., P. R. Cullis, and M. Bloom. 1990. Modulation of the orientational order profile of the lipid acyl chain in the $L_\alpha$ phase. *Eur. Biophys. J.* 19: 55-62.

Leadbetter, A. J. 1979. Structural studies of nematic, smectic A, and smectic C phases. *In* The Molecular Physics of Liquid Crystals. G. R. Luckhurst and G. W. Gray, eds. Academic Press, London.

Leadbetter, A. J., and E. K. Norris. 1979. Distribution functions in three liquid crystals from x-ray diffraction measurements. *Mol. Phys.* 38: 669-686.

Leadbetter, A. J., and P. G. Wrighton. 1979. Order parameters in $S_A$, $S_C$ and N phases by x-ray diffraction. *J. Phys. Colloq. France*. 40: C3-234-242.

Lecuyer, H., and D. G. Dervichian. 1969. Structure of aqueous mixtures of lecithin and cholesterol. *J. Mol. Biol.* 45: 39-57.

Lentz, B. R., Y. Barenholz, and T. E. Thompson. 1976. Fluorescence depolarization studies of phase transitions and fluidity in phospholipid bilayers. 2. Two-component phosphatidylcholine liposomes. *Biochemistry*. 15: 4529-4537.

Levine, Y. K. 1970. X-ray diffraction studies of oriented bimolecular layers of phospholipids. Ph. D. Thesis, University of London.

Levine, Y. K., and M. H. F. Wilkins. 1971. Structure of oriented lipid bilayers. *Nature New Biol.* 230: 69-72.

Li, L., and J.-X. Cheng. 2006. Coexisting stripe- and patch-shaped domains in giant unilamellar vesicles. *Biochemistry.* 45: 11819-11826.

Lindblom, G., L. B.-Å Johansson, and G. Arvidson. 1981. Effect of cholesterol in membranes. Pulsed nuclear magnetic resonance measurements of lipid lateral diffusion. *Biochemistry.* 20: 2204-2207.

Liu, Y. 2003. New method to obtain structure of biomembranes using diffuse x-ray scattering: application to fluid phase DOPC lipid bilayers. Ph. D. Thesis, Carnegie Mellon University.

Liu, Y., and J. F. Nagle. 2004. Diffuse scattering provides material parameters and electron density profiles of biomembranes. *Phys. Rev. E.* 69: 040901(R).

London, E. 2005. How principles of domain formation in model membranes may explain ambiguities concerning lipid raft formation in cells. *Biochim. Biophys. Acta*. 1746: 203-220.

Luzzati, V. 1968. X-ray diffraction studies of lipid-water systems. *In* Biological membranes: physical fact and function. D. Chapman, ed. Academic Press, London.

Mabrey, S., P. L. Mateo, and J. M. Sturtevant. 1978. High-sensitivity scanning calorimetric study of mixtures of cholesterol with dimyristoyl- and dipalmitoylphosphatidylcholines. *Biochemistry*. 17: 2464-2468.

Maier, V. W., and A. Saupe. 1958. Eine einfache molekulare Theorie des nematischen kristallinflüssigen Zustandes. *Z. Naturforsch.* 13a: 564-566.

Maier, V. W., and A. Saupe. 1959. Eine einfache molekular-statistische Theorie der nematischen kristallinflüssigen Phase. Teil I. *Z. Naturforsch.* 14a: 882-889.

Maier, V. W., and A. Saupe. 1960. Eine einfache molekular-statistische Theorie der nematischen kristallinflüssigen Phase. Teil II. *Z. Naturforsch.* 15a: 287-292.

Mathai, J., S. Tristram-Nagle, J. F. Nagle, and M. L. Zeidel. 2007. Structural determinants of water permeability through the lipid membrane. To be submitted to *The Journal of General Physiology*.

Maulik, P. R., and G. G. Shipley. 1996a. Interactions of *n*-stearoyl sphingomyelin with cholesterol and dipalmitoylphosphatidylcholine in bilayer membranes. *Biophys. J.* 70: 2256-2265.

Maulik, P. R., and G. G. Shipley. 1996b. N-palmitoyl sphingomyelin bilayers: structure and interactions with cholesterol and dipalmitoylphosphatidylcholine. *Biochemistry*. 35: 8025-8034.

McConnell, H. and A. Radhakrishnan. 2006. Theory of deuterium NMR of sterol-phospholipid membranes. *Proc. Natl. Acad. Sci.* 103: 1184-1189.

McConnell, H. M., and M. Vrljic. 2003. Liquid-liquid immiscibility in membranes. *Annu. Rev. Biophys. Biomol. Struct.* 32: 469-492.

McIntosh, T. J. 1978. The effect of cholesterol on the structure of phosphatidylcholine bilayers. *Biochim. Biophys. Acta.* 513: 43-58.

McIntosh, T. J., and S. A. Simon. 1986. Area per molecule and distribution of water in fully hydrated dilauroylphosphatidylethanolamine bilayers. *Biochemistry.* 25: 4948-4952.

McMullen, T. P. W., and R. N. McElhaney. 1995. New aspects of the interaction of cholesterol with dipalmitoylphosphatidylcholine bilayers as revealed by high-sensitivity differential scanning calorimetry. *Biochim. Biophys. Acta.* 1234: 90-98.

Megha, and London, E. 2004. Ceramide selectively displaces cholesterol from ordered lipid domains (rafts): implications for lipid raft structure and function. *J. Biol. Chem.* 279: 9997-10004.

Meyer, H. W., K. Semmler, and P. J. Quinn. 1997. The effect of sterols on structures formed in the gel/subgel phase state of dipalmitoylphosphatidylcholine bilayers. *Mol. Membr. Biol.* 14: 187-193.

Mortensen, K., W. Pfeiffer, E. Sackmann, and W. Knoll. 1988. Structural properties of a phosphatidylcholine-cholesterol system as studied by small-angle neutron scattering: ripple structure and phase diagram. *Biochim. Biophys. Acta.* 945: 221-245.

Motulsky, H., and A. Christopoulos. 2004. Fitting models to biological data using linear and nonlinear regression: a practical guide to curve fitting. Oxford University Press, New York.

Munro, S. 2003. Lipid rafts: elusive or illusive? *Cell*. 115: 377-388.

Münster, C., J. Lu, S. Schinzel, B. Bechinger, and T. Salditt. 2000. Grazing incidence x-ray diffraction of highly aligned phospholipid membranes containing the antimicrobial peptide magainin 2. *Eur. Biophys. J.* 28: 683-688.

Nagle, J. F. 1993. Area/lipid of bilayers from NMR. *Biophys. J.* 64: 1476-1481.

Nagle, J. F., and S. Tristram-Nagle. 2000. Structure of lipid bilayers. *Biochim. Biophys. Acta*. 1469: 159-195.

Nagle, J. F., and D. A. Wilkinson. 1978. Lecithin bilayers. Density measurements and molecular interactions. *Biophys. J.* 23: 159-175.

Needham, D., T. J. McIntosh, and E. Evans. 1988. Thermomechanical and transition properties of dimyristoylphosphatidylcholine/cholesterol bilayers. *Biochemistry*. 27: 4668-4673.

Needham, D., and Nunn, R.S. 1990. Elastic deformation and failure of lipid bilayer membranes containing cholesterol. *Biophys. J.* 58: 997-1009.

Nezil, F. A., and M. Bloom. 1992. Combined influence of cholesterol and synthetic amphiphilic peptides upon bilayer thickness in model membranes. *Biophys. J.* 61: 1176-1183.

Nicolini, C., P. Thiyagarajan, and R. Winter. 2004. Small-scale composition fluctuations and microdomain formation in lipid raft models as revealed by small-angle neutron scattering. *Phys. Chem. Chem. Phys.* 6: 5531-5534.

Nishimura, S. Y., M. Vrljic, L. O. Klein, H. M. McConnell, and W. E. Moerner. 2006. Cholesterol depletion induces solid-like regions in the plasma membrane. *Biophys. J.* 90: 927-938.

Oldenbourg, R., X. Wen, R. B. Meyer, and D. L. D. Caspar. 1988. Orientational distribution function in nematic tobacco-mosaic-virus liquid crystals measured by x-ray diffraction. *Phys. Rev. Lett.* 61: 1851-1854.

Oldfield, E., M. Meadows, D. Rice, and R. Jacobs. 1978. Spectroscopic studies of specifically deuterium labeled membrane systems. Nuclear magnetic resonance investigation of the effects of cholesterol in model systems. *Biochemistry*. 17: 2727-2740.

Özdilek, C., E. Mendes, and S. J. Picken. 2006. Nematic phase formation of Boehmite in polyamide-6 nanocomposites. *Polymer.* 47: 2189-2197.

Pan, J., S. Tristram-Nagle, N. Kučerka, and J. F. Nagle. 2007. Temperature dependence of structure, bending rigidity, and bilayer interactions of dioleoylphosphatidylchonine. Manuscript in progress.

Paranjpe, A. S., and V. K. Kelkar. 1984. Chain ordering in the nematic phase of 40BA. *Mol. Cryst. Liq. Cryst.* 102: 289-294.

Paré, Chantal, and M. Lafleur. 1998. Polymorphism of POPE/cholesterol system: a $^{2}$H nuclear magnetic resonance and infrared spectroscopic investigation. *Biophys. J.* 74: 899-909.

Pencer, J., T. T. Mills, V. Anghel, S. Krueger, R. M. Epand, and J. Katsaras. 2005. Detection of submicron-sized raft-like domains in membranes by small-angle neutron scattering. *Eur. Phys. J. E.* 18: 447-458.

Perly, B., I. Smith, and H. Jarell. 1985. Effects of the replacement of a double-bond by a cyclopropane ring in phosphatidylethanolamine- a 2H NMR relaxation study. *Biochemistry.* 24: 1055-1063.

Petrache, H. I., S. W. Dodd, and M. F. Brown. 2000. Area per lipid and acyl length distributions in fluid phosphatidylcholines determined by $^{2}$H NMR spectroscopy. *Biophys. J.* 79: 3172-3192.

Petrache, H. I., D. Harries, and V. A. Parsegian. 2005. Alteration of lipid membrane rigidity by cholesterol and its metabolic precursors. *Macromol. Symp.* 219: 39-50.

Picken, S. J. 1989. Clearing temperatures of aramid solutions in sulfuric acid. *Macromolecules.* 22: 1766-1771.

Polozov, I. V., and K. Gawrisch. 2006. Characterization of the liquid-ordered state by proton MAS NMR. *Biophys. J.* 90: 2051-2061.

Potma, E. O., and X. S. Xie. 2005. Direct visualization of lipid phase segregation in single lipid bilayers with coherent anti-stokes Raman scattering microscopy. *Chem. Phys. Chem.* 6: 77-79.

Purdy, K. R., Z. Dogic, S. Fraden, A. Rühm, L. Lurio, and S. G. J. Mochrie. 2003. Measuring the nematic order of suspensions of colloidal fd virus by x-ray diffraction and optical birefringence. *Phys. Rev. E.* 67: 031708.

Pynn, R. 1975. X-ray and neutron diffraction by nematic liquid crystals. *Acta Cryst.* A31: 323-327.

Radhakrishnan, A., and H. McConnell. 2005. Condensed complexes in vesicles containing cholesterol and phospholipids. *Proc. Nat. Acad. Sci.* 102: 12662-12666.

Rand, R. P., and V. A. Parsegian. 1989. Hydration forces between phospholipid bilayers. *Biochim. Biophys. Acta.* 988: 351-376.

Rand, R. P., V. A. Parsegian, J. A. C. Henry, L. J. Lis, and M. McAlister. 1980. The effect of cholesterol on measured interaction and compressibility of dipalmitoylphosphatidylcholine bilayers. *Can. J. Biochem.* 58: 959-968.

Recktenwald, D. J., and H. M. McConnell. 1981. Phase equilibria in binary mixtures of phosphatidylcholine and cholesterol. *Biochemistry.* 20: 4505-4510.

Reinl, H., T. Brumm, and T. M. Bayerl. 1992. Changes in the physical properties of the liquid-ordered phase with temperature in binary mixtures of DPPC with cholesterol: a $^{2}$H -NMR, FT-IR, DSC, and neutron scattering study. *Biophys. J.* 61: 1025-1035.

Roe, R.-J. 2000. Methods of x-ray and neutron scattering in polymer science. Oxford University Press, New York.

Rubenstein, J. L. R., B. A. Smith, and H. M. McConnell. 1979. Lateral diffusion in binary mixtures of cholesterol and phosphatidylcholines. *Proc. Natl. Acad. Sci. USA.* 76: 15-18.

Samsonov, A. V., I. Mihalyov, and F. S. Cohen. 2001. Characterization of cholesterol-sphingomyelin domains and their dynamics in bilayer membranes. *Biophys. J.* 81: 1486-1500.

Sankaram, M. B., and T. E. Thompson. 1990. Modulation of phospholipid acyl chain order by cholesterol. A solid-state $^{2}$H nuclear magnetic resonance study. *Biochemisrty.* 29: 10676-10684.

Sankaram, M. B., and T. E. Thompson. 1991. Cholesterol-induced fluid-phase immiscibility in membranes. *Proc. Natl. Acad. Sci. USA.* 88: 8686-8690.

Savenko, S. V., and M. Dijkstra. 2004. Accuracy of measuring the nematic order from intensity scatter: a simulation study. *Phys. Rev. E.* 70: 011705.

Scheidt, H. A., D. Huster, and K. Gawrisch. 2005. Diffusion of cholesterol and its precursors in lipid membranes studied by $^{1}$H pulsed field gradient magic angle spinning NMR. *Biophys. J.* 89: 2504-2512.

Schindler, H., and J. Seelig. 1975. Deuterium order parameters in relation to thermodynamic properties of a phospholipid bilayer. A statistical mechanical interpretation. *Biochemistry*. 14: 2283-2287.

Seelig, J., and J. L. Browning. 1978. General features of phospholipid conformation in membranes. *FEBS Lett.* 92: 41-44.

Seelig, J., and W. Niederberger. 1974. Deuterium-labeled lipids as structural probes in liquid crystalline bilayers. A deuterium magnetic resonance study. *J. Amer. Chem. Soc.* 96: 2069-2072.

Seelig, A., and J. Seelig. 1974. The dynamic structure of fatty acyl chains in a phospholipid bilayer measured by deuterium magnetic resonance. *Biochemistry*. 13: 4839-4845.

Sega, M., G. Garberoglio, P. Brocca, and L. Cantù. 2007. Microscopic structure of phospholipid bilayers: comparison between molecular dynamics simulations and wide-angle x-ray spectra. *J. Phys. Chem. B.* 111: 2484-2489.

Shimshick, E. J., and H. M. McConnell. 1973. Lateral phase separations in binary mixtures of cholesterol and phospholipids. *Biochem. Biophys. Res. Commun.* 53: 446-451.

Silvius, J. R. 2003. Role of cholesterol in lipid raft formation: lessons from lipid model systems. *Biochim. Biophys. Acta.* 1610: 174-183.

Simons, K., and E. Ikonen. 1997. Functional rafts in cell membranes. *Nature*. 387: 569-572.

Simons, K., and G. van Meer. 1988. Lipid sorting in epithelial cells. *Biochemistry*. 27: 6197-6202.

Simons, K., and W. L. C. Vaz. 2004. Model systems, lipid rafts, and cell membranes. *Annu. Rev. Biophys. Biomol. Struct.* 33: 269-295.

Singer, S. J., and G. L. Nicholson. 1972. The fluid mosaic model of the structure of cell membranes. *Science*. 175: 720-731.

Smith, G. S., E. B. Sirota, C. R. Safinya, and N. A. Clark. 1988. Structure of the Lβ phases in a hydrated phosphatidylcholine multimembrane. *Phys. Rev. Lett.* 60: 813-816.

Smondyrev, A. M., and M. L. Berkowitz. 1999. Structure of dipalmitoylphosphatidylcholine/cholesterol bilayer at low and high cholesterol concentrations: molecular dynamics simulation. *Biophys. J.* 77: 2075-2089.

Spaar, A., and T. Salditt. 2003. Short range order of hydrocarbon chains in fluid phospholipid bilayers studied by x-ray diffraction from highly oriented membranes. *Biophys. J.* 85: 1576-1584.

Spaar, A., C. Münster, and T. Salditt. 2004. Conformation of peptides in lipid membranes studied by x-ray grazing incidence scattering. *Biophys. J.* 87: 396-407.

Spiegel, M. R. 1998. Schaum's mathematical handbook of formulas and tables. McGraw-Hill, New York.

Stockton, G. W., and I. C. Smith. 1976. A deuterium nuclear magnetic resonance study of the condensing effect of cholesterol on egg phosphatidylcholine bilayer membranes. I. Perdeuterated fatty acid probes. *Chem. Phys. Lipids.* 17: 251-263.

Stottrup, B. L., D. S. Stevens, and S. L. Keller. 2005. Miscibility of ternary mixtures of phospholipids and cholesterol in monolayers, and application to bilayer systems. *Biophys. J.* 88: 269-276.

Sun, W.-J., R. M. Suter, M. A. Knewtson, C. R. Worthington, S. Tristram-Nagle, R. Zhang, and J. F. Nagle. 1994. Order and disorder in fully hydrated unoriented bilayers of gel phase dipalmitoylphosphatidylcholine. *Phys. Rev. E.* 49: 4665-4676.

Tardieu, A., V. Luzzati, and F. C. Reman. 1973. Structure and polymorphism of the hydrocarbon chains of lipids: a study of lecithin-water phases. *J. Mol. Biol.* 75: 711-733.

Tate, M. W., S. M. Gruner, and E. F. Eikenberry. 1997. Coupling format variations in x-ray detectors based on charge coupled devices. *Rev. Sci. Instrum.* 68: 47-54.

Thewalt, J. L., and M. Bloom. 1992. Phosphatidylcholine: cholesterol phase diagrams. *Biophys. J.* 63: 1176-1181.

Tristram-Nagle, S. 2007. Preparation of oriented, fully hydrated lipid samples for structure determination using x-ray scattering. *In* Methods in membrane lipids. A. M. Dopico, ed. Humana Press, Totowa.

Tristram-Nagle, S., Y. Liu, J. Legleiter, and J. F. Nagle. 2002. Structure of gel phase DMPC determined by x-ray diffraction. *Biophys. J.* 83: 3324-3335.

Tristram-Nagle, S., and J. F. Nagle. 2007. HIV-fusion peptide decreases bending energy, promotes curved fusion intermediates. Accepted by *Biophys. J.*

Tristram-Nagle, S., H. I. Petrache, and J. F. Nagle. 1998. Structure and interactions of fully hydrated dioleoylphosphatidylcholine bilayers. *Biophys. J.* 75: 917-925.

Tristram-Nagle, S., J. N. Sachs, N. Kučerka, S. E. Feller, and J. F. Nagle. 2007. Strategy for structure determination of lipid/cholesterol bilayers. 2007 Biophysical Society Meeting Abstracts. *Biophys. J.*, Supplement, 425a, Abstract, 2038-Pos.

Tristram-Nagle, S., R. Zhang, R. M. Suter, C. R. Worthington, W.-J. Sun, and J. F. Nagle. 1993. Measurement of chain tilt angle in fully hydrated bilayers of gel phase lecithins. *Biophys. J.* 64: 1097-1109.

Urbina, J. A., S. Pekerar, H.-b. Le, J. Patterson, B. Montez, and E. Oldfield. 1995. Molecular order and dynamics of phosphatidylcholine bilayer membranes in the presence of cholesterol, ergosterol, and lanosterol: a comparative study using $^{2}$H-, $^{13}$C-, and $^{31}$P-NMR spectroscopy. *Biochim. Biophys. Acta.* 1238: 163-176.

Vainshtein, B. K. 1966. Diffraction of x-rays by chain molecules. Elsevier, Amsterdam.

Veatch, S. L. 2004. Liquid immiscibility in model bilayer lipid membranes. Ph. D. Thesis, University of Washington.

Veatch, S. L. 2007. From fluctuations to phase separation: lateral organization in model membranes containing cholesterol. Review submitted.

Veatch, S. L., and S. L. Keller. 2003a. A closer look at the canonical raft mixture in model membrane studies. *Biophys. J.* 84: 725-726.

Veatch, S. L., and S. L. Keller. 2003b. Separation of liquid phases in giant vesicles of ternary mixtures of phospholipids and cholesterol. *Biophys. J.* 85: 3074-3083.

Veatch, S. L., and S. L. Keller. 2005a. Miscibility phase diagrams of giant vesicles containing sphingomyelin. *Phys. Rev. Lett.* 94: 148101.

Veatch, S. L., and S. L. Keller. 2005b. Seeing spots: complex phase behavior in simple membranes. *Biochim. Biophys. Acta.* 1746: 172-185.

Veatch, S. L., K. Gawrisch, and S. L. Keller. 2006. Closed-loop miscibility gap and quantitative tie-lines in ternary membranes containing diphytanoyl PC. *Biophys. J.* 90: 4428-4436.

Veatch, S.L., I. V. Polozov, K. Gawrisch, and S. L. Keller. 2004. Liquid domains in vesicles investigated by NMR and fluorescence microscopy. *Biophys. J.* 86: 2910-2922.

Veatch, S. L., S. S. W. Leung, R. E. W. Hancock, and J. L. Thewalt. 2007a. Fluorescent probes alter miscibility phase boundaries in ternary vesicles. *J. Phys. Chem. B.* 111: 502-504.

Veatch, S. L., O. Soubias, S. L. Keller, and K. Gawrisch. 2007b. Critical fluctuations in domain-forming lipid mixtures. Submitted to *Proc. Natl. Acad. Sci. USA.*

Vist, M. R., and J. H. Davis. 1990. Phase equilibria of cholesterol/dipalmitoylphosphatidylcholine mixtures: $^{2}H$ nuclear magnetic resonance and differential scanning calorimetry. *Biochemistry.* 29: 451-464.

Wang, J., Megha, and E. London. 2004. Relationship between sterol/steroid structure and participation in ordered lipid domains (lipid rafts): implications for lipid raft structure and function. *Biochemistry*. 43: 1010-1018.

Wang, T.-Y., and J. R. Silvius. 2001. Cholesterol does not induce segregation of liquid-ordered domains in bilayers modeling the inner leaflet of the plasma membrane. *Biophys. J.* 81: 2762-2773.

Warren, B. E. 1933. X-ray diffraction in long chain liquids. *Phys. Rev*. 44: 969-973.

Warren, B. E. 1969. X-ray diffraction. Addison-Wesley, Reading.

Warschawski, D. E., and P. F. Devaux. 2005. Order parameters of unsaturated phospholipids in membranes and the effect of cholesterol: a $^{1}H$-$^{13}C$ solid-state NMR study at natural abundance. *Eur. Biophys. J.* 34: 987-996.

Wechsler, A., A. Brafman, M. Shafir, M. Heverin, H. Gottlieb, G. Damari, S. Gozlan-Kelner, I. Spivak, O. Moshkin, E. Fridman, Y. Becker, R. Skaliter, P. Einat, A. Faerman, I. Björkhem, and E. Feinstein. 2003. Generation of viable cholesterol-free mice. *Science.* 302: 2087.

Xu, X., R. Bittman, G. Duportail, D. Heissler, C. Vilcheze, and E. London. 2001. Effect of the structure of natural sterols and sphingolipids on the formation of ordered sphingolipid/sterol domains (rafts). *J. Biol. Chem.* 276: 33540-33546.

Xu, X., and E. London. 2000. The effect of sterol structure on membrane lipid domains reveals how cholesterol can induce lipid domain formation. *Biochemistry.* 39: 843-849.

Yang, L., and H. W. Huang. 2002. Observation of a membrane fusion intermediate structure. *Science.* 297: 1877-1879.

Yeagle, P. L. 1985. Cholesterol and the cell membrane. *Biochim. Biophys. Acta.* 822: 267-287.

Zhao, J., J. Wu, F. A. Heberle, T. T. Mills, P. Klawitter, G. Huang, G. Costanza, and G. W. Feigenson. 2007a. Phase studies of model biomembranes: complex behavior of DSPC/DOPC/cholesterol. submitted to *Biochim. Biophys. Acta.*

Zhao, J., J. Wu, H. Shao, F. Kong, N. Jain, G. Hunt, and G. W. Feigenson. 2007b. Phase studies of model biomembranes: macroscopic coexistence of Lα + Lβ, with light-induced coexistence of Lα + Lo phases. Submitted to *Biochim. Biophys. Acta.*

Zuckermann, M. J., J. H. Ipsen, and O. G. Mouritsen. 1993. Theoretical studies of the phase behavior of lipid bilayers containing cholesterol. *In* Cholesterol in Membrane Models. L. Finegold, ed. CRC Press, Boca Raton.